THE UNIVERSITY
of LIVERPOOL

Characterisation of Building Materials and Indoor Radio Channel

Thesis submitted in accordance with the
requirements of the University of Liverpool
for the degree of Doctor of Philosophy

in

Department of Electrical Engineering and Electronics

By

Jietao Zhang

April 2003

To my family,

I don't know where I would be without you.

Abstract

The proliferation of wireless communication systems used in business and residential areas has resulted in a growing demand for a better understanding of the characteristics of radio propagation within the environments.

The interaction of propagating radio waves with building structures is mainly governed by the mechanisms of reflection, transmission and diffraction, which are determined by the dielectric properties of the building structures. As part of an investigation into the effects of building materials on radio channel characteristics, a free-space monostatic measurement system has been developed for *in-situ* characterisation of various building materials. Using this system, the constitutive parameters, namely, the permittivity, conductivity and thickness of the building materials under test can be simultaneously determined. These parameters are used for the calculation of the radio channel model input coefficients, namely, reflection coefficient, transmission coefficient and diffraction coefficient.

A 3D ray-tracing algorithm based on Geometric Optics (GO) and Uniform Diffraction Theory (UTD) has been developed for the indoor radio channel characterisation. With the use of the geometry blueprint and the constitutive parameters of building structures, both narrow- and wide-band channel parameters can be predicted. A substantial improvement in the efficiency of the model can be achieved by the proper definition of elements in the geometric database and the utilisation of a ray tree algorithm. A further enhancement in the efficiency without serious accuracy degradation can be achieved with the development of a simplified ray-tracing model.

The effects of dielectric properties of the building structures on radio propagation have been investigated using the ray-tracing model. Simulation results have shown that to some extent the indoor radio channel is sensitive to the building dielectric properties. This justifies the use of free-space *in-situ* characterisation of building structures for accurate radio channel modelling.

Acknowledgements

I would like to express my sincere thanks to my supervisor Dr Yi Huang, for his constant encouragement and guidance throughout the course of this research. The financial support and invaluable advice from him are particularly appreciated.

I wish to acknowledge the helpful discussions with the members of RF Engineering and Communication Group in the Department of Electrical Engineering & Electronics. Particularly, I would like to express my appreciations to Mr D. Kemp, Dr M. Nakhkash, Dr S. Naruniranat and Mr J. Davis for their invaluable discussions and help. Also, appreciation and thanks go to Mrs B. Lussey for her constant help.

Finally, my greatest appreciation must go to my parents and my brother and sister for their love, understanding, encouragement and enormous support during all the time.

Contents

List of Figures

List of Tables

Chapter 1

Introduction

The growth of wireless communications in the last two decades has been spectacular, placing an ever-increasing demand on ubiquitous communications. Thanks to the cellular concept in wireless communications, the dream that a communication user may have access to another user "anytime, anywhere" to exchange "any kind" of information appears not far away [1], [2]. The cellular mobile communications industry has recently become one of the fastest-growing industries of all time. The extent to which system and technology, as well as service and application aspects of mobile communications has progressed in the past few years is breathtaking, with the number of users increasing dramatically. This evolution is due to a wide set of social, technological, and market forces.

Third-generation (3G) communication systems – the Universal Mobile Telecommunication System (UMTS) [3], which are currently under intensive development, will provide a single set of standards which can meet a wide range of wireless requirements, and a variety of voice, data and video communication services will be available. The development of UMTS is based on the success of the global system for mobile communications (GSM) [4] and is designed in such a way as to be perceived by customers as a broadband evolution of the second-generation (2G) technologies. It aims at integrating all different services of 2G systems, while providing true mobile multimedia capabilities. UMTS will deliver information directly to users and provide access to new and innovative services and applications beyond the capabilities of the current 2G systems. It has the capability to provide low-cost, high-capacity mobile communications, whilst offering data rates up to 2 Mbps with global roaming and other advanced features [3].

UMTS represents a new generation of global mobile communication systems in which personal services will be based on a combination of wireless/mobile and fixed services. It is aiming to provide a seamless end-to-end link between users. To achieve such huge communication capacity, the radio access network of UMTS is built in a hierarchical structure as shown in Fig. 1.1, with the deployment of several cellular network levels covering the populated areas of the earth. The pico-cell in-building layer, the micro-cell layer and the macro-cell layer are overlapped each other, providing full terrestrial coverage. Full global coverage will be provided by the highest layer -- the satellite system.

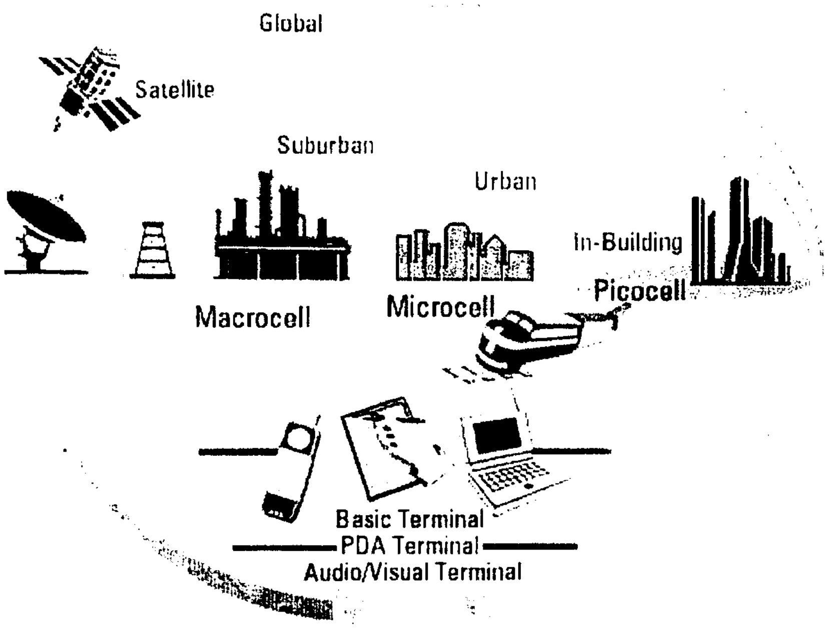

Figure 1.1: Hierarchical cell structure of UMTS [3].

1.1 Indoor Wireless Communications

As the demand for mobile communications grows, especially in densely populated urban areas and indoor environments, smaller and smaller cells are necessary due to the scarcity of spectrum resources. Micro- and pico-cells are usually formed for providing mobile communications within these areas. Higher system capacity is often achieved by minimising the cell size thus enabling increased frequency reuse [4]. The definitions of micro- and pico-cells are [5]:

Micro-cells: – Designed for high traffic densities in urban and suburban areas to users both outdoors and within buildings. Base station antenna heights are lower than nearby building rooftops, thus the coverage area is defined by the street layout. A typical cell dimension is within 500 m.

Pico-cells: – Customed for very high traffic density or high data rate applications within an indoor environment. Users may be both mobile and fixed. A typical example of fixed users is the computers interconnected by wireless local area networks (WLANs). The coverage area is defined by the shape and characteristics of rooms, and the service quality is dictated by the presence of furniture and people.

Indoor wireless communications are increasingly popular for cellular communications in high-traffic areas. They cover a wide variety of situations ranging from communications with users walking in railway stations, airports, office and residential buildings, and shopping malls, etc. to wireless data transmission between computers or robots in motion. Indoor wireless solutions offer distinct advantages over cable networks, such as mobility of users, elimination of cabling, and the flexibility to change, and creates various new communication services. Micro-cells provide the indoor coverage, a requirement when the signal from outdoor cells is weak or when additional capacity is needed. If the base station is located inside a building, a pico-cell is formed for mobile communications between indoor subscribers. Indoor WLANs, which conform to IEEE802.11b (working in globally available unlicensed ISM band around 2.4 GHz) or IEEE802.11a (working at 5.0 GHz) standards [6], have also attracted a lot of attention from equipment manufacturers, because they represent the merging of two of the fastest-growing segments of the computer industry, i.e. LANs and mobile computing. The newly proposed systems working in the 2.45 GHz region, such as HomeRF [7] and Bluetooth [8] capable of providing the basis for communications between portable devices in an ad hoc fashion by creating personal area network, also have wide applications in indoor environments.

1.2 Objective of the Research

Indoor wireless communications offer a highly attractive means of combined voice and data transmission and are expected to play a significant role in the deployment of personal communication systems. As well as stimulating financial investment in such systems, this has also given rise to a large number of technical challenges, many of which rely on an in-depth understanding of the characteristics of wireless channels for their solution. Detailed knowledge of radio propagation inside buildings is essential, not only for the successful design of new indoor wireless communications systems, but also for the accurate planning and successful deployment of currently existing systems.

This thesis is concerned with the study of radio propagation characteristics within indoor environments. The objective of the research is divided into the following areas:

(1) Measurement of the dielectric properties of building materials;
(2) Prediction of the indoor radio propagation channel.

Radio waves propagating inside indoor environments interact with the building structures by various mechanisms: reflection, transmission and diffraction [9]. These propagation mechanisms complement the basic effects of wave attenuation and phase velocity and provide a basis for practical prediction of system performance. In practice, boundaries between media, such as the walls and the air, the ground and the air, etc., form electromagnetic discontinuities where the properties of radio waves are changed. These boundary effects give rise to modifications in the amplitude, phase and direction of radio waves. To quantify the effects of building structures on indoor propagating radio waves, the knowledge of the dielectric properties of building materials is required. In this research, a free-space measurement system capable of deriving the dielectric parameters of building materials has been developed and tested. It allows quick *in-situ* characterisation of the dielectric properties of building materials in a non-destructive way.

The prediction of radio propagation characteristics within indoor environments is required in order to facilitate the implementation of various wireless communication systems, such as providing estimation of the system coverage and evaluation of transmission scheme for broadband networks. To analyse indoor radio propagation, a method capable of modelling the propagation mechanisms in the designated environment is required, since these mechanisms account for the propagation characteristics of the radio channel. In this research, a site-specific three-dimensional (3D) prediction model based on the ray-tracing method has been developed. The model is capable of providing comprehensive narrow- and wide-band parameters of a radio channel. Incorporating a user-defined database, the model can be used to investigate radio propagation within any indoor environment.

1.3 Overview of the Thesis

The preceding sections discussed the importance and objective of the research. Following on from this introduction, the remainder of the thesis is structured into six chapters:

Chapter 2 describes an *in-situ* measurement solution to the characterisation of building materials. A monostatic free-space measurement system has been developed for this purpose. The experimental and subsequent data processing procedures are described. Results of the measurements conducted on sample materials in laboratory environments and on various building materials in real sites are presented. A discussion of the results is also provided.

Chapter 3 reviews the radio channel characteristics and important channel parameters. Different channel modelling methods, ranging from empirical to deterministic models, are presented and compared.

Chapter 4 describes the development of our 3D ray-tracing model. Various aspects regarding design of the model such as the database, the ray-tracing algorithm, and the mathematical formulas are presented. A new ray tree algorithm based on the projection of 3D structures into 2D scenes is described, by which the efficiency of the model is significantly improved.

Chapter 5 presents the indoor simulations using the ray-tracing model described above. Evaluation of the model is performed by the comparison of simulation results of some particular scenarios with published data and with field measurement data. Simulation results of the radio channels in the building of Department of Electrical Engineering and Electronics are presented to extract their statistical characteristics. A simplified ray-tracing model for the purpose of reducing the computation time is described.

Chapter 6 presents a numerical study of the effects of building dielectric properties on the indoor radio propagation. Their effects in outdoor environments are discussed briefly; while in the indoor environments they are investigated in more details. Simulation results of both narrow- and wide-band channel parameters are compared with different dielectric parameters assigned to the building materials in the database.

Finally, Chapter 7 presents a summary of the work and some indications of future developments expected in the research.

Chapter 2

In-Situ Characterisation of Building Materials

2.1 Introduction

The measurement of the electromagnetic properties of materials is based on the fact that the electromagnetic energy propagates through the material under test and is partially transmitted/reflected due to discontinuities in electromagnetic parameters of the material, i.e., the permittivity, permeability and conductivity. A source radiates an electromagnetic wave into the material. The subsequent transmitted/reflected wave, which is captured by the receiving antenna, is processed to extract the desired information.

Measurements of the electromagnetic properties of materials have attracted many research activities in recent years [10-21], due to the increasing demands in various applications. Examples can be found in medical (classification of organic tissue), military (radar reflections on materials) and commercial sectors (electronic materials characterisation), etc.

Conventionally, the cavity, transmission line, and waveguide methods have been extensively employed for this purpose [10-12]. In these methods, a sample of the material under test is inserted into a waveguide or coaxial transmission line. The electromagnetic parameters of the material are determined from the measurement of its scattering parameter or propagation constant. The main disadvantage of these methods is the necessity to machine the material samples into a specific size and shape in order to fit into a material holder or resonator. In other words, these methods are destructive to the material under test. Moreover, the accuracy of measurements is limited for materials that cannot be machined precisely into the waveguide cross-section or cavity. In the context of characterisation of building materials, it is unlikely to obtain a sample since the material under test is usually physically fixed, such as a wall and a window. Therefore, these methods are neither practical nor preferred due to their destructive nature.

The method of using an open-ended coaxial probe offers some promise in non-destructive characterisation of materials and has been successfully employed [13], [14]. In this method, a coaxial probe is pressed against the surface of the material under test and the measured reflection coefficient is used to extract its electromagnetic parameters. However, there are two main drawbacks of this technique, which limits its range of applications. One is that the upper useful frequency range is limited by the occurrence of higher-order modes; the other is that the probe aperture needs to be in extremely good contact with material under test and a small gap between them can cause a large error in the measured electromagnetic parameters due to the existence of higher order modes at the aperture [14]. For example, a change of up to 80% error in the measured permittivity of an alumina sample is found for a 1.0-mm wide air gap in between the inner conductor and the material surface [15]. The coaxial probe measurement method is therefore suitable only for planar materials with a smooth surface or for materials in liquid form. For typical building materials whose surfaces are not perfectly flat and smooth, the open-ended coaxial method is not preferred. Moreover, the open-ended coaxial probe only measure the local material properties near the contact points of the probes, and local variations of the properties may have significant influences on the measurement results. Some inhomogeneities are expected in building materials and the effective dielectric properties need to be measured rather than the dielectric properties of a sub-section of the material.

Another method for measurements of the electromagnetic parameters is the free-space technique [16-22], which has been extensively investigated. In this method, antennas are used instead to transmit signals to and receive signals from the material under test. Considering the material as a two-port network, the measured S-parameters are used to predict the electromagnetic parameters of the material. The free-space technique can offer several advantages over the aforementioned methods as follows:

- The material under test can be measured over a wide frequency span, unlike waveguide or cavity methods that require a sample to be fitted into a fixture for each band;
- Materials such as composites are inhomogeneous due to variations in manufacturing processes. Because of inhomogeneity, the unwanted higher order modes can be excited at an air dielectric interface in waveguides and cavities.
- Measurements using the free-space technique are non-destructive and non-contact. Because of this feature, this method is particularly suitable for the measurements in high-/low-temperature environments.

In view of the above advantages, the free-space measurement technique is preferred for our applications. There are three basic methods used to measure the electromagnetic properties of materials: 1) the transmission coefficient measurement [16-18]; 2) the reflection coefficient measurement [19-21]; and 3) a combination of the above two [22]. For measurements of the transmission coefficient of a material, the material under test is placed between the transmitting and receiving antennas separated a certain distance apart, and the electromagnetic wave transmitted through the material is detected and processed to extract its electromagnetic parameters. In this measurement configuration, the precise alignment between the axes of the transmitting and receiving antennas is required in the procedures of both system calibration using the thru-reflect-line (TRL) method [17] and the real measurements. For *in-situ* measurements, the antennas are unlikely able to be precisely aligned because of the blockage of the material, which limits this application mostly to laboratory environments where both antennas are precisely aligned before placing a material sample in between. For measurements of the reflection coefficient of a material, two antennas with the same incident angles to the surface of the material under test are generally used as the transmitting and receiving antennas, respectively. This is called bistatic measurement system [19]. By varying the incident angles of the two antennas simultaneously, the reflected signal from the material is detected and used to extract its electromagnetic parameters. The drawback of this method is that measurements in the case of oblique incidence results in low signal-to-noise ratio (SNR) and hence more difficult to extract the desired information. Moreover, both antennas need to be positioned at the same angle towards the centre of the material under test, which makes the system configuration much time-consuming and difficult.

For our *in-situ* measurements of building materials, the transmission coefficient measurement method is not preferred because of the difficulty in precise alignment of both antennas. The bistatic reflection coefficient measurement method is neither preferred due to low SNR obtained. For our applications, a monostatic measurement system, which employs only one antenna directing at normal incidence to the material surface, is proposed because of its ease in the system configuration and hence more suitable for quick and routine measurements.

In this chapter, an experimental solution is presented for the non-destructive, non-contact, and *in-situ* characterisation of dielectric building materials using a monostatic free-space measurement system. Being a non-destructive and non-contact method, the technique is well suited for quick and routine evaluation of broadband material characteristics. Section 2.2 describes the configuration of our free-space measurement system. In Section 2.3, a brief description of the theory behind the free-space measurement method and the technique for data inversion are given. Section 2.4 describes the measurement procedure and the processing of measurement data. Section 2.5 provides examples of measurements of some known materials, which are used to validate the measurement technique. Section 2.6 deals with the *in-situ* measurements on some typical building materials including walls, windows and doors, etc. Results of the measurements are presented and discussed. Section 2.7 is devoted to the analysis of the measurement system.

2.2 System Configuration

A schematic diagram of the free-space experiment system is shown in Fig. 2.1. The measurement system consists of a network analyser and a TEM horn antenna. The antenna is connected to the S parameter test set of the network analyser via a coaxial cable and coaxial to TEM horn antenna connector. The network analyser both generates the signal transmitted to the antenna and captures the signal received by the antenna. The data recorded by the network analyser is then downloaded to a personal computer for data processing and inversion. The microwave signal generated from the network analyser is fed to the antenna, which focuses the energy where the material under test of thickness d is placed. The material is in general either a single-layered homogeneous material or a multi-layered composite. The front surface of the material is oriented such that the normal to its surface is aligned with the axis of the antenna. The separation between the surface and the aperture of the antenna is defined as R. Compared to other existing free-space measurement systems, the desired features of our free-space measurement system are as follows:

- The measurement system should be portable, i.e., the system should be small in size and light in weight;

- The measurement system should be at low cost;
- The system configuration should be simple enough for routine measurements;
- It should be capable of extracting the dielectric parameters of single- or multi-layered materials.

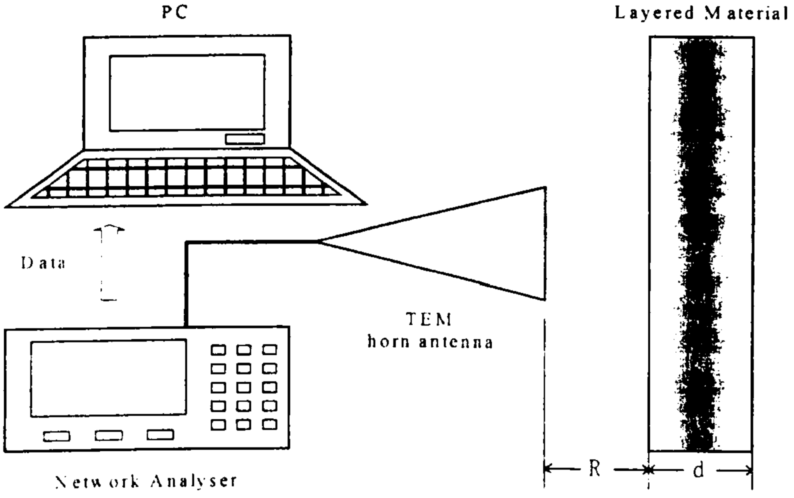

Figure 2.1: Schematic diagram of the measurement system configuration.

In order to fulfil the above features, use is made of a handheld vector network analyser 'SiteMaster S331B' manufactured by Anritsu [23] and a small-sized TEM horn antenna developed by the RF Engineering and Communication Group in Department of Electrical Engineering and Electronics, University of Liverpool. Utilising these two components, a portable and compact measurement system (illustrated in the photograph of Fig. 2.2) has been developed.

The SiteMaster is a single-port S parameter test vector network analyser which works in a continuous-wave swept-frequency mode. It generates a constant-amplitude swept-frequency sinusoidal signal over a tuneable frequency range of 25 MHz – 3.0 GHz. In our measurement system, the whole frequency range is utilised because it provides the maximum available frequency bandwidth. The signal generated is therefore equivalent to generating a short pulse sequence in the time domain. The maximum number of sampling points in the frequency domain is 1601, resulting in about 2 MHz resolution. The SiteMaster is capable of measuring return loss of up to 54 dB, with 0.01 dB resolution.

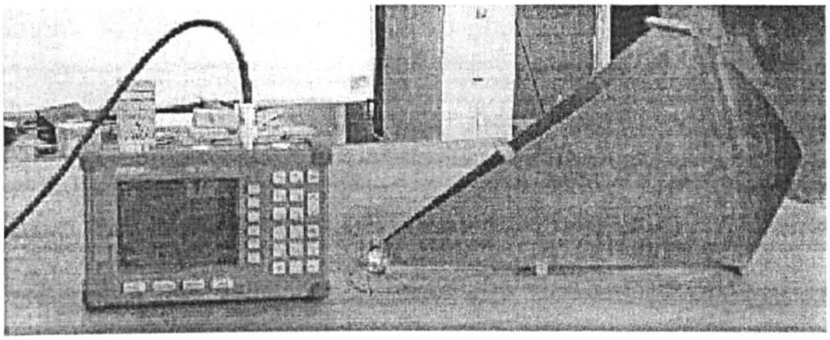

Figure 2.2: Photograph of the SiteMaster and the TEM horn antenna.

In conjunction with the network analyser, a TEM horn antenna has been developed for radiation of short pulses. The advantage of utilising a TEM horn antenna is that it can transmit travelling waves over a wide frequency band and has a linear phase characteristic over this band. Moreover, a TEM horn antenna has the capability of high directivity, which is preferred for reducing reflected signals from sources other than the material under test. In general, a TEM horn antenna consists of a pair of triangular conductors forming a V-shaped structure in which a TEM wave propagates along the axis of the V. The design of the TEM horn antenna developed for this measurement system is based on the design proposed by Huston [24]. It consists of two V-shaped copper plates tapered and flared at the aperture of the antenna. The profile of the metal flaring are optimised so that the characteristic impedance in each cross section of the antenna gradually changes from the impedance of the interconnecting coaxial cable near the feed point ($50\ \Omega$) to the impedance of air in the vicinity of the aperture ($377\ \Omega$). This gradually tapered impedance matching ensures that reflections from all antenna cross-sections are minimised. The dimensions of the TEM horn antenna are small: the antenna aperture is 30 cm by 15 cm and its longitudinal length is 50 cm. The weight of the antenna is light because it is formed with two 1.5 mm-thick copper plates. The small physical dimensions make the antenna suitable for portable applications.

The characteristics of the TEM horn antenna in connection with the network analyser can be experimentally obtained by placing the measurement system in an open area and by measuring the one-port parameter $S_{11}(j\omega)$. The time-domain characteristics $S_{11}(t)$ can then be obtained using Inverse Fast Fourier Transform (IFFT). Afterwards, one can apply time-gating over $S_{11}(t)$ to filter out the ground reflection, and finally obtain the improved $S_{11}(j\omega)$ by the Fast Fourier Transform (FFT) of the filtered $S_{11}(t)$. This is applicable due to the fact that the wideband measurement system has the ability to temporally resolve desired reflection from spurious and unwanted signals. Time-gating enables us to extract the desired reflected signal by applying an appropriate time window over the measured signals in the time domain. The improved $S_{11}(j\omega)$ is then assumed as the characteristics of the antenna system. Fig. 2.3 shows the measured voltage standing wave ratio (VSWR) of the TEM horn antenna. It is observed VSWR of the antenna is low within a wide frequency band (VSWR $<$ 3 from around 520 MHz up to 3000 MHz). VSWR of the antenna is deemed to be sufficiently low to ensure efficient radiation of the signal generated by the network analyser into free space.

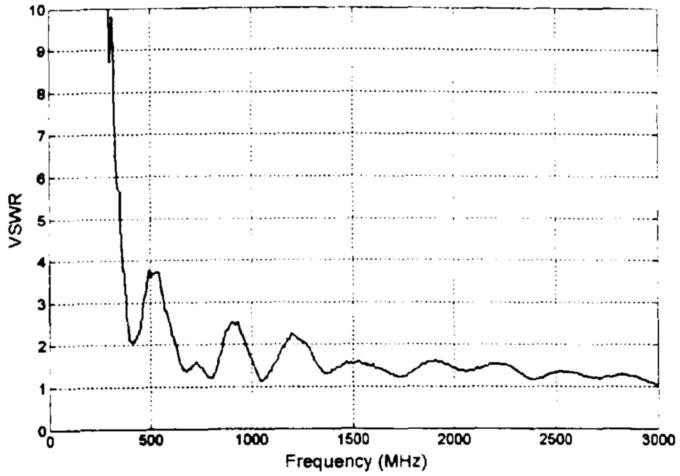

Figure 2.3: VSWR of the TEM horn antenna system.

2.3 Theory and Data Reconstruction

For our free-space measurements, the reflection coefficient of the material under test is measured at various frequencies and used to reconstruct its dielectric parameters. In this section, the theory of the measurement relating the dielectric parameters to the measured data and the inversion algorithm for the reconstruction of the dielectric parameters from the measured data are briefly described.

2.3.1 The Forward Model

Electromagnetic-wave theory is the physical model that used to predict the radio propagation of electromagnetic waves in materials. For our free-space measurement system, the signal transmitted from the TEM horn antenna propagates through the material under test and is partially reflected from the material due to its electromagnetic discontinuity with free space, and, if the material is multi-layered, the electromagnetic discontinuities between each layer as well.

Assume that a TEM wave from the horn antenna is incident at a normal angle on a multi-layered material consisting of M homogeneous layers. The dielectric properties of the multi-layered material are analysed, based on a model which treats each lamina as a homogeneous and isotropic material and then using a computational method to cascade the wave-transmission matrices [25]. The geometry of a M-ply laminated composite is illustrated in Fig. 2.4. The mth layer is characterised by its permittivity ε_m, conductivity σ_m, permeability μ_m and thickness d_m. In practice, many typical materials exhibit only dielectric properties, therefore it is assumed that the material is non-magnetic, i.e., $\mu_m = \mu_0$, where the permeability of free space is $\mu_0 = 4\pi \times 10^{-7}$ H/m. The permittivity is $\varepsilon_m = \varepsilon_r \cdot \varepsilon_0$, where ε_r is termed relative permittivity and the permittivity of free space

$\varepsilon_0 = 10^{-9}/36\pi$ F/m. For simplicity, the permittivity mentioned later in this thesis is referred to as the relative permittivity.

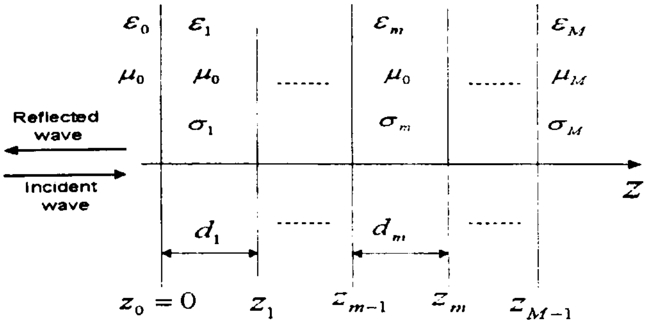

Figure 2.4: An illustration of the structure of an M-layered material.

The reflection coefficient Γ of the material at $z_0 = 0$ is given by

$$\Gamma(\omega) = \frac{Y_0 - W_1}{Y_0 + W_1} \tag{2.1}$$

where ω is the angular frequency. W_1 can be derived from

$$W_m = Y_m \frac{W_{m+1} + Y_m \tanh(\gamma_m d_m)}{Y_m + W_{m+1} \tanh(\gamma_m d_m)} \tag{2.2}$$

where $m = 1, 2, \ldots, M-1$. There is no up-going wave in the lowest layer M, so that W_M is given by $W_M = Y_M$. By analogy to transmission line as the intrinsic admittance of the mth layer, Y_m is given by

$$Y_m = \frac{\gamma_m}{j\omega\mu_0} \tag{2.3}$$

where the propagation constant of the mth layer, γ_m, is expressed as

$$\gamma_m = \sqrt{j\mu_0\sigma_m\omega - \mu_0\varepsilon_m\omega^2} \tag{2.4}$$

Eqs. (2.1) - (2.4) show the implicit relation between the dielectric properties of a layered material and its reflection coefficient for normally incident electromagnetic waves. Starting from the (*M-1*)th layer, the reflection coefficient of the multi-layered material can be calculated in an iterative way, provided that the information on ε_m , σ_m and d_m of each layer is given. The permittivity, conductivity and thickness of each layer in a multi-layered material are referred to as its constitutive parameters. From Eq. (2.1) and the definitions that follow, it is possible to obtain the reflection coefficient of the material in terms of these parameters. The above equations form the forward model whose objective is to generate the reflection data for a given material. It is noted that the free-space measurement of a material generally only involves predicting its dielectric parameters. The thickness of the material is either pre-known [18-21], [23], or is assumed sufficiently thick so that its effect is negligible [22]. However, in practice, a building structure is of a finite thickness and the information on the thickness is important for the calculation of its reflection and transmission coefficients. Moreover, the thickness of a building structure is sometimes unknown. Therefore, in addition to predicting the dielectric parameters, the thickness of the material under test is also of interest and needs to be predicted.

2.3.2 Data Reconstruction

For the free-space measurement, the reflection coefficient of the material under test is measured and then processed in order to derive its constitutive parameters. This is called an inverse problem and the processing is referred to as data reconstruction. The forward model reveals the relation between the constitutive parameters of a material and its reflection coefficient for normally incident waves. Conversely one can perform the inverse operation and derive the constitutive parameters from the reflection coefficient of the material. However, obtaining the exact solution for these parameters is not straightforward.

In the reflectivity model-based inversion, the constitutive parameters of a multi-layered material are reconstructed by the successive minimisation of the Mean Square Error (MSE) obtained from the difference in the reflection coefficient between the measured data and the one calculated from the forward model. In this way, the inversion problem turns into parameter optimisation of an objective function, which here is the MSE function. For our measurements, the measured reflection coefficients at different frequencies are used in the minimisation process. Let $\Gamma_1, \Gamma_2, \ldots, \Gamma_N$ be the calculated reflection coefficients from the forward model sampled at N frequencies, and RC_1 , RC_2 , ..., RC_M be the corresponding measured reflection coefficients. Furthermore, let $\mathbf{x}$ be a point in a multi-dimensional space with the dimension given by all constitutive parameters used to define a M-layered material. For a non-magnetic material, this point can be expressed as

$$\begin{aligned} \mathbf{x} &= (x_1, x_2, x_3, \ldots, x_{D-1}, x_D) \\ &= (\varepsilon_1, \sigma_1, d_1, \ldots, \varepsilon_M, \sigma_M) \end{aligned} \tag{2.5}$$

where $D = 3M - 1$. The objective function MSE for the data inversion is then defined as

$$\delta(\mathbf{x}) = \frac{1}{N} \sum_{i=1}^{N} \left| RC_i - \Gamma_i(\mathbf{x}) \right|^2 \tag{2.6}$$

The value of this function indicates the closeness of the fit between the measured data and the calculated data derived analytically from the forward model. Both the magnitude and the phase of the measured reflection coefficient are optimised to the forward model over the measurement frequency range. The constitutive parameters of the material are predicted by minimising the function $\delta(\mathbf{x})$, i.e., the minimum value of $\delta(\mathbf{x})$ yields the predicted value of $\mathbf{x}$.

In general, the forward model is non-linear and a large number of variables may be involved, depending on the structure of the material under test. For example, given the frequencies of interest, for a single-layered material, the variables used to calculate its reflection coefficient are its permittivity, conductivity and thickness based on the assumption that the dielectric properties of the material are frequency independent. If the dielectric properties are frequency-dependent, which is generally the case, more variables are involved in the expression of its reflection coefficient. For a multi-layered material, the actual number of variables involved in the minimisation process is proportional to the number of layers of the material. From the measurement data point of view, the actual composite of the material under test is unknown, so that the number of layers of the material is a guess. Because of the non-linearity of the forward model and the possible large number of variables involved in the inversion problem, the resultant objective function may have several minima. Therefore, a suitable minimisation algorithm should be employed in order to guarantee that a global minimum is found.

Fig. 2.5 shows an example of an objective function $\delta(\mathbf{x})$ with respect to its variable $\mathbf{x}$, where $\mathbf{x}$ can be a single- or multi-dimensional variable. Five local minima of $\delta(\mathbf{x})$ corresponding to its variable denoted as $\mathbf{x}_1'$, $\mathbf{x}_2'$, ..., $\mathbf{x}_5'$, are seen, among which $\mathbf{x}_3'$ (re-denoted as $\mathbf{x}''$) yields the global minimum of $\delta(\mathbf{x})$ and $\mathbf{x}''$ is the expected value from the minimisation procedure.

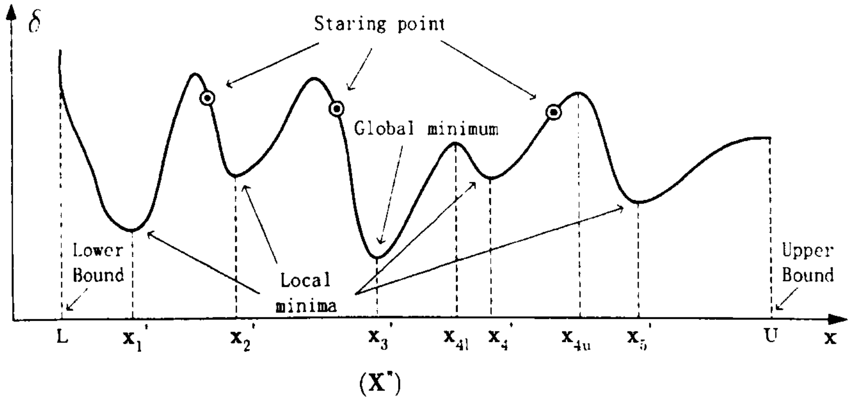

Figure 2.5: Example of an objective function having several local minima.

For our application, a reconstruction algorithm based on the multi-level single-linkage (MLSL) method [112] and its improvement [26], [113] is chosen to find the global minimum of the objective function defined by Eq. (2.6). The algorithm is a global minimisation method which incorporates a local minimisation procedure and a procedure of appropriately selecting the starting points across the whole variable range for the local minimisation procedure.

Given a starting point (initial guess of the solution $\mathbf{x}$), local minimisation methods such as the modified-Newton method [114] can efficiently find the minimum in the neighbourhood of it. The modified-Newton method is based on searching the objective function in a direction determined by its gradient and the Hessian matrix. By randomly locating the starting point within the whole optimisation region, repeating a local minimisation procedure can find the global minimum of the function. The main drawback of this approach is that when many randomly selected starting points are used, the same minimum may be found several times, thus the method is inefficient.

In the MLSL method, two regions, namely the feasible and the attraction regions, are defined. A feasible region S is defined within which all parameters $\mathbf{x}$ to be determined are restricted (between the lower bound L and upper bound U shown in the figure). An attraction region of a local minimum $\delta(\mathbf{x}')$ is defined as the set of points in S, starting from which a given local search procedure converges to $\delta(\mathbf{x}')$. For example, the set of all points of $\mathbf{x}$ between $\mathbf{x}_{4l}$ and $\mathbf{x}_{4u}$ shown in Fig. 2.5 is the attraction region of $\mathbf{x}_4'$. The idea behind the MLSL method is that the algorithm iteratively finds the local minima of the objective function, until the region of attraction of the local minima can effectively represent the whole feasible region. The procedure of the method is described as follows. Firstly, choose N_p test sample points uniformly distributed within S and calculate the objective function. Secondly, determine a set of reduced sample points N_q with the smallest objective function values resulted from the previous calculation ($N_q < N_p$), and select starting points from them. Selection of the starting points is based on the criteria that the starting point $\mathbf{x}$ has not been used previously, and that there is no sample point $\mathbf{y}$ within a critical distance, defined in [112], of $\mathbf{x}$ with $\delta(\mathbf{x}) < \delta(\mathbf{y})$. Thirdly, perform the local minimisation procedure from the selected starting points. Carrying on these steps iteratively, until the Bayesian stopping rule, defined in [112], is satisfied and then the lowest local minimum found is taken as the global minimum.

Adaptive random search algorithm (ARS) has been proposed in [26], [113] to enhance the efficiency and reliability of the MLSL method. The idea behind the ARS algorithm is to minimise a function derived from the transformation of the objective function δ instead of minimising δ directly. Let δ' denote the transformed version of δ. The value of $\delta'(\mathbf{x})$ is the minimum obtained if a local optimisation method with a starting point $\mathbf{x}$ is applied to the objective function δ. The function δ' therefore acquires constant values in the attraction regions of the minima of δ. Fig. 2.6 illustrates the transformation of the function shown in Fig. 2.5. The transformed function has the following properties which are advantageous for minimisation: 1) the number of the values of δ' is finite; 2) δ' has fewer local minima than does δ; and 3) the attraction regions of δ' are wider than or equal to those of δ. For example, in Fig. 2.6, δ' has five discrete values and there are three local minima of δ' are seen with three attraction regions, whereas the original function δ has infinite values and there are five local minima associated with five attraction regions. The wider attraction region for the global minimum of δ' would result in the higher probability and efficiency of finding it by a local search procedure. In the example shown in Fig. 2.6, performing three local searches, instead of five for the original function δ, gives the global minimum of δ' which is also the global minimum of δ. The basic principle of the ARS algorithm is that at each iteration, when the ARS algorithm finds a local minimum of δ, the neighbourhood region of $\mathbf{x}$ is gradually expanded, following the rules defined in [113], until it covers the entire feasible region of $\mathbf{x}$.

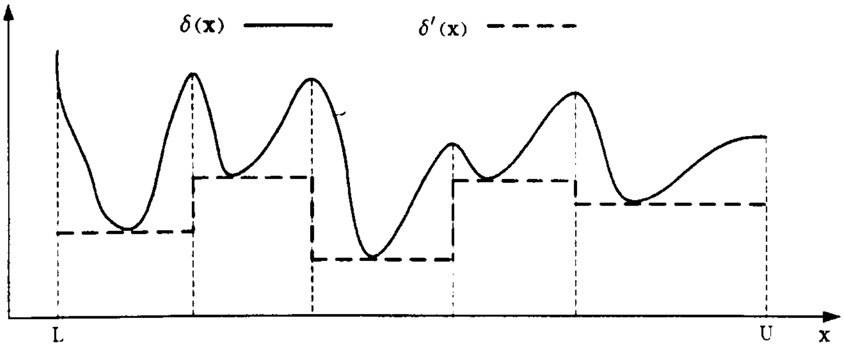

Figure 2.6: Transformation of a function by a local minimisation method.

In our application, assume that the material consists of M layers with different constitutive parameters. If the measured reflected signal is free of noise, the value of MSE derived based on the assumption of an M-layered model will be $\delta_M = 0$ and those values of MSEs derived on the assumption of less than M layers will be given by $\delta_k > 0$, for $k = 1, 2, \ldots, M\text{-}1$. The value of MSE derived based on the assumption of an $(M+1)$layered model should also be zero, i.e., $\delta_{M+1} = 0$. In this case, either the predicted thickness of the $(M+1)$th layer converges to zero, or the dielectric parameters predicted for the $(M+1)$th layer are the same as those predicted for the Mth layer. In contrast, if the measured reflected signal is contaminated by noise, the value of MSE derived based on the assumption of any number of layers is greater than zero. However, provided that the level of noise is manageable, if the number of layers assumed is less than the real number of layers, the values of MSEs are generally much higher than those derived on the assumption that the number of layers is the same as or larger than the real value. Therefore, the actual number of layers may be determined by a comparison of the values of MSEs derived based on the assumption of different numbers of layers.

2.4 Measurement of Reflection Coefficient

2.4.1 Measurement Procedure

Before conducting any measurement, calibration of the measurement system is necessary in order to compensate for the frequency response of the cable and connector, and of the measurement equipment itself. For the network analyser, the one-port S_{11} calibration can be performed up to the coaxial to antenna connector using the standard calibration kit, i.e., open-short-load terminations. The characteristic of the TEM horn antenna also has an impact on the measurement and should be taken into account. Calibration of the antenna system is addressed in this section.

The accuracy of measurements using the free-space system configuration shown in Fig. 2.1 is dependent on the precise alignment of the axis of the antenna system. Particular care has been given to ensure that the measurement plane has the correct orientation. To conduct a measurement on an unknown material (also referred to as a sample) in a laboratory environment, a three-step procedure is required to obtain the reflection coefficient of the sample. The three-step procedure is summarised as follows

(1) The measurement system is configured in an ordinary laboratory environment with no sample present. The resultant signal is captured by the antenna and stored in the network analyser, recorded as $r_b(f)$.

(2) The dielectric sample is then placed in the measurement system at a separation R (shown in Fig. 2.1) from the aperture of the antenna. The received signal by the antenna is stored and recorded as $r_s(f)$.

(3) The sample is removed and replaced by a metal plate of equal size. The separation between the aperture of the antenna and the metal plate remains unchanged. The received signal is then stored and recorded as $r_m(f)$.

During the above measurement procedure, the measurement system should remain stationary in order not to induce additional measurement noise due to the movement of the system. The reflected signals stored using the above procedure are those arising from the environment, the sample and the metal plate, respectively. These measurement data are recorded in the frequency domain and are then downloaded to a personal computer for post-processing and inversion.

2.4.2 Derivation of Reflection Coefficient

After the three-step measurement procedure, the desired reflected signals both from the sample and from the metal plate are embedded with undesired signals from surrounding environment such as laboratory walls, the floor, etc. and the internal reflected signals of the antenna, as well as multiple reflections between the sample and the aperture of the antenna.

The undesired signals are unrelated to the reflectivity characteristics of the sample/metal plate but have similar spectral characteristics to the reflected signals from them. These undesired signals should be suppressed or eliminated in order to obtain the real reflected signal from the sample/metal plate. For this purpose, the measured signals in the frequency domain are transformed into the time domain by applying IFFT, resulting in $r_b(t)$, $r_s(t)$, and $r_m(t)$ waveforms, respectively. Being a wideband system, it has the inherent ability to provide high temporal and spatial resolution, by which the signals generated from different sources can be distinguished by different time of arrival at the antenna. Several subtractions are required to extract the reflected waveform from the sample/metal plate. The computed waveform derived in step 2 is subtracted from that in step 1, resulting in the waveform reflected from the sample, together with disturbances such as multiple reflected signals between the antenna and the sample. The reflected signals from undesired objects surrounding the measurement system are eliminated after such subtraction operation. The internal reflections of the antenna are also eliminated. Likewise, the subtraction of the measured waveform derived in step 3 from that in step 1 results in the waveform response attributable to the metal plate.

After these operations, the reflected signals generated from the shadow region of the sample are suppressed to some extent but not fully eliminated. Moreover, the multiple reflections between the aperture of the antenna and the material/metal plate are still in existence and cannot be eliminated solely by these subtraction operations. In order to eliminate these undesired signals, time-gating is applied to the resultant signals from each subtraction operation. Undesired signals such as the multiple reflections between the aperture of the antenna and the sample/metal plate, which return to the antenna much later in time than the reflected signal from the sample/metal plate, will now be eliminated by the time-gating in a straightforward way. After the time-gating, the resultant waveforms can be attributed to reflections from the sample/metal plate. The derivation of these results has been obtained by signal processing in the time domain in conjunction with time-gating, thus solving the problems which are difficult to solve in the frequency domain.

An estimate of the reflection coefficient of the sample can be obtained by comparing the reflected signal from the sample and that from the metal plate. In other words, the measured reflected signal from the metal plate is used for system calibration. Since the reflection coefficient of a metal plate is -1 for normally incident waves, the signal reflected from the metal plate can be considered as the transmitted signal from the antenna with a 180° phase shift. The final desired frequency dependent reflection coefficient $RC(\omega)$ of the sample is obtained by the frequency-domain deconvolution suggested by Nahman and Guillaume [27], which is given by

$$RC(\omega)=\frac{\mathrm{FFT}\left\{\text{time-gated}\left[r_s(t)-r_b(t)\right]\right\}}{\mathrm{FFT}\left\{\text{time-gated}\left[r_m(t)-r_b(t)\right]\right\}} \tag{2.7}$$

Here the phase information of the reflected signals has been taken into account. In general, RC is not the same quantity as the true reflection coefficient of the sample, which is given by the ratio of the reflected to incident fields. Instead, it is the ratio of two reflected field quantities. However, because a metal plate with its surface normally oriented along the axis of the antenna and with the same dimensions as the sample under test is used as a reference, RC gives a strong indication of the sample reflectivity and can be assumed to be the reflection coefficient of the sample. The constitutive parameters of the sample are then predicted from its measured complex frequency dependent reflection coefficient RC.

2.5 Validation of Measurement Technique

In order to assess the effectiveness and accuracy of the measurement system, a few dielectric material samples with known permittivity have been chosen and measured. The free-space method using our measurement system configuration can be evaluated by comparing the constitutive parameters derived from our measurements and the reference data. In this section, the measurement results of a few single- and multi-layered samples are presented.

2.5.1 Single-Layered Sample Cases

Measurements of the reflection coefficient of a square planar polymer (PE500) panel have been conducted. The dimensions of the sample is 1.2 m in width, 1.2 m in height, and 4 cm in thickness. The permittivity ε_r of PE500 is 2.3 at 1 MHz and is regarded to be constant over a wide frequency range. Information on its conductivity has not been provided by the manufacturer. Nevertheless, it is believed that the conductivity of PE500 should be very low. An aluminium plate with the same transverse dimensions as the PE500 sample was used for calibration purposes. The PE500 sample was placed and self-supported at a separation of 40 cm from the aperture of the antenna. The normal to the centre of the sample surface was aligned with the axis of the antenna. Measurements following the aforementioned three-step procedure have been conducted and the corresponding measured raw data from the SiteMaster in the frequency domain are shown in Fig. 2.7. The received signals in each step were not purely the responses of the antenna, the sample and the metal plate, respectively. They were all contaminated, to different degrees, by the reflected signals from surrounding environments and the possible multiple reflections. It is impossible to filter out these undesired signals in the frequency domain, because they appear in the same frequency band as the desired signals do. Transforming the signals from the frequency domain to the time domain is an alternative way to analyse the signals and extract the desired ones.

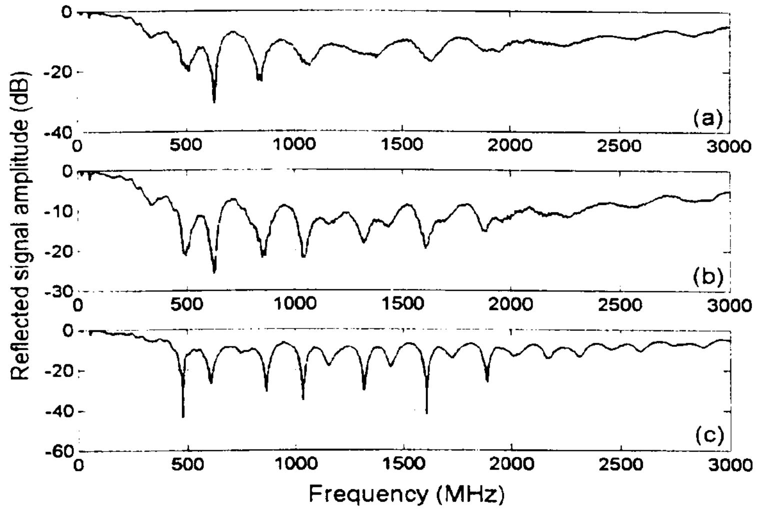

Figure 2.7: Measured reflected signals in the frequency domain: (a) when no sample is present; (b) from the PE500 sample; (c) from the metal plate.

The signals shown in Fig 2.7 are transformed into the time domain and are displayed in Fig. 2.8. As expected, the received waveforms are seen to be very complicated, with many peaks indicating various reflected signals from different sources. Two sets of reflected signals are very similar both in quantity and in time delay for all three measurements. The first peak is in close proximity to the time origin – the reference point at the coaxial to antenna connector. This reflected signal is attributed to the reflection from the antenna feeding point. Further away in time from the first peak is the second part of the reflected waveforms which is much more complicated. It is composed of the various reflections from the antenna aperture, tips of the antenna mouth and the supporting structure of the antenna. The waveforms further away in the range of 7 ns – 10 ns are both relatively weak compared to the first two parts of the reflected waveforms for the measurements conducted with or without the PE500 present. However, a closer look will reveal that the waveforms are observed slightly different from each other, both in shape and in quantity. For the measurement on the metal plate, the waveforms at these time intervals are remarkably high compared to the above two observations. Looking at the time of arrival of these strong reflected signals, we conclude that these are attributed to the reflections from the metal plate, clearly identifiable because of the high reflectivity of the metal plate. On the other hand, because the dielectric properties of the PE500 sample are closer to those of free space, the observed reflected signals from the sample are relatively low and therefore cannot be easily identified.

Following the subtraction operations presented above, the reflected waveforms from the sample/metal plate can be easily recognised. Fig. 2.9 shows the resultant waveforms. Starting from about 7 ns, the reflected signals from the sample/metal plate consist of a major pulse and some ringing attributable to the antenna characteristics. The reflected signals from the PE500 sample and the metal plate differ from each other in quantity due to their respective reflectivity. It is interesting to note that in the time intervals of 10 ~ 13 ns, there are prominent reflected signals, particularly for the measurement of the metal plate. These are not the direct reflected signals from the sample/metal plate to the antenna. Instead, they are the second order reflected signals, i.e., the multiple reflections from the sample/metal plate to the aperture of the antenna. These undesired signals can be eliminated by time-gating.

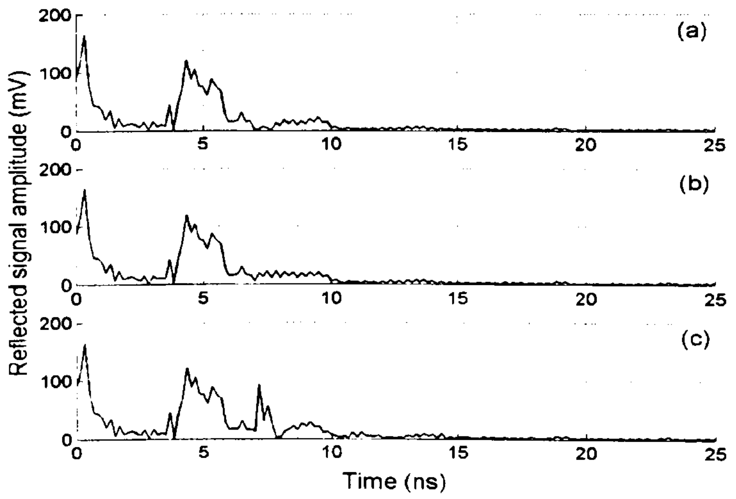

Figure 2.8: Measured reflected signals in the time domain: (a) when no sample is present; (b) from the PE500 sample; (c) from the metal plate.

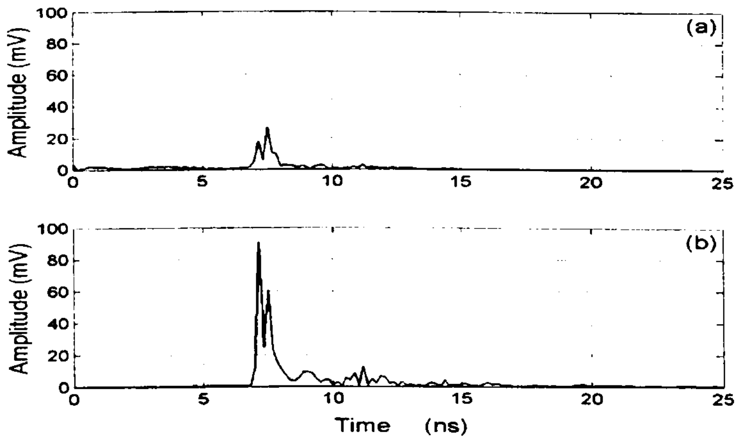

Figure 2.9: The resultant waveforms after the subtraction of: (a) the signals in Step 2 from those in Step 1; (b) the signals in Step 3 from those in Step 1.

The time-gated reflected signals from the sample/metal plate were used to calculate the reflection coefficient of the PE500 sample. The dielectric properties of materials are generally functions of frequency. Considering the fact that the complex permittivity ($\hat{\varepsilon} = \varepsilon_0 \varepsilon_r - j\sigma / \omega$) of materials has a physical interpretation, several frequency dependent models have been proposed in literature [28]. Among these the Cole-Cole model provides a good approximation of the dispersive behaviours of many materials. According to this model, the complex relative permittivity is defined as

$$\hat{\varepsilon}_r = \varepsilon^{\infty} + \frac{\varepsilon^{s} - \varepsilon^{\infty}}{1 + (j\omega\tau)^{\alpha}} - j\frac{\sigma}{\omega\varepsilon_0} \tag{2.8}$$

where σ is the conductivity; ε^{s} is the static permittivity (at zero frequency); ε^{∞} is the permittivity at infinite frequency; τ is the time constant of relaxation; and α is the Cole-Cole relaxation distribution parameter that requires a value in the interval [0, 1]. By incorporating the Cole-Cole model into the optimisation algorithm, the constitutive parameters of the PE500 sample are predicted. The thickness of the sample is found to be 4.018 cm from the optimisation procedure. The predicted permittivity and conductivity of the PE500 sample are shown in Fig. 2.10, from which we notice that both the permittivity and conductivity remain constant in the measurement frequency range, even though their frequency-dependent characteristics have been taken into account. The predicted permittivity is 2.3105 and, as expected, the predicted conductivity is very low. Fig. 2.11 shows the measured reflection coefficient and the predicted one derived from the forward model using the constitutive parameters found from the optimisation process. A close correlation between the measured and predicted reflectivity of the sample and between the predicted and reference data for the constitutive parameters is obtained. The good agreement serves to validate our measurement technique.

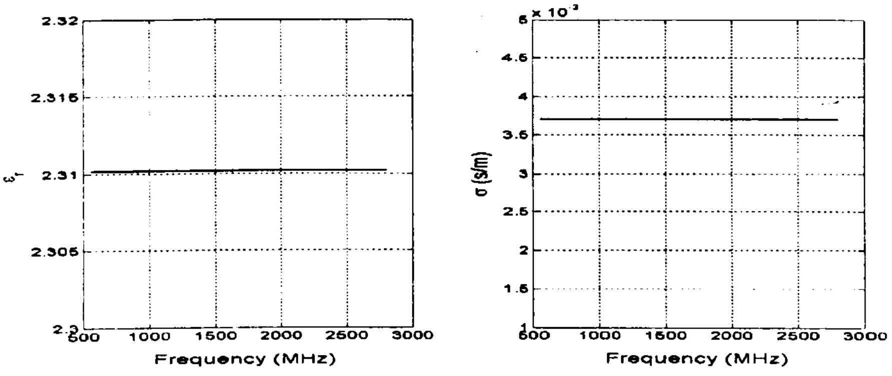

Figure 2.10: Predicted permittivity and conductivity of PE500.

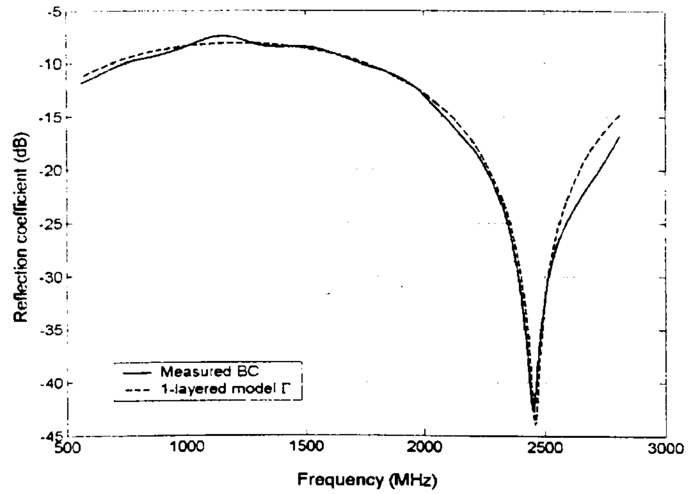

Figure 2.11: The measured and predicted reflection coefficient of PE500.

2.5.2 Determination of Sample-Antenna Separation

The inaccuracies in the measurements using our free-space system are mainly due to: 1) the diffraction effects at the edges of the sample; 2) the plane wave approximation employed in the forward model; and 3) the multiple reflections between the sample and the aperture of the antenna. In reality, the separation between the sample and the antenna should be well defined. If the sample-antenna separation is excessively large, the signals diffracted by the edges of the sample are received by the antenna and consequently contaminate the reflected signals. If this separation is too small, the sample is in the near field of the antenna where the transmitted waveform from the antenna is not plane wave, and hence the forward model cannot be well applied to this inversion problem. Moreover, the multiple reflections between the sample and the antenna cannot be effectively eliminated when the sample-antenna separation is very small. There is a trade-off between these two issues. However, a short sample-antenna separation is usually preferred because it can provide higher SNR than that with a large sample-antenna separation.

In order to determine an appropriate sample-antenna separation for our measurement system, we have conducted measurements on the PE500 and another polymer (Tufnol) panel being placed at sequential intervals of 30 cm, 35 cm, 40 cm, 45 cm, 50 cm, 60 cm and 100 cm apart from the aperture of the antenna. The Tufnol sample has the same transverse dimensions as the PE500 sample and is 2.5 cm thick. The surface of the Tufnol sample is not flat but slightly curved. The permittivity of Tufnol is 4.5 and its conductivity is unknown. Figs. 2.12 – 2.14 show the predicted permittivity, conductivity and thicknesses of the PE500 and the Tufnol samples by employing a single-layered model in the optimisation process. The predicted permittivity of PE500 is very close to the nominal value of 2.3 at sample-antenna separation from 40 cm to 50 cm. However, a trend of higher values at larger separations and lower values at smaller separations is observed. The predicted conductivity varies significantly when the separation is changed from 50 cm to 60 cm and upwards. The predicted thickness of the sample appears in good accordance with the real value. Viewing the predicted constitutive parameters at all separations, it is found that the sample-antenna separation between 40 cm and 45 cm gives overall the optimal prediction. For the measurement results of the Tufnol sample, more irregular trend of the variations of predicted parameters is seen. We think this is attributed to the non-planar effect of its surface. Nevertheless, similar to the results obtained from the PE500 sample, the results of the Tufnol sample at sample-antenna separation of 40 cm – 45 cm presents the optimal prediction of the permittivity and thickness, even though the sample is curved in shape. The experiment conducted on non-planar objects [17] also reveals that the curvature does not significantly affect the measured permittivity of cylindrical surfaces if the radii of curvature are large. Viewing the prediction results for both material samples, we conclude that the optimal sample-antenna separation for our measurement system is in the range of 40 ~ 45 cm. Smaller or larger sample-antenna separation may induce measurement errors, due to either the near-field effect and multiple reflections or the diffraction effects of the sample edges.

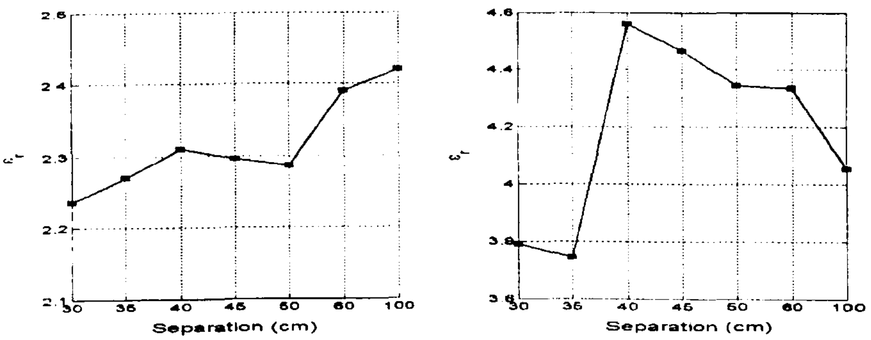

(a) (b)

Figure 2.12: Predicted permittivity of (a) PE500 and (b) Tufnol at different sample-antenna separations.

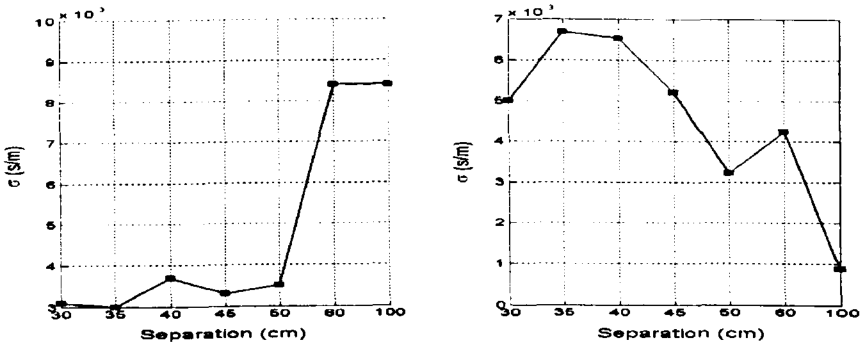

(a) (b)

Figure 2.13: Predicted conductivity of (a) PE500 and (b) Tufnol at different sample-antenna separations.

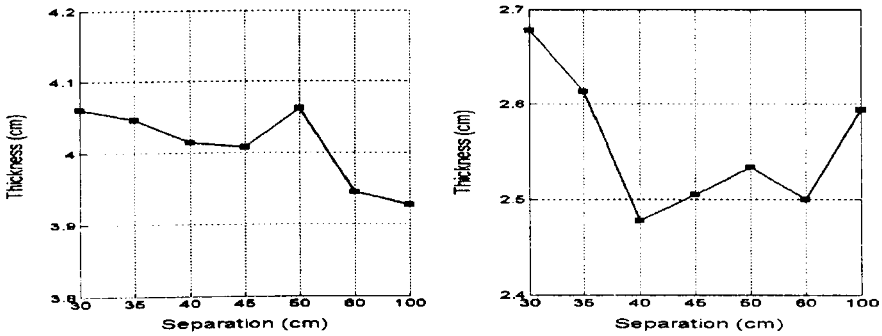

(a) (b)

Figure 2.14: Predicted thickness of (a) PE500 and (b) Tufnol at different sample-antenna separations.

2.5.3 A Multi-Layered Sample Case

From the above discussion, we fix the sample-antenna separation at 40 cm for all our consequent measurements as it can give a good prediction of the constitutive parameters of the sample. A measurement of a three-layered material has been conducted and the results are presented in this subsection. This is used to further test the usefulness of our measurement system, as well as the reliability of the optimisation algorithm. The three-layered material is made up of a panel of Tufnol, attached by two panels of PE500 of different thicknesses on each side. The transverse dimensions of these three panels are 1.2 m × 1.2 m. The constitutive parameters of this three-layered sample are listed in Table 2.1. Table 2.2 gives the predicted constitutive parameters of the composite material on the assumption of different numbers of layers. The constitutive parameters are listed in the form of $[\varepsilon_r; \sigma; d]$ for each layer. When applying the single-layered model, the Cole-Cole model was employed to describe the frequency dependent dielectric properties. When applying multi-layered models, the dielectric properties of the material were assumed constant over the measurement frequency range, for the purpose of saving the computation time.

Table 2.1: The actual constitutive parameters of the three-layered material.

Reference Data	**Layer 1 (PE500)**	**Layer 2 (Tufnol)**	**Layer 3 (PE500)**
ε_r	2.3	4.5	2.3
σ (s/m)	–	–	–
d (cm)	4.0	2.5	2.0

Table 2.2: Predicted constitutive parameters [ε_r ; σ ; d] of the three-layered material based on the assumption of different numbers of layers.

	Single-layered Model	**Two-layered Model**	**Three-layered Model**	**Four-layered Model**
1st layer	[2.41: 0.014; 8.25]	[2.94; 0.015; 3.25]	[2.43; 0.000; 3.88]	[2.50; 0.000; 3.81]
2nd layer		[6.59; 0.170: 2.87]	[4.78; 0.000: 2.71]	[5.33; 0.016: 2.85]
3rd layer			[2.33: 0.026: 1.78]	[2.34; 0.048; 1.73]
4th layer				[1.08; 0.021: 10.01]
MSE	4.01×10^{-2}	1.23×10^{-2}	1.14×10^{-3}	6.08×10^{-4}

It can be seen from Table 2.2 that the value of MSE is decreased as the assumed number of layers is increased. This is because the more layers included in the derivation of reflection coefficient, the more variables involved in the forward model, and hence the greater the probability of matching the predicted data with the measured ones. The value of MSE is decreased monotonously as the assumed number of layers is increased, however, this variation is not linear. For example, the value of MSE for the three-layered model is decreased by an order from that for the two-layered model. On the other hand, the values of MSEs for the single- and two-layered models, and that for the three- and four-layered models are on the same order. This indicates that compared to the two-layered model, the three-layered model gives rise to a substantial improvement in describing the reflectivity of the material. For this reason, the single- and two-layered models are not able to represent the reflectivity and cannot be used to describe the material. The four-layered model provides a better match with the measured reflection coefficient than the three-layered model does. However, looking at the constitutive parameters of the fourth layer in the four-layered model, it is apparent that the fourth layer is a close-to-air material of relatively large thickness. This is attributed to the measurement errors. Since the measurement data cannot exactly represent the true reflection coefficient of the material, an additional layer of close-to-air material can help improve the closeness between the measurement data and the predicted data. With this information, it is clear from Table 2.2 that the sample can be described as a three-layered material. The predicted constitutive parameters in the three-layered model are in reasonably good agreement with the reference parameters listed in Table 2.1. Inaccuracy of the parameters can be partially attributed to the fact that the Tufnol panel was curved, forming air gaps with both PE500 panels, which resulted in the measurement errors.

Fig. 2.15 shows the measured reflection coefficient, together with the predicted ones derived from the forward model based on the assumption of different numbers of layers. Large discrepancies in the reflection coefficient between the measured and those predicted from both the single- and two-layered forward models are clearly observed. This confirms that neither the single- nor the two-layered model can represent the actual reflectivity of the material. In contrast, both the three- and four-layered models give good representations of the reflectivity of the material. A better correlation between the measured reflection coefficient and that predicted from the four-layered model is seen, which is due to the presence of measurement noise and higher flexibility of the model. Nevertheless, the three-layered model gives a good agreement with the measured reflection coefficient. This example testifies that employing our measurement system with the optimisation algorithm, the constitutive parameters of a multi-layered material can be successfully reconstructed. The number of layers, the permittivity, the conductivity and the thickness of each layer can be determined simultaneously.

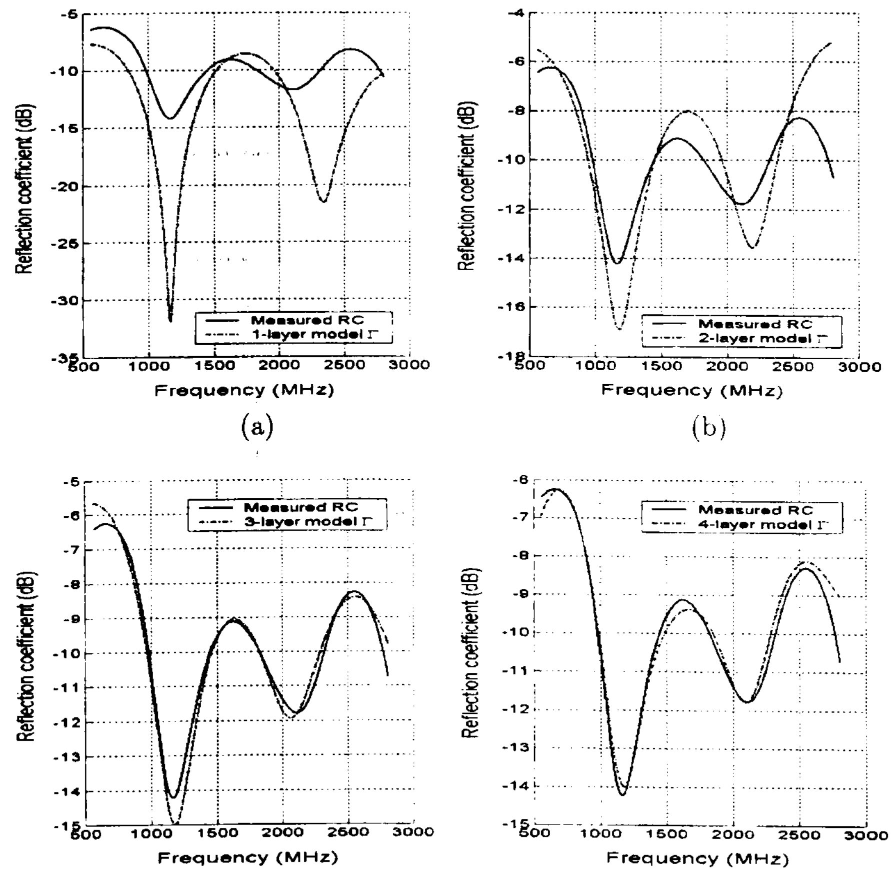

(a) (b)

(c) (d)

Figure 2.15: Reflection coefficient of the three-layered material derived from the measurement data and from the forward model.

2.6 Measurements of Building Materials

In the preceding section, the measurement results of a few single- and multi-layered materials are discussed. Good agreements on the constitutive parameters of the samples between the predicted and the reference data are observed and these demonstrate the usefulness and effectiveness of our measurement technique. In this section, results of the *in-situ* measurements of some typical building materials in the building of Department of Electrical Engineering and Electronics are presented.

For the measurements conducted in laboratory environments, the material under test and a metal plate are placed carefully in front of the antenna and measured in sequence for the derivation of the reflection coefficient of the material. However, from the *in-situ* measurement point of view, the three-step measurement procedure is unrealistic and cumbersome. Firstly, it is impossible to obtain the real background signal without the presence of the material under test. This is because the building structures are generally fixed and cannot be moved. Secondly, for the measurement conducted on the metal plate, a metal plate cannot be backed by supporting structures and should therefore be firmly affixed to the building structure under test, which requires tedious preparation work. Therefore, the measurement procedure described above needs to be improved and simplified, particularly for quick *in-situ* evaluations of building materials.

For this purpose, the TEM horn antenna has been housed in a cardboard box with the separation between the aperture of the antenna and the mouth of the box being 40 cm. The photograph of the antenna is shown in Fig. 2.16. For *in-situ* measurements, the antenna system is firstly configured in a common room with relative large free space area. By directing the antenna to a large space, we can obtain the background signals as the representative of the antenna characteristics. The effect of the housing box has been taken into account in this measurement. By placing a metal plate in contact with the mouth of the antenna box, the reflected signal attributable to the metal plate is then obtained. The data obtained from these two measurements are regarded as the measurement data in step 1 and step 3 as described in Section 2.4.1. These data are kept for data processing in all subsequent measurements on the building materials. When conducting the *in-situ* measurement on a particular building structure, we place the mouth of the antenna box in contact with the structure and obtain its reflected signal. Incorporating the measurement data previously obtained in the room environment and those from the metal plate, the measured reflected signal from the building structure is then processed to predict its constitutive parameters. *In-situ* measurements of some typical building materials such as partition walls, windows, wooden doors and glass walls (illustrated in the photograph of Fig. 2.17) have been conducted.

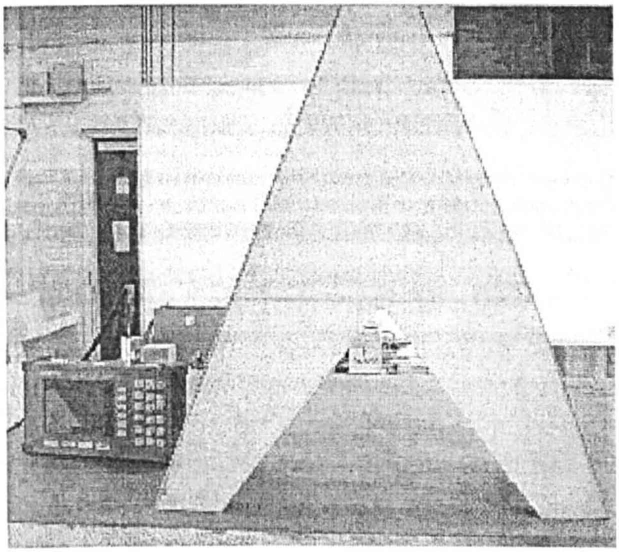

Figure 2.16: Photograph of the TEM horn antenna housed in a cardboard box.

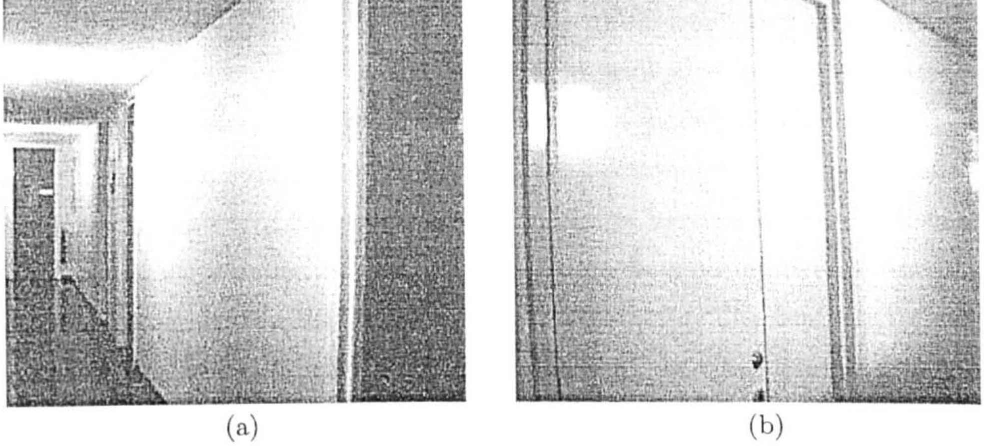

(a)

(b)

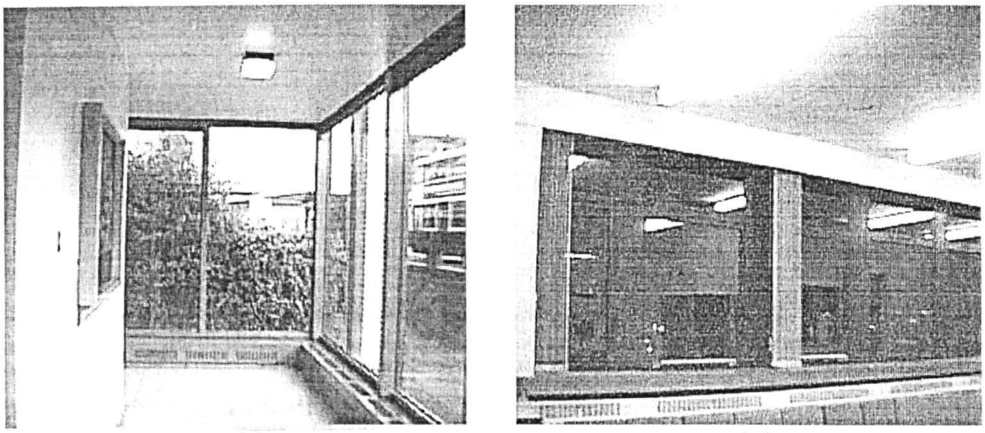

(c) (d)

Figure 2.17: Building structures being measured: (a) the internal wall; (b) the wooden door; (c) the glass wall; and (d) the window.

2.6.1 Measurements of Internal Walls

Fig. 2.17 (a) shows the internal wall being measured. It is one of the common walls used to partition offices in the building. The wall being measured is located on the fifth floor of the building, with its outer surface forming one side of the corridor and its inner surface embracing an office. The internal wall is about 11 ~ 12 cm thick and is likely to be made of concrete material.

The measurement of the wall was conducted in the corridor which is about 1.5 m wide. Due to the limited physical environment, the other side of the corridor formed by another partition wall also generates scattered signals to the antenna. Even though the TEM horn antenna has a good directivity which suppresses the backward reflections from the other side of the corridor, however, this measurement noise is inevitable. The wall being measured has been checked to ensure that there was no immediate furniture in close proximity to the inner surface of the wall. The scattered signals from other furniture in the office surrounded by the wall can effectively be eliminated by time-gating, due to their later time of arrival than the reflected signal from the wall.

Table 2.3 gives the predicted constitutive parameters of the internal wall derived from various single- and multi-layered models. The frequency dependent Cole-Cole model was also employed to describe the dielectric properties of the internal wall in the single-layered model. The predicted permittivity and conductivity listed in the single-layered model are the average values over the measurement frequency range. Frequency independent dielectric properties model was employed for multi-layered cases. It is noted that, being on the same order, the values of MSEs are not significantly decreased from the single- to the four-layered models. This indicates that using the four-layered model does not, compared to the single-layered model, provide a substantial improvement in representing the reflectivity of the internal wall. Analysing the predicted constitutive parameters from the three- and four-layered models, we find that either a single- or a two-layered close-to-air material is present in these models. Therefore, the internal wall can be approximated as a two-layered material.

Table 2.3: Predicted constitutive parameters [ε_r ; σ ; d] of the internal wall based on the assumption of different numbers of layers.

	Single-layered Model	**Two-layered Model**	**Three-layered Model**	**Four-layered Model**
1st layer	[5.02; 0.022; 11.42]	[4.94; 0.007; 5.57]	[4.94; 0.001; 5.43]	[4.98; 0.000; 5.36]
2nd layer		[5.89; 0.052; 5.49]	[5.68; 0.055; 5.65]	[5.67; 0.056; 5.69]
3rd layer			[1.05; 0.008; 9.65]	[1.03; 0.009; 6.75]
4th layer				[1.35; 0.016; 18.8]
MSE	3.21×10^{-3}	2.33×10^{-3}	2.08×10^{-3}	1.49×10^{-3}

Fig. 2.18 shows the measured reflection coefficient, together with the predicted ones calculated from the forward models based on the assumption of different numbers of layers. Peaks and troughs exhibit in the measured reflection coefficient, which is an evidence of multi-ray reflection mechanisms. Because of the finite thickness of the wall, the reflection coefficient exhibits "resonance" characteristics at certain frequencies. Unlike the comparisons shown in Fig. 2.15, the predicted reflection coefficients derived from the single- to the four-layered models are in rather good agreement with the measured reflection coefficient. Peaks and troughs exhibited in the measured reflection coefficient are well represented by each model. Employing models with larger number of layers results in better representation of the reflectivity, however, this improvement is not significant. The predicted reflection coefficient derived from the single-layered model is in good quality agreement with the measured one. The predicted permittivity and conductivity from the single-layered model are in between those predicted for each layer from the two-layered model. The thickness of the wall predicted from the two-layered model is 11.06 cm, which is in reasonably good agreement with that predicted from the single-layered model (11.42 cm). For this reason, the constitutive parameters predicted from the single-layered model are regarded as the effective parameters of the wall.

The permittivity and conductivity predicted from the single-layered model are shown in Fig. 2.19. The parameters in the Cole-Cole model are determined from the optimisation process and used to construct the permittivity and conductivity profiles. Frequency dependent characteristics of the dielectric parameters are clearly observed. The variations of the predicted permittivity are found to be small, compared to those of the conductivity. To further test the reliability of the measurement method, three other internal walls of the same type in the building have been measured, two of which are located on the sixth floor and the other is located on the fifth floor in a different site from the wall discussed above. The predicted constitutive parameters of these walls are summarised in

Table 2.4. Reasonably good consistence on the predicted constitutive parameters of the inter walls are obtained.

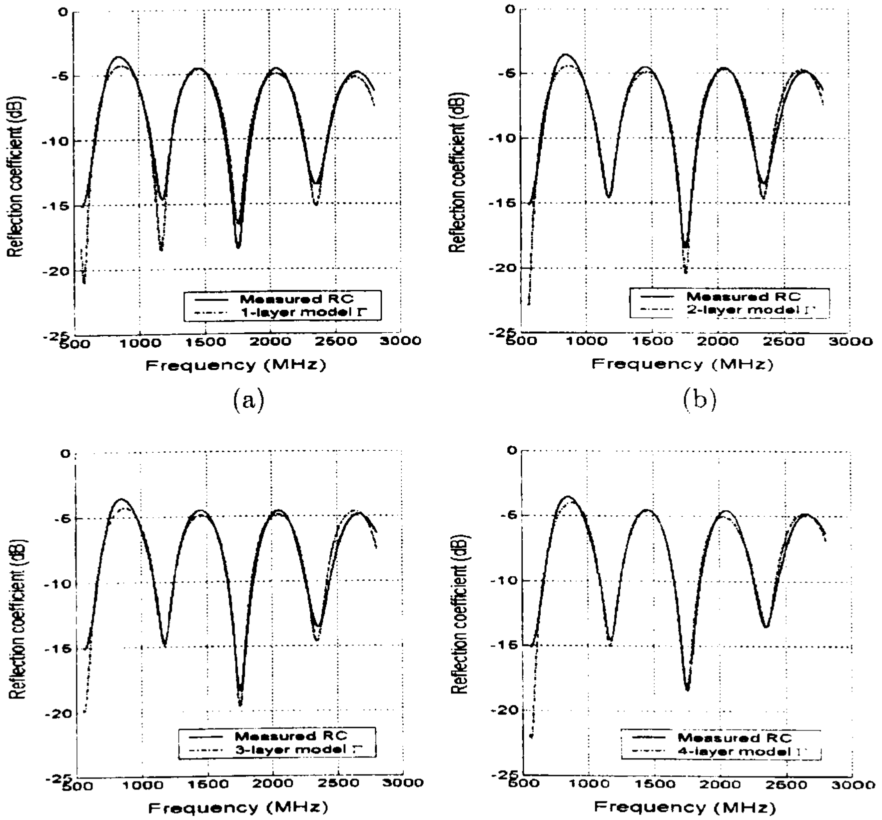

(a) (b)

(c) (d)

Figure 2.18: Reflection coefficient of the internal wall derived from the measurement data and from the forward model.

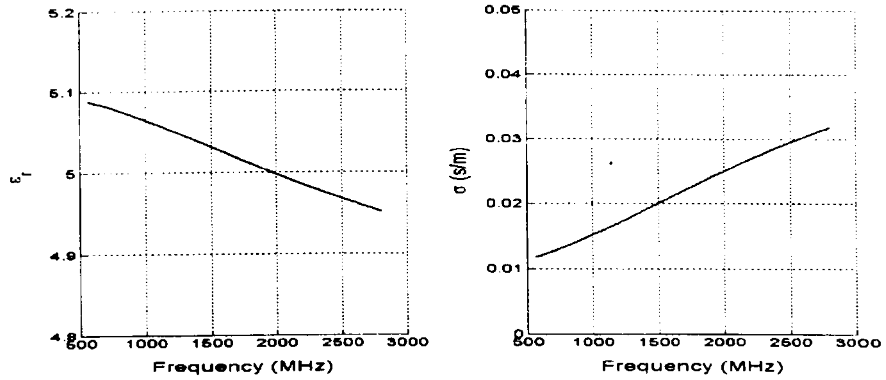

Figure 2.19: Predicted permittivity and conductivity of the internal wall.

Table 2.4: Predicted constitutive parameters of three internal walls using the single-layered model and the average values.

	Wall 1	**Wall 2**	**Wall 3**	**Average**
ε_r	5.11	4.87	5.06	5.01
σ (s/m)	0.036	0.018	0.031	0.028
d (cm)	11.24	11.67	11.22	11.37

2.6.2 Measurements of Wooden Doors

Fig. 2.17 (b) shows the wooden door being measured. It is a common door of a research room in B Block of the building. The door being measured is located on the second floor with transverse dimensions of about 1.0 m × 2.0 m. The thickness of the door was measured accurately to be 4.5 cm. The measurement was conducted in an environment similar to that conducted on the internal wall, which was in the corridor of about 1.5 m width. In addition to the backward reflections from the other side of the corridor, the metallic handle, lock and hinge of the door also scatters electromagnetic waves which contribut to the reflected signal from the door.

Table 2.5 gives the predicted constitutive parameters of the wooden door derived from various single- and multi-layered models. The values of MSEs are found not decreased significantly from the single- to the three-layered models. Analysing the predicted constitutive parameters from the three-layered model, we find that one layer of close-to-air material is present. Comparing the constitutive parameters predicted from the single- and the two-layered models, it seems more difficult to judge whether the single-layered or the two-layered model gives a better description of the wooden door. The thickness predicted from the single-layered model (4.76 cm) is in better agreement with the real value of the thickness of the door, compared to that predicted from the two-layered model (4.98 cm in total). We think that the presence of the metallic features within the door would give rise to undesired scattered signals which contaminate the reflected signal merely from the door. These signals could not be eliminated from that reflected from the wooden door by time-gating.

Table 2.5: Predicted constitutive parameters [ε_r : σ : d] of the wooden door based on the assumption of different numbers of layers.

	Single-layered Model	**Two-layered Model**	**Three-layered Model**
1^{st} layer	[2.84; 0.022; 4.76]	[2.49; 0.044: 2.53]	[2.48: 0.044: 2.13]
2^{nd} layer		[2.43; 0.000: 2.45]	[2.61; 0.000; 2.76]
3^{rd} layer			[1.12; 0.000: 24.26]
MSE	8.11×10^{-4}	5.36×10^{-4}	2.82×10^{-4}

Fig. 2.20 shows the measured reflection coefficient, together with the predicted one calculated from the forward model using the single-layered model. Reasonably good agreement between the measured and the predicted reflection coefficients is observed. Thus, the single-layered model can be used to approximate the reflectivity of the wooden door. The permittivity and conductivity predicted from the single-layered model is shown in Fig. 2.21. The predicted permittivity is in reasonably good agreement with those found for wood materials in literature, although the actual composite may be different. However, the predicted conductivity is higher than we previously expected. We think there are two possibilities to cause this inaccuracy. One is that the scattered signals from the metallic features contaminated the real reflected signal from the wooden door, which may result in higher predicted conductivity. The other is that the free space method is inherently less accurate for characterising low loss material [29]. With the presence of measurement noise, the predicted conductivity is expected to be less accurate than the predicted permittivity. Three other wooden doors of different research rooms have also been measured and the predicted constitutive parameters using the single-layered model for each door are listed in Table 2.6. As expected, the predicted values are not as

consistent as those found for the measurements of the internal walls. Nevertheless, the average values of the predicted parameters, particularly for the permittivity and thickness, are found in reasonably good agreement with the real material.

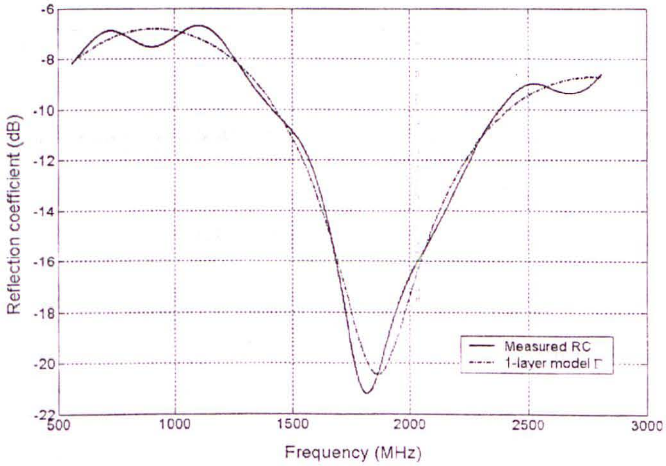

Figure 2.20: Reflection coefficient of the wooden door derived from the measurement data and from the forward model.

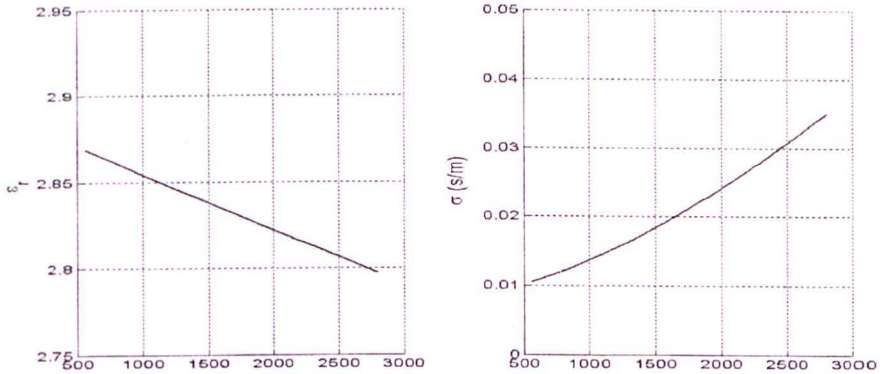

Figure 2.21: Predicted permittivity and conductivity of the wooden door.

Table 2.6: Predicted constitutive parameters of three wooden doors using the single-layered model and the average values.

	Door 1	**Door 2**	**Door 3**	**Average**
ε_r	2.96	2.64	3.16	2.92
σ (s/m)	0.026	0.038	0.016	0.027
d (cm)	4.69	4.92	4.86	4.82

2.6.3 Measurements of Glass Walls

Fig. 2.17 (c) shows a glass wall being measured. It is located on the ground floor of the building. Each panel of the glass walls has transverse dimensions of about 1.5 m × 3.0 m and is surrounded by metallic frames. The thickness of the glass wall is unknown. The measurement on the glass wall was conducted in the corridor shown in the figure. The corridor is about 1.8 m wide and there is a large space outside the glass wall, which provides a good environment for the measurement. Because the glass wall has a relatively large area, the scattered signals from the metallic frames surrounding the glass wall can be eliminated by time-gating.

Table 2.7 gives the predicted constitutive parameters of the glass wall derived from various single- and multi-layered models. Analysing the predicted constitutive parameters from the single- to the three-layered models, we find that the glass wall can be well approximated as a single-layered material. This conclusion is in accordance with the reality. Small variations of the values of MSEs derived based on the assumption of different numbers of layers reveal that the effects of the metallic frames are insignificant because they can be effectively eliminated from the reflected signal from the glass wall. This results in low measurement noise and hence good measurement accuracy.

Table 2.7: Predicted parameters [ε_r ; σ ; d] of the glass wall based on the assumption of different numbers of layers.

	Single-layered Model	**Two-layered Model**	**Three-layered Model**
1st layer	[7.07; 0.03; 0.57]	[7.38; 0.020; 0.54]	[7.18; 0.000; 0.58]
2nd layer		[1.08; 0.000; 20.71]	[1.13; 0.001; 6.77]
3rd layer			[1.08; 0.000; 13.72]
MSE	8.87×10^{-4}	7.36×10^{-4}	5.59×10^{-4}

Fig. 2.22 shows the measured reflection, together with the predicted one calculated from the forward model using the single-layered model. The predicted reflection coefficient is in good agreement with the measured one. Unlike those observed in the above measurements, the measured reflection coefficient does not exhibit peaks and troughs in the frequency range. This is due to the thin thickness of the glass wall. The predicted permittivity and conductivity using the single-layered model are shown in Fig. 2.21. Although the frequency dependent characteristics have been taken into account, both the permittivity and conductivity appear constant in the measurement frequency range. Being a supporting structure used in buildings, the glass walls are generally metalised. Therefore the conductivity of the glass wall we measured is expected to be relatively high.

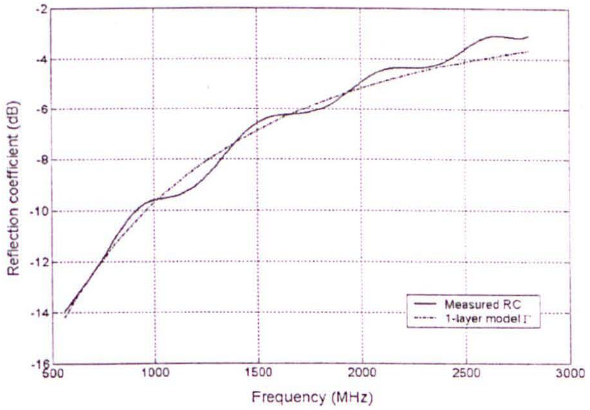

Figure 2.22: Reflection coefficient of the glass wall derived from the measurement data and from the forward model.

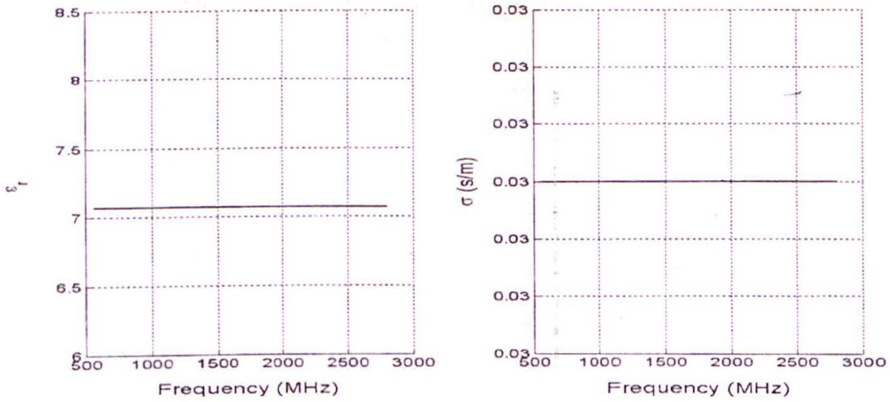

Figure 2.23: Predicted permittivity and conductivity of the glass wall.

Table 2.8 lists the predicted constitutive parameters from three other measurements of the glass walls in different sites on the ground floor. Again, good consistency of the parameters predicted for different glass walls are seen. This indicates that the measurements of the glass walls yield good accuracy.

Table 2.8: Predicted constitutive parameters of three glass walls using the single-layered model and the average values.

	Glass wall 1	Glass wall 2	Glass wall 3	Average
ε_r	7.00	7.03	7.05	7.02
σ (s/m)	0.036	0.028	0.032	0.032
d (cm)	0.59	0.55	0.57	0.57

2.6.4 Measurements of Windows

Fig. 2.17 (d) shows a window being measured. It is one of the many located in the conference room on the sixth floor of the building. Each window has transverse dimensions of about 1.2 m × 1.0 m and is surrounded by metallic frames. The thickness of the window was accurately measured to be 2.5 cm. A measurement of the window was conducted in the conference room shown in the figure. The furniture in close proximity to the window was removed before conducting the measurement. However, because of the relatively small dimensions of the window, the metallic frames surrounding the window may generate strong scattered signals to contaminate the reflected signal from the window.

Table 2.9 gives the predicted constitutive parameters of the window derived from various single- and multi-layered models. Analysing the predicted constitutive parameters from the single- to the three-layered models, we find that the window can be roughly approximated as a single-layered material. Small variations of the values of MSEs calculated from different layered models are seen. However, compared to the close-to-air materials found in the redundant multi-layered models for other building materials discussed above, the permittivity of the close-to-air materials computed from the two- and three-layered models here are relatively high. This indicates that the single-layered model can be used to approximate the material, however, it is not as good as that used for describing the other measured materials.

Table 2.9: Predicted parameters [ε_r ; σ ; d] of the window based on the assumption of different numbers of layers.

	Single-layered Model	**Two-layered Model**	**Three-layered Model**
1st layer	[3.61; 0.013; 2.75]	[4.66; 0.000; 2.53]	[3.86; 0.014; 2.75]
2nd layer		[1.64; 0.029; 18.98]	[1.20; 0.015; 20.25]
3rd layer			[1.69; 0.000; 12.16]
MSE	2.73×10^{-3}	1.81×10^{-3}	1.53×10^{-3}

Fig. 2.24 shows the measured reflection, together with the predicted one calculated from the forward model using the single-layered model. The measured reflection coefficient exhibits irregular fluctuations, which indicates that the reflected signal from the window is contaminated by

undesired signals from other sources. We think the metallic frames are the most likely sources which generate strong scattered signals. Because of the relatively small dimensions of the window and the finite temporal resolution of our measurement system, the signals scattered from the metallic frames cannot be sufficiently eliminated by time-gating. Nevertheless, the single-layered model incorporating the predicted constitutive parameters is shown in reasonably good quality agreement with the measured reflection coefficient. The predicted permittivity and conductivity using the single-layered model are shown in Fig. 2.25. Both the permittivity and conductivity appear constant in the measurement frequency range.

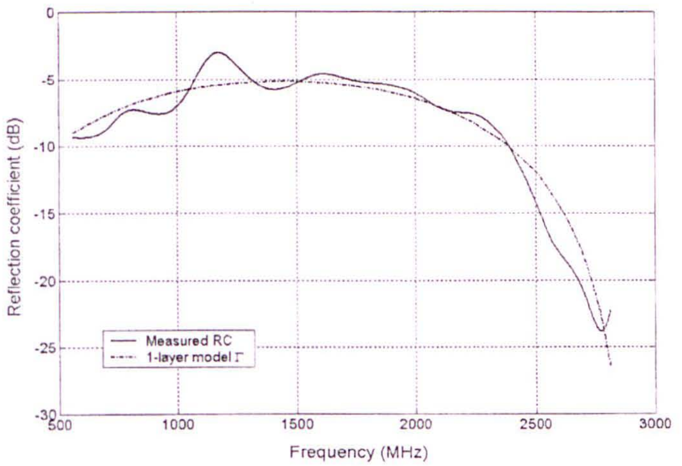

Figure 2.24: Reflection coefficient of the window derived from the measurement data and from the forward model.

Three other windows with one located in the same common room as that measured above and two located in the foyer of the second floor have been measured. Table 2.10 lists the predicted constitutive parameters derived from the measurement data. Large variations in the predicted dielectric parameters, particularly for the conductivity values, of each window are found. This indicates that the measurements on the windows are not as accurate as those on the other materials. Using a lens antenna with focused beam [17] or an ultra-wide-band system with high temporal resolution [30] is supposed to give better measurement accuracy, due to its higher capability of suppressing or distinguishing undesired signals generated by surrounding clutters near to the material being measured.

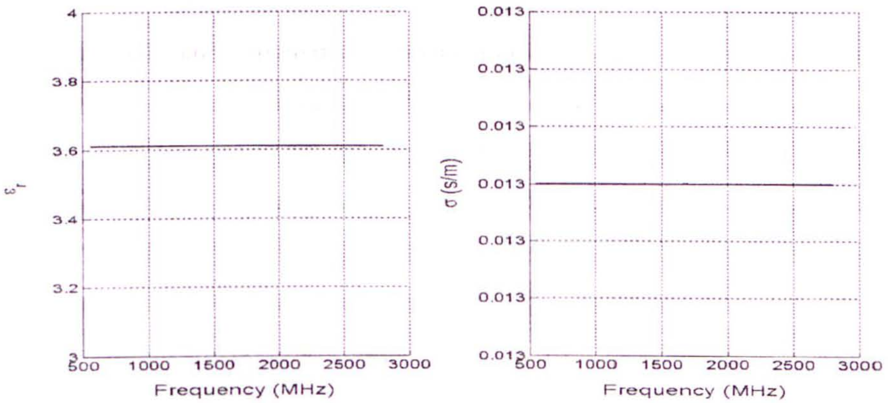

Figure 2.25: Predicted permittivity and conductivity of the window.

Table 2.10: Predicted constitutive parameters of three windows using the single-layered model and the average values.

	Window 1	Window 2	Window 3	Average
ε_r	3.71	3.42	3.50	3.54
σ (s/m)	0.015	0.033	0.024	0.024
d (cm)	2.83	2.67	2.81	2.77

2.7 Analysis of the Measurement System

2.7.1 Justification of the Measurement System

Fig. 2.26 shows the approximate dimensions of the E-plane of the TEM horn and the distance between the antenna and the material under test.

Spherical electromagnetic waves are generated at the feeding point of the TEM horn and propagate towards the antenna aperture. For the assumption of plane wave projection on the surface of the material, the distance δ_d, defined as the path length difference between a wave travelling along the side and along the axis of the horn, needs to satisfy the condition that $\delta_d < \lambda/10$ [115]. In this case, the path lengths from all parts of the antenna to the surface of the material are in phase or nearly so. From the dimensions of the antenna and the distance given in the figure, one can calculate that the path length difference δ_d is 1.01 cm. At 3 GHz, the highest operating frequency of our measurement system, the wavelength in free space is 10 cm, which is about ten times δ_d. Therefore, the wavefront at the surface of MUT on the E-plane has the property of plane wave. On the H-plane, the transverse dimension of the TEM horn is 30 cm, resulting in δ_d as high as 2.02 cm. That is, at operating frequencies below 1.5 GHz, the wavefront on the surface of the material on the H-plane has the property of plane wave. Overall, the wavefront of projection on the surface of the MUT can be regarded as quasi-plane wave. Such an assumption is valid, as can be seen from the measurement results of the PE500 sample material. The accuracy of both predicted permittivity and predicted thickness of the PE500 are well within 1%.

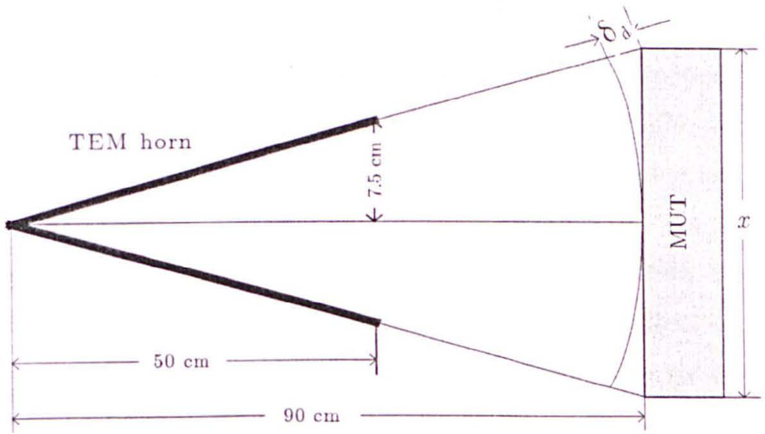

Figure 2.26: Approximate geometry of the E-plane view of the TEM horn antenna and the antenna-material distance used in analysis.

Due to the lack of facility for accurate measurements of the antenna radiation pattern, the TEM horn has been measured on the top of the Electrical Engineering building, where some scattering from environmental objects such as handrails and the floor are expected. Fig. 2.27 shows the measured field pattern of the TEM horn on its E-plane at 2.0 GHz, in which a 3-dB beamwidth of about 30° is seen. According to the analysis in [17], the diffraction effects due to edges of the material under test are negligible if the material dimension is greater than or equal to three times the 3-dB beamwidth. In our case, when the material is placed at 40 cm away from the aperture of the TEM horn, one can calculate that if the transverse dimension of the material is about 1.45 m × 1.45 m, then the diffraction effects of the edges are negligible. This means that in the measurement of PE500, reflected signals from the whole area of its surface are received by the TEM horn, together with some diffractions from its edges. However, because of utilising time-gating, the actual diffracted signals can be effectively removed. It can be seen in Fig. 2.9, the reflected signal from the metal plate is at 7 ns. In addition, a small diffracted signal from edges of the metal plate is observed at about 8.5 ns. Since the distance between the feeding point and the surface of the metal plate is 90 cm and the transverse length of the metal plate is 60 cm, the path length difference between the reflected wave and the diffracted wave is 18 cm, resulting in the round-trip travelling time of about 1.2 ns. Fig. 2.9 also indicates that if the transverse dimension of the metal plate is further reduced, then the diffracted signals will merge into the reflected signals, resulting in contaminating the measured signals. If so, the time-gating cannot effectively remove these diffracted signals from the reflected ones. As an example, comparing the measurement results of the glass wall and those of the window in Section 2.6, one can find that the measured reflection coefficient of the window (shown in Fig. 2.24) is more irregular than that of the glass wall (shown in Fig. 2.22). This can be explained by the fact that the transverse dimensions of the window are 1.0 m × 1.0 m and it is surrounded with metallic frames, whereas the transverse dimensions of the glass wall are 3.0 m × 1.5 m. The round-trip time difference between the signal from the window and that from the metallic frames is 0.8 ns, giving rise to partial overlap of both signals in the time domain. In this case, the time-gating cannot effectively separate both signals as compared with the case shown in Fig 2.9. When measuring the wooden door, even though the width of the door is 1.0m, the frame of the door is also made from wood, which yields much less significant diffracted signals for contamination. From all of our measurement results, we find that a material of transverse dimensions greater than 1.2 m × 1.2 m can be thought of diffraction effects free, either by implementing the time-gating if needed, or the diffraction effects are negligible.

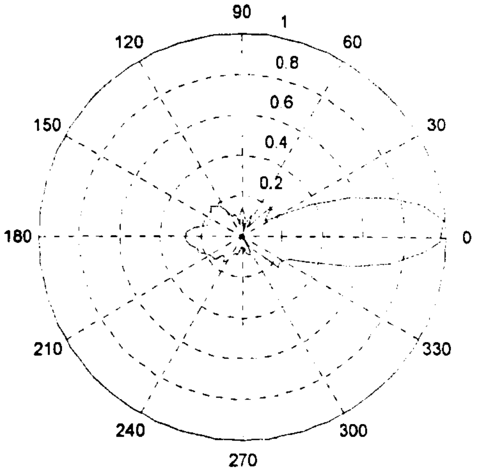

Figure 2.27: Measured E-plane radiation pattern at 2.0 GHz.

2.7.2. Effects of Non-Co-Plane Calibration

Before conducting measurements of a material at a certain distance, the antenna system needs to be calibrated by placing a metal plate at the same distance. If the metal plate is not exactly placed at the same distance, the calibration procedure will give rise to measurement errors. Another example would be that if the surface of the material is not smooth or is curved, then the metal plate cannot be closely attached to its surface, thus the reference plane for the calibration is different from that for measurements of the material. This is referred to non-co-plane calibration. In section 2.5.2, the surfaces of the Tufnol sample are non-uniformly curved, so that when doing calibration, there is a gap between the metal plate and the front-surface of the sample. It was observed that the gap could be varied from 0.5 cm to 1.5 cm at different positions. To illustrate the effects of this non-co-plane calibration, we simulate an example in which the gap between the Tufnol and the metal plate is varied from 0.25 cm to 1.0 cm. The constitutive parameters of the Tufnol sample are assumed as $\varepsilon_r = 4.5$, $\sigma = 0.00$ s/m and $d = 2.5$ cm. Fig. 2.28 shows the predicted constitutive parameters. The negative gap width represents the case where the metal plate is placed closer to the antenna than is the sample, whereas the positive gap width represents the case where the sample is placed closer to the antenna than is the metal plate. It is clearly seen that with ±1 cm gap, the predicted permittivity can have about 6% errors, while the predicted thickness can have about 5% errors. However, the predicted conductivity has much larger errors. This is because the free-space measurement is inherently more accurate for predicting the permittivity than for predicting the conductivity. The simulation results show that a small gap between the material and the calibrating plate leads to phase shift of the measured reflection coefficient, which in turn gives rise to erroneous prediction of the constitutive parameters of the material. Many samples with different constitutive parameters have been tested and about 5% errors of predicted permittivity are generally found when the gap is ±1 cm.

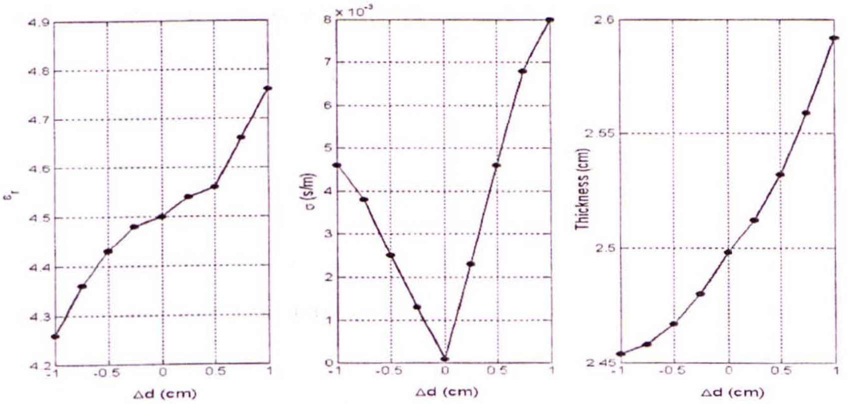

Figure 2.28: Predicted constitutive parameters versus different gap width between the metal plate and the Tufnol sample.

2.7.3 Range of Measurable Material Thickness

Because of the limited bandwidth of the measurement system, whether the reflected signals from different discontinuities of the material can be resolved is dependent on the material's constitutive parameters. As an example, Fig. 2.29 shows the effect of system bandwidth on the detected reflection signals of a single-layered material whose constitutive parameters are $\varepsilon_r = 4.0$, $\sigma = 0.001$ s/m and $d = 1.0$ cm. The time delay between each element of multiple-reflections inside the material is given by

$$t_d = \frac{2d\sqrt{\hat{\varepsilon}_r}}{c} \tag{2.9}$$

where $\hat{\varepsilon}_r$ is the complex relative permittivity of the material. For a low-loss material, the approximation of $\hat{\varepsilon}_r = \varepsilon_r$ can be made in the above equation. In this example, the time delay is calculated to be about 0.1333 ns. When the system bandwidth is 1000 GHz, multiple reflections of the material can be clearly seen as pulse-like signals. The reference plane is assumed as the front-surface of the sample, so that the first pulse corresponding to the reflection from the front-surface of the material occurs at the time origin. The second pulse corresponds to the reflection from its back-surface. The third pulse corresponds to the reflection from its back-front-back-surfaces. When the system bandwidth is reduced to 7.5 GHz, the multiple reflections are still resolvable. However, when the bandwidth is further reduced, as in our case that BW = 3.0 GHz, the multiply reflected signals cannot be resolved. Moreover, it is seen that the detected multiply reflected signals are overlapped and time-shifted due to the convolution of the material response and the transmitted signals. In spite of this, it may still be possible to extract the constitutive parameters of the material. For this example, the predicted constitutive parameters are $\varepsilon_r = 4.13$, $\sigma = 0.002$ s/m and $d = 1.04$ cm, which is in good agreement with the real parameters.

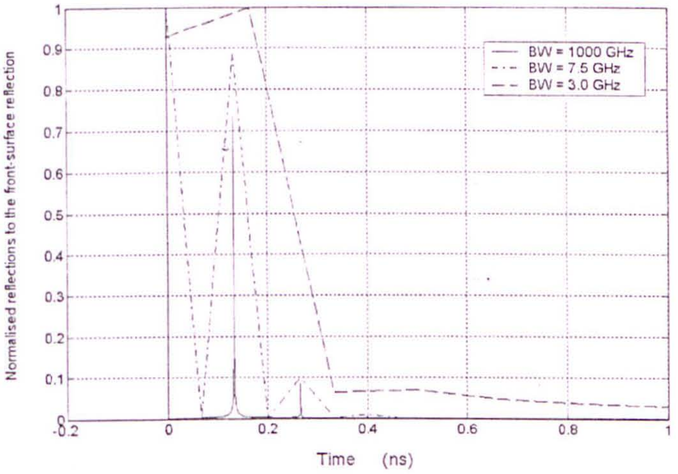

Figure 2.29: Detected reflected signals of a sample with different system bandwidths.

Multiple reflections within the material result in infinite series of reflected signals in the time domain. Therefore, applying the time-gating at any time interval will result in cutting off the useful information. In this subsection, we would investigate under what condition the constitutive parameters are able to be predicted with reasonable accuracy, even though some reflected signals are lost due to the time-gating process. The reflection coefficient of the nth multiple reflections of the material can be given by

$$\Gamma_1 = \frac{1-\sqrt{\hat{\varepsilon}_r}}{1+\sqrt{\hat{\varepsilon}_r}} \tag{2.10}$$

$$\Gamma_n = e^{-2\gamma d(n-1)} \frac{4\sqrt{\hat{\varepsilon}_r}\left(\sqrt{\hat{\varepsilon}_r}-1\right)^{2n-3}}{\left(1+\sqrt{\hat{\varepsilon}_r}\right)^{2n-1}}, \qquad (n>1) \tag{2.11}$$

where γ is the propagation constant of the material. Eq. (2.11) shows that as the conductivity of the material is increased, the strengths of multiple reflections are decreased. Fig. 2.30 shows the normalised magnitude of nth multiple reflection with respect to the front-surface reflection, i.e., $|\Gamma_n|/|\Gamma_1|$, for non-lossy materials. It is clearly seen that as the permittivity of the material is increased, the effects of higher-order multiple reflections become more significant.

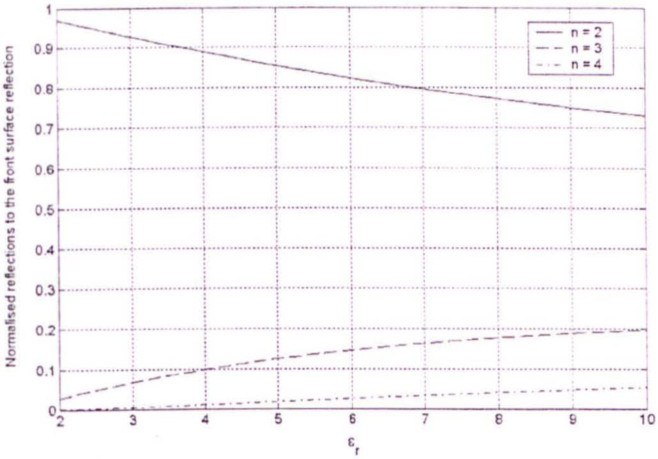

Fig. 2.30: Normalised nth reflection to the front-surface reflection of material with different permittivities.

To examine the degree of significance of multiple reflections for determining the constitutive parameters, a single-layered material with constitutive parameters of $\varepsilon_r = 9.0$, $\sigma = 0.001$ s/m and $d = 15$ cm is used as an example. Fig. 2.31 shows the multiple reflection signals in the time domain using 3 GHz bandwidth detector. With different time-gating width, the multiple reflection signals are truncated and transformed into the frequency domain. The signals in the frequency domain are shown in Fig. 2.32. It can be seen that as long as the first two reflections are accounted for, the reflection coefficient of the material appears the same resonance as that taking all multiple reflections into account. The predicted constitutive parameters for including nth reflection are listed in Table 2.11. By including two reflections, i.e., the front-surface and back-surface reflections, the predicted permittivity are in reasonably good agreement with about 5% error, and the predicted thickness is more accurate within 2% error. If only the front-surface reflection is taken into account, the predicted constitutive parameters are meaningless. This is due to the fact that accounting only for the front-surface reflection would effectively assume the material is infinitely thick or no reflected signals are generated by the back-surface due to high loss of the material. For materials with lower permittivity or higher conductivity, the contributions of more-than-three reflections are smaller, which indicates that the prediction error given in this example can be regarded as an upper bond error in many cases.

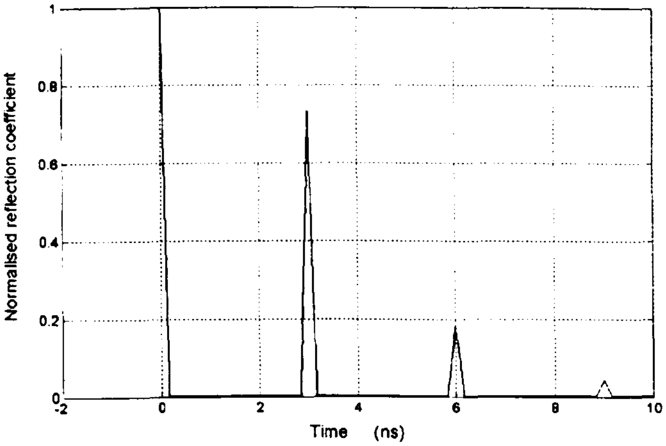

Fig. 2.31: Multiply reflected signals in the time domain.

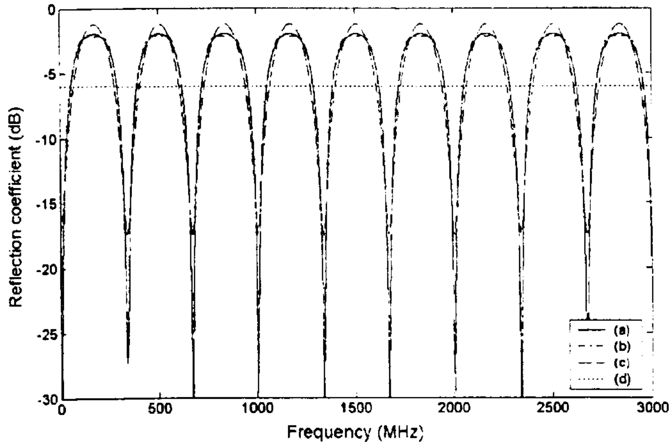

Fig. 2.32: Calculated reflection coefficient for different time-gating: (a) including all reflections: (b) including first three reflections: (c) including first two reflections: and (d) including the first reflection only.

Table 2.11: Predicted constitutive parameters of the 15 cm-thick material.

	$n \approx \infty$	n = 3	n = 2	n = 1
ε_r	9.0	8.87	8.52	5.50
σ (s/m)	0.001	0.001	0.002	0.64
d (cm)	15.0	15.09	15.25	0.748

We have examined many materials with different constitutive parameters and the simulation results show that taking first two reflected signals of the material can always give predicted results within 5% error. Moreover. it is found that if the thickness of the material is above 1/8 of thickness defined in Eq. (2.9) when t_d represents the temporal resolution of the system. good predictions of the permittivity can be obtained within 5% error. This value of thickness can be considered as the lower bond of measurable material thickness of our system. Taking into account that our TEM horn is separated at 40 cm distance to the material under test, the measurable thickness of the material is also determined by the existence of the material-antenna-material reflection. Fig. 2.33 gives the upper bond and lower bond of the measurable thickness for different materials. The upper bond of measurable material thickness is determined by that the first two reflections of the material would not overlap with the contaminating signal of the material-antenna-material reflection.

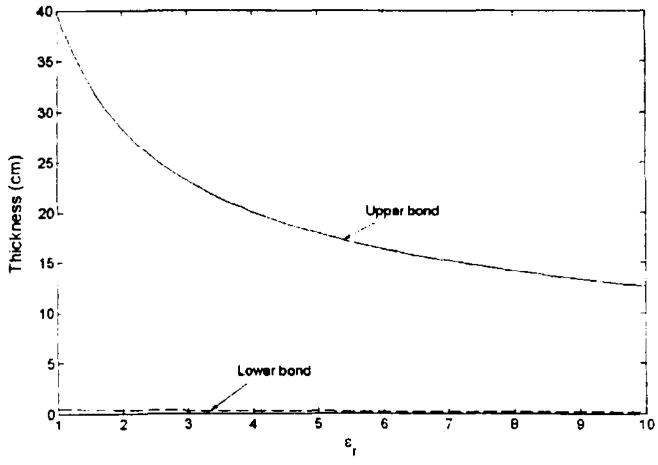

Fig. 2.33 The measurable thickness for different materials.

2.8 Summary

This chapter reports on *in-situ* characterisation of building materials using the free-space measurement technique. During the research work, a monostatic free-space measurement system working in the UHF frequency band has been developed. The major advantages of this system are its portability and ease in configuration, which is most suitable for efficient routine measurements. The monostatic system configuration also offers the following advantages: 1) during the measurement procedure, it does not demand system reconfigurations which may lead to further sources of measurement errors; and 2) it is also possible to conduct *in-situ* measurement of a building structure with access from only one side.

By employing an advanced optimisation algorithm that searches the global minimum of the difference between the measured reflection data and the analytical data calculated from a forward model, the number of layers. the permittivity, conductivity and thickness of each layer of the layered material can be simultaneously determined. Measurement results of some known materials in laboratory environments have demonstrated the reliability and effectiveness of the measurement method. *In-situ* measurements of some typical building materials in the building of Department of Electrical Engineering and Electronics have been conducted. Even though we do not have other technique to compare with the results obtained from our free-space measurements, the results of these materials generally agree with the published data and this demonstrates the usefulness of our free-space system for *in-situ* characterisation of building materials.

The extraction of the constitutive parameters of various building materials is very useful for the investigation of radio wave propagation within indoor environments. Characterisation of a specific radio channel which includes man-made structures requires the knowledge of the reflection and transmission properties of these materials. The predicted constitutive parameters can be used to develop simple and empirically accurate reflection and transmission coefficients of various building materials for arbitrarily incident waves with arbitrary polarisations. With the knowledge of the reflectivity and transmittivity of environmental building materials. interactions between the propagating waves and surrounding building structures can be mathematically modelled.

In addition to the application of dielectric property measurement. the antenna system developed can also find applications in other areas due to its wide bandwidth and good directivity. An example would be the ground penetrating radar (GPR) system for underground object detection. Compared to the conventional GPR system which utilises element antennas such as dipole and bowtie [120], utilisation of the TEM horn eliminates the requirement of close contact of antenna with the ground for good energy coupling and improves the measurement SNR.

Chapter 3

Indoor Channel Characteristics and Modelling

3.1 Introduction

In a wireless communication system, an information source attempts to send information to a destination via space. The signal transmitted from the source will propagate in the environment where both the transmitter (Tx) and receiver (Rx) are, and interact with the structures within the environment until it reaches the Rx. The transmission medium, including all radio propagation effects within, is referred to as a radio channel.

The radio channel places one of the fundamental limitations on the performance of wireless communication systems. An understanding of the radio channel is an essential part of the understanding of the operation, design and analysis of any wireless communication system. For example, the frequency reuse concept has been successfully employed in commercial mobile communications to facilitate high capacity [4]. In this case, background noise and co-channel interference become primary factors limiting the system performance. In designing these systems, it is necessary to balance the need to provide an adequate signal for each user and at the same time to limit the co-channel interference due to signals intended for other users. Finding such a balance requires detailed understanding of the radio channel characteristics. In digital wireless communications, the maximum data transmission rate and the bit error rate (BER) are also determined by the time dispersion characteristics of the radio channel. For the purpose of channel characteristic modelling, theoretical or experimental propagation study has to be undertaken. The propagation models should be able to provide estimates of signal strength and time dispersion characteristics in various radio environments.

In connection with the advanced wireless communication systems such as UMTS, wireless local area networks (WLANs), cordless telephones, and Bluetooth, indoor wireless applications for which both the Tx and Rx are within indoor environments are becoming more important aspects. Prediction of the indoor radio propagation characteristics is therefore becoming increasingly important. This chapter is devoted to the description of the radio channel and its modelling methods. Section 3.2 describes the radio channel characteristics which affect the radio propagation properties. Section 3.3 describes the channel parameters used as a measure of the radio channel characteristics. Section 3.4 reviews and compares various radio channel modelling methods currently being used or under development.

3.2 Radio Channel Characteristics

3.2.1 Multipath Propagation

The mechanisms governing indoor radio propagation are diverse, but can generally be attributed to reflection, transmission, diffraction, and scattering [9]. Reflection occurs when a propagating wave impinges upon an object which has very large dimensions compared to the wavelength of the wave. The propagating wave may also penetrate through the object depending on the electromagnetic properties, giving rise to transmission. Diffraction occurs when a propagating wave impinges upon a sharp edge within the environment. Scattering occurs when the medium through which the radio wave propagates consists of objects with small dimensions compared to the wavelength of the wave, and where the number of obstacles per unit volume is large. In indoor radio propagation, reflection and transmission generally occur at large objects such as building walls, windows, and doors, etc. Diffraction normally occurs at building corners, edges of window frames, and the junction of two objects. Scattering occurs on rough surfaces, small objects like furniture, or by other irregularities in the environment.

In a radio channel, the transmitted signals arrive at a Rx via the above mechanisms. Fig. 3.1 shows a simple but practical radio propagation scenario where both Tx and Rx are surrounded by a few objects. Several waves, in addition to the direct wave between the Tx and Rx, arrive at the Rx through different paths. This is referred to as multipath propagation. Due to different locations and electromagnetic properties of the objects, each of the waves arriving at the Rx has a different time delay, strength attenuation and phase. These multiple versions of the transmitted signal interfere with each other at the Rx, resulting in a phenomenon termed fading [31]. Multipath is the principal degrading factor of the signal transmission quality. It causes signal fluctuations in analogue communications and possible inter-symbol interference (ISI) in digital communications.

The existence of multipath within an environment where the communication systems are deployed gives rise to a highly complex radio channel. In order for system engineers to be able to determine optimum methods of mitigating the impairments caused by multipath propagation, it is essential that the radio channel be properly characterised.

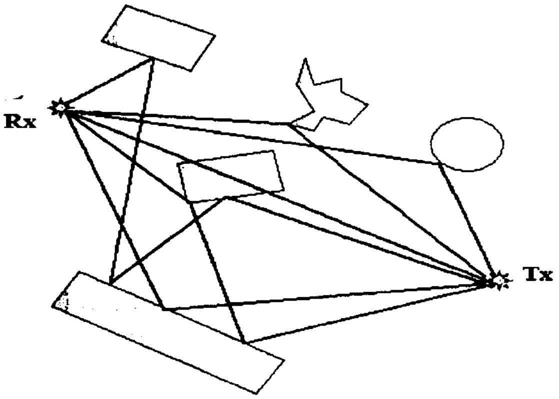

Figure 3.1: An illustration of a multipath propagation.

3.2.2 Baseband Channel Impulse Response

Wireless communications in the UHF and millimetre frequency bands always undergo the process that the information is modulated to a carrier frequency for transmission, while at the Rx the signal is demodulated to extract the information. Thus, the radio channel is a band-pass channel. Because of the equivalence of band-pass and baseband response [9], the radio channel can be described by a complex baseband impulse response. Analysis of the radio channel using baseband complex envelope offers two important advantages: 1) we can analyse the transmission channel and perform a computer simulation of the system using low-frequency band signals, instead of the rapidly varying band-pass signals; and 2) we can accurately recover the shape of the original transmitted signal by implementing a filter in the baseband, instead of the radio frequency band. In this case, the radio channel can be modelled as a linear filter with a time-varying baseband impulse response, where the time variation is due to the Rx motion in space and other time-varying characteristics of the channel such as displacement of surrounding objects. The effect of the radio channel on transmission of radio signals can be determined from the baseband channel response.

Assume that the Tx transmits a unit impulse signal $\delta(t)$ over a multipath radio channel. Due to the multipath propagation, the received signal at the Rx consists of a series of attenuated, time-delayed, and phase shifted replicas of the transmitted signal. The received train of impulses is termed the impulse response. Let N denote the total number of possible multipath components, the baseband channel impulse response can be expressed as [9]

$$h(t,\tau)=\sum_{i=0}^{N-1} a_i(t,\tau)\exp\left\{j\left[\omega_c\tau_i(t)+\phi_i(t,\tau)\right]\right\}\cdot\delta\left[\tau-\tau_i(t)\right] \qquad (3.1)$$

where t represents the time variations due to the Rx motion or time-varying characteristics of the channel; τ represents the channel multipath delay for a fixed time value; $a_i(t,\tau)$ and $\tau_i(t)$ are the real amplitudes and excess delay of the received *i*th multipath component at time t; ω_c is the angular carrier frequency; and the phase term $\omega_c\tau_i(t)+\phi_i(t,\tau)$ represents the phase shift due to free space propagation of the received *i*th multipath component, plus any additional phase shift encountered in the channel. The channel impulse response is essentially a wideband channel description. However, because of its generality, it also has the advantage that can be used to obtain the radio channel response to the transmission of any signal by convolving the transmitted signal with $h(t,\tau)$. As a result, it can be used to predict and compare the performance of different wireless communication systems and transmission bandwidths in a particular radio channel condition.

Generally, the radio propagation channel is time varying. However, many physical channels possess fading statistics that can be assumed as stationary over short periods of time or over small spatial distances. These channels are classified as wide-sense stationary (WSS). The radio channel is further simplified by assuming that the surrounding objects contribute to the received signal as uncorrelated scattering (US). These types of channels are then termed wide-sense stationary uncorrelated scattering (WSSUS) channels [31] in which channel impulse response can be simplified as

$$h(\tau) = \sum_{i=0}^{N-1} a_i \exp\left[-j(\omega_c \tau_i + \phi_i)\right] \cdot \delta(\tau - \tau_i) \tag{3.2}$$

3.2.3 Narrow- and Wide-Band Signal Fading

Due to multipath propagation, the signals arriving at the Rx interfere with each other and produce signal fading when the Rx is moved. This is the primary effect of the radio channel on the propagating waves, and thus needs to be well understood. Fig. 3.2 illustrates a typical received signal by a mobile terminal moving away from the Tx, from which three different types of fading are extracted. The received signal strength changes rapidly when the Rx is moved from one point to another in the environment.

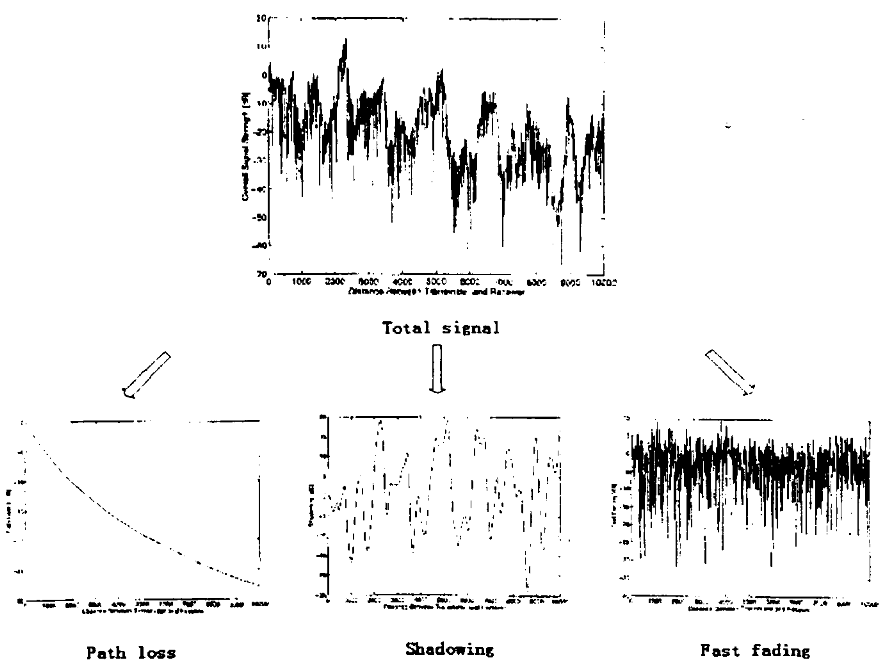

Figure 3.2: The received signal decomposed into three types of fading [5].

Path loss, shadowing (or slow-fading) and fast-fading are three types of fading generally observed in a received signal. These fading processes vary as the relative position of the Tx and Rx changes and as any contributing objects within the environment are moved. Path loss is an overall decrease in field strength which arises as the Tx-Rx distance is increased. Superimposed on path loss is the shadowing, or known as slow-fading, which is due to the varying nature of the propagation environment. Fast fading is further superimposed on the shadowing due to interference between multiple waves arriving at the Rx. For a given Tx-Rx distance, the path loss is constant. However, because the particular clutter (walls, furniture, etc.) along a path at a given distance will be different for every path, the received signal varies with respect to the nominal value given by path loss. Some paths may suffer increased loss, while the other may have increased signal strength. This phenomenon is termed shadowing or slow fading. Local mean signal strength, measured within a few tens of wavelengths distance, normally 10 ~ 20 wavelengths in indoor environments and larger value of 40 wavelengths in outdoor environments, is a good indication of the shadowing effect, and signal variations up to 20 dB are commonly observed in indoor environments. In addition to the shadowing effect, rapid fluctuations of the signal can be seen. Multiple waves arriving at the Rx have different phases and are combined vectorially. Fast-fading is the result of either constructive or destructive interference between these multiple waves which arrive at the Rx with different propagation delays, strengths and phases. This small-scale signal strength may vary, on the scale of half-wavelength distance, from peak levels of a few decibels above the mean level to 30 dB or more below the peaks in deep fades.

Traditional analogue wireless communication systems and more advanced digital communication systems respond differently to the multipath channel fading. This is attributed to the fact that the bandwidth of analogue communication systems is much smaller than that of digital communication systems. For a comparison of their responses to a particular radio channel, it is intuitive to consider two types of communications: the pulse communication and the continuous wave (CW) communication. In the first case, the Rx has infinitely wide bandwidth and can resolve each individual incoming multipath component, hence the received signal is, as shown in Eq. (3.2), a series of time-delayed pulses with different magnitudes and phases. In the second case, however, the waves via multiple paths all arrive at the Rx at essentially the same time, so that the Rx cannot resolve individual incoming multipath components. The received signal is then expressed as

$$y = \exp(-j\omega_c\tau)\cdot\sum_{i=0}^{N-1} a_i \exp(-j\phi_i) \tag{3.3}$$

It is clearly seen that the received signal envelope is the summation of all incoming waves combined vectorially. As the Rx is moved over a short distance, even a fraction of the propagating wavelength long, scatters in the vicinity of the Rx cause small variations of the path length of each multipath wave. These small variations do not cause significant modification of the magnitude, but can produce significant phase difference for each multipath wave. Vectorial combination of the received multipath components may cause the signal strength dramatically different at points only a short distance apart, as shown in Fig. 3.2, depending on the distribution of phases among the received waves.

In practice, any wireless communication system is of a finite bandwidth. On the other hand, the radio channel is also of a finite bandwidth, over which the radio channel has a constant gain and a linear phase response. The bandwidth of the radio channel depends on the time delay characteristic of each multipath component [9].

If the transmitted signal bandwidth is much smaller than the bandwidth of the radio channel, the amplitude of the received signal will vary rapidly, but the signal will not be distorted in time, as in the case of fast-fading observed for the aforementioned CW signals.

If the transmitted signal bandwidth is increased but still smaller than the bandwidth of the multipath channel, as in the case of general digital communication with low date transmission rates, the spectral characteristics of the transmitted signal are still preserved at the Rx. In the time domain analysis, when the transmitted signal is of a finite duration, multipath components arriving with time delays smaller than the transmitted signal duration cannot be resolved as contributions from distinct paths and are detected as a smeared single component which is the partial overlap of multiple pulses [33]. The amplitude of this broadened pulse depends on the relative phases of individual wave contributions and will exhibit fading when the Rx is moved over a distance of a fraction of the wavelength. Depending on whether the relative delays are large compared to the transmitted pulse, the signal may experience significant distortion and cause ISI. On the other hand, multipath components arriving with time delays larger than the transmitted signal duration can be resolved as a series of delayed and attenuated pulses of the original transmitted signal.

If the transmitted signal bandwidth is greater than the bandwidth of the multipath channel, the received signal will be distorted because of different attenuated and time-delayed multipath pulses. Most of the multipath pulses can be resolved by the Rx and the received signal strength will not fade much over a local area. High-speed digital transmission is much likely to experience this multipath distortion and the ISI problem. In the frequency domain, the spectral characteristics of the transmitted signal are no longer preserved at the Rx. Spectral components of the transmitted signal are affected by the channel in different ways and the received signal envelope is a function of frequency, resulting in a phenomenon known as frequency selective fading [9]. In comparison, for the case that the transmitted signal bandwidth is smaller than the channel bandwidth, flat fading is said to exist.

In general, different signals will undergo different types of fading. The type of fading experienced by a signal propagating through a radio channel depends on the nature of the transmitted signal with respect to the characteristics of the channel. In narrow-band transmissions, the multipath channel causes fluctuation in the envelope and phase of the received signal. In wide-band pulse transmission, the effect of channel is to produce a series of delayed and attenuated echoes for each transmitted pulse.

3.3 Channel Parameters

The baseband channel impulse response can be used to fully characterise the radio channel. However, from an engineering point of view, it is difficult to characterise the radio channel by observing the channel response at each field point within the environment where the communication systems are to be deployed. Instead, channel parameters derived from the channel response, which describe the behaviour of the propagation channel, are much more useful and meaningful for system design and planning. In this section, the channel parameters within the scope of the research are given.

3.3.1 Path Loss

Path loss (PL) between a pair of antennas is defined by the ratio of the transmitted power P_T to the received power P_R . usually described in decibels. This quantity is the characteristic of the propagation path. It is a parameter which can predict the power level of the wireless communication system and the space coverage of the base station. Note that due to the reciprocity, PL is the same no matter which antenna is at the Tx and which is at the Rx. Friis [34] firstly derived the relationship in a free-space propagation environment. The basic free-space propagation path loss is due to the geometric spherical expansion of waves and can be given by

$$\frac{P_T}{P_R} = \frac{(4\pi d)^2}{G_T G_R \lambda^2} \tag{3.4}$$

where G_T and G_R are the transmitting antenna and receiving antenna gains, respectively; d is the Tx-Rx distance: and λ is the wavelength of propagating wave. An inverse square law with distance is seen for the power radiation. Also can be seen is that at higher frequencies the range for a given path loss is reduced, as a result, more cells are required to cover a given area. In order to express *PL* independently of the system parameters G_T and G_R in the above equation, *PL* is generally described by referring to the received power at reference point, i.e.

$$PL(d)[\text{dB}] = 10\log_{10}(P_T / P_R) - PL(d_0) \qquad (3.5)$$

where $PL(d_0)$ is the measured received power at reference point normally positioned at 1 m away from the Tx ($d_0 = 1$ m). The propagation loss, thus defined, can be used to describe the propagation medium essentially independently of the system gains and losses. *PL* includes all of the possible elements of loss associated with interactions between the propagating wave and any objects in the environment where both the Tx and Rx are. It is used for constructing a link budget, which is usually the first step in the design and analysis of a wireless communication system.

In reality, besides the primary geometric spreading factor in free-space power radiation described in Eq. (3.4), additional spreading occurs because of multiple reflections due to the multipath wave interference. These multiple-reflection effects can result in the power law of propagation being between inverse third and fifth power with distance [9]. *PL* of the radio channel can therefore be described by a simple model which includes the path loss exponent and the standard deviation (STD) of *PL* as [31]

$$PL(d)[\text{dB}] = PL(d_0) + 10n\log(d / d_0) + X_\sigma \qquad (3.6)$$

where n is the path loss exponent indicating how fast the path loss increases with distance; X_σ is a zero-mean Gaussian distributed random variable with standard deviation σ, both in decibels.

3.3.2 Time Dispersion Parameters

For digital communication systems, the time dispersion characteristic of the radio channel is an important issue for determining appropriate data transmission rates to prevent inter-symbol interference. The channel impulse response $h(\tau)$ is the full characterisation of a radio channel, from which the time dispersion parameters can be defined. The power delay profile, which gives the time distribution of the received signal power from a transmitted δ-pulse, is defined as [9]

$$P(\tau) = |h(\tau)|^2 = \sum_{k=1}^{N} a_k^2\,\delta(\tau - \tau_k) \tag{3.7}$$

In order to compare different multipath channels and to develop some general design guildlines for wireless systems, parameters that grossly quantify the multipath channel are used. From a power delay profile, the time dispersion parameters can be determined. The time dispersive properties of a wideband multipath channel are most commonly quantified by the mean excess delay ($\bar{\tau}$) and RMS delay spread (τ_{rms}). The mean excess delay is the first moment of the power delay profile defined as [9]

$$\bar{\tau} = \frac{\sum_k P(\tau_k)\,\tau_k}{\sum_k P(\tau_k)} = \frac{\sum_k a_k^2 \tau_k}{\sum_k a_k^2} \tag{3.8}$$

RMS delay spread is the square root of the second central moment of the power delay profile defined as

$$\tau_{rms} = \sqrt{\overline{\tau^2} - (\bar{\tau})^2} \tag{3.9}$$

where

$$\overline{\tau^2} = \frac{\sum_k P(\tau_k)\,\tau_k^2}{\sum_k P(\tau_k)} = \frac{\sum_k a_k^2 \tau_k^2}{\sum_k a_k^2} \tag{3.10}$$

These delays are measured relative to the first detectable signal reaching the Rx at $\tau_0 = 0$. Eqs. (3.9) and (3.10) do not rely on the absolute power level of $P(\tau)$, but only the relative amplitudes of the multipath components within $P(\tau)$. Strong echoes with long delays relative to the first detectable path contribute significantly to τ_{rms}. Performance of a wireless communication system is very sensitive to the value of τ_{rms} [35]. It is a good measure of the channel's multipath spread and gives an indication of the potential for inter-symbol interference, from which the BER can be calculated. More specifically, analysis and simulation studies have shown that the maximum transmission data rate that can be reliably supported by an indoor wireless channel is a few percent of τ_{rms} without diversity or equalisation [36]. Therefore, detailed analysis of τ_{rms} can provide valuable information to designers of digital wireless communication systems.

3.3.3 Frequency Selectivity Parameter

The radio channel can be considered as a bandpass filter with a certain bandwidth. If the bandwidth of transmitted signal is greater than channel's bandwidth, then the radio channel creates frequency selective fading on the received signal, i.e., different frequency components of the transmitted signal experiences different gain and phase response possessed by the radio channel. The frequency-selective behaviour of the radio channel can be obtained at the Rx by observing the correlation between two signals at different frequencies. The coherence bandwidth Bc is the statistical average bandwidth of the radio channel, over which the signal propagation characteristics are correlated. The definition of the coherence is based on the complex autocorrelation function $|R_T(\omega)|$ of the channel's frequency response. For WSSUS channels, $R_T(\omega)$ is related to the power delay profile via a Fourier transform as [31]

$$R_T(\omega) = \int_{-\infty}^{+\infty} P(\tau) e^{-j\omega\tau} \, d\tau \tag{3.11}$$

$R_T(\omega)$ is also known as the frequency correlation function (FCF), and the channel coherence bandwidth Bc is the smallest value of ω for which $R_T(\omega)$ equals some specific correlation level, e.g. 0.5 or 0.9. An example of a power delay profile and its FCF is shown in Fig. 3.3. Time dispersion gives rise to a spread power delay profile. Bc is a frequency-domain channel parameter which is useful for the evaluation of a communication system and also provides data for the design of systems which employ frequency diversity for improvement of performance [37].

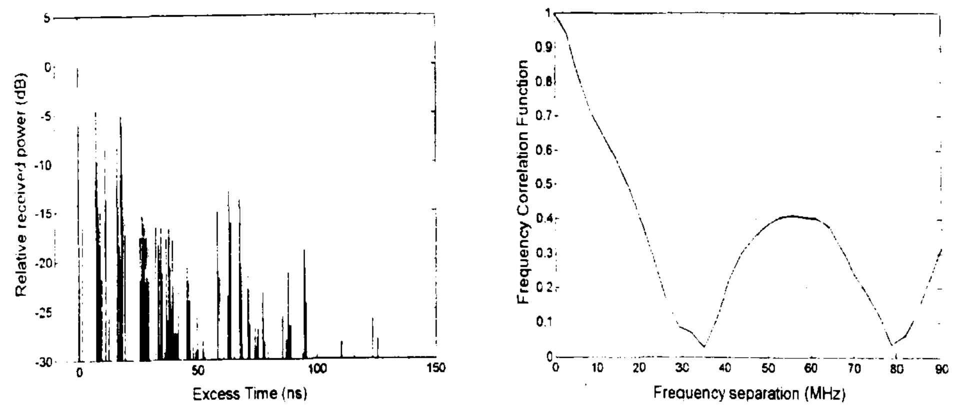

(a) (b)

Figure 3.3: An example of (a) a power delay profile and (b) its frequency correlation function.

3.4 Indoor Radio Channel Modelling

The development of optimally designed wireless communication systems requires a thorough understanding of the radio propagation characteristics of the environment where the systems are to be deployed. Reflection, transmission and diffraction are generally the dominant mechanisms that impact the radio propagation within indoor environments. A radio channel model capable of describing these mechanisms is in great need to help system designers prior to the deployment of wireless communication systems. System coverage, determined by the system power link budget according to the path loss characteristics and the impact of co-channel interference in frequency reuse system, is the basic consideration in the design and installation of wireless communication systems. Also, the transceiver's complexity is affected significantly by the time dispersion characteristics of the radio environment. In general, indoor radio channel models should be able to predict the system coverage and the time dispersion characteristics of the channel in an indoor environment.

Modelling the radio channel has historically been one of the most difficult parts of wireless radio system design. The channel models can be classified into empirical models and site-specific models. In general, statistical models need extensive measurement data and do not provide site-specific information. Site-specific propagation models provide site-specific information but require considerable detail of the layout of the environment.

3.4.1 Empirical Channel Modelling

In various complex environments, the propagation process is too complicated to enable a purely theoretical analysis. As a result, the channel modelling is typically performed in a statistical fashion, based on measurements conducted specifically for an intended communication environment. This empirical method relies on extensive sets of measured data and fitting curves or analytical expressions to these data to derive a mathematical channel description. In this way, the parameters of the channel impulse response can be statistically modelled. This approach has attracted a lot of research activities for the investigation of indoor radio channels [46], [48], [50], [84], [88], and several models have been proposed. A summary of these models can be found in [5], [31]. This empirical modelling has the property of implicitly taking into account all factors of the radio channel, either known or unknown. However, radio propagation characteristics may be sensitive to the environment where the system is deployed, so that measurements in one scenario may not be applicable to another.

While these empirical models are very fast in computing the field strength, they have two major drawbacks. Firstly, the channel path loss and time dispersion characteristics vary significantly in various indoor environments. For example, channel characteristics in an office building are very different from that in a factory building due to their differences in geometry, and materials used in building structures, etc. This indicates that indoor channel is highly dependent on the type of building (layout, dimensions, etc.) and the electromagnetic properties of environmental structures. Therefore, a purely empirical model must always be subjected to stringent validation by testing it on data sets collected at locations and transmission frequencies other than those used to produce the model in the first place. Secondly, due to the complex nature of indoor environments and the highly varying multipath characteristics, conducting experiments on the premises of potential customers is much time-consuming and expensive, whereas the application of measurement data to other scenarios may not be vary accurate.

3.4.2 Deterministic Channel Modelling

As discussed above, the empirical model can provide typical examples of channel impulse responses but cannot predict the impulse response associated with a particular location. For an accurate modelling of the representative channel characteristics, one should have reliable knowledge of the physical propagation mechanisms. The complex nature of indoor environments makes it necessary to take into account the geometrical and electromagnetic characteristics of the environment and other objects present inside the propagation environment, in order to develop an accurate model of the propagation channel. Thanks to the development of computer visualisation technique, accurate geometry data of building blueprints can readily be presented in a form suitable for propagation predictions. Prediction model which incorporates with scenario geometry data is termed deterministic model, or site-specific model [9]. Once a propagation model has been verified, an environment can be quickly entered into the model to provide propagation characteristics for initial system evaluation.

Deterministic radio propagation prediction is a highly complicated electromagnetic problem. The complexity of the scenario (random in certain aspects) makes it computationally intensive to predict radio propagation with a high degree of accuracy. Depending on the characteristics of the environments, several techniques have been used in the deterministic models, among which the rigorous and ray-based methods are most commonly used.

(1) Rigorous methods:

In principle, ultimate details of the multipath propagation may be obtained by solving Maxwell's equations with boundary conditions which express the physical properties of the walls and other structures that scatter the radio waves. Finite-difference time-domain (FDTD) method [38] is a numerical solution to Maxwell's equations, which is widely used for solving electromagnetic problems. Taking into account of wave interactions in propagation inherently, The FDTD method can yield accurate narrow- and wide-band information on the propagation channel, and the statistics of multipath propagation directly. However, The FDTD method requires a discretisation of the objects in elements with dimensions lower than a fraction of the wavelength (typically $\lambda/8$). Since the electrical size of a typical building structure is very large compared to the wavelength in the

UHF and millimetre frequency bands, the number of resultant elements for a typical indoor scenario becomes enormous. Consequently, the amount of memory size and computation time required by the FDTD method makes this technique infeasible in conventional channel modelling. Nevertheless, due to its high prediction accuracy, the FDTD method has been used in small areas [79], [89] to yield insight into the fundamental processes that affect building propagation.

(2) Ray-based methods:

Ray tracing is an important topic in the world of computer graphics. Several ray propagation models have been developed for computer visualisation applications [39], [40]. They simulate the propagation of light, i.e. electromagnetic wave in the visible frequency range. For frequencies in the UHF and millimetre frequency bands, the wavelengths of propagating waves are significantly smaller than the typical dimensions of building structures. As a result, electromagnetic wave propagation in these frequency bands is similar to the light propagation in the sense that both behave in a ray-like fashion. Due to this common aspect, many propagation models in wireless communications are incorporated with techniques of visual rendering and then adapted to the special characteristics of the UHF and millimetre wave propagation. The ray-based methods describe the radio wave emitted from the Tx in terms of individual rays. By tracing these rays and their interactions with surrounding objects on their journey to the Rx, the ray-based methods calculate the unfolded length of each ray and its associated field strength. Field strengths of those rays that can reach the Rx are added up to compute the total received signal strength by the Rx. Comparison of the radio prediction by ray approximations and exact integration of scattered field strength [41] further justifies that ray approximation is valid in indoor environments, irrespective of the finite extent of the building structures. The ray-based methods can be mush less demanding of computation resource than the methods based on Maxwell's equations and can provide much more details than empirical models. Using the ray-based method, the properties of each multipath ray arriving at the Rx can be deterministically obtained, from which the power delay profile, and hence the channel response, can be computed. As a result, a comprehensive information on the radio channel characteristics can be obtained.

The ray-based methods proposed for the propagation prediction are generally classified into two main groups: the ray-launching technique based on the shooting and bouncing rays (SBR) method, and the ray-tracing technique based on the image method. These two techniques differ from each other in the sense that they trace the rays based on different methods. Fig. 3.4 illustrates these two methods in a two-dimensional reflection-only environment. As for the computation of field strength at the Rx, they perform in a similar way.

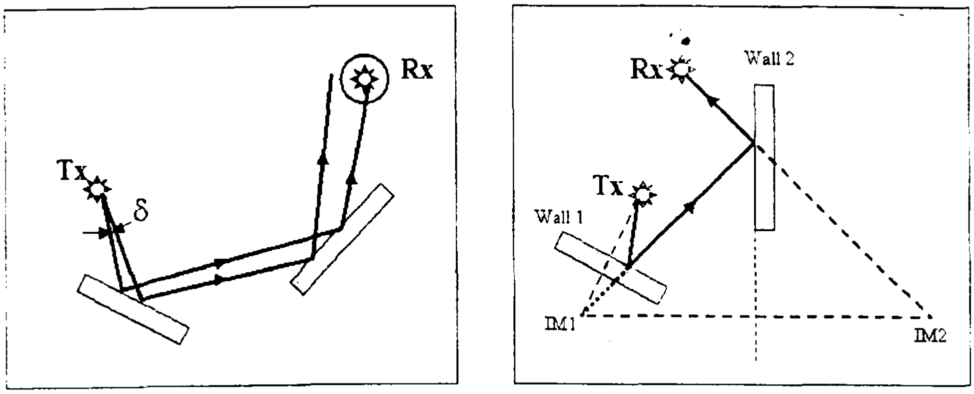

(a) (b)

Figure 3.4: Ray tracing principle of (a) the ray-launching method and (b) the ray-tracing method.

(a) Ray-launching method:

The ray-launching method is a forward method that traces the rays in all directions from the Tx to the Rx. Assuming a spherical radiation of the transmitted electromagnetic wave, the radiation sphere is divided into numerous sections, each with a constant angular separation δ [42] as shown in Fig. 3.4(a). Thereby, the propagating wave from the Tx is modelled as multiple ray tubes covering all directions in space, with each constrained in a section of the sphere. As an example, for a maximum angular separation of one degree between rays, 40,000 ray tubes need to be launched in all directions. As the ray tube advances, it may encounter environmental objects and its cross section increases. The intersection of a ray tube with all the objects in the scenario is computed. The resultant ray tube is then tested to see if it illuminates the Rx. Next, the reflected ray tube originated from the intersection point advances in another direction. The reflected ray tube is then tested to see if it illuminates the Rx. The propagation of each ray tube is traced until its field strength level drops below a certain threshold level. Selection of a threshold should be in accordance to the background noise and sensitivity of the Rx. This process is repeated up to the number of multiple reflections which are to be taken into account, and for each ray tube originated from the Tx.

Since the Tx and Rx are modelled as points and the number of the ray tubes traced is finite, a reception sphere centred in the Rx needs to be employed to determine if a ray tube reaches the Rx. This is illustrated as the capture circle in two-dimensional scenario in Fig. 3.4(a). The radius of the reception sphere must be carefully chosen to ensure that one ray, but only one, originated from the Tx and reflected from the same set of objects will illuminate the Rx. The adequate value for the radius is dependent on the unfolded length of the ray tube [42], [43].

The ray-launching method has been successfully used in some complex environments. For example, references [44-47] dealt with outdoor microcellular channel prediction, and [48-52] dealt with indoor channel prediction. Even though, the ray-launching method has the following disadvantages:

- A large number of ray tubes must be launched despite whether or not these rays arrive at the Rx, which in some cases wastes a lot of computation time.
- The accuracy of results depends on the number of ray tubes launched. By increasing the angular separation between neighbouring rays thus reducing the number of ray tubes, some propagation paths can be missed and therefore causes error: whereas reducing the separation is inefficient because some paths will be represented by more than one ray tube.
- It requires a large number of reception tests at the Rx and the accuracy of results relies on the radius of the reception sphere at the Rx and spatial resolution of the distance between the Tx and Rx.
- This method also presents serious difficulties when the edge diffraction is incorporated into the model [53]. As will be discussed in the next chapter, a ray incident on an edge will produces infinite diffracted rays, so it is extremely difficult to incorporate the edge-diffracted rays using this method.

(b) Ray-tracing method:

The ray-tracing method is a backward method which associates virtual sources with every object and traces the rays from the Rx back to the Tx. It is based on the image theory and the assumption that the specular reflection occurs when a ray interacts with an object in the environment. By assuming every object surface in the scenario as a mirror, the ray-tracing method starts by constructing the images of the Tx with respect to all object surfaces. For multiple reflections, the next step is to find the image of the Tx image with respect to another object surface where the second point of reflection will be located. For example, the image IM1 shown in Fig. 3.4(b) is the image of the Tx with respect to wall 1 and image IM2 is the image of IM1 with respect to wall 2. Following the same rule, this process is repeated up to the desired number of reflections. The lines between each image and the Rx are then constructed. The line connecting the Rx with the highest-level image IM2 is then tested to see if it crosses the image plane (wall 2) at the location of the object surface. If this location exists, the intersection point is a valid reflection point, and this testing process is repeated for the line connecting current image (IM2) with the next lower-level image (IM1) to see if it has valid reflection point on the lower-level image plane (wall 1). This process is repeated until the ray is traced back to the Tx. During this process, if any reflection point is tested as invalid, i.e., the intersection point does not lie on the actual object surface, this ray is considered as invalid and thus eliminated.

There are several advantages offered by the ray-tracing method. First, the method is a point-to-point tracing technique, hence does not require reception tests as needed in the ray-launching method. In this case, the Rx is positioned at an infinitesimally small point so that paths are neither duplicated nor missed, and each path is calculated precisely. This improves the prediction accuracy and computation efficiency. The ray-tracing technique can also easily incorporate the effects of diffraction by building edges and corners. Finally, for simple environments, the various permutations of reflecting walls are significantly fewer than the number of paths which need to be considered to give a similar result using the ray-launching method. Nevertheless, extensive ray-object tests are still in need for validation of reflection points on object surfaces. Thus, the selection of scatters to generate the images becomes extremely difficult for complex environment. Some prediction models based on the image theory have been developed recently [63], [77], [91], [98], [118].

In this research, the ray-tracing method based on image theory is developed for the characterisation of indoor radio channels. This model is based on a full 3D approach which takes into account all wave interactions with environmental objects such as building walls, floors and ceilings. In indoor environments, the horizontal partitions such as ceilings and floors could make significant effects on radio propagation and thus need to be accounted for. This model can also readily be simplified into a two-dimensional model, which is applicable to some cases such as the outdoor microcellular propagation prediction.

3.5 Summary

In this chapter, the concept of radio channel is introduced and its characteristic is briefly described in terms of channel parameters. From a system point of view, an indoor radio environment can be modelled as a fading multipath channel with baseband equivalent impulse response which represents the electromagnetic properties of different propagation rays from a Tx to a Rx. Channel modelling based on different approaches are discussed and some literature covering the work which has been performed on channel characterisation and modelling is also provided. Site-specific computer-based modelling is an effective approach for the characterisation of indoor radio channels due to its accuracy and the capability of producing both narrow- and wide-band channel parameters.

Chapter 4

Implementation of Ray-Tracing Model

4.1 Introduction

In the preceding chapter, various channel modelling methods have been discussed. Indoor environment is highly cluttered for radio propagation due to the existence of a large number of building structures. Accurate prediction of radio propagation within indoor environments requires deterministic modelling in combination with site-specific environmental information.

This chapter is dedicated to describing the development of our 3D ray-tracing model based on image theory for prediction of radio propagation within indoor environments. The model makes use of the geometrical optics (GO) and the uniform theory of diffraction (UTD) [54] to analyse the radio wave interactions with building structures on its propagation. The model is developed in a 3D sense so that environmental objects in 3D space are taken into account. Section 4.2 describes the principle of the ray-tracing method. Section 4.3 deals with the database required by the model. Comprehensive database structures and parameters are described. In section

4.4, a ray tree algorithm based on the illumination zone concept is presented, by which the efficiency of ray-tracing model can be significantly improved. Section 4.5 describes how the ray-tracing algorithm verifies and determines the exact paths of individual rays. Section 4.6 describes the computation of reflection and transmission fields based on the GO theory. Section 4.7 describes the computation of diffraction fields based on the UTD theory. Calculation of the overall signal strengths at the Rx is described in Section 4.8.

4.2 Principle of Ray-Tracing Method

The ray-tracing method is a deterministic characterisation technique for construction of the radio channel impulse response, from which the radio channel characteristics can be fully understood. From a general point of view, the ray-tracing algorithm consists of two main functional blocks, i.e., the determination of the ray paths between the Tx and Rx, and the evaluation of the corresponding electromagnetic field strength.

A site-specific propagation tool includes, as a fundamental element, a ray tracer. Point-to-point ray tracing is the preferred methodology due to its accuracy. In indoor environments, multiple reflections between wall-to-wall, wall-to-ceiling/floor, wall-to-ceiling/floor-to-wall, as well as the diffractions by building edges/corners and subsequent reflections must be taken into account. Transmission through building structures is another important propagation mechanism and should also be accounted for. These multiple rays interact with environmental objects, resulting in an extremely complex problem of tracing the ray propagation. In our ray-tracing algorithm, each ray emitted from the Tx is traced based on the image theory and the general Fermat's principle [54] to determine its propagation path when interacting with surrounding building structures. The ray tracer process is implemented in a full 3D sense, i.e., all building structures in 3D space are taken into account.

After the determination of all ray paths from the Tx to the Rx, the field strength associated with each ray is computed based on the GO/UTD methods. When a ray interacts with a wall panel, both reflection from and transmission through the wall occur. For each existing ray, the reflected/transmitted field strengths for every ray-wall interaction are computed by the GO and subsequently multiplied by each other, resulting in the field strength associated with the ray. The UTD is used to account for the diffraction loss when the rays encounter building corners/edges. With the knowledge of the path trajectory and the associated field strength of each multipath ray, the channel impulse response can be fully obtained from the ray-tracing model.

The ray-tracing model developed in this research is a software package that traces the multipath ray propagation based on image theory and employs 3D GO/UTD methods for the computation of electromagnetic field strengths, with user-defined environmental database. The software package is written in Visual C++ codes. It has the following main modules:

- The database module which describes the site-specific environmental information, on both geometry and electromagnetic properties;
- The module of generating a ray tree which is used to accelerate the computation;
- The module which verifies and computes the trajectories of the ray paths which exist in the ray tree;
- The GO/UTD module which computes the electric field strength of the combination of multipath rays arriving at the Rx;
- The post-process module that allows the computation of a comprehensive number of narrow- and wide-band channel parameters.

4.3 Database

Database of the environment is required in a site-specific channel prediction model. The database in our model consists of the geometrical and electromagnetic description of the indoor environment in the region under study, as well as the parameters of the simulated communication system. The database of our ray-tracing model includes the followings information:

- Geometrical description of the environmental objects (the locations, dimensions and shapes);
- Type of each building structure and its constitutive parameters (the permittivity, conductivity and thickness).
- Parameters of both the Tx and Rx (the antenna positions, orientations, radiation patterns, transmission power, and the operating frequency);

In the database of our ray-tracing model, rectangular portions of each individual structure, together with the assigned individual constitutive parameters, are varied to reproduce the actual discontinuities (walls, doors, and windows, etc.) and their corresponding electromagnetic properties. By combining these models appropriately, a great number of different environments can be analysed.

4.3.1 Geometrical Description of Environmental Objects

For modelling of the radio propagation environment, the application of GO/UTD to a given propagation scenario requires the decomposition of a given configuration into simple geometrical configurations from which the reflection, transmission and diffraction coefficients can be calculated. For this purpose, a specific data structure has been developed to describe the geometry of different elements existing in the environment. Since a GO based model is used, only objects with dimensions that are much larger than the wavelengths in the UHF frequency band are considered. It is not practical to include small-scale features within the environment. For instance, exit signs, doorknobs, door hinges, and furniture are not included in the model. The modelling of building geometry includes large objects such as walls, ceilings/floors, partitions, windows and doors, etc. The inclusion of large objects only is justified since the goal of this work is to predict large-scale average path loss and time dispersion which are influenced by major changes in the geometry surrounding the Tx and Rx, but not by the small-scale fluctuations of a narrow band signal. Moreover, experimental and theoretical analyses in indoor environments [55-58] verify that furniture and irregularity of building surface generally cause variation in the signal's phase and the field in the vicinity of the scattering site, but do not significantly affect the local mean signal strength that a propagation model usually predicts, unless they are large and directly obstruct the propagation path [55].

In the database, all geometrical descriptions in 3D space are described in a Cartesian coordinate system, where any position is related to the system origin using x, y and z axes. Large environmental objects are modelled by means of flat facets, in which the building geometry is described as a collection of finite rectangular planar polygons (facets) freely positioned in the space, with the spatial coordinates of individual structure dimensions listed in the database. Since flat facets are the most abundant elements in these environments, use of this form of environmental modelling to represent indoor scenarios is suitable. In addition, edges between pairs of these facets are also included in the database.

Our ray-tracing model makes use of a vector database. All facets and edges in the database are defined by vector notations. The "facet vector" arrangement helps both the use of the GO/UTD method and the efficient facet-search process for a large number of facets in the database. Fig. 4.1

illustrates a rectangular wall structure defined in vector notation in 3D space. In the database, the width, height, and position of each facet are described. The wall is modelled as a facet with its position vector W pointing from the coordinate origin to the corner of the facet. The dimension of the facet is defined by vectors U and V. The normal to this facet is defined by a unit vector n̂ resulting from the normalised cross-product of U and V, i.e.,

$$\hat{\mathbf{n}} = \frac{\mathbf{U} \times \mathbf{V}}{\left| \mathbf{U} \times \mathbf{V} \right|} \tag{4.1}$$

For indoor radio channel prediction, it is necessary to have a 3D database of the environmental geometry in order to account for the effects of both horizontal facets such as ceilings and floors and vertical facets such as walls. In the database, the normal vector n̂ of a facet can be in any direction to describe the 3D environment. This 3D model is indispensable, particularly when accounting for the influence of floors and ceilings. In our database, the floors and ceilings are considered to lie in the x-y plane and the directions normal to them are in the z-axis direction. Other objects vertical to the floors are considered as arbitrarily directed.

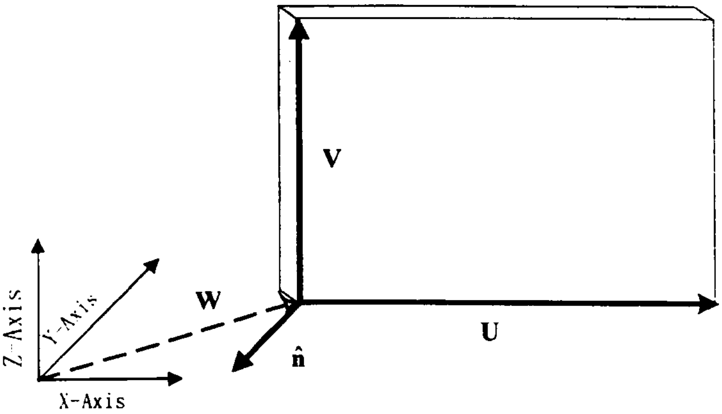

Figure 4.1: An illustration of the facet model.

Due to the fact that some structures in the environment are embedded in others, such as doors and windows are generally embedded in walls, our database distinguishes them as minor and major facets. Facets having the capability of embedding other facets, such as walls, are defined as major facets. Those facets embedded on major facets, such as doors and windows, are defined as minor facets. The major facet and its embedded minor facets share the same plane in space and the same normal unit vector but have different electromagnetic properties and possibly different thicknesses. The geometrical descriptions of both major and minor facets are exactly the same as illustrated in Fig. 4.1. However, due to their hypotaxis relationship, they have different priorities and are dealt with at different stages of the ray-tracing procedure. In the database, each major facet is given an integer number for identification (ID) for the purpose of ray-facet intersection searching in the ray-tracing algorithm at later stage, and each minor facet is assigned the same ID as the major facet in which it is embedded.

Assigning major and minor facets in the database has the advantage of reducing the number of facets necessary for the ray-facet intersection searching process and thus improves the computation efficiency. As an example, Fig. 4.2 shows a typical wall with two windows and a door embedded. In a usual way as described in [59], the whole facet is divided into several rectangles separated by dashed lines and ten facets in total are modelled in the database. All these facets have different IDs and therefore ten facets are used in the ray-facet intersection searching process. In contrast, one major facet and three minor facets (two windows and one door) are modelled in our database. Only the major facet is used in the ray-facet intersection searching process. The minor facets are not used until the process of determining the ray intersection point on the surface and the subsequent computation of the associated field strength. If a ray does not have an intersection with the major facet, then all minor facets embedded in the major facet are abandoned by the ray-tracing procedure. As will be discussed later, the computation time for the ray-tracing algorithm is strongly dependent on the number of facets used for ray-facet intersection searching. Our major-minor facets classification greatly reduces the number of facets that are necessary for the ray-facet intersection searching and thus dramatically saves computation time.

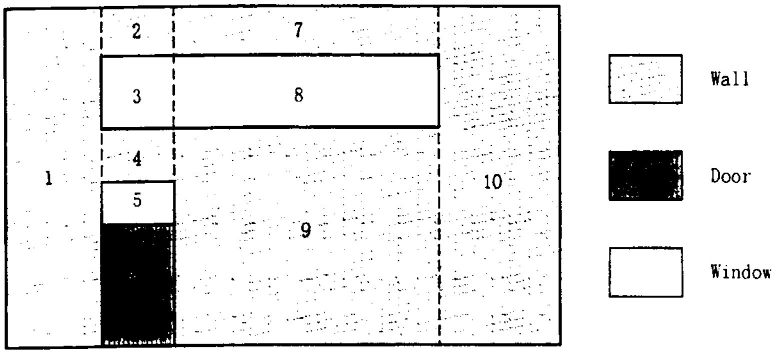

Figure 4.2: An illustration of the major and minor facets arrangement.

In addition to facets used to account for reflection and transmission mechanisms, the diffraction mechanism arising at building edges should be taken into account. An edge is defined by the common boundary shared by two facets, as shown in Fig. 4.3. Since in the geometric model the facets are assumed flat, all edges in the database are straight. The parameters used to describe an edge are its starting point position W, length of the edge h, the unit direction vector $\hat{\mathbf{e}}$, and IDs of the pair of facets forming the edge, as well as the angle of the wedge α (angle formed by the facets).

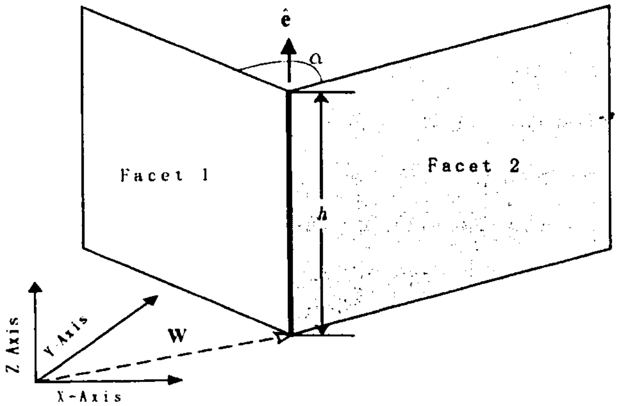

Figure 4.3: An illustration of an edge definition in the database.

4.3.2 Dielectric Description of Environmental Objects

All physical models require the constitutive parameters of the building structures as an input. The facets included in the database will typically have a variety of structures, such as metallic board, single- and multi-layered dielectric slabs, and their electromagnetic properties may be very complex. A simplified model describing their electromagnetic properties is necessary to model the ray-facet interaction process within a general-purpose model. Our ray-tracing model can work with all facets that are modelled as single- or multi-layered materials, where each layer is assumed as a homogeneous dielectric slab. The electromagnetic properties of each layer in the model are effective properties, and it is essential that the reflected and transmitted field are the same as in the real structure. This model works particularly well for structures of simple composition such as glass windows and wooden panels. For more complex structures such as reinforced concrete walls, the simplified model which ignores the effect of metal studs appears adequate [61]. Building structures are assumed as dielectric slabs, so the constitutive parameters of each layer in a structure include its permittivity, conductivity and thickness. The relative permeability μ_r is assumed as 1.

Information on the thickness of each building structure is given in the database. In the context of outdoor propagation, the influence of the through-building transmission is often negligible. When a ray is transmitted through an external building wall, it is rapidly attenuated due to the subsequent obstacles that it encounters after the transmission. Therefore, the field associated with the rays that return to the outdoor environment are negligible [62-64]. Building walls in outdoor scenarios are consequently characterised as semi-infinite structures, i.e., the thickness of building wall is assumed to be infinite. On the other hand, for indoor radio propagation, the rays transmitted through building structures play an important role, particularly in non-line-of-sight (NLOS) regions. Transmission is an important propagation mechanism for indoor propagation and must be accounted for. Accordingly, in indoor prediction models, information on the thickness of each building structure will be required for the calculation of its reflection and transmission coefficients. These constitutive parameters are assigned manually to individual facets in the database. In appendix A, the layout of each floor of the Electrical Engineering building and the associated constitutive parameters are given. These data are used for the simulations performed in the research.

4.3.3 Description of the Tx and Rx Parameters

In our ray-tracing model, both the Tx and Rx positions can be assigned fixed values for single-point simulations, or along a designated route for multi-point simulations. In the database, the initial Tx and Rx positions are given. The Tx/Rx route direction, length and spatial resolution are specified for multi-point simulation. The transmitted power and the operating frequency are also specified in the database for field calculations.

An advantage of ray-tracing models over other propagation models is the ability to incorporate antenna radiation patterns and particularly, to consider the effects of the radiation pattern on individual rays. Since in our model the geometry of each ray is examined in 3D space, both the azimuth and elevation angles of arrival at the antennas are available, and hence, the model is capable of using 3D radiation patterns. The inclusion of the radiation patterns of the transmitting and receiving antennas is important as it accounts for both the initial field strength of each ray emitted from the Tx and the Rx reception characteristics. Moreover, in the database, the transmitting and receiving antennas can be steered in any direction in space and hence, the radio channel characteristics can be examined for any antenna orientation. In addtion, the types and orientations of both transmitting and receiving antennas are specified and the ray-tracing model will incorporate this information to compute the corresponding field strengths at any field point.

The predicted transmitted electric field strength is proportional to the transmitting antenna pattern in the direction of the transmitted wave multiplied with the component of the transmitted electric field along the plane of the transmission direction and the transmitting antenna axis [60]. A similar process is performed at the Rx to compute the received electric field strength. Note that, the radiation pattern of an antenna is normally expressed in spherical coordinate system, whereas our ray-tracing model uses the Cartesian coordinate system. Vector transformation from the spherical coordinate system to the Cartesian coordinate system is needed for field computation at the Tx. Field computation in between the Tx and Rx uses Cartesian coordinate system. Vector transformation from the Cartesian coordinate system to the spherical coordinate system is needed for field computation at the Rx. Formulas for the transformation between these coordinate systems can be found in [53].

4.4 Ray Tree Algorithm

To determine all possible propagation paths from the Tx to Rx, an algorithm is required, which should be able to compute all ray paths including the corresponding diffraction, reflection and transmission points. The primary problem in applying ray method is to find these ray paths. The nature of the ray-tracing model is such that it starts a ray at a single transmitting point, and finds all possible ray interactions with surrounding objects based on image theory, until the ray finally reaches the Rx. Note that the ray paths are reciprocal, so that the results apply to transmission by both the base station and the subscriber unit. In practice, this point-to-point ray-tracing approach to find all possible ray propagation paths requires high computation time. Thus, acceleration techniques are often required in order to make this approach computationally efficient. In this section, the image concept for ray path searching and determination is presented. An acceleration technique based on computing the so-called "ray tree" is also described. It comprises a tree-like list of images for possible interactions between the ray and the environmental objects. With the implementation of this ray tree, the computation time of the ray-tracing process is reduced, thus making the ray-tracing algorithm more practical and computationally efficient.

4.4.1 Image Concept and Path Determination

Among all the scattering mechanisms that occur during wave propagation within indoor environment, specular reflection is one of the dominant effects on the wave propagation. In UHF and microwave frequency bands, rays incident on building structures experience strong reflections in the specular direction. In the ray-tracing model, tracing such specular reflected rays is the most time-consuming process. To facilitate this, we use the concept of multiple images and the generalized Fermat's principle to determine all reflection paths. From the ray approximation of the GO and the theory of image, every major facet in the database is assumed as a mirror and we have that all reflections from a point source with respect to a facet seem to originate from another virtual source, called the image source generated in the mirror. The image of a source point with respect to a facet in 3D space is defined in Figure 4.4, where the image is behind the facet and the source is in front of it; the straight line connecting the source point with its image is perpendicular to the corresponding facet, and both the source point and its image are equidistant from the facet. The image is of the same size and magnitude as the source, but is laterally inverted [53]. The image position I is situated symmetrically to its source point S with respect to the facet and is given by

$$\mathbf{I} = \mathbf{S} - \left[2(\mathbf{S} - \mathbf{W}) \cdot \hat{\mathbf{n}}\right]\hat{\mathbf{n}} \tag{4.2}$$

W is the vector position of the facet corner and $\hat{n}$ is the unit vector normal to the facet, as defined in the previous database section; Q_r is the intersection point between the image-observation line and the facet. Given a source point and a facet, the reflected ray in the facet can be considered as the ray radiated from the virtual source point – image.

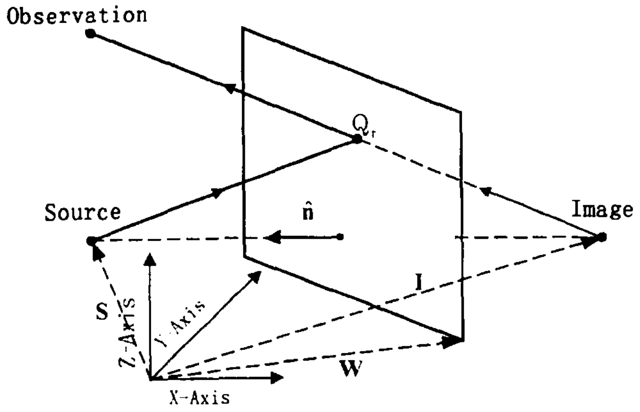

Figure 4.4: Image of a source and the actual reflected ray path.

A ray with multiple reflections can be constructed by considering the image as a new point source and continuing the image-creation process recursively. By determining these multiple images of the source with respect to all major facets in the database, the ray paths can therefore be determined with the information on the corresponding intersection points. The generalised Fermat's principle states that in the case of a ray in a homogeneous medium, the path followed by a ray is always such that the optical path is a minimum [54]. Therefore, a multi-section straight line connection of source point – intersection point(s) – observation point yields the actual propagation ray path. Figure 4.5 illustrates a simple 2D scenario and some of the reflected ray paths. In a 2D description, a facet in a 3D environment is described as a line segment. The single-reflection propagation path from wall 1 can be obtained by directly connecting the transmitting point Tx, reflection point Q_{11} with the receiving point Rx, i.e., Tx-Q_{11}-Rx. Likewise, path Tx-Q_{21}-Q_{22}-Rx represents a ray experiencing double reflections from wall 1 and then wall 2.

To compute the actual ray path, the image of the Tx with respect to wall 1, denoted by I_{11}, is firstly determined. Connecting the line Rx - I_{11} across wall 1 leads to its intersection point Q_{11} on the wall. After the determination of Q_{11}, the direct-line connection of these three points yields the actual ray path Tx-Q_{11}-Rx and the unfolded length is the actual ray path length. Likewise, By determining the image I_{21} of Tx with respect to wall 1 and the image I_{22} of I_{21} with respect to wall 2, the corresponding intersection points Q_{21} and Q_{22} can be determined backwards from the receiving point Rx and the actual ray path can therefore be computed. It should be noted that images I_{11} and I_{21} are at the same position in space however, I_{11} is the first intersection point in a single-reflection path and I_{21} is the first intersection point in a double-reflection path. They must be distinguished because they have different positions in the ray-tracing process. In practice, both the single-reflection path from wall 2 and the double-reflection path from wall 2 followed by wall 1 also exist. Moreover, higher order reflections, such as the treble-reflection from wall 1 to wall 2 then back to wall 1, also exists, thus yielding numerous ray paths that actually exist between Tx and Rx even in a very simple scenario.

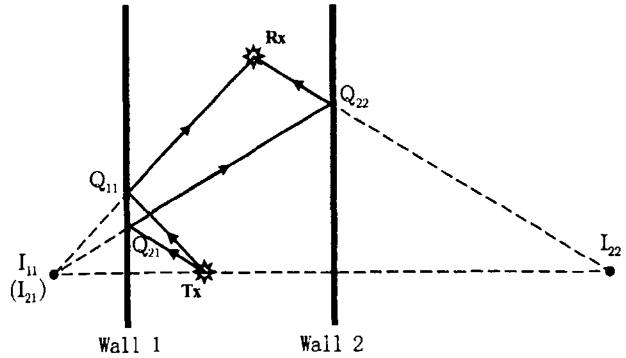

Figure 4.5: An illustration of the determination of a ray path.

4.4.2 Ray Tree Concept

Following the image concept described above, it is easy to generate the images of a source with respect to all major facets in the database. These images then serve as sources for a second round of reflections, and so forth. An image with respect to a specific facet in the database can act as a source with respect to other facets for generating images of higher order reflections. If there are M reflecting planes in the database, then there are M first-order, i.e., one-reflection, images of a source, $M(M-1)$ two-reflection images, $M(M-1)(M-1)$ three-reflection images, etc. The images can thus be arranged as a tree-like graph. The first branch is M-fold; all the later ones are $(M-1)$-fold. With squared-off reflecting planes it is possible for some of these images to coincide in space, but the algorithm should treat them separately because they have different positions in the graph. In contrast to the ray-launching approach, the one-to-one correspondence between images and rays is thus a useful way to avoid treating rays which leave the source but do not reach the destination of interest. Algorithms based on image theory naturally avoid processing those irrelevant rays and save computation time. Nevertheless, the number of images generated for an arbitrary scenario would be enormous. As an example, Fig. 4.6 shows a simple 2D scenario of two rooms consisting of five walls in the database. The Tx is located in one of the rooms. Correspondingly, a tree-like image graph used for the ray-tracing process is illustrated in Fig. 4.7, in which for simplicity only some branches of the tree are shown for describing up to treble reflections. The number circled in this figure represents the image of the Tx with respect to each corresponding numbered wall. The graph starts at the Tx, and comprises several layers that contain the images of the Tx, the second-layer images of the first-layer images, and so forth.

Consider M reflecting planes in the database with N reflections being taken into account, the number of images generated in the graph is $M(M-1)^{N-1}$ and consequently the same number of possible reflected ray paths need to be determined. Meanwhile, these reflected rays may undergo multiple transmissions through environmental objects before reaching the Rx. The main problem with the ray method is the high amount of computation time required to analyse these large number of rays which undergo multiple reflections and transmissions. This is attributed to the large number of ray-wall intersection tests and subsequent determination of ray paths which need to be performed for every ray which undergoes a user-defined order of reflections. This problem is prominent particularly in a complex scenario where the number of objects used to represent the environment is very high.

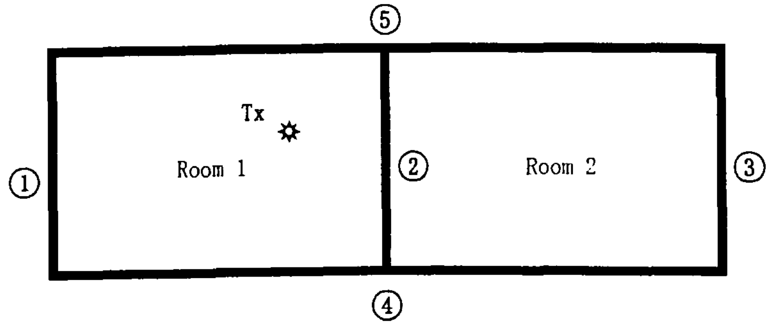

Figure 4.6: A simple 2D scenario used for generating the ray tree.

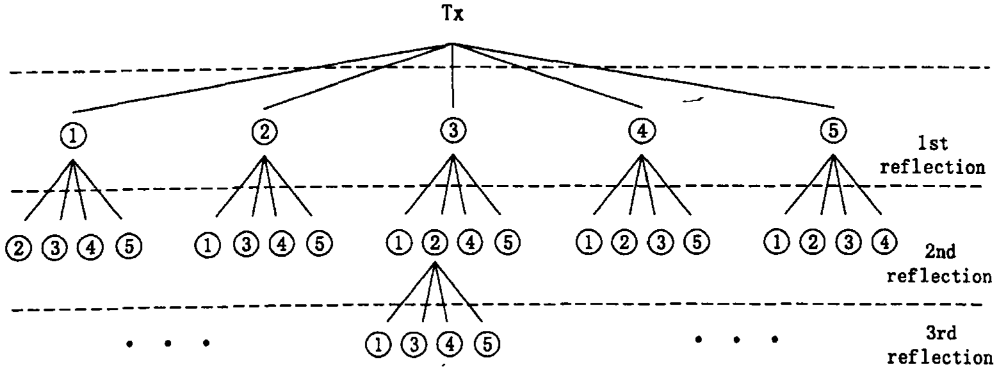

Figure 4.7: A tree-like graph of images generated from the 2D scenario.

The operation of generating images and ray paths discussed above assumes, in effect, that all reflectors are infinite planes. However, in the real world, the facets stored in the database are of finite-size and some rays may miss them. Thus many locations listed on the wall sequence may represent walls which are invisible from some particular Rx positions. As a result, the actual number of reflected rays reaching Rx is much less than the nominal value given above. For instance, the nominal number of images generated in the graph for three-reflections shown in Fig. 4.7 is calculated to be 80 . However, in Fig. 4.6, the image of Tx with respect to wall 2 for the first order reflection is on the right-hand side of wall 2. According to the image theory, when this image serves as a source for the second order reflection, the second order reflector must be on the left-hand side of wall 2 . Consequently, wall 3 in the scenario is "invisible" to this image and will not act as the second order reflector for this image. Wall 3 in the second branch in layer 2 of the list in Fig. 4.7 therefore should be eliminated and the total number of images considered is then reduced.

Determining whether an image of the source is visible at the Rx is to determine whether the assumed reflected ray intersects all the necessary facets and reaches the Rx. If an intersection point exists on the plane containing the facet but not on the finite-sized facet, it is a fictitious intersection point. A ray path containing such fictitious intersection points is referred to as spurious ray path and does not exist in reality. Only a reflected path with all its intersection points located on the corresponding reflecting facets is a real ray path which should be counted. Those spurious ray paths should be eliminated during the ray-tracing process. The earlier to find out the spurious ray paths, the greater saving in computation time and the higher efficiency which can be achieved. Following on from this, the normal image graph should be modified in order to allow the elimination of most of the spurious ray paths before the computation of the exact ray paths and their associated field strengths. A ray tree algorithm based on the image graph is developed to achieve this goal. It only contains the possible images while eliminating those impossible images which appeare in the image graph. Such acceleration technique can help reduce computation time significantly.

4.4.3 3D Scenario Projection

To verify the visibility of an image to a specific field point with respect to an environmental object defined in 3D space is extremely complex. For an arbitrarily located rectangular facet, the portion visible to the image is a truncated cone. The cone is enclosed by four planes that extend from the image through the four edges of the facet, which strictly speaking makes it an oblique four-faced pyramid. The cone is truncated by deleting the portion of it from the image to the facet. The visibility process requires to test whether the field point is within the truncated cone. Only those field points within the truncated cone which are visible to the image should be considered. This process has to be performed in a 3D sense, which makes computer programming very complicated and takes a large amount of computation time for visibility test.

Although the visibility test is a 3D problem, we can combine 2D ray-tracing and 3D geometry to solve it in an efficient way. In order to facilitate the visibility test, we project the 3D scenario into three 2D planes, i.e., x-y plane, y-z plane, and x-z plane, respectively. This projection concept is schematically shown in Figure 4.8, where one floor (A) and two vertical walls (B and C) exist in the scenario. The normal vectors of these facets are defined in z-, y- and x-axis directions, respectively. The projection process simplifies the 3D scenario into 2D description, but without losing any essential information. Unlike other approaches, we can compute a 3D scenario's true 3D ray path, rather than combining 2D results as presented in [91]. The process of testing rays in 3D scenario can then be decomposed in a few combined testing processes in 2D scenarios. For instance, for double-reflection test on walls B and C, the projected scenario on the x-y plane is studied; for treble-reflection test on walls C, A and B, the projected scenarios on the x-z plane and subsequently the y-z plane are studied. Note that, the order of planes of study is in accordance with the facet sequence of interest. In 2D space, each facet in the database is described by a line-segment instead of a panel. Therefore, the visibility test is carried out in a 2D way, that is, to test whether the straight line connecting the image with the field point falls in the 2D area constrained by two lines connecting two individual extremities of the line-segment with the image. This makes the program much more manageable.

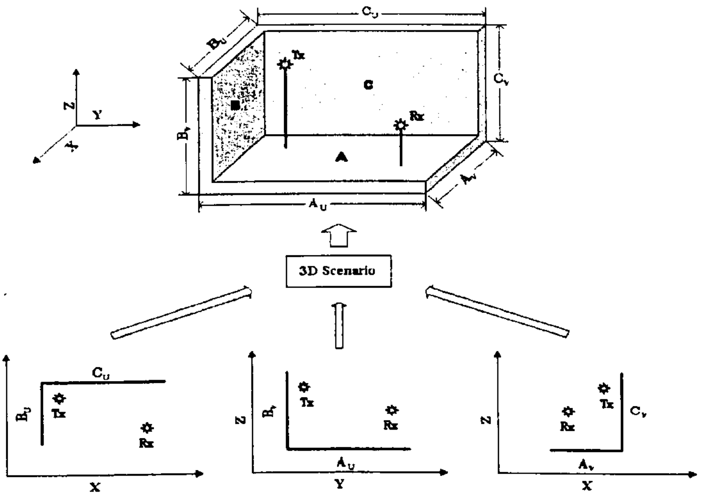

Figure 4.8: Projection of 3D scenario into 2D planes.

4.4.4 Illumination Zone Algorithm

After the process of projecting a 3D scenario into 2D planes, the illumination zone concept is employed, which is the core of the ray tree algorithm. One of the most significant characteristics of our ray-tracing model is that each image is associated with a specific illumination zone, i.e., the area for which the image can give a valid path. This is the space on the opposite side of the plane containing the reflecting facet which is used to generate the image. The use of an illumination zone significantly reduces the number of images and the time for ray-facet intersection searching, and makes it possible for the model to study large complex environments and trace thousands of rays efficiently. Fig. 4.9 (a) illustrates the illumination zone concept for a single-reflection case. Due to the finite dimension of a facet $[P_1, P_2]$ (conventionally we still call it facet even though it is a line-segment), the image can only illuminate the area coloured in grey. As a result, only points in this specific spatial region (known as the illumination zone), can lead to a real reflection path from the facet to the Tx. For instance, Rx1 is in the illumination zone of the image I, therefore a ray can be reflected from this facet and reaches Rx1. The path Tx-Q_r-Rx1 is a real propagation path that undergoes a single-reflection on the facet $[P_1, P_2]$. Rx2 is not in the illumination zone of the image, therefore the reflection point Q_r' determined by the image method is outside the facet, consequently, the path Tx-Q_r'-Rx2 is a spurious path and does not exist in reality.

Consider a double-reflection case illustrated in Fig. 4.9 (b), where the illumination zone of the image I with respect to facet 1 is shown. A portion of facet 2 is in the illumination zone of facet 1, whereas facet 3 is totally out of the illumination zone. Considering facet 1 as the reflector of the first-order reflection, facet 2 may be able to generate the second-order reflection. As a condition necessary for double reflection, the reflection point on the second-order reflector must lie in the illumination zone of the first order reflector. In this case, the extension of the line $\overline{IP_2}$ intersects the facet $[Q_1,Q_2]$ at point T. As a result, only a portion of facet 2 $[T,Q_2]$ can act as the reflector for the second-order reflection. If we know the image of I with respect to facet 2 and the Rx position, the double reflection ray path can be determined. In contrast, because facet 3 is not in the illumination zone of the image I, the first-order reflector facet 1 cannot see facet 3, hence the double-reflection ray path with the intersection point on facet 3 is definitely non-existent. As a result, there is no need to determine the image of I with respect to facet 3 and consequently saves computation time.

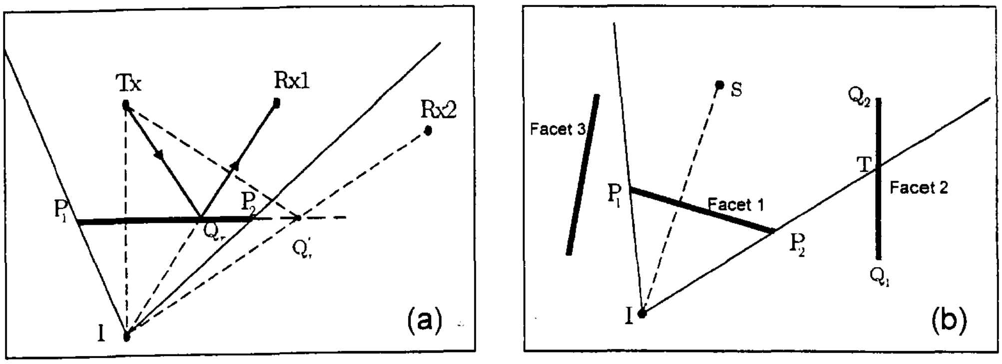

Figure 4.9: The illumination zone for (a) a single reflection and (b) a double reflection cases.

With this technique, only facets inside the illumination zone of the current image are used for the formation of new images, and moreover, these new images are not valid for the entire facet, but only for the facet illuminated by the "parent" image. The illumination zones of high order reflection images tend to get narrower and this prevents the number of images increasing exponentially with the order of ray interactions within the environment. Hence, the number of images is reduced dramatically since only those images that are capable of producing valid paths are generated and stored in the image table.

As a general approach, we will examine the illumination zone in basic facet arrangements in 2D sense. For two arbitrary facets in the environment, they can be classified into two categories: Facets that can illuminate other facets and facets that cannot. In the first case, because no illumination zone exists, the facets which cannot be seen from the "parent" facet are abandoned in the generation of the ray tree. In the second case, the two facets can be further classified into two categories: 1) two facets have no intersection, as shown in Fig. 4.10 (a); and 2) two facets have a common edge, as shown in Fig. 4.10 (b).

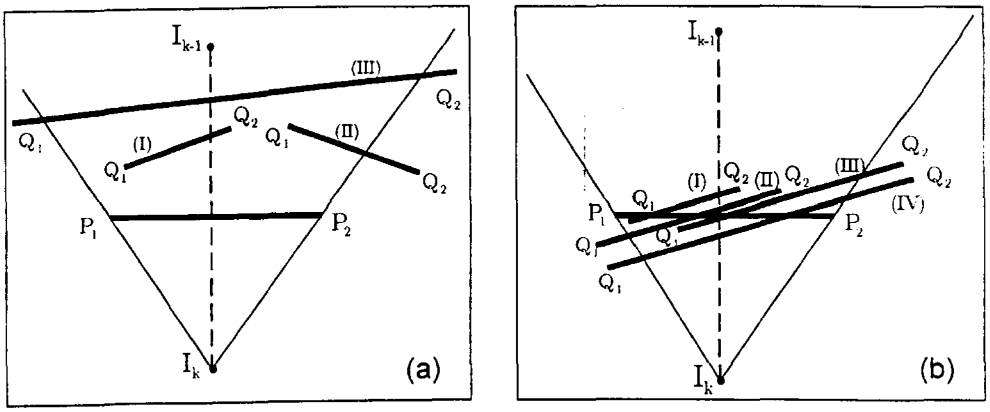

Figure 4.10: The illumination zone when (a) two facets have no intersection; and (b) two facets have intersection.

In Fig. 4.10 (a), we assume the $(k-1)$th level image of a ray is I_{k-1}, and its image with respect to the facet $[P_1,P_2]$ is I_k, which corresponds to the kth level image in the image graph. The immediate concern is to examine the illumination zone of the image I_{k+1} of source I_k with respect to the potential $(k+1)$th reflector $[Q_1,Q_2]$. It should be noted that the positions P_1 and P_2 are inter-changeable, and so are Q_1 and Q_2. There are three types of potential reflectors in this category as shown in the figure:

- (I) $[Q_1,Q_2]$ is completely within the illumination zone: both $\overline{I_kP_1}$ and $\overline{I_kP_2}$ do not cross the facet;
- (II) $[Q_1,Q_2]$ is partially within the illumination zone: either $\overline{I_kP_1}$ or $\overline{I_kP_2}$ crosses the facet;

- (III) $[Q_1, Q_2]$ is partially within the illumination zone: both $\overline{I_kP_1}$ and $\overline{I_kP_2}$ cross the facet.

In case (I), the whole facet of the potential $(k+1)$th reflector $[Q_1, Q_2]$ is illuminated by the image source I_k and therefore will act as a new reflector. In case (II), a portion of $[Q_1, Q_2]$ including one edge of the facet is illuminated by the image source I_k and this part will act as a new reflector. In case (III), a mid-portion of $[Q_1, Q_2]$ is illuminated by I_k and will act as a new reflector. Fig. 4.11 illustrates the corresponding illumination zones for these situations.

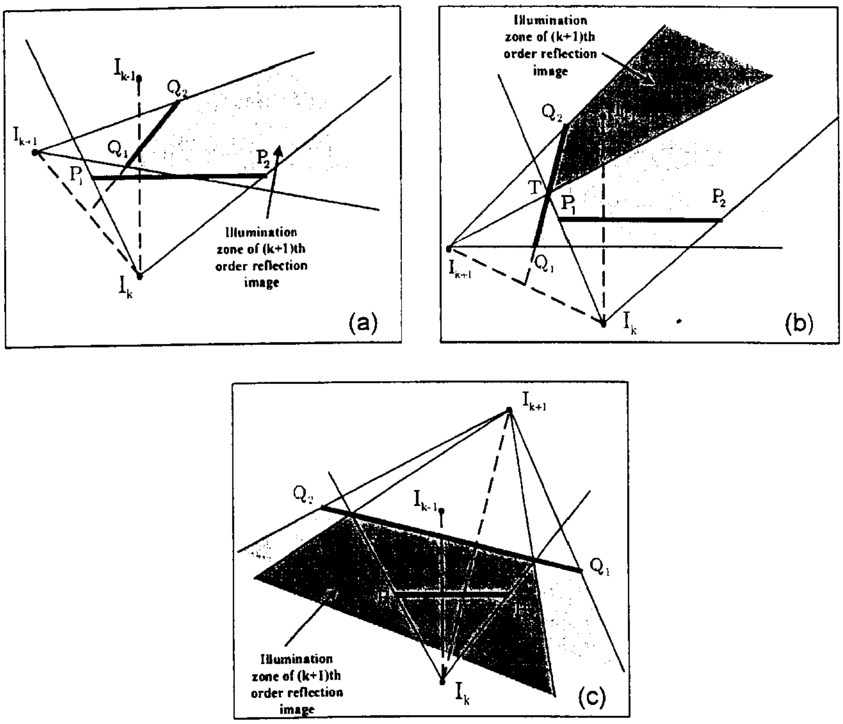

Figure 4.11: The illumination zone when two facets have no intersection: (a) case (I); (b) case (II); and (c) case (III).

In Fig. 4.10 (b) where the potential reflector has a common edge with the kth level reflector, there are four types of potential reflectors in this category:

- (I) $[Q_1,Q_2]$ is completely within the area confined by lines $\overline{I_kP_1}$ and $\overline{I_kP_2}$: both lines $\overline{I_kQ_1}$ and I_kQ_2 cross $[P_1,P_2]$;
- (II) A portion of $[Q_1,Q_2]$ is within the area confined by lines $\overline{I_kP_1}$ and $\overline{I_kP_2}$: line I_kP_1 crosses facet $[Q_1,Q_2]$ and line I_kQ_2 crosses $[P_1,P_2]$;
- (III) A portion of $[Q_1,Q_2]$ is within the area confined by lines $\overline{I_kP_1}$ and $\overline{I_kP_2}$: line $\overline{I_kQ_1}$ crosses facet $[P_1,P_2]$ and line $\overline{I_kP_2}$ crosses $[Q_1,Q_2]$;
- (IV) A portion of $[Q_1,Q_2]$ is within the area confined by lines $\overline{I_kP_1}$ and $\overline{I_kP_2}$: both lines I_kP_1 and $\overline{I_kP_2}$ cross $[Q_1,Q_2]$.

Likewise, Fig. 4.12 illustrates the corresponding illumination zones for these situations. As can be seen from Figs. 4.11 and 4.12, the illumination zone is generally irregular in shape and thus makes programming much more complicated.

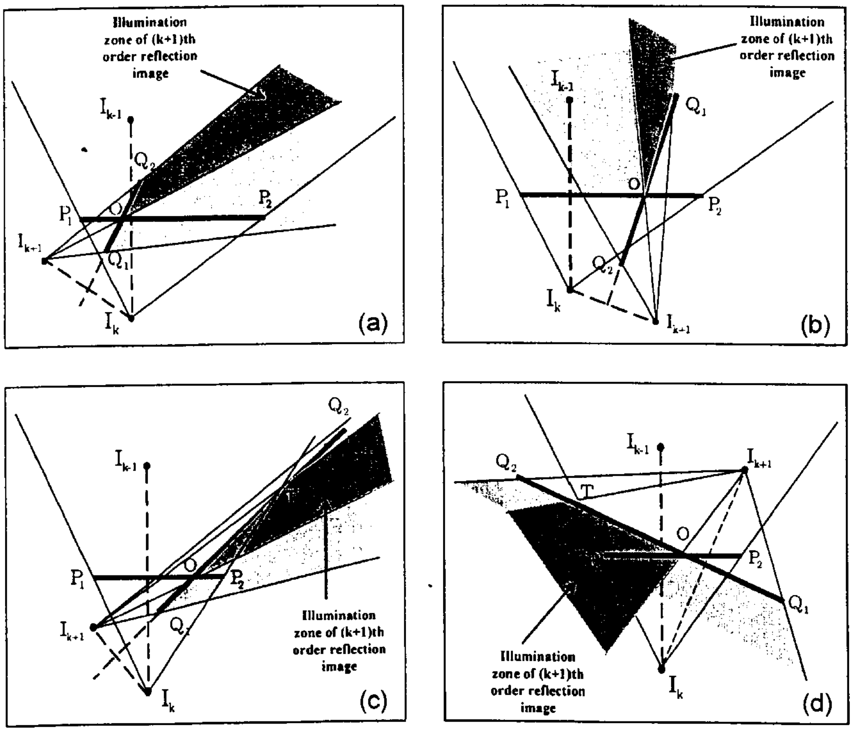

Figure 4.12: The illumination zone when two facets have a common edge: (a) case (I); (b) case (II); (c) case (III); and (d) case (VI).

4.4.5 Implementation of Ray Tree

With the illumination zone algorithm developed above, a ray tree consisting of user-defined number of levels can be fully developed. The number of levels of the ray tree corresponds to the number of reflections considered in the ray-tracing algorithm. The construction of the ray tree is similar to the image graph shown in Fig. 4.7, but each node in the ray tree comprises the image and its associated information. Assume that there are M major facets in the database. The ray tree starts from the Tx at level 0. All major facets W_i ($i = 1$ to M) in the database are assumed as potential reflectors and the locations of the images of Tx with respect to these facets, denoted by I_{1j} ($j = 1$ to M), are computed and stored in the ray tree at level 1, resulting in M branches at level 1 of the tree. At level 2, each branch of I_{1j} at level 1 is treated individually. The illumination zone of each I_{1j} with respect to its corresponding facet W_j is computed. All facets other than the one associated with I_{1j}, W_i ($i \neq j$), are tested for their visibility to I_{1j}. Only those visible to I_{1j} are considered as potential reflectors and the images of I_{1j}, denoted by I_{2i}, with respect to them are computed and stored in the ray tree.

If the facet is invisible to I_{1j}, the image of I_{1j} with respect to the facet is considered non-existent and its corresponding branch at level 2 is simply cut off from the ray tree. From the relation between the facet associated with I_{1j} and the facet associated with I_{2i}, the illumination zone of I_{2i} is computed and used for the facet visibility test and image generation (I_{3k}, $k = 1$ to M) at level 3. Likewise, at level l, for any image I_{lj} and its corresponding facet, a branch is traced to facets at level $(l+1)$ visible to I_{lj} for visibility test and image generation. By repeating this recursive scheme, a complete ray tree consisting of user-defined number of levels can be built up, provided the location of Tx is known. It is worth noting that the computation of the images in the ray tree is independent on the location of the Rx. It is only related to the physical geometry of the environment and the location of the Tx.

The position of an image in the ray tree specifies the facets which have contributed as reflectors, but not those facets which have contributed as transmitting panels. For an observation point in the illumination zone of an image, the straight line between the point and the intersecting point on the facet associated with the image may have intersections with other facets. Consider an image I_{li} with respect to facet W_i at level l of the ray tree and its image $I_{(l+1)j}$ with respect to facet W_j at level $(l+1)$. All facets except W_j in the database are tested for their visibility to the image I_{li}. Only the facets which are, at least partially, within the illumination zone of I_{li} can be potential transmitting facets to the ray having intersection points on both reflecting facets W_i and W_j. Those facets which are completely outside the illumination zone of I_{li} will definitely not contribute as transmitting facets. The IDs of the facets that succeed in the visibility tests are stored, in conjunction with I_{li}, at level l of the ray tree. The advantage of this process is that, when determining whether a reflecting ray transmits through a facet on its journey from the reflection point on W_i to the reflection point on W_j, the ray-tracing algorithm only needs to search the facets among those having succeeded in the visibility tests, instead of all facets in the database.

If the highest level of the ray tree is N, then all rays experiencing up to Nth order reflections are taken into account in the ray-tracing model. For an arbitrarily positioned Rx, not all branches in the ray tree can give rise to a propagation path connecting the Tx with the Rx. Only when the Rx is within the illumination zone of the image I_{Ni}, the actual ray path is possibly existent. To facilitate the visibility test of the Rx to any I_{Ni}, the information on the portions of all facets W_i which can give illumination of each I_{Ni} are computed and stored in the ray tree as well.

For a fully implemented ray tree, at any level l $(0 < l < N)$, each individual image I_{li}, the ID of its corresponding facet W_i, and the IDs of possible transmitting facets are stored in the ray tree. At level N of the ray tree, in addition to these, the information on the portion of facet W_i which can give illumination of image I_{Ni} is also stored. The advantage of configuring the ray tree in this form is that from the relative position of I_{Ni} with respect to the Rx, it enables us to quickly identify which of the images I_{Ni} will contribute to the received signal at the Rx, and which of the images will not contribute. This is easily done by examining whether the Rx is within the illumination zone of a particular image. For the Rx which has a reflection point on facet W_i, the next step is to check whether the path connecting the reflection point with the image $I_{(N-1)j}$ at level $(N-1)$ is valid. The algorithm for the ray validation will be described later in this chapter. By following this process recursively from level N backward to level 0 of the ray tree, all possible rays can be found. This can be performed simply by reading the ray tree.

4.4.6 Computation Efficiency by Ray Tree

The use of the ray tree algorithm can dramatically improve the operating speed of the ray-tracing model since most of unnecessary computation is avoided, whereas the accuracy of modelling remains. To illustrate this improvement, a number of ray trees are generated on various floors in the Electrical Engineering building. Fig. 4.13 shows the layout of the 6th floor of the building, together with six Tx locations used to generate the ray trees and five Rx locations used to test the simulation time. The locations of these transmitters and receivers are chosen arbitrarily to represent the whole floor.

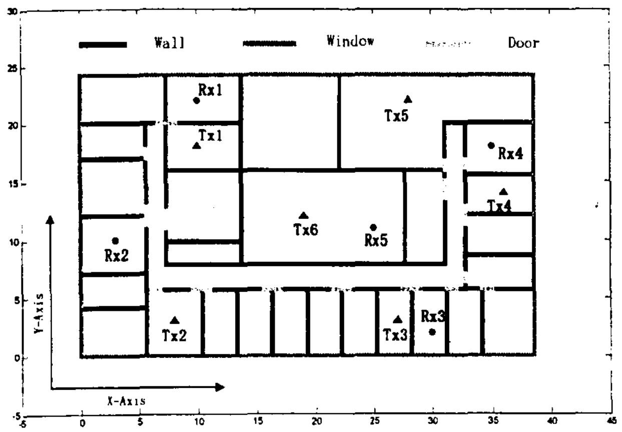

Figure 4.13: Blueprint of the sixth floor and the Tx and Rx locations.

There are 35 major facets for the description of the 6th floor in the database. Correspondingly, if N reflections are considered in the ray-tracing algorithm, then there are $35 \cdot 34^{N-1}$ images that need to be searched in a standard way. In contrast, the number of images that need to be searched after the implementation of the ray tree is significantly reduced. Table 4.1 gives the number of images that needs to be searched for different Tx locations, with or without implementing the ray tree. It is shown that, as the number of reflections included is increased, the actual number of images that needs to be searched in the standard ray-tracing algorithm is increased exponentially, whereas the number of images that need to be searched after the implementation of the ray tree is substantially lower. The larger the number of reflections considered, the higher the efficiency that can be achieved by implementing the ray tree. For different Tx locations, the number of images which need to be searched in the standard ray-tracing algorithm is constant, whereas this number is varied after the implementation of the ray tree. This is because any ray tree is started from the Tx and is dependent on its location. Once the relative position of the Tx with respect to environmental structures is changed, the structure of the ray tree is changed and the resultant number of images is therefore changed. However, this change is found not drastic for the Tx locations tested. This can be explained that even though Tx location is changed, the relative position between each facet is constant and therefore the image-facet relation is relative steady at mid-levels of the ray tree.

Table 4.1: The number of facets required for search in the ray-tracing algorithm for the scenario shown in Fig. 4.13.

	N = 0	**N = 1**	**N = 2**	**N = 3**	**N = 4**	**N = 5**
Standard	1	35	1190	40460	1375640	46771760
Tx1	1	35	521	6192	66456	659736
Tx2	1	35	537	6373	69381	705315
Tx3	1	35	568	6934	76747	785495
Tx4	1	35	506	5880	62602	618006
Tx5	1	35	472	5279	55417	536273
Tx6	1	35	514	6255	68588	693902

To further test the efficiency of the implementation of the ray tree, the same five Tx positions on the x-y plane are also chosen to generate the ray tree for the 2nd, 3rd, 4th and 5th floors of the building. There are 22, 21, 27, 32 major facets in the database for each of these floors, respectively. On each floor, the number of images calculated for all Tx locations are averaged to represent for that floor. The average number of images is calculated for different value of N, and their normalised values with respect to the nominal value calculated from the standard ray-tracing algorithm are shown in Fig. 4.14. It shows that as the level of ray tree increases, the number of actual images generated is much less than the nominal value. At level 2 of the ray tree, the illumination zone of an image at level 1 is narrower than that of Tx at level 0. Likewise, at level 3, the illumination zone of an image at level 2 is narrower than that of the image at level 1. As the ray tree evolves, the more levels the ray tree has, the narrower illumination zone for each image is obtained. On the other hand, as the level of ray tree increases, the nominal number of images generated is increased in an exponential way. This shows that as the level of ray tree increases, a higher efficiency can be achieved by implementing the ray tree. It is seen that for $N = 4$ in the few indoor scenarios examined, the number of images that used from the ray tree is generally less then 10% of the nominal value. It is also shown in the figure that as the number of facets in the environment increases, higher efficiency can be achieved. This indicates that the implementation of the ray tree will result in higher efficiency when applied to more complex scenarios.

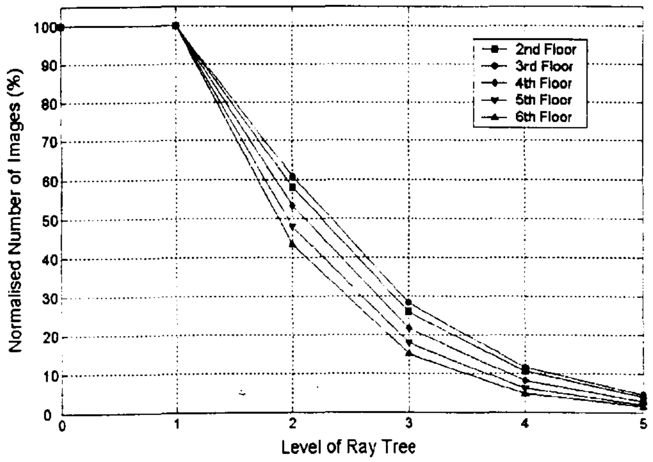

Figure 4.14: Normalised number of images required for search on different floors.

On the sixth floor, we assume Tx is located in the middle of the floor, i.e., Tx6 shown in Fig. 4.13. Five arbitrarily located receiver positions Rx1 to Rx5 are chosen to compute the signal strength at these points. Fig. 4.15 shows the normalised computation time derived by taking the ratio of the computation time with ray tree implementation to the computation without. A significant improvement can be obtained by implementing the ray tree. Assuming that the ray tree has one level, on average about 50% of computation time can be saved by implementing the ray tree. The computation time is reduced by more than 90% if the ray tree has five levels, i.e., five reflections are taken into account in each ray path. For each Rx location, similar improvements are achieved, which shows that the same degree of improvement can be applicable to any Rx locations in the scenario. This indicates that in a ray-tracing model, a significant amount of computation time is spent on the ray-facet intersection searching process. Therefore, the elimination of the impossible images, as the ray tree does, at an early stage of the ray-tracing procedure is a very efficient way to improve the performance of the ray-tracing model.

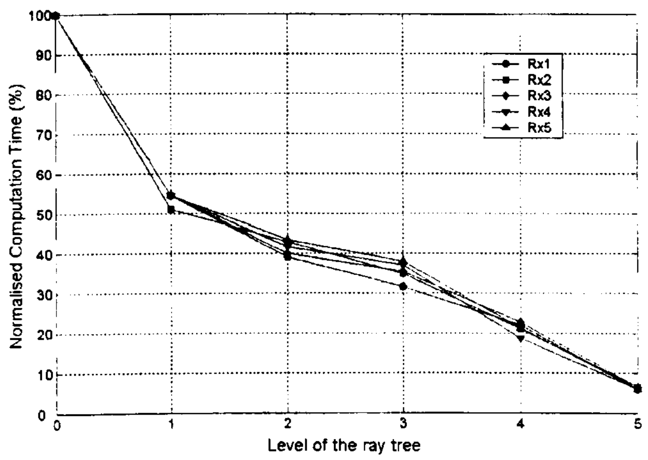

Figure 4.15: Normalised computation time of the ray-tracing model.

4.4 Ray Verification and Path Computation

After the implementation of the ray tree, all possible rays from the Tx to Rx with corresponding intersecting facets in a 3D scenario are obtained. It remains to determine each of these rays whether or not exists in reality and if so the corresponding path length. This is necessary for any deterministic model in order to accurately compute the contribution of each ray at the received field strength and the associated propagation delay.

4.5.1 Intersection Point Determination

Consider a ray which has several intersections with the environmental objects, coupled by reflection and transmission mechanisms before it reaches the Rx. The major difficulty encountered in image-based ray-tracing models is the determination of the exact reflection/transmission points at all facets in a 3D scenario. Information on these points is required to compute the actual ray path and the corresponding propagation delay. This process is performed for all possible propagation paths obtained from the ray tree. Conceptually, the method works by tracing the rays for all images and by performing intersection tests on every facet encountered in the determination of the intersection points.

Unlike the ray tree that can be generated in 2D space, the intersection test has to be performed in fully 3D sense. Fig. 4.16 illustrates the process for determining the intersection point of a ray on a facet in 3D space. Define the ray connecting a source $\mathbf{R}_s$ with an observation point $\mathbf{R}_o$ in terms of its origin and direction vector given by [39]

$$\hat{\mathbf{R}}_d = \frac{\mathbf{R}_o - \mathbf{R}_s}{\left|\mathbf{R}_o - \mathbf{R}_s\right|} \tag{4.3}$$

from which the ray is defined as

$$\mathbf{R}(t) = \mathbf{R}_s + \mathbf{R}_d \cdot t \tag{4.4}$$

where t is the distance from the source point. A plane in 3D space is defined as

$$\text{Plane} \equiv A \cdot x + B \cdot y + C \cdot z + D = 0 \tag{4.5}$$

where $A^2 + B^2 + C^2 = 1$. The unit vector normal to the plane is given by $\hat{\mathbf{n}} = [\ A\ \ B\ \ C\ ]$, and the distance from the Cartesian coordinate system origin to the plane is D. The distance from the ray's origin to the intersection with the plane is derived by simply substituting the expansion of Eq. (4.4) into Eq. (4.5) and solving for t, resulting in the following in vector notation as

$$t = \frac{-(\hat{\mathbf{n}} \cdot \mathbf{R}_s + D)}{\hat{\mathbf{n}} \cdot \mathbf{R}_d} \tag{4.6}$$

By the definition of t, the ray from the source to the observation point has an intersection with the plane only when the parameter t calculated from Eq. (4.6) satisfies the condition $0 < t < |\mathbf{R}_o - \mathbf{R}_s|$. With the information on t, the intersection point on the plane is obtained from Eq. (4.4). Finally, it is necessary to determine whether or not the intersection point is on the finite-size facet on the intersecting plane. To do this, the intersection point $\mathbf{R}_p$ with respect to the corner $\mathbf{R}_c$ of the facet is defined by vector $\mathbf{P} = \mathbf{R}_p - \mathbf{R}_c$. To ensure the intersection point is within the facet, the following equations must be satisfied:

$$0 < \mathbf{P} \cdot \mathbf{U} < |\mathbf{U}|^2 \tag{4.7}$$

$$0 < \mathbf{P} \cdot \mathbf{V} < |\mathbf{V}|^2 \tag{4.8}$$

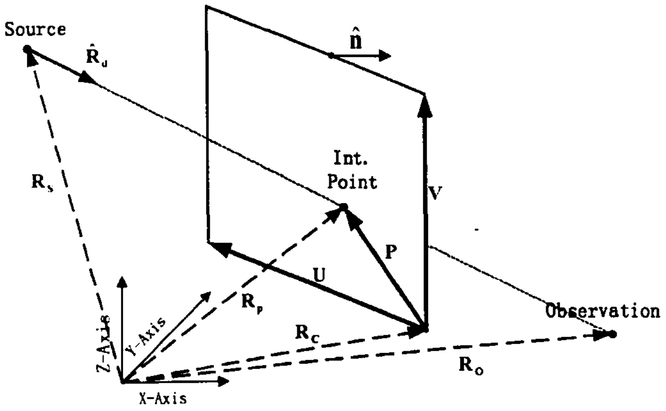

Figure 4.16: An illustration of a ray intersecting with a facet in 3D space.

This intersection point determination process is performed in the same way for both reflection and transmission cases. If a ray has an intersection with the plane but outside the reflecting facet, it is a spurious ray and should not be counted. For the verification of a ray, this intersection point determination process has to be performed on each intersecting facet. This is done in a step-by-step manner from the Rx back to the Tx. A ray is valid only when it has all valid intersection points on the reflecting facets with which it interacts. At any stage, if the intersection point is tested invalid, the ray is cut off and the program stops the subsequent tests.

4.5.2 Calculation of Path Length and Time Delay

After the determination of intersection points on each facet, we can identify which of the many rays generated from the ray tree will contribute to the total signal at the Rx. The exact 3D path is determined by reading the images from the ray tree in order to perform the backward ray tracing from the Rx to Tx. For a valid ray from the Tx to Rx, the path length is the summation of the distance between each two intersection points and the distance from the Tx to the first intersection point, as well as the distance from the last intersection point to the Rx.

Due to the path length difference of each ray from the Tx to Rx, each ray will undergo a different time delay. This means that each ray originating from the Tx will arrive at the Rx at different time. The time delay is quantified by the ratio of the path length s to the wave speed (assumed as the speed of light in free space $c = 3\times10^8$ m/s), i.e., s/c. Consequently, the phase associated with each ray, expressed as e^{-jks} (k is the wave number), is different. These time delays and phase differences have great impacts on wireless system performance. In narrow-band systems, the time delay difference generally cannot be resolved by the Rx however, the associated phase may have large variations in the range of $[0,2\pi]$, resulting in a fast-fading phenomenon. In wide-band systems, most of the time delay differences can be resolved by the Rx, resulting in a time-delayed sequences received signal.

4.6 GO Reflection and Transmission

When a radio wave propagating in one medium encounters a boundary with another medium having different electromagnetic properties, it will be partially reflected back into the first medium and partially transmitted into the second medium. The direction of propagation, phase and amplitudes of the reflected and transmitted waves are determined by the boundary conditions at the interface [65], which require that the tangential components of the total electric field **E** and the total magnetic field **H** be continuous across the boundary.

Considering the Tx as a point source, it radiates spherical waves towards the space. However, the electric and magnetic fields throughout small regions of space surrounding individual ray paths satisfy the usual uniform plane wave relationships at any point along the rays [54]; hence the rays can be approximated as local plane waves. This approximation simplifies the modelling of radio wave propagation. For instance, interference patterns and related phenomena produced by multipath arrivals can be modelled using the superposition of plane waves. Almost all boundary effects on radio wave propagation can be understood in terms of combinations of simple mechanisms operating on plane waves [5].

When a signal is reflected off or transmitted through an object, the degree of signal attenuation and the amount of phase change depend on the complex reflection and transmission coefficients, respectively. Calculating these coefficients of the composite structures is a classic problem. The techniques employed range from analytical techniques like Floquet analysis and mode matching to full numerical approaches like method of moment (MOM), finite element, and finite-difference methods. They are capable of high accuracy, but are computationally intensive and, hence, is not preferred in signal-prediction models. For the ray-tracing model, efficient close-form expressions for calculating both the reflection and transmission coefficients for composite structures are desired. Consequently, the Geometrical Optics (GO) method has been considered for the modelling of reflection and transmission mechanisms. In this method, the propagation of the electromagnetic field is modelled as rays, which represent discrete local plane waves originated from point sources and propagate in 3D space. Each ray has an associated wavefront, a vectorial value of the electric field, and a phase term. Snell's law of reflection and the law of transmission based on Fermat's principle [5], which are obtained by satisfying the boundary conditions exactly and Maxwell's equations approximately, are the basics in the GO method for calculating the reflection and transmission coefficients.

4.6.1 Local Ray-Fixed Coordinate System

In this subsection, we introduce the local ray-fixed coordinate system to describe the polarisation of the incident, reflected and transmitted GO fields between two media. The purpose of the introduction of the local ray-fixed coordinate system is to facilitate the field calculation when a ray interacts with building structures in 3D space. The local ray-fixed coordinate is a coordinate system whose coordinate-axes are determined by the direction of the incident ray and the normal unit vector of the reflecting boundary. A diagram showing the directions of the incident and reflected plane waves for a planar boundary between two media is illustrated in Fig. 4.17, which has been drawn assuming that the incident plane wave propagates parallel to the x-z plane, making an angle θ_i with the normal to the boundary $\hat{\mathbf{n}}$. The reflected and transmitted waves in this case will also propagate parallel to the *x-z* plane.

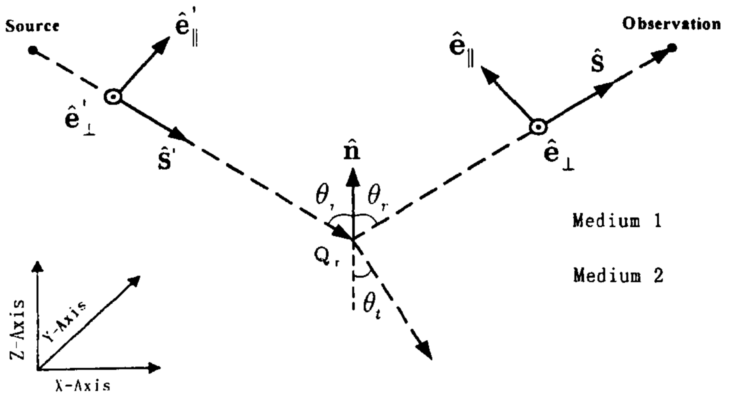

Figure 4.17: An illustration of the local-ray fixed coordinate system.

The unit vector $\hat{s}'$ is the direction vector of the incident ray that imprints on the boundary surface at the reflecting point Q_r. Let $\hat{\mathbf{n}}$ be the unit vector normal to the surface, the plane of incidence is thus defined by the plane containing both unit vectors $\hat{s}'$ and $\hat{\mathbf{n}}$ (the *x-z* plane). In the local-ray fixed coordinate system, the incident electric field $\mathbf{E}^i$ at Q_r is decomposed into two possible polarisations and they are considered separately. One polarisation has the electric field perpendicular to the plane of incidence ($\hat{e}_{\perp}'$) and is termed TE wave. The other has the electric field parallel to the plane of incidence ($\hat{e}_{\parallel}'$) and is termed TM wave. Similarly, the reflected electric field $\mathbf{E}^r$ at Q_r can be decomposed into components parallel ($\hat{e}_{\parallel}$) and perpendicular ($\hat{e}_{\perp}$) to the plane of reflection (the *x-z* plane). From geometrical point of view, the following relations hold true [66]:

$$\hat{e}_{\perp}' = \frac{\hat{s}' \times \hat{n}}{\left|\hat{s}' \times \hat{n}\right|} \tag{4.9}$$

$$\hat{e}_{\parallel}' = \hat{e}_{\perp}' \times \hat{s}' \tag{4.10}$$

$$\hat{e}_{\perp} = \hat{e}_{\perp}' \tag{4.11}$$

$$\hat{\mathbf{e}}_{\|} = 2\left(\hat{\mathbf{n}}\cdot\hat{\mathbf{e}}'_{\|}\right)\hat{\mathbf{n}} - \hat{\mathbf{e}}'_{\|} \tag{4.12}$$

$$\hat{\mathbf{s}} = \hat{\mathbf{s}}' - 2\left(\hat{\mathbf{n}}\cdot\hat{\mathbf{s}}'\right)\hat{\mathbf{n}} \tag{4.13}$$

In addition to reflection occurring at the boundary surface between the two media, the electromagnetic field also penetrates from medium 1 into medium 2 , provided medium 2 is not perfectly conducting. Unlike the reflected field which depolarises the incident field at the boundary, the transmitted field retains the polarisation characteristics of the incident field. According to the law of reflection and the law of transmission, the angles of the reflected and transmitted rays are related to the incident angle as follows:

$$\theta_i = \theta_r \tag{4.14}$$

$$\frac{\sin\theta_i}{\sin\theta_t} = \sqrt{\frac{\hat{\varepsilon}_2\mu_2}{\hat{\varepsilon}_1\mu_1}} \tag{4.15}$$

where $\hat{\varepsilon}_1$ and $\hat{\varepsilon}_2$ are the complex permittivity of medium 1 and medium 2, respectively; μ_1 and μ_2 are the permeability of each medium.

4.6.2 Reflected and Transmitted Fields

The complex reflection coefficient is defined by the ratio of the reflected to the incident electric-field strengths and the complex transmission coefficient is defined by the ratio of the transmitted to the incident electric-field strengths. As discussed above, it is convenient to decompose the incident wave into TE and TM components whose reflection coefficients can then be calculated in a straightforward manner. The total reflected field is the sum of the reflected TE and TM waves. Assuming medium 1 as free space and medium 2 as a dielectric with complex relative permittivity $\hat{\varepsilon}_r$ and unity relative permeability ($\mu_r = 1$), the Fresnel reflection coefficient for both polarisations is given by [65]

$$R_{\parallel} = \frac{\cos\theta_i - \sqrt{\hat{\varepsilon}_r - \sin^2\theta_i}}{\cos\theta_i + \sqrt{\hat{\varepsilon}_r - \sin^2\theta_i}} \tag{4.16}$$

$$R_{\perp} = \frac{\hat{\varepsilon}_r\cos\theta_i - \sqrt{\hat{\varepsilon}_r - \sin^2\theta_i}}{\hat{\varepsilon}_r\cos\theta_i + \sqrt{\hat{\varepsilon}_r - \sin^2\theta_i}} \tag{4.17}$$

It is seen that the reflection coefficient is a function of the complex permittivity of the object that the signal rays encounter. Other factors affecting the reflection of the signal are the angle of incidence and the relative polarisation. Effects of the reflector on the propagating wave are different for the two polarisation components of the incident wave.

In reality, a building structure has a finite thickness such that when a ray is transmitted through a building structure, it suffers two transmissions: first, from the exterior medium to the structure and, secondly, from the structure to the exterior medium. Similarly, the reflection phenomenon in a structure of finite thickness is different from that in an interface between two media, as given in Eqs. (4.16) and (4.17). Hence, to be coherent, when the structure thickness is considered in the transmission effect, the reflections must also be treated considering the finite structure thickness. If a building structure consists of a few layers of materials, the interaction between the propagating wave with the structure is much more complicated. For the purpose of characterising the building structures as simple and accurate as possible, we describe any structure in the database as a single- or multi-layered material with specific dielectric parameters and thickness for each layer. Each layer in the material is assumed homogenous, i.e., the dielectric parameters are constant within the layer. Because the incident angle θ_i of a propagating wave can be any value between 0° and 90°, the wave-transmission matrices method [24] used in Chapter 2 is not applicable. Kong [67] has studied the reflection and transmission mechanisms of a multi-layered material for incident waves at any angles. Formulas for the derivation of these coefficients are given in Appendix B.

In the local ray-fixed coordinate system, the incident, reflected and transmitted fields are decomposed into two polarisation components and can be written as

$$\mathbf{E}^i = E^i_{\parallel}\hat{\mathbf{e}}^i_{\parallel} + E^i_{\perp}\hat{\mathbf{e}}^i_{\perp} \tag{4.18}$$

$$\mathbf{E}^r = E^r_{\parallel}\hat{\mathbf{e}}_{\parallel} + E^r_{\perp}\hat{\mathbf{e}}_{\perp} \tag{4.19}$$

$$\mathbf{E}^t = E^t_{\parallel}\hat{\mathbf{e}}^i_{\parallel} + E^t_{\perp}\hat{\mathbf{e}}^i_{\perp} \tag{4.20}$$

With the reflection and transmission coefficients derived above, the reflected and transmitted fields can be expressed in the local-ray fixed coordinate system as

$$\begin{bmatrix} E^r_{\parallel} \\ E^r_{\perp} \end{bmatrix} = \begin{bmatrix} R_{\parallel} & 0 \\ 0 & R_{\perp} \end{bmatrix} \begin{bmatrix} E^i_{\parallel}(Q_r) \\ E^i_{\perp}(Q_r) \end{bmatrix} \frac{1}{s+s'} \cdot e^{-jk(s+s')} \tag{4.21}$$

$$\begin{bmatrix} E^t_{\parallel} \\ E^t_{\perp} \end{bmatrix} = \begin{bmatrix} T_{\parallel} & 0 \\ 0 & T_{\perp} \end{bmatrix} \begin{bmatrix} E^i_{\parallel}(Q_r) \\ E^i_{\perp}(Q_r) \end{bmatrix} \frac{1}{s+s'} \cdot e^{-jk(s+s')} \tag{4.22}$$

where s is the distance from the source point to the reflection point and s' is that from the reflection point to the observation point. The term $1/(s+s')$ is the spreading factor for spherical wave incidence on the boundary, accounting for the energy losses as the ray propagates. The reflected and transmitted fields also can be expressed in dyadic form as

$$\mathbf{E}^r = \mathbf{E}^i \cdot \mathbf{R}\frac{1}{s+s'}e^{-jk(s+s')} \tag{4.23}$$

$$\mathbf{E}^t = \mathbf{E}^i \cdot \mathbf{T}\frac{1}{s+s'}e^{-jk(s+s')} \tag{4.24}$$

where the dyadic reflection and transmission coefficients are given by

$$\mathbf{R} = \hat{\mathbf{e}}^i_{\parallel}\hat{\mathbf{e}}_{\parallel}R_{\parallel} + \hat{\mathbf{e}}^i_{\perp}\hat{\mathbf{e}}_{\perp}R_{\perp} \tag{4.25}$$

$$\mathbf{T} = \hat{\mathbf{e}}^i_{\parallel}\hat{\mathbf{e}}^i_{\parallel}T_{\parallel} + \hat{\mathbf{e}}^i_{\perp}\hat{\mathbf{e}}^i_{\perp}T_{\perp} \tag{4.26}$$

Tracing rays in 3D space using a global coordinate system requires that the reflection and transmission coefficients of the propagating field must be represented by 3×3 matrix, if the polarisation of the field is included. The components of the matrix sometimes are difficult and time-consuming to compute. With the local ray-fixed axis coordinate, the dyadic reflection and transmission coefficients are reduced to a 2×2 matrix, hence simplifies the computation.

4.7 The Uniform Theory of Diffraction

In addition to reflection and transmission, diffraction is another basic propagation mechanism which governs radio propagation with surrounding structures. The diffracted waves resulting from an obstructing structure are present throughout the space and even behind the obstacle (shadow regions), giving rise to electromagnetic fields around the obstacle, whether or not a line-of-sight path exists between the Tx and Rx.

The GO is incapable of predicting electromagnetic fields in the shadow regions, and therefore is inaccurate in these areas. Because electromagnetic fields have to be smooth everywhere and the discontinuities across the shadow boundaries does not occur in nature, the failure of the GO to predict correct fields in the shadow regions is a serious shortcoming. The geometrical theory of diffraction (GTD) has been developed [73] by Keller in an attempt to compensate for the shortcoming of the GO. By adding diffracted rays Keller succeeded in correcting the deficiency in the GO which predicts zero fields in the shadow regions. However, his approach still had shortcomings where the diffracted fields become singular in the transition regions surrounding the shadow boundaries, i.e., the predicted diffracted fields adjacent to the shadow boundaries becomes infinite. Based on the GTD, Kouyoumjian and Pathak [74] developed the Uniform Theory of Diffraction (UTD) for high frequency radio propagation. They had performed an asymptotic analysis and found that, by multiplying the diffraction coefficients by a transition function, the diffracted fields remain bounded across the shadow boundaries. The form of the transition function is such that it approaches zero at the same rate as that at which the diffraction coefficients become singular across the shadow boundaries, so that the resultant diffracted fields remain bounded across the shadow boundaries. Thus, a ray-based uniform diffraction theory has been successfully developed for calculation of the diffracted field everywhere in space. as long as the incident fields are ray optical and reflection and diffraction events can be considered as local phenomena, which is valid at high-frequency radio propagation.

4.7.1 Edge-Fixed Coordinate System

Fig. 4.18 shows a typical scenario of edge diffraction phenomenon, where Q_d denotes the diffraction point at the edge. The concept of the diffraction cone is also illustrated in the figure. A ray is incident at an angle β_0' with respect to the edge and consequently generates the diffracted rays which form a cone with half-angle β_0, where $\beta_0' = \beta_0$ due to the law of diffraction. One incident ray thus will results in an infinite number of diffracted rays lying on the diffraction cone. In general, since the diffraction mechanism radiates the energy in all directions, the diffracted field strength attenuates rapidly with distance. At the point of diffraction, we define a unit vector $\hat{e}$ tangential to the edge. The incident ray propagates in the direction defined by the unit vector of $\hat{s}'$ and the diffracted ray propagates in the direction defined by $\hat{s}$. s' and s are the distances from the source to the diffraction point and from the diffraction point to the observation point, respectively. The diffraction angle β_0' can be found as

$$\sin\beta_0 = \left|\hat{s}' \times \hat{e}\right| = \left|\hat{s} \times \hat{e}\right| \tag{4.27}$$

Given the direction of propagation of the incident ray and the position of the observation point, the diffraction point thus will be the point on the edge that satisfies Eq. (4.27). It is noted that in the case where $\beta_0 = 90^\circ$, the incident ray is perpendicular to the edge and the diffraction cone degenerates to a disk. It is customary to label the two faces of the wedge the o-face and n-face, respectively. The wedge is assumed to have an interior angle α that is related to the parameter n by $\alpha = (2-n)\pi$. When $\alpha = \pi/2$, i.e. $n = 1.5$, the wedge has a right interior angle and is considered as a general case in indoor environments where an edge is formed by two structures perpendicular to each other.

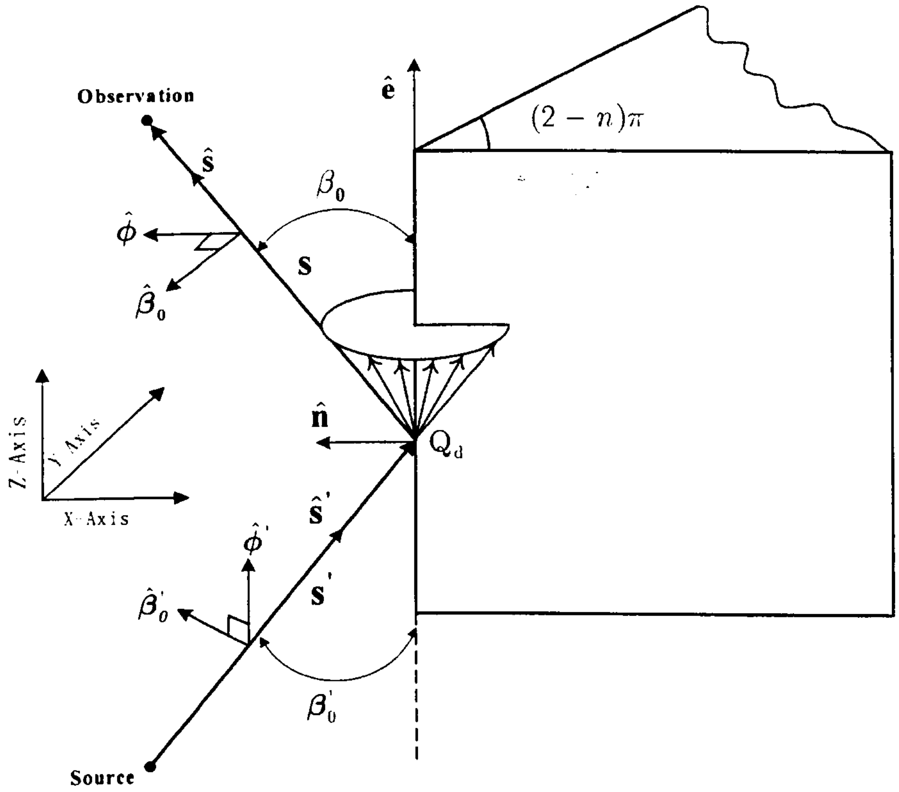

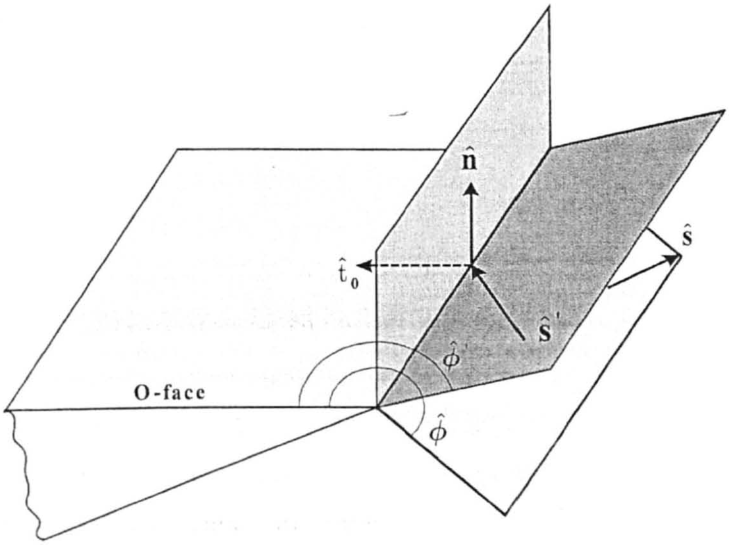

Figure 4.18: Geometry and the edge-fixed coordinate system for UTD application.

Similar to the local ray-fixed coordinate system used for the calculation of the dyadic reflection and transmission coefficients, the edge-fixed coordinate system is used here for calculation of the diffraction coefficient. The edge-fixed coordinate system is also shown in Fig. 4.18. The edge-fixed plane of incidence is defined as the plane containing $\hat{e}$ and $\hat{s}'$. The diffracted field components then are parallel and perpendicular to the edge-fixed plane of diffraction which is defined as the plane containing $\hat{e}$ and $\hat{s}$. In the edge-fixed coordinate system, an arbitrary polarised incident field is decomposed into $\hat{\beta}_0'$ and $\hat{\phi}'$ components and the resultant diffracted field into $\hat{\beta}_0$ and $\hat{\phi}$ components, respectively, where

$$\hat{\phi}' = -\frac{\hat{e}\times\hat{s}'}{|\hat{e}\times\hat{s}'|} \tag{4.28}$$

$$\hat{\beta}_0' = \hat{\phi}'\times\hat{s}' \tag{4.29}$$

$$\hat{\phi} = \frac{\hat{e}\times\hat{s}}{|\hat{e}\times\hat{s}|} \tag{4.30}$$

$$\hat{\beta}_0 = \hat{s}\times\hat{\phi} \tag{4.31}$$

Thus, fields which lie in the edge-fixed planes of incidence and diffraction will be $\hat{\beta}_0'$ and $\hat{\beta}_0$ polarised, respectively, whereas fields perpendicular to the edge-fixed planes of incidence and diffraction are $\hat{\phi}'$ and $\hat{\phi}$ polarised, respectively. ϕ' and ϕ in Fig. 4.18 are defined as the incident and diffracted angles in a plane perpendicular to the edge measured with respect to the o-face. The components of s' and s which lie in the plane perpendicular to the edge are given by

$$s_t' = \left|\hat{s}' - (\hat{s}' \cdot \hat{e})\hat{e}\right| \tag{4.32}$$

$$s_t = \left|\hat{s} - (\hat{s} \cdot \hat{e})\hat{e}\right| \tag{4.33}$$

Let the unit vector tangential to the o-face be $\hat{\mathbf{t}}_0 = \hat{\mathbf{n}}_0 \times \hat{e}$, where $\hat{\mathbf{n}}_0$ denotes the unit vector normal to the o-face at Q_d . It is noted that the direction of $\hat{e}$ should be such that $\hat{\mathbf{t}}_0$ points towards the o-face, as shown in Fig. 4.18. Using Eqs. (4.32) and (4.33), two unit vectors lying in the plane perpendicular to the edge are defined as

$$\hat{s}_t' = \frac{\hat{s}' - (\hat{s}' \cdot \hat{e})\hat{e}}{\left|\hat{s}' - (\hat{s}' \cdot \hat{e})\hat{e}\right|} \tag{4.34}$$

$$\hat{s}_t = \frac{\hat{s} - (\hat{s} \cdot \hat{e})\hat{e}}{\left|\hat{s} - (\hat{s} \cdot \hat{e})\hat{e}\right|} \tag{4.35}$$

The angles ϕ' and ϕ are therefore given by

$$\phi' = \pi - \left[\pi - \arccos\left(-\hat{s}_t' \cdot \hat{\mathbf{t}}_0\right)\right] \cdot \operatorname{sgn}\left(-\hat{s}_t' \cdot \hat{\mathbf{n}}_0\right) \tag{4.36}$$

$$\phi = \pi - \left[\pi - \arccos\left(-\hat{s}_t \cdot \hat{\mathbf{t}}_0\right)\right] \cdot \operatorname{sgn}\left(-\hat{s}_t \cdot \hat{\mathbf{n}}_0\right) \tag{4.37}$$

where $\operatorname{sgn}(x)$ is a sign function.

4.7.2 Diffracted Fields

In analogy to the definitions of the reflection and transmission coefficients, the diffracted fields from an edge can also be decomposed into soft (perpendicular) and hard (parallel) polarisations, i.e., D_s and D_h, respectively. McNamara [54] has studied the diffraction mechanisms of a wedge for incident waves at any angles. Formulas for the derivation of the diffraction coefficient are given in Appendix C.

In the edge-fixed coordinate system, $\hat{\beta}_0'$ and $\hat{\beta}_0$ polarised fields are associated with the soft diffraction coefficient D_s, whereas $\hat{\phi}'$ and $\hat{\phi}$ polarised fields are associated with the hard diffraction coefficient D_h. The incident and diffracted fields can be written as

$$\mathbf{E}^i = E^i_{\beta_0'}\hat{\beta}_0' + E^i_{\phi'}\hat{\phi}' \tag{4.38}$$

$$\mathbf{E}^d = E^d_{\beta_0}\hat{\beta}_0 + E^d_{\phi}\hat{\phi} \tag{4.39}$$

With the diffraction coefficient derived above, the 3D UTD diffracted fields from an edge can be expressed in the edge-fixed coordinate system as

$$\begin{bmatrix} E^d_{\beta_0} \\ E^d_{\phi} \end{bmatrix} = \begin{bmatrix} -D_s & 0 \\ 0 & -D_h \end{bmatrix} \begin{bmatrix} E^i_{\beta_0'}(Q_d) \\ E^i_{\phi'}(Q_d) \end{bmatrix} \sqrt{\frac{s'}{s(s+s')}} \cdot e^{-jks} \tag{4.40}$$

where the square-root factor is the spreading factor for spherical wave incidence on an edge [65]. Using the edge-fixed coordinate system, the diffraction coefficient reduces to a diagonal 2×2 matrix. Eq. (4.40) can be expressed in dyadic form as

$$\mathbf{E}^d = \mathbf{E}^i \cdot \mathbf{D}\sqrt{\frac{s'}{s(s+s')}} \cdot e^{-jks} \tag{4.41}$$

where the dyadic diffraction coefficient is given by

$$\mathbf{D} = -\hat{\beta}_0'\hat{\beta}_0 D_s - \hat{\phi}'\hat{\phi} D_h \tag{4.42}$$

These equations for the diffracted field around corners are straightforward to implement in computer programs. For the case of double wedge diffraction, the diffraction coefficient is extended to solve the problem [68].

4.8 Field Strength Computation

For a valid ray from the Tx to Rx, the path length and the associated time delay are computed based on the information on the Tx position, the Rx position, and all the ray's interaction points on facets or edges. At each intersection point, the incident field is decomposed into components parallel and perpendicular to the incident plane. The electromagnetic field propagation is then evaluated in terms of a plane wave undergoing reflection, transmission or diffraction. The resultant field is computed using the corresponding dyadic reflection, transmission or diffraction coefficients which are calculated based on the electromagnetic properties of the intersecting facet or edge. By the multiplication of these processes at all intersection points encountered by the ray, we obtain the complex polarisation components (of different magnitude and phase) of the field associated with the valid ray which arrives at the Rx. Mathematically, the complex received field amplitude $\mathbf{E}_n$ of the nth ray arriving at the Rx can be expressed as

$$\mathbf{E}_n = a_n t_n \left[\prod_j \boldsymbol{R}_j \prod_k \boldsymbol{T}_k \prod_l A_l(s',s) \boldsymbol{D}_l \right] \frac{e^{-jkd_n}}{d_n} \tag{4.43}$$

where a_n represents the complex transmitted signal amplitude (V); t_n is the radiation patterns of both the Tx and Rx in the direction of ray; $\boldsymbol{R}_j$ is the complex reflection coefficient for the jth reflection; $\boldsymbol{T}_k$ is the complex transmission coefficient for the kth transmission; $\boldsymbol{D}_l$ is the complex diffraction coefficient for the lth diffraction with a spatial spreading factor $A_l(s',s)$; and e^{-jkd_n} is the propagation phase factor for the ray path length d_n.

With the information on each ray's complex polarised field at the Rx, the total received field is the summation of these time-delayed contributions from all different rays arriving from different directions. The contribution to the total field associated with each ray is evaluated in terms of the electric field vector at the Rx, and the received field computation is implemented using 3D vector analysis with each ray being considered individually. There are two types of summation generally used for the radio channel modelling. One is referred to the vector summation; and the other is referred to the power summation. In the vector summation, each received field is decomposed, using a common Cartesian coordinate system, into a triad of complex components $\mathbf{E}_x$, $\mathbf{E}_y$, and $\mathbf{E}_z$. The total received field $\mathbf{E}_{tot}$ is obtained by adding all respective components of each ray. Mathematically, assuming N rays arrive at the Rx, the received field vector can be expressed as

$$\mathbf{E}_{tot} = \left(\sum_{i=1}^{N} \mathbf{E}_{ix}\right)\hat{a}_x + \left(\sum_{i=1}^{N} \mathbf{E}_{iy}\right)\hat{a}_y + \left(\sum_{i=1}^{N} \mathbf{E}_{iz}\right)\hat{a}_z \tag{4.44}$$

where $\hat{a}_x$, $\hat{a}_y$ and $\hat{a}_z$ are unit vectors in the x-, y- and z-axis direction. The corresponding received field strength can therefore be given by

$$E_{tot} = \sqrt{\left|\sum_{i=1}^{N} \mathbf{E}_{ix}\right|^2 + \left|\sum_{i=1}^{N} \mathbf{E}_{iy}\right|^2 + \left|\sum_{i=1}^{N} \mathbf{E}_{iz}\right|^2} \tag{4.45}$$

In the power summation, the received field strength E_{tot} is obtained by adding the individual field strength of each ray as

$$E_{tot} = \sum_{i=1}^{N} E_i = \sum_{i=1}^{N} \sqrt{|\mathbf{E}_{ix}|^2 + |\mathbf{E}_{iy}|^2 + |\mathbf{E}_{iz}|^2} \tag{4.46}$$

In the vector summation process, the electric fields associated with individual rays arriving at the Rx are vectorially combined to yield the received field, and hence can account for the fast-fading phenomenon. In the power summation, the vectorially combined field is smoothed out by adding incoherently the field strength of each ray. Thus, it is used to account for the received field in wide-band systems, in which the received field strength is simply the sum of the field strength of each multipath component. When amplitudes of individual multipath components are uncorrelated, or phases of individual multipath components are independent and identically distributed over $[0, 2\pi)$, the average received signal strength over distances of a few wavelengths for a narrow-band signal is equivalent to that for a wide-band signal [9]. Thus it is seen that the received local ensemble average signal strength of both narrow-band and wide-band signals are equivalent. This equivalency has been observed well in indoor signal measurements [69,70], while in outdoor environments the power summation is sometimes less accurate to represent the local average signal strength for narrow-band signal [71] and the vector summation is generally preferable, particularly in LOS conditions. Theoretical analysis [72] has shown that the power summation gives a sufficiently good approximation of local mean signal strength for narrow-band signal in complex environments.

4.9 Summary

Ray tracing represents the high frequency limit of the exact solution for electromagnetic fields based on GO/UTD theory and can give quick approximate solutions when the exact solution cannot be found. It is a physically tractable method of predicting radio propagation in complex environments. In this chapter, the procedures of developing our indoor 3D ray-tracing program are described. A brief description and the hierarchy charts of the programme codes are given in Appendix D of this thesis.

Using the image method and the illumination zone concept, a new ray tree algorithm has been developed to identify all possible Tx-to-Rx rays. This algorithm is based on the projection of a 3D scenario into 2D planes, and is capable of supporting all structures in 3D space. It works by generating an image tree for each base station location, considering all environmental structures in a given area as reflectors. By searching the ray tree, all valid rays from the Tx to Rx are traced and determined. The algorithm has been demonstrated to significantly improve computation efficiency of the ray-tracing model, particularly when complex scenarios are simulated.

Our ray-tracing model implements direct, reflected, transmitted, and diffracted waves represented by the rays. Each propagation mechanism is treated separately. At each reflection/transmission or diffraction point, the local ray-fixed coordinate system or the edge-fixed coordinate system is used, together with appropriate dyadic reflection/transmission or diffraction coefficients. Complex, vectorial field components are computed based on the GO/UTD. The total received field is determined by combining individual contributions. The model incorporates 3D antenna radiation patterns, plus the electromagnetic fields at any point in the space are computed using 3D vector mathematics. This feature can provide comprehensive information on the radio channel, not only the field strength but also polarisation characteristics. The 3D ray-tracing prediction tool developed can be used in the performance analysis and design of radio communication systems.

Chapter 5

Indoor Ray-Tracing Simulations

5.1 Introduction

A 3D ray-tracing model for the prediction of indoor radio propagation has been described in the preceding chapter. The ray-tracing algorithm traces the multipath ray propagations from the Tx to the Rx for a given building database, and computes the field strength of each ray from the obtained path profiles, followed by total field strength computation. In this chapter, the results of simulations performed on various scenarios using the ray-tracing model are presented and discussed. In section 5.2, the prediction accuracy of the model is assessed by comparisons between our simulation results and the published data or measurement data. Its ability to model the reflection, transmission and diffraction mechanisms is evaluated. Section 5.3 presents the effects of the number of reflections included in the ray-tracing model. The number of reflections affects not only the simulation accuracy but also the computation efficiency of the model. Proper selection of this value is addressed in this section. Section 5.4 presents the results of simulations performed in the building of Department of Electrical Engineering and Electronics. Some statistical characteristics of the radio channel are extracted. Section 5.5 describes the development of a simplified ray-tracing model, which offers an improvement in the efficiency of the standard ray-tracing model, whilst retaining good prediction accuracy in comparison with empirical approaches.

5.2 Model Evaluation

In order to assess the performance of our ray-tracing model, the prediction results from the model incorporated with specific database should be compared with available information, either from other published simulation results or from field measurements. Three comparisons in path loss (PL) prediction between our model and other simulations/measurements are presented in this section to access the accuracy of our ray-tracing model.

5.2.1 Reflection Mechanism Validation

In [75], Chen used a ray-launching model to simulate the radio wave propagation inside a straight corridor scenario. In his simulation, a corridor was oriented in the x-axis direction with a cross section of 4 m × 3 m. The corridor was composed of two 25-cm-thick sidewalls and 13-cm-thick ceiling and floor. The sidewalls were assumed as dielectric slabs with $\varepsilon_r = 6$ and $\sigma = 0.02$ s/m; and the ceiling and floor were assumed as reinforced concrete modelled by a dielectric slab with $\varepsilon_r = 4$ and $\sigma = 0.02$ s/m backed by a perfectly electrical conducting plate. The Tx was located inside the corridor at position $[x_t, y_t, z_t] = (0, 2, 2.85)$. The Rx was originally located at (5, 2, 1.8) and then moved in the x-axis direction away from the Tx. Both the transmitting and receiving antennas were assumed as electric dipoles operating at 1.0 GHz. Fig. 5.1 (a) shows the simulated *PL* versus the Tx-Rx distance from Chen's model. In comparison, the simulation result from our ray-tracing model is shown in Fig. 5.1 (b). It is found that the *PL* predicted from our ray-tracing model compares favourably with Chen's result.

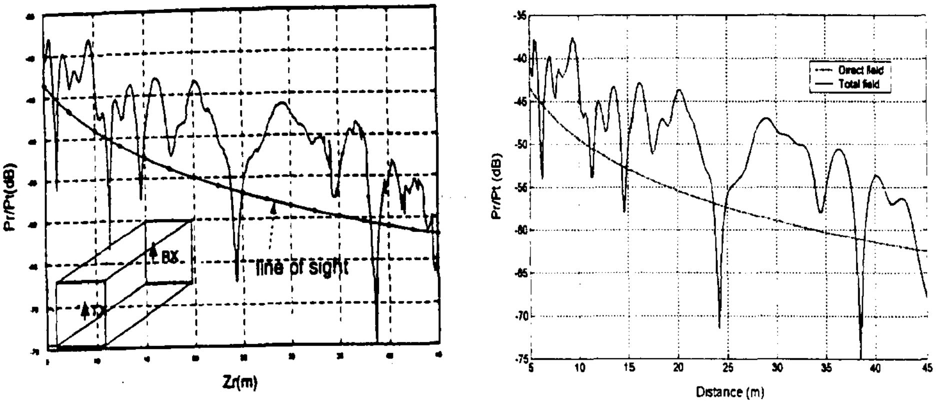

(a) (b)

Figure 5.1: Predicted *PL* in a corridor scenario: (a) from the simulation in [75]; (b) from our ray-tracing model.

In this scenario, multiple reflections from the ceiling, floor and sidewalls, along with the direct ray between the Tx and the Rx, are the principle mechanisms governing the radio wave propagation. It is observed that at most Rx locations the predicted received signal strength is higher than that under free space condition. This is due to waveguide effects within the corridor, as the propagating waves are reflected back from the surrounding walls, ceiling and floor. The large variation in the predicted received signal envelopes is caused by interference of the multipath incoming rays. The frequency of this variation is seen to decrease as the Rx is moved away from the Tx. This is due to the reduced rate of change in the differential path lengths between the direct ray and the reflected rays as the Tx-Rx distance is increased.

5.2.2 Diffraction Mechanism Validation

In [76], Chen used a ray-launching model to simulate the radio wave propagation inside a rectangular room with a metallic closet. In this case, the metallic closet will produce strong reflection from its surfaces and diffraction by its edges. Fig. 5.2 shows the layout of the scenario. The room was 21 m × 10 m × 3 m in dimension, composed of four sidewalls, a floor and a ceiling. The constitutive parameters of these structures were the same as in the previous example. A 0.6 m wide, 7 m long and 2 m high metallic closet was located in the middle of the room. The Tx was located at (3, 2, 2.5). The Rx was originally located at (5, 8, 1.5) and then moved in the x-axis direction along the route designated by a dash line in the figure. Both the transmitting and receiving antennas were assumed as electric dipoles operating at 1.0 GHz. Torres [77] also simulated the wave propagation in this scenario. The simulated *PL* versus the Rx location from their models are shown in Fig. 5.3 (a), in which Torres's simulation result is upper-shifted 15 dB for clear comparison with Chen's result. The simulation result of our ray-tracing model is shown in Fig. 5.3 (b). Clearly, our simulation result is in good agreement with Torres's result. However, the result from Chen's model is slightly different, which can be explained by a consideration of different propagation medium properties assumed in his model. In [76], Chen introduced a small loss into the medium in the room with $\hat{\varepsilon}_r = 1 - j0.005$, whereas in Torres's and our models the medium in the room was assumed as non-lossy medium with $\hat{\varepsilon}_r = 1$.

It can be concluded from Fig. 5.3 that before the Rx is moved across the metallic cabinet, the direct path between the Tx and Rx exists and plays a significant role in wave propagation. In this region, the strength of diffracted rays by the edges of the cabinet is generally more than 10 dB lower than that of the direct ray. In contrast, multiple reflections from the sidewalls, floor, ceiling and surfaces of the cabinet, interfere with the direct ray either constructively or destructively and cause the fast-fading phenomenon at the received signal envelopes. Direct path and multiple reflections are the dominant propagation mechanisms in this region. When the Rx is passed over the cabinet where the direct path is blocked, the diffracted rays contribute more significantly to the received signal. In this region, diffraction by the edges of the cabinet and multiple reflections are the dominant propagation mechanisms.

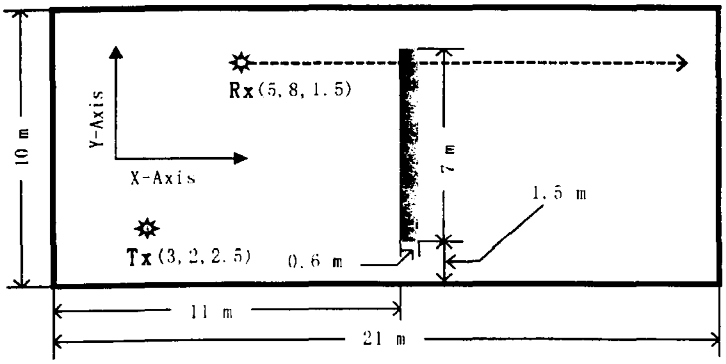

Figure 5.2: Layout of a rectangular room with a metallic closet where the simulation was performed by Chen [76] and Torres [77].

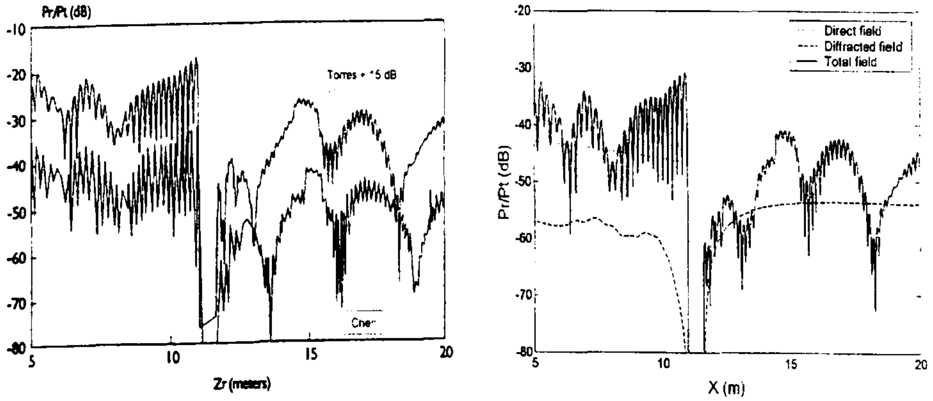

(a) (b)

Figure 5.3: Predicted *PL* in a rectangular room with a metallic closet: (a) from the simulations in [76] and [77]; (b) from our ray-tracing model.

5.2.3 Transmission Mechanism Validation

As a third example, we investigate the wave propagation through building structures. Horikoshi [78] measured the wave penetration through a building exterior wall at 1.29 GHz. Fig. 5.4 shows the layout of an empty room where the measurement was conducted. A room of 16 m × 6 m was illuminated by a Tx at distance of 888 m away from the exterior wall and incident at an angle of 3° off the normal of the wall surface and the route of the Rx movement was 1 m behind the exterior wall, illustrated by O_1O_2 in the figure. The exterior wall of the room was covered with four metal-framed windows and three concrete posts which separated the windows. All other sides were made of concrete walls and wooden doors. The concrete posts and sidewalls had the same dielectric properties, with the thickness of the post being twice that of the sidewall. A vertically polarized Yagi array of 23 elements and a standard dipole antenna were used as the transmitting antenna and receiving antennas respectively in the measurement.

In [79], Wang used a ray-launching model to simulate the wave propagation in this scenario. A vertically polarised half-wave dipole was assumed as the transmitting antenna instead of the Yagi array in the simulation. The measured and simulated *PL* are shown in Fig. 5.5 (a). Wang's ray-launching model only considered reflection and transmission mechanisms, and the diffraction effects of the window frames were not included. Instead, the FDTD method was applied to compute the wave propagation from the window frames and the concrete posts. Wang claimed that the hybrid model based on the ray-launching method and the FDTD method yielded better prediction accuracy. It is seen in Fig. 5.5 (a) that the result from the ray-launching model shows a rather smooth signal variation because of the GO approximation, and the result from the hybrid method can reproduce the fast-fading phenomenon observed in the measured signal envelope. Fig. 5.5 (b) shows the predicted *PL* from our ray-tracing model, displaying the simulation results from the ray-tracing model with and without the inclusion of diffraction effects. In [78], the dimension of the field strength of the measured data was not clear and the antenna factors were unknown, therefore we can only compare the relative strength of the received signal and its variation.

The prediction results from our ray-tracing model are in reasonably good agreement with those from Wang and Horikoshi. It can be seen that the concrete posts result in excessive penetration loss when the Rx is located behind them. The results from our model also suggest that the fast-fading phenomenon at the received signal envelope can be reproduced by the inclusion of diffraction effects of the window frames. Yang [80] also compared the prediction results from his ray-launching model with the measurement results, but the diffraction effects were neither considered in his model. A relatively smooth signal variation, due to the exclusion of diffraction effects, was obtained. As discussed in Chapter 3, the ray-launching method has the inherent difficulty of computing the diffraction by edges.

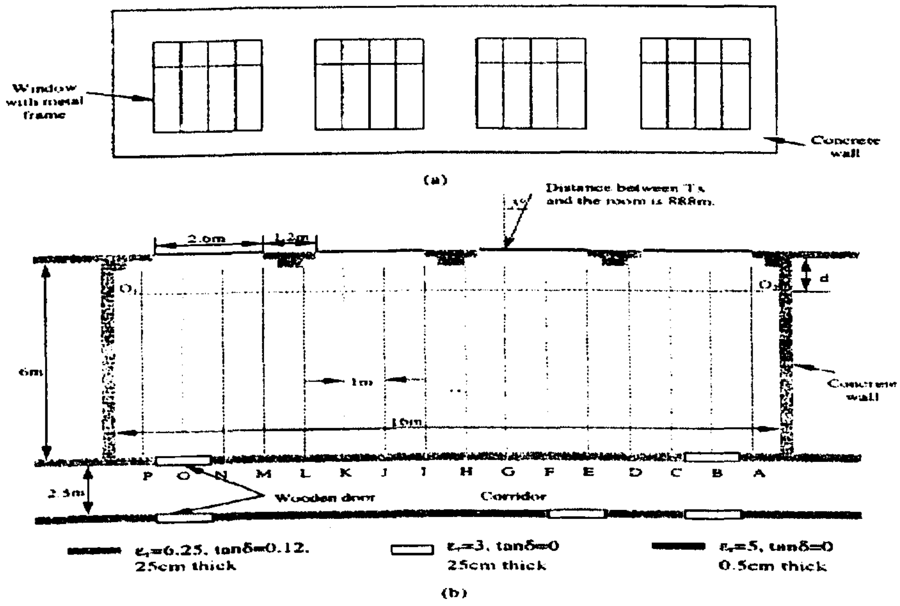

Figure 5.4: The scenario of a concrete room: (a) side view; (b) top view.

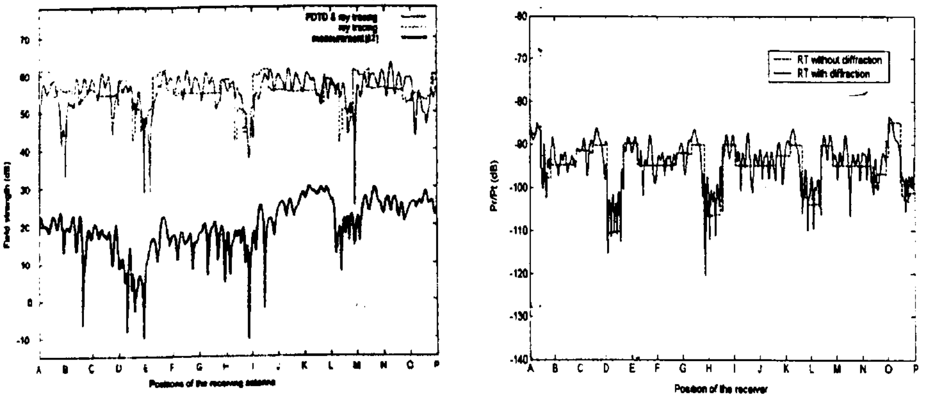

(a) (b)

Figure 5.5: Predicted *PL* of the wave penetration through exterior walls of a room: (a) from the measurement in [78] and the simulation in [79]; (b) from our ray-tracing model.

5.2.4 Comparison with Field Measurement Data

As the last validation example, we compare the results from our model with those from the measurements conducted by Zheng [81] in a laboratory on the fourth floor in the building of Department of Electrical Engineering and Electronics. Fig. 5.6 shows the layout of the laboratory, which has horizontal dimensions of 23 m × 8.5 m and a height of 3.4 m. The laboratory is covered with two sidewalls having large glass windows and two internal walls in conjunction with other laboratories. Cabinets, workbenches and experimental equipments are the major furniture in the laboratory. In the measurement, the Tx was located in the middle of the laboratory at 2 m high above the floor. The Rx was located 2 m high above the floor and moved in the passageway along the designated route shown in the figure. Two vertical discone antennas were used for the Tx and Rx. The measurements were conducted at both 815 MHz and 1.8 GHz. In the simulation, we only include the large cabinets and workbenches in the database, excluding other small furniture such as experimental equipments and chairs, etc. The measured and simulated *PL* versus the Tx-Rx distance at both frequencies are shown in Fig. 5.7.

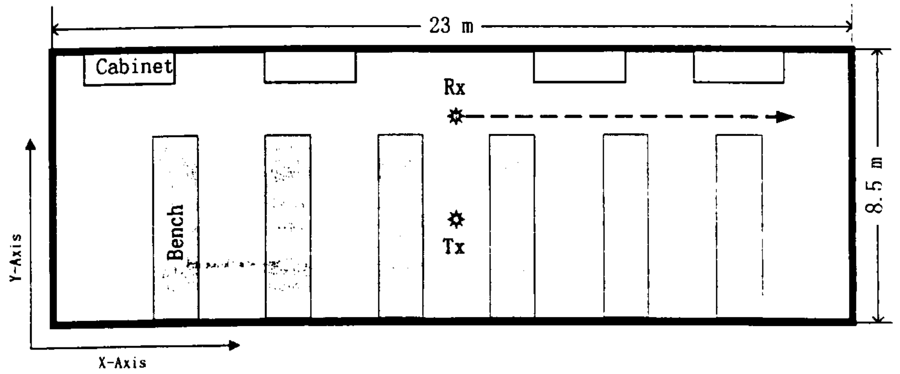

Figure 5.6: Layout of the laboratory where the field measurements were conducted by Zheng [81].

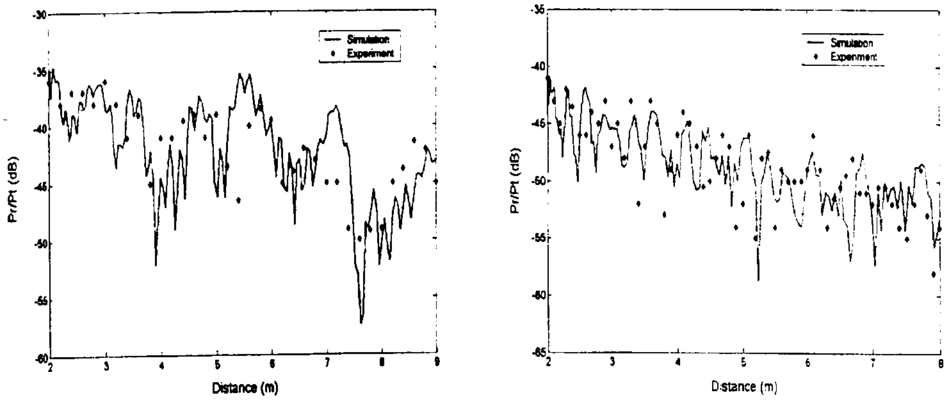

(a) (b)

Figure 5.7: Measured and predicted *PL* at: (a) 815 MHz; (b) 1800 MHz.

Reproduction of the measured signal levels is impossible, since a lot of assumptions have been made in the simulation due to the lack of accurate structure information and the neglect of small furniture. However, Fig 5.7 shows that the simulation results can follow the trend of the measured *PL* profiles. There is a good general agreement between the predicted and measured signal strengths, particularly if a running mean of the experiment data is considered. It is noted that most of the laboratory equipments are covered with metallic cases which can cause significant signal scattering. The scattering yields significant fluctuation at the received signal, but has an insignificant effect on the mean signal level. At some distances, the fading is not correctly predicted and this can be partially attributed to the fact that the equipment features were not included in the database. Also can be seen from the figure is that the fast-fading pattern of the received signal strength at 1.8 GHz is more rapid than that at 815 MHz. The phase difference between two arbitrary arriving rays is much greater at 1.8 GHz than that at 815 MHz because of the shorter wavelength. Consequently, the vectorial summation of all arriving rays results in more rapid signal fluctuations at 1.8 GHz than those at 815 MHz. The same trend of fading phenomenon is observed in measurement conducted in a laboratory at 893 MHz and 37.2 GHz [82]. The path loss exponents reported from the measurement were 1.65 and 1.80 at 815 MHz and 1.8 GHz, respectively. The predicted exponents from our simulations were 1.69 and 1.76 at these two frequencies.

5.3 Effects of the Number of Reflections

Because the ray-tracing model is based on a ray approximation technique which considers every ray originated from the Tx to the Rx, the prediction accuracy of the model is dependent on the number of rays that has been taken into account. Since a ray can propagate by reflection, transmission, diffraction and a combination of them, possible rays originated from the Tx to the Rx are uncountable, even for a simple scenario. This can be illustrated in the development of a ray tree. In theory, any ray tree can have an infinite number of levels accounting for all possible rays from the Tx to the Rx. The number of levels of a ray tree corresponds to the number of reflections that has been taken into account and a limited number of levels have to be considered for developing a ray tree.

As expected, prediction accuracy increases with the number of reflections included in each ray path. However, the computation time increases exponentially with the number of reflections considered. Thus it is critically important to understand the minimum number of reflections which needs to be included for achieving the desired level of accuracy and for reducing the computation complexity. In reality, the radio signal strength diminishes rapidly with the number of building structures encountered, i.e., rays experiencing high reflections have very little contribution to the overall received field strength. Including these rays in the ray-tracing process offers little improvement in the prediction accuracy. When solving electromagnetic wave propagation by ray-tracing methods, it is helpful to only take into account rays which have significant contributions to the overall received field strength. This is part of the inevitable trade-off between accuracy and computation complexity. So far, it seems that a consistent conclusion has not been reached yet on how many multiple reflected rays should be included for accurate predictions by a ray-based model. Moreover, its effects on prediction accuracy of channel time domain parameters have not been studied. In this section, we quantify the prediction accuracy and the computation time for our ray-tracing model. This is performed by comparing results of predictions of both narrow- and wide-band channel parameters including different number of reflections.

The necessary number of reflections N is determined by two factors: 1) when ray strength falls below a specified threshold and 2) when the received field envelop converges. When including N reflections, the ray-tracing model accounts for all rays that experience up to and including N reflections on their journey to the Rx. To simulate the effects of the value of N on prediction accuracy of our model, the Tx was located at $[x_t, y_t, z_t] = (10.0, 5.0, 13.2)$ on the third floor of the Electrical Engineering building, while the Rx was moved along two routes on the same floor, corresponding to the LOS and NLOS cases, respectively.

In the LOS case, the Rx was moved from $[x_r, y_r, z_r] = (15.0, 5.0, 11.8)$ to (25.0, 5.0, 11.8) for a total length of 10 m, while in the NLOS case the Rx is moved from $[x_r, y_r, z_r] = (15.0, 20.0, 11.8)$ to $(25.0, 20.0, 11.8)$. Figs. 5.8 and 5.9 show the predicted *PL* and RMS delay spread (τ_{rms}) against the Tx-Rx distance in the LOS and NLOS regions, respectively. Power summation of multipath rays is used instead of the vector summation in order to remove the effects of the fast-fading. Contributions of the components experiencing different number of reflections to the overall received signal strength are clearly observed. In *PL* prediction, $N = 0$ refers to the case that only the direct ray between the Tx and the Rx has been taken into account. In τ_{rms} prediction however, at least one reflection has to be included in the simulation. It is observed from the figure that both the predicted *PL* and τ_{rms} tend to converge as the value of N is increased.

Prediction accuracy of the mean values of both parameters is quantified by calculating the errors between the simulated mean values with different value of N. This is illustrated in Fig. 5.10 for both LOS and NLOS cases. The label in the horizontal axis refers to the error level using different values of N. For instance, the error level Err10 in *PL* prediction is defined as the difference between the predicted mean *PL* including the direct ray and the first-order reflected rays and that including the direct ray only. The definition of error level corresponding to τ_{rms} prediction is the same, but the first level is Err21 . It is seen that essentially the average of the prediction error is decreased monotonically as the number of reflections is increased. The prediction error of *PL* in the LOS region is smaller than that in the NLOS region. For instance, the observed mean *PL* error between prediction including direct ray only and that including direct ray and four reflections is 2.9 dB in the LOS region and this error is increased to 6.4 dB in the NLOS region. This is due to the fact that in the LOS region the direct ray has dominant effect on the received signal strength. The reflected rays and consequently, the number of reflections, have less significant effect on the prediction of overall received signal strength. Meanwhile, small errors (less than 1 dB) in the predicted path loss are observed when going from three to five reflections in both regions. This indicates that three reflections are enough in PL prediction. On the other hand, the prediction error of τ_{rms} is large for small number of reflections included. The predicted mean τ_{rms} when including one reflection is 8.49 ns in the LOS region and 11.67 ns in the NLOS region, respectively. Upon comparing the predicted error shown in Fig. 5.10 (b), it is noted that errors of 4.84% and 8.39% are generated when decreasing the number of reflections from four to three in the LOS and NLOS regions, respectively. This indicates that even three reflections are sufficient for predicting PL, more reflections are necessary to be included for accurate prediction of τ_{rms}. This is due to the fact that τ_{rms} is dependent not only on the strength of individual incident ray, but also on the time-delay characteristics of the rays. Therefore, τ_{rms} is more site-dependent with respect to PL. Comparing the predicted error arising from the inclusion of four instead of five reflections, figures of 0.36% and 3.81% are obtained in the LOS and NLOS regions, respectively. This indicates that four reflections are sufficient for prediction of channel τ_{rms}.

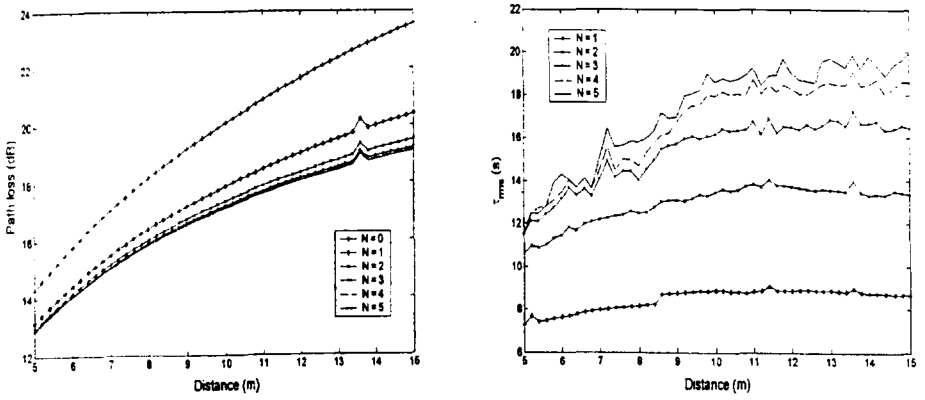

Figure 5.8: Predicted PL and τ_{rms} in the LOS region.

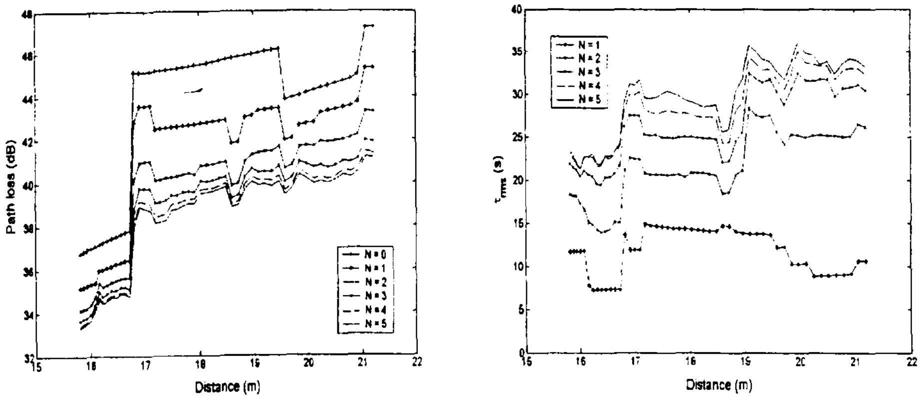

Figure 5.9: Predicted PL and τ_{rms} in the NLOS region.

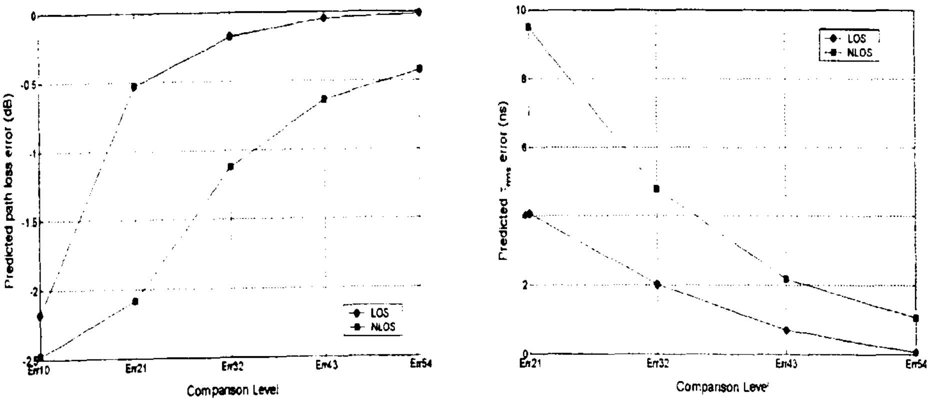

Figure 5.10: Error of the predicted PL and τ_{rms} with different number of reflections.

As discussed in the preceding chapter, the computation time of the ray-tracing algorithm increases exponential with the number of reflections included in the model. It is also found that the computation time is relatively constant for different Rx locations on one floor. Fig. 5.11 shows the average computation time of the above simulations at a single Rx location. In view of the computation time for four reflections and for five reflections, it is found that the enhancement of prediction accuracy of within 1 dB for PL and 5% for τ_{rms} in both the LOS and NLOS regions can be achieved, at the cost of the computation time rising from less than 5 seconds to more than 30 seconds. This insignificant improvement in prediction accuracy does not justify the additional computation time required, particularly for complex scenarios with large number of structures. On considering all the comparisons made above, four reflections are deemed to be sufficient for predicting both *PL* and τ_{rms} in all scenarios.

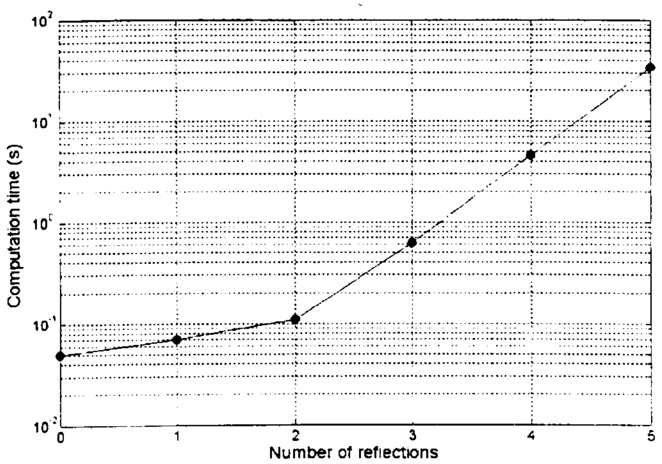

Figure 5.11: The computation time versus the number of reflections included in the ray-tracing model.

5.4 Indoor Simulations

5.4.1 Simulation Configurations

The increasing demand for the deployment of wireless communication systems with the advert of 3G mobile systems, has prompted further investigations of indoor radio channel in the 2.0 GHz frequency band. A good understanding of indoor radio propagation is essential since a large number of channel resources and high data transmission rate are most likely to be offered in these environments. This requires comprehensive characterisation of both narrow- and wide-band channels. Channel predictions using our ray-tracing model have been performed in the Electrical Engineering building to extract overall statistical channel characteristics.

The simulations have been performed on individual floors of the building, where both the Tx and Rx were assumed on the same floor for each simulation. The floors in modern office buildings are generally constructed of reinforced concrete or concrete over corrugated steel panels. This construction seriously limits signal transmission between floors. For example, 26 dB cross-floor isolation was measured by Arnold [83]. Propagation through floors is usually important for interference studies only [84]. It is foreseen that typical applications are operated on a single floor. On the other hand, this construction does not eliminate reflections from the floor and ceiling. Therefore, for our simulations on each floor, only the building structures including the floor and ceiling in the storey are included in the database of the ray-tracing model.

The Electrical Engineering building is a typical six-storey complex consisting of multiple offices, lecture rooms and laboratories. The building has dimensions of 38.6 m × 24.5 m in the horizontal plane and 3.4 m in height for each storey. Due to the availability of the building geometry database, simulations have been performed only from the second to the sixth floor. On each floor, the Tx was centrally located, i.e., $[x_t, y_t, z_t] = (10.0, 5.0, z_i)$, where z_i denotes the height of the Tx on the ith floor which is 2.8 m above the floor level. Fig. 5.12 shows the building layout of the sixth floor and the Rx locations used for the simulations, in which the Rx was moved along circle lines concentric to the Tx location with different radius r ranging from 1 m to 21 meters in 0.5 m increments. The height of Rx was assumed to be 1.6 m above the floor level. There were 100 Rx locations along each circle line. For large values of r, Rx locations that outside the building layout were neglected in the simulations. This arrangement resulted in 3190 Rx locations on the floor for the simulations.

The same plan of Rx locations was also applied to the other floors. Typical half-wavelength vertically polarised dipoles were assumed for both the transmitting and receiving antennas. The power delay profile at each Rx location was computed by the ray-tracing model, from which a variety of channel parameters such as the path loss, RMS delay spread and coherence bandwidth are obtained. These channel parameters can provide valuable information for design and analysis of the wireless communication system which is to be deployed in the environments.

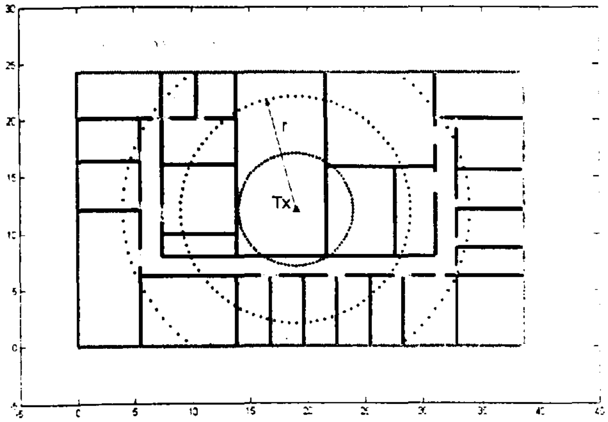

Figure 5.12: Blueprint of the sixth floor and the Tx and Rx locations.

5.4.2 Path Loss Characteristics

On each floor, the received CW signal strength at 3190 Rx locations were computed to yield the *PL* characteristics of the floor. Fig. 5.13 (a)-(e) show the scatter plots of predicted *PL* (relative to the signal strength at 1 m distance from the Tx), against the Tx-Rx distance on each floor. At each Rx location, the power summation operation is used for the computation of the received signal strength, leading to the average *PL* characteristics around that point. On each floor, large path loss variations of 40 - 50 dB are observed for the Tx-Rx distance from 1 m to 21 m.

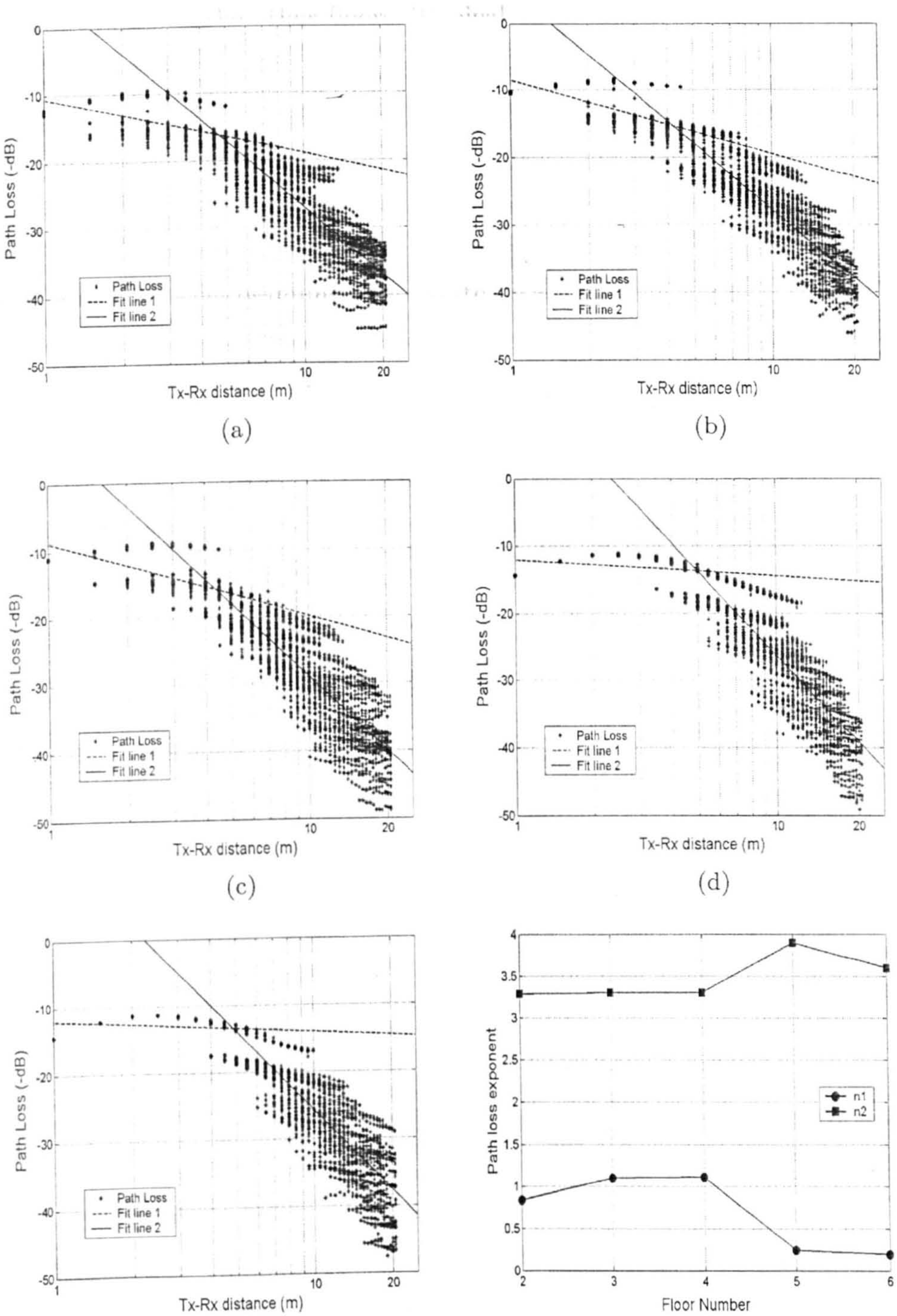

(a) (b)

(c) (d)

(e) (f)

Figure 5.13: Predicted *PL* characteristics on each floor: (a) Floor 2; (b) Floor 3; (c) Floor 4; (d) Floor 5; (e) Floor 6; and (f) the *PL* exponents on each floor.

A straight line indicating the relation between the predicted *PL* and the Tx-Rx distance in logarithm scale is a meaningful way to describe the large-scale *PL* characteristics of the radio channel. Definition of the large-scale path loss is given in Eq. (3.6), where the path loss exponent n is the slope of the straight line. To extract the large-scale *PL* characteristics from the predicted *PL*, a linear regression is used to compute values of n from the simulation data in a minimum mean square error (MMSE) sense. The determination of the exponent n for two data sets $\langle x_i \rangle$ and $\langle y_i \rangle$ is given by [85]

$$n = \frac{\sum_{i=1}^{m} (x_i - \bar{x})(y_i - \bar{y})}{\sum_{i=1}^{m} (x_i - \bar{x})^2} \tag{5.1}$$

where $\bar{x}$ and $\bar{y}$ are the sample means of the data sets of set size m, respectively. In view of the *PL* characteristics on each floor, it is observed that *PL* is generally decreased slowly with the Tx-Rx distance within 5 m, while it is decreased more rapidly with Tx-Rx distance greater than 5 m. Therefore, we employed two regression lines to fit into the predicted *PL*, before and after 5 m. The calculated two path loss exponents on each floor are given in Fig. 5.13 (f), where $n1$ denotes the exponent in the first region and $n2$ in the second region. The calculated values of $n1$ are all blow 1.5. In contrast to the path loss exponents calculated on the second to the fourth floors, the values of $n1$ calculated on the fifth and sixth floors are very small resulting in nearly constant *PL*. This is because on these two floors, there are very few walls in existence within 5 m to the Tx, thus very little variation of *PL* is expected within such a short Tx-Rx distance. On the other hand, in the second region, the *PL* characteristics on each floor appear much similar to each other with exponent $n2$ in the range from 3.3 to 3.8. These results are consistent with previous measurements reported for other buildings [32], [83]. It is also observed that the shadowing, which is defined as the difference of path loss at different Rx locations with constant Tx-Rx distance, is generally involved variations from 15 dB to 20 dB. This is due to the varying nature of particular obstructions between the Tx and the Rx.

5.4.3 RMS Delay Spread versus Path Loss

The channel RMS delay spread τ_{rms} defined in Eq. (3.9) is a measure of multipath conditions in a radio channel and is inversely proportional to the maximum useable data transmission rate of a channel. It is an important parameter for characterising the wide-band channel properties for digital wireless communication systems. On each floor, 3190 power delay profiles were processed to compute the channel τ_{rms} at different Rx locations. To calculate τ_{rms} from a power delay profile, all multipath components of amplitudes within 30 dB of the peak values were included.

The predicted channel τ_{rms} characteristics on different floors are given in Table 5.1. It is found that on different floors, the mean τ_{rms} and its standard deviation have similar values, indicating different floors have similar statistical channel τ_{rms} characteristics, even though the detailed structures on each floor are different. The 90% value of τ_{rms} is computed from the cumulative distribution function of τ_{rms} at the probability of 0.9. For example, there are 90% of the Rx locations on the second floor where the predicted τ_{rms} have values less than 21.58 ns. This value indicates the maximum allowable τ_{rms} and is regarded as the worst expected situation for data transmission in the environment. Our simulation results of the maximum τ_{rms} on each floor show that this value is around 20 ns.

Table 5.1: Predicted τ_{rms} characteristics on each floor.

	Floor 2	**Floor 3**	**Floor 4**	**Floor 5**	**Floor 6**
$\overline{\tau}_{rms}$	14.55	14.55	14.25	13.85	15.96
STD (τ_{rms})	4.92	4.93	3.56	3.76	4.79
τ_{rms} **(90%)**	21.58	21.03	19.01	19.03	22.15

The scatter plots of the predicted τ_{rms} against *PL* on each floor are shown in Fig. 5.14 (a)-(e). It is shown that τ_{rms} and *PL* are generally linearly related. The cross-correlation coefficient is a good measure of qualifying the linear relation between two variables. The cross-correlation coefficient between two data sets $\langle x_i \rangle$ and $\langle y_i \rangle$ is given by [71]

$$\rho\langle x, y\rangle = \frac{\sum_{i=1}^{m}(x_i - \overline{x})(y_i - \overline{y})}{\sqrt{\sum_{i=1}^{m}(x_i - \overline{x})^2 \sum_{j=1}^{m}(y_j - \overline{y})^2}} \tag{5.2}$$

The calculated cross-correlation coefficient between the predicted τ_{rms} and path loss on each floor are shown in Fig. 5.14 (f). A high correlation between these two channel parameters is seen on the third floor. However, this correlation becomes the lowest on the sixth floor. Measurements on an office building by Hashemi [100] indicated linear dependence of τ_{rms} on the path loss. However, uncorrelated dependence between these two was observed in measurements conducted by Rappaport [69]. Our simulation results indicate that the correlation between these two parameters is highly site-dependent.

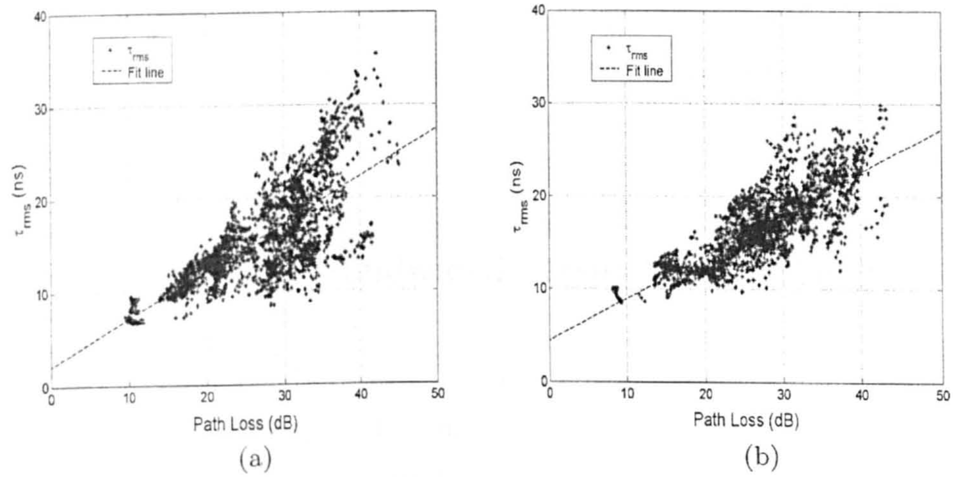

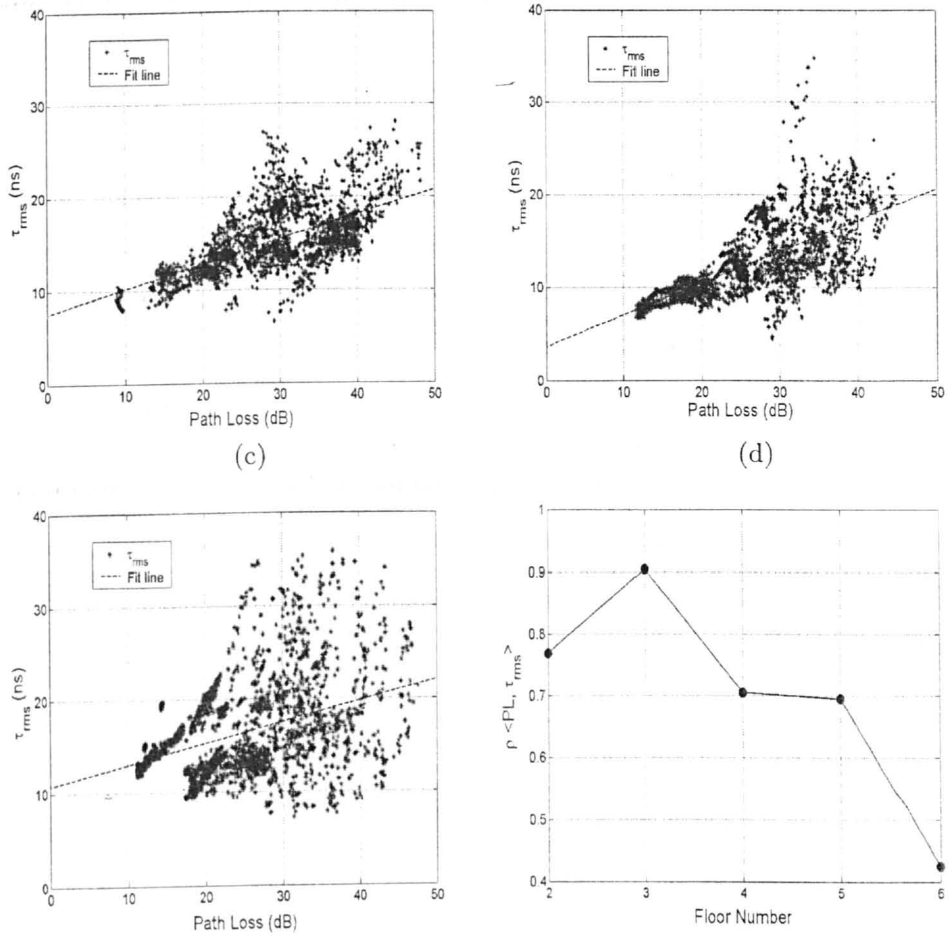

(c) (d)

(e) (f)

Figure 5.14: Predicted τ_{rms} versus *PL* on each floor: (a) Floor 2; (b) Floor 3; (c) Floor 4; (d) Floor 5; (e) Floor 6; and (f) the cross-correlation coefficients between the predicted *PL* and τ_{rms} on each floor.

5.4.4 Coherence Bandwidth versus RMS Delay Spread

The coherence bandwidth Bc, calculated from the frequency correlation function defined in Chapter 3, is used to describe the frequency selectivity of the radio channel. To simulate the Bc, Fourier transforms of 3190 power delay profiles on each floor are performed, from which the frequency correlation function is computed. At each Rx location, the coherence bandwidth for a correlation level of 0.9 is calculated and is referred to as Bc_{09}. Table 5.2 lists the statistical coherence bandwidth on different floors. The coherence bandwidths on different floors also show similar statistical values. The 10% value of Bc_{09} is, in contrast to the 90% value of τ_{rms}, generally regarded as the best case, indicating the minimum coherence bandwidth of the environment. Our simulation results that the minimum Bc_{09} values on each floor are above 4.0 MHz. This indicates that for the transmission of digital signals within the bandwidth of 4.0 MHz, the radio channel serves as a band-pass filter with flat frequency response.

Table 5.2: Predicted Bc_{09} characteristics on each floor.

	Floor 2	Floor 3	Floor 4	Floor 5	Floor 6
$\overline{Bc_{09}}$ (MHz)	7.02	7.06	6.72	7.47	6.37
STD (Bc_{09})	2.10	2.69	1.56	2.37	1.68
Bc_{09} (10%)	4.73	4.40	5.00	4.97	4.34

The relation between Bc and τ_{rms} has been investigated and the form $Bc = 1/(\alpha \cdot \tau_{rms})$, where α is a coefficient, was proposed [101], [102]. We have performed the simulations on all floors. Their relation in the form $Bc = C\tau_{rms}^{-\beta}$, where Bc is expressed in (MHz) and τ_{rms} in (ns) [103], was considered. The parameters inside the model are found by fitting the curve $Bc = C\tau_{rms}^{-\beta}$ to Bc ~ τ_{rms}. Table 5.3 gives the parameters found from the simulations performed on each floor. Since the values of β for each floor are always less than unity, it is found that compared to $Bc = 1/(\alpha \cdot \tau_{rms})$, $Bc = C\tau_{rms}^{-\beta}$ gives a better description of their relation. Fig. 5.15 (a)-(e) shows the relation between them. A log-log transformation of the pairs (τ_{rms} , Bc) was performed so that their relation becomes linear. The correlation between them are calculated and shown in Fig. 5.15 (f). High correlation between these two parameters for each floor is observed.

Table 5.3: Predicted parameters of C and β on each floor.

	Floor 2	**Floor 3**	**Floor 4**	**Floor 5**	**Floor 6**
C	63.39	68.87	61.38	69.61	68.96
β	0.8467	0.8849	0.8405	0.8928	0.8840

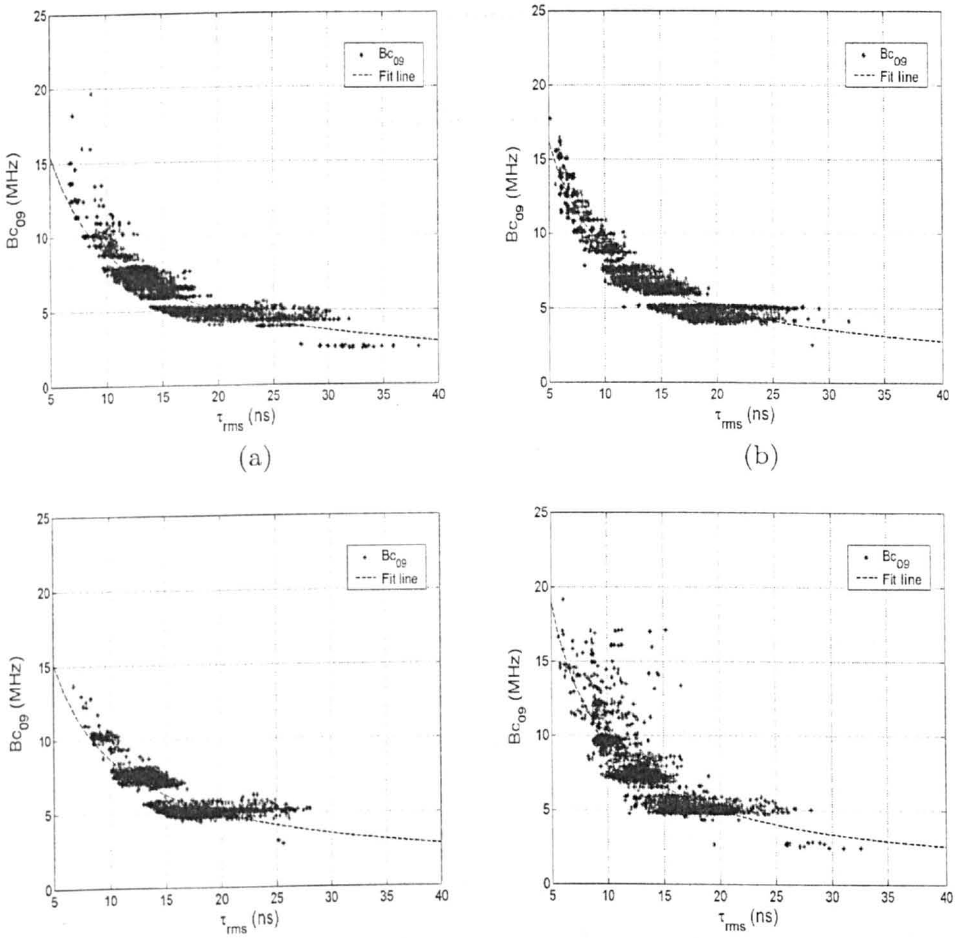

(a) (b)

(c) (d)

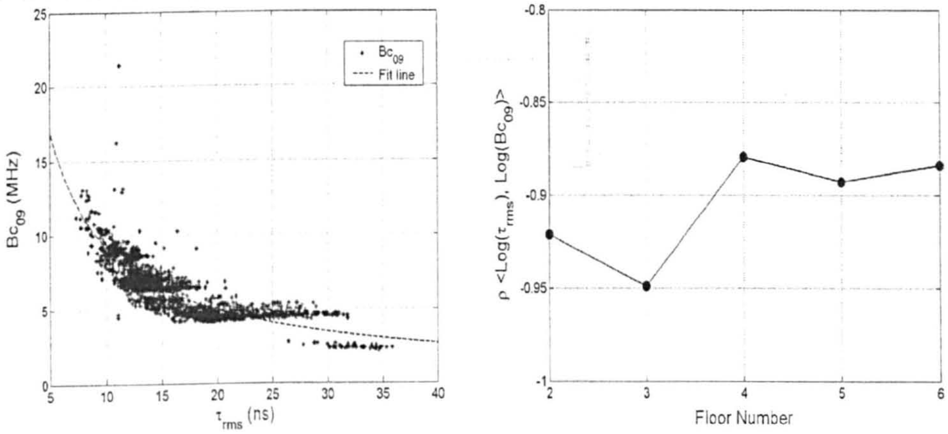

(e) (f)

Figure 5.15: Predicted Bc_{09} versus τ_{rms} on each floor: (a) Floor 2; (b) Floor 3; (c) Floor 4; (d) Floor 5; (e) Floor 6; and (f) the cross-correlation coefficients between logarithmic τ_{rms} and logarithmic Bc_{09} .

5.5 The Simplified Ray-tracing Model

The ray-tracing model offers accurate predictions of radio propagation, thanks to its consideration of detailed physical environments where the systems are to be deployed. However, the computation time is high, particularly for complex environments. In contrast, the empirical model offers the advantages of straightforward application and much less computation time, but in return the accuracy is often uncertain. In this section, we describe a simplified ray-tracing model, which can be thought of being in the middle ground between the empirical and the ordinary ray-tracing model. The objective of the simplified model is to reduce the computation time of conventional ray-tracing model without significant accuracy degradation.

In the empirical approach to model the *PL* characteristics, *PL* is usually considered as the attenuation of the direct ray between the Tx and the Rx

[104], [105]. The field strength attenuation caused by the intersecting walls is taken into account, however, the effects of signal reflections/diffractions from surrounding building structures are neglected in the model. In contrast, the ray-tracing model takes into account the direct ray as well as all reflections/diffractions from surrounding structures and takes the form of

$$P_r(d)\,[\mathrm{w}] = P_{dir}(d) + \sum_{i=1}^{M} P_{rd}(d) \tag{5.3}$$

where P_{dir} accounts for the power received from the direct ray; P_{rd} accounts for the power received from all possible reflected and diffracted signals from the building structures, and M is the number of reflections and diffractions considered in the model. It is noted that the wall attenuation loss has been considered inherently in the first term P_{dir} if the direct ray encounters wall intersections, and in the second term P_{rd} if any reflected or diffracted rays encounters wall intersections.

The empirical approach has inherent limitations for its application due to the neglect of radio propagation effects of surrounding building structures and therefore may be inaccurate when applied to some environments. This is particularly true when the direct ray is blocked by a metallic structure. Measurements conducted in a complex building showed that the empirical model cannot give accurate prediction on the channel *PL*, and the effects of the diffractions by the building structures should be included [110]. In our simplified model, the received power at the Rx is given by

$$P_r(d)\,[\mathrm{w}] = P_{dir}(d) + xd \cdot P_{rd}(d) \tag{5.4}$$

where x is a tuneable coefficient. The idea of the simplified model is to reduce the value of M in Eq. (5.3) to 1, so that the computation time can be dramatically reduced. As the Rx is moved away from the Tx, the direct ray becomes less dominant and the effects of the reflected and diffracted rays become more significant. This is particularly true when the direct ray is heavily blocked with intersecting walls. The Tx-Rx distance d is used as a coefficient to account for such effects.

By employing the same Tx and Rx plan as in the preceding sections, simulations of the *PL* characteristics using our simplified model have been performed. *PL* predicted by the ray-tracing model is assumed as the real value, whereas *PL* predicted by the simplified model is tuned to best fit the real value for each floor case. The values of x on each floor are found to be 0.23, 0.21, 0.24, 0.22 and 0.23, respectively. The comparisons between the real values and those predicted using the simplified model and the empirical model were made. They are presented in Fig. 5.16 as scatter plots. Prediction errors between the ray-tracing model and the simplified model and the empirical model are also shown in Fig. 5.16. The prediction results from the simplified model are observed to a give better correlation with those by the ray-tracing model, yielding a reasonably good prediction of the *PL*. Substantial improvements on the predicted *PL*, particularly for large Tx-Rx distances, are observed using the simplified model compared to the empirical approach. This is expected because the empirical approach does not take into account all reflected fields from surrounding building structures.

For all Tx-Rx distances, the prediction errors generated by the simplified model are generally within 4 dB. In contrast, these errors generated by the empirical model are increased as the Tx-Rx distance is increased and can vary by up to 10 ~ 25 dB for the Tx-Rx distance over 15 m. Since only the first-reflection from building structures is considered in the simplified model, the computation time of the prediction can be kept very low. The superiority of the simplified model over the empirical model is clearly seen. The reasonably good agreement between the predicted results verifies the ability of the simplified model to predict the path loss coverage. The model is shown to fit the simulations and may be extended to other buildings by adjusting its parameters.

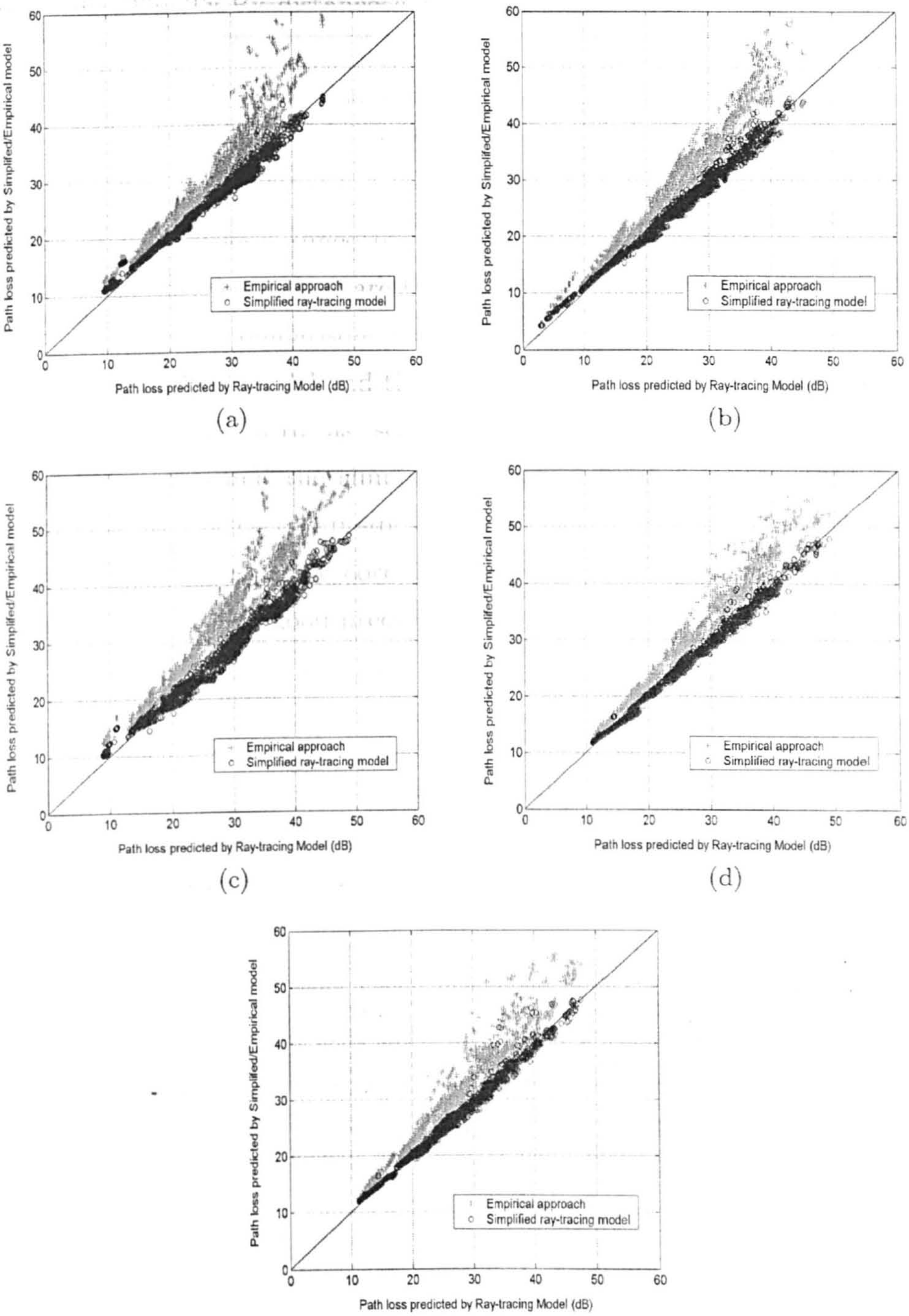

(a) (b) (c) (d) (e)

Figure 5.16: Scatter plots of comparisons of the predicted *PL* using the ray-tracing model with that using the simplified model and the empirical model: (a): Floor 2; (b): Floor 3; (c): Floor 4; (d): Floor 5; (e): Floor 6.

5.6 Summary

This chapter reports on some simulation results of indoor radio channels by our ray-tracing model. The accuracy of the ray-tracing model is evaluated by comparing with other simulation results and field measurement data. Good agreement in the predicted *PL* characteristics demonstrates the accuracy of the ray-tracing model.

When applying the ray-tracing model to any environment, the number of reflections needs to be carefully determined, because it affects both prediction accuracy and the computation time. By predicting *PL* and τ_{rms} with different number of reflections considered in the ray-tracing model, we found that setting the number to four is the optimum in terms of both computation efficiency and model accuracy.

Simulations of *PL*, τ_{rms} and Bc have been performed in the Electrical Engineering building. Some statistics of the indoor channels are obtained. It is found that τ_{rms} may or may not be proportional to *PL*. Good correlation is observed in some cases only. This is attributed to the fact that the channel τ_{rms} is highly site-dependent, while the *PL* characteristic is less. The relation between Bc and τ_{rms} is found to be well described by the model of $\mathrm{Bc} = C\,\tau_{rms}^{-\beta}$.

A simplified ray-tracing model is presented for the prediction of *PL* in indoor environments. It is found that the simplified model yields better prediction results compared to the empirical model. Reasonably good accuracy with low computation time can be achieved by the simplified model.

Chapter 6

Effects of Building Parameters on Ray-Tracing Prediction

6.1 Introduction

In the implementation of the ray-tracing model, the building geometry and the constitutive parameters of each building structure are employed as the input database. Consequently, the accuracy of prediction results from the ray-tracing model is dependent on the accuracy of the building layout and the associated dielectric parameters of the building structures. An inaccurate database may lead to prediction errors when using the ray-tracing model for channel characterisation. To verify the degree of prediction inaccuracy caused by inaccurate characterisation of building parameters, testing the sensitivity of prediction results to different building parameter configurations is an effective approach. In this chapter, the sensitivity of prediction results from the ray-tracing model to different constitutive parameters of the building structures is studied.

In wireless communications, radio waves experience different propagation modes such as transmission, reflection and diffraction from surrounding building structures. Effects of the above propagation mechanisms on the propagating wave are determined by the dielectric properties of the building structures included in the database. Therefore, to obtain accurate channel characteristics from the ray-tracing model, a good knowledge of their dielectric properties is required. However, wide variations of dielectric parameters of different types of building materials in the UHF and millimetre frequency bands are reported in literature. A brief summary of various dielectric parameters of materials such as concrete walls, brick walls, wooden panels and glass windows is listed in Table 6.1. Various permittivity and conductivity values are also used for other building materials. It should be noted that these dielectric parameters are heavily dependent on the exact constituents of the given material and the operating frequency.

In general, there are two approaches to assigning the dielectric parameters of building structures in the database. One is to assign the assumed values of dielectric parameters to different building materials, as listed in the above table, in the database. Alternatively, before undertaking complete predictions, preliminary field measurements in some limited sites are conducted. Meanwhile, different building dielectric parameters are employed into a simulation model to predict radio propagation in these sites. Afterwards, the dielectric parameters employed in the simulation model are "tuned" to give the closest match between predictions and measurements. After the tuning process, the optimum dielectric parameters are then employed in the simulation model for channel characterisation in all sites [97–99]. However, the question now arises as how sensitive the prediction model is to the building dielectric parameters employed in the database.

To our knowledge, very limited studies on the effects of inaccuracies in the building database have been carried out. References [98], [107-109] studied the outdoor prediction with different dielectric parameters representing building walls, and [106] studied their effects in the indoor environment. In [107], both ground and building walls were assigned with the same dielectric parameters as $\varepsilon_r = 15$ and σ values in the range of 0 ~

7 s/m. Simulation results indicated that with $\varepsilon_r = 15$, the signal strength is insensitive to the change of σ in the LOS region, whereas the signal level depends on σ in the NLOS region. With σ being higher than 2 s/m, a change of ε_r from 10 ~ 15 does not produce significant changes in both LOS and NLOS path loss. In [108], the simulation results in an urban microcellular environment indicate the insensitivity of the received signal power to the building dielectric parameters. (ε_r =15, σ =7 s/m) and ($\varepsilon_r = 3$, $\sigma = 0.005$ s/m) were used to represented for the ground and building walls. It was found that for a quasi-line-of-sight (QLOS) case, the differences of the predicted *PL* were less than 1 dB with ε_r remaining constant and σ changed to 20 s/m for the ground and 0.05 s/m for the walls. In [98], three set of electric parameters ($\varepsilon_r = 5$, $\sigma = 10^{-4}$ s/m), ($\varepsilon_r = 10$, $\sigma = 10^{-4}$ s/m) and ($\varepsilon_r = 5$, $\sigma = 2$ s/m) were used to characterise building walls. The prediction results from a 2D model accounting only for building wall reflection and diffraction is compared to measured path loss in urban QLOS region. The compassion showed that the first configuration was best fitted to measurements while the other two configurations could give up to 20 dB discrepancies. In [109], comparison on the path loss prediction in a small urban city showed that $\varepsilon_r = 5$ and $\sigma = 10^{-4}$ s/m are most accurate for representing building wall reflections, whereas up to about 10 dB error occurs when using different ε_r values ranging from 2 to 10. In [106], a theoretical analysis based on waveguide model of the path loss inside building showed that different constitutive parameters would lead to different reflectivity and transmittivity of in-building structure.

There is a lack of systematic investigation of the effects of inaccuracies of building dielectric parameters on the prediction accuracy, particularly for indoor channel predictions. Moreover, the above investigations only consider the effects on the channel path loss characteristics. Their effects on the wide-band channel prediction also need to be investigated.

Table 6.1: Summary of various dielectric parameters used for typical building materials in literature.

Material	ε_r	σ **(s/m)**	**Frequency (MHz)**	**Reference**
Concrete	4	0.2	1900	[41]
	9	0.1	900 & 2440	[56]
	7	0.06 ~ 0.1	900 ~ 2440	[50]
	4 ~ 6	0.017 ~ 0.05	3000	[90]
	6.25	0.1	2400	[91]
Brick Wall	4.26	0.01	1800	[53]
	5	0.01 ~ 0.02	900 & 1800	[80]
	3	0.005	1823	[79]
	8	0.016	2400	[91]
	3.58	0.11	5800	[92]
Wooden Panel	5	0.0084	2440	[93]
	1.6	0	1800	[94]
	3	0	900 & 1800	[80]
	4.26	0.01	1800	[53]
	2	0.01	1800 & 2500	[95]
Glass Window	3.0	0	1800	[94]
	3.0	0.0056	1000	[5]
	3.8 ~ 8	0	3000	[90]
	2.5	0.1	900	[96]
	5.0	0.003	1800 & 2500	[95]

In this chapter, the effects of different constitutive parameters (both dielectric parameters and structure thickness) on the prediction results from the ray-tracing model are studied. For outdoor radio channel characterisation, building walls are assumed as a homogeneous material of an infinite thickness, i.e. half-space material. Prediction models usually take into account only specular reflections from the building walls and ground, as well as diffractions by the building corners. Transmission through buildings is assumed weak enough so as to be neglected in the prediction model. This assumption has been justified by outdoor channel measurements [62], [64]. In contrast, in indoor radio channel characterisation, each building structure is modelled as a single- or multi-layered material of a finite thickness. Transmission through building structures is an important propagation mechanism for indoor radio propagation and must be accounted for in the prediction model. Section 6.2 presents the prediction results of the channel *PL* characteristics from the ray-tracing model in a simple outdoor scenario. A comparison between prediction results from the model employing different dielectric parameters in the database is given. In Section 6.3 deals with the comparison of both predicted channel *PL* and τ_{rms} within indoor environments. Effects of the accuracy of the constitutive parameters of the building structures on both narrow- and wide-band channel predictions are presented.

6.2 Outdoor Predictions

In this section, the effects of dielectric parameters assigned to building walls on the outdoor channel prediction is briefly discussed, as it is not the primary objective of this research. In outdoor building characterisation, since real building surfaces are made up of a complex pattern of windows and other structures with different wall materials, in the majority of the published work, the reflectivity of the buildings is obtained by assuming that the building structures are either perfect conductors or single half-space materials with assumed average ε_r and σ. The reflected electric field strengths are computed using the formulas for the Fresnel reflection coefficient shown in Eqs. (4.16) and (4.17) in Chapter 4. Figs. 6.1 and 6.2 show the reflection coefficient of a half-space material against various ε_r and σ values at different incident angles, where Γ_h represents the reflection coefficient for the horizontal incident electric field polarisation, and Γ_v represents for the vertical polarisation. It is shown for a constant σ, increasing ε_r will result in higher reflection of the material for both incident field polarisations. Likewise, the reflectivity is also increased as σ becomes higher. The trend of the variation of the reflection coefficient is monotonous with respect to the changes of both ε_r and σ.

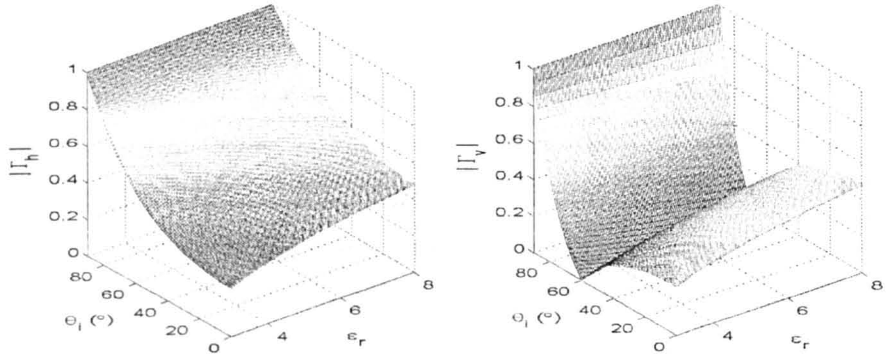

Figure 6.1: Magnitude of the reflection coefficient of an infinitely thick material with $\sigma = 0.0$ s/m versus different ε_r values.

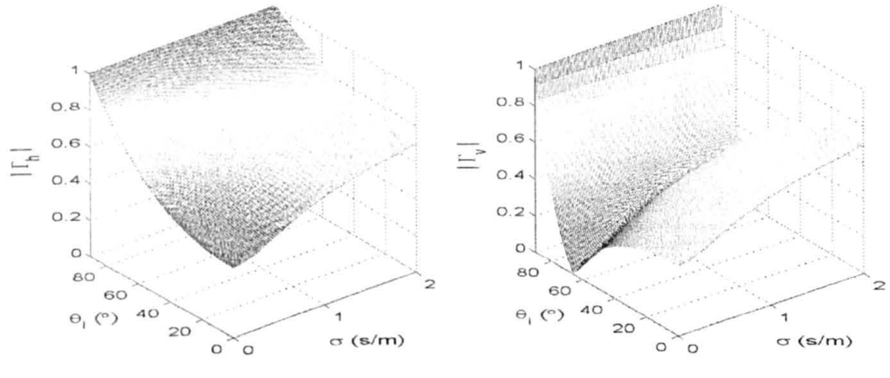

Figure 6.2: Magnitude of the reflection coefficient of an infinitely thick material with $\varepsilon_r = 5.0$ versus different σ values.

In an outdoor channel prediction, we consider a simple artificial scenario shown in Fig. 6.3, where nine buildings with dimensions of 40 m × 40 m × 20 m and the ground are included in the database. Each street was assumed 20 m wide. The Tx was fixed in the upper street, and the Rx was moved either in Route (1) or Route (2), corresponding to the LOS and NLOS regions, respectively. Both the transmitting and receiving antennas were assumed as vertical half-wavelength dipoles. The height of the Tx was 5 m above the ground and the Rx height was 2 m. Our ray-tracing model has been employed to simulate the reflections from the building walls and ground, as well as the diffractions by the building corners. Roof-top diffractions by the buildings are neglected in the simulation. The ground was characterised with $\varepsilon_r = 15$ and $\sigma = 7$, while the building walls were characterised with ε_r in the range of 4 ~ 8 and σ in the range of 0 ~ 2 s/m. Employing different ε_r and σ configurations of the building walls as the input to the database, we have predicted the *PL* characteristics in the two designated Rx routes. Although the scenario simulated is artificially simple, it can give some indications of the effects of different building dielectric parameters on radio propagation within outdoor environments.

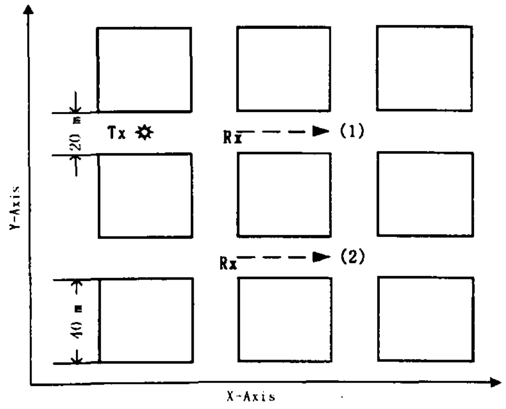

Figure 6.3: Layout of an outdoor scenario and the Tx and Rx locations.

In the simulation of the effects of different ε_r configurations on the predicted channel *PL* characteristics, σ of all building walls was assumed constant with $\sigma = 0.0$, while ε_r of each building wall was assumed values of 4.0, 5.0, 6.0, 7.0 and 8.0. In the simulation of the effects of different σ configurations, ε_r of all building walls was assumed constant with $\varepsilon_r = 5.0$, while σ of each wall was assumed values of 0.0, 0.5, 1.0, 1.5 and 2.0 s/m. It has been found from the simulations performed in the LOS region that the employment of different ε_r and σ configurations yields very little difference in the predicted *PL*. Fig. 6.4 shows the predicted average path loss $\overline{PL}$ when the Rx was moved in Route (1), with respect to different ε_r and σ configurations. As ε_r increases, $\overline{PL}$ is decreased slightly and the same trend is noted when observing the variation of $\overline{PL}$ with respect to σ. This can be explained by the fact that in the LOS region, the direct ray between the Tx and Rx plays a dominant role in radio propagation, whereas reflections from the building walls, the ground and diffractions by the building corners contribute much less to the received signal. On the other hand, as ε_r or σ increases, the reflection coefficients of building walls become higher, resulting in stronger reflected field at the Rx. Consequently, slightly lower *PL* at the Rx is predicted.

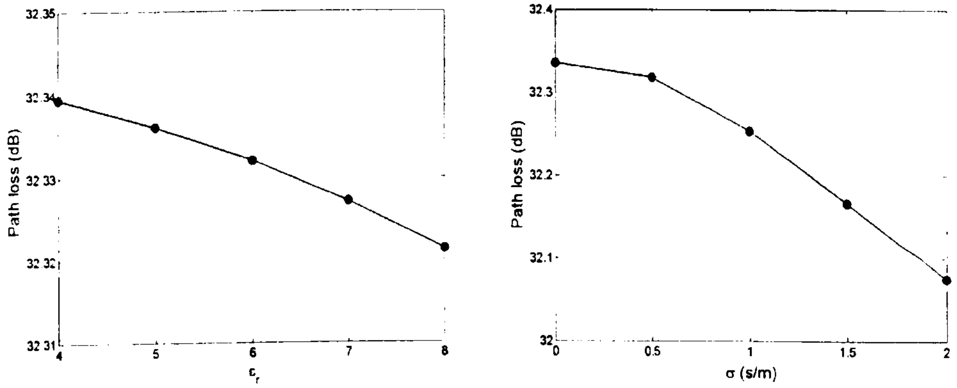

(a) (b)

Figure 6.4: Effects of ε_r and σ on the predicted *PL* in Route 1: (a) effects of ε_r; (b) effects of σ.

In the NLOS region the direct ray is blocked by the buildings, therefore the multiple-reflections from the buildings and ground, in combination with the diffractions by the building corners, play dominant roles in radio propagation. Because of this, it is expected that the effects of ε_r and σ would be more significant than in the LOS region. Fig. 6.5 shows the predicted *PL* with different ε_r and σ configurations along the Rx displacement path. A significant difference in comparison with the LOS case is the effects of ε_r and σ on the predicted *PL*. Up to 20 dB differences in the predicted *PL* between using the lowest ε_r value and the highest ε_r value are observed, and *PL* is decreased as ε_r increases. The similar observation applies to the effects of σ. This provides a strong indication that the received signal strength is much more dependent on the assumed building dielectric parameters due to the dominant roles of the multiple-reflections and diffractions. Nevertheless, the *PL* characteristics along the Tx-Rx path remain similar, thus indicating that the ray-tracing model can predict the trends of *PL* reasonably well within a wide range of ε_r and σ values. It seems that the *PL* characteristics in the NLOS region follows the trend of the variations of the reflectivity of ε_r and σ. The similar conclusion was drawn in [109].

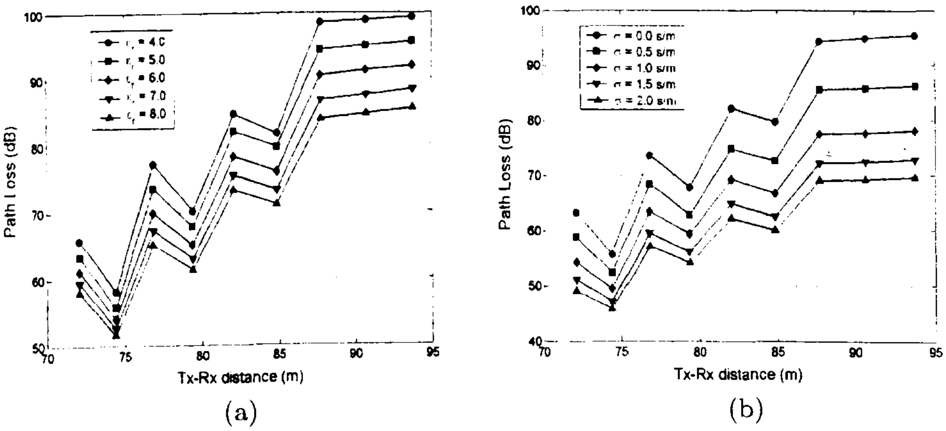

(a) (b)

Figure 6.5: Effects of ε_r and σ on the predicted *PL* in Route 2: (a) effects of ε_r; (b) effects of σ.

6.3 Indoor Predictions

Unlike building characterisation in outdoor environments, the building structures in indoor environments are characterised as single- or multi-layered materials of a finite thickness. The reflection and transmission coefficients of these finite-thick materials are calculated using formulas given in Appendix B. In this section, the effects of different dielectric parameters assigned to the building structures on the ray-tracing prediction results in indoor environments are studied. The effects of the thicknesses of the building structures are also discussed. Within the scope of this research, both PL and τ_{rms} that representing the narrow- and wide-band channel parameters are predicted and discussed.

6.3.1 Simulation Scenarios

To simulate the effects of constitutive parameters (the dielectric parameters and the thickness) of building structures on the prediction results from the ray-tracing model, two Rx routes in the LOS region and two in the NLOS region were considered on the second floor of the Electrical Engineering building, whereas the Tx was assumed fixed at a location on the same floor. In addition, simulations have also been performed on the fifth floor of this building (whose layout is dissimilar to the second floor), to test the generality of the simulation results. Figs. 6.6 and 6.7 show the layout of the second and the fifth floors, and the Tx and Rx locations used on each floor. On the second floor, the Tx was located in the foyer at the location $(x_t, y_t, z_t) = (19.0, 22.0, 9.8)$, while the Rx was moved in four designated routes shown in Fig. 6.6. Routes (1) and (2) correspond to the LOS region, and Routes (3) and (4) correspond to the NLOS region, respectively. In each route, the Rx was moved in 0.1 m increments over a total length of 5 m. On the fifth floor, the Tx was assumed at two locations as shown in Fig. 6.7. Route (1) and (3) correspond to the Tx located at "Tx1" and the Rx moved in the LOS and NLOS regions, respectively. Route (2) and (4) correspond to the Rx moved in the QLOS and NLOS regions, while the Tx was located at "Tx2". It is worth noting that these Tx-Rx locations were chosen randomly, for the purpose of representing the generality of the simulation results.

Among the different dielectric parameters discussed in the beginning of this chapter, reasonable dielectric parameters have been assigned to characterise the building structures in the Electrical Engineering building as reference parameters. Table A.1 in Appendix A lists these values for the building external walls, internal walls, doors and glass windows of the building. Employing these parameters as an input to the database, the ray-tracing model has been used to predict both *PL* and τ_{rms} at all Rx locations designated in Figs. 6.6 and 6.7. The prediction results are referred to as the reference prediction results.

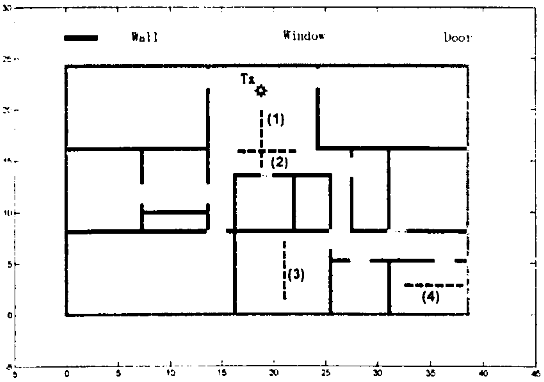

Figure 6.6: Layout of the second floor and the Tx and Rx locations.

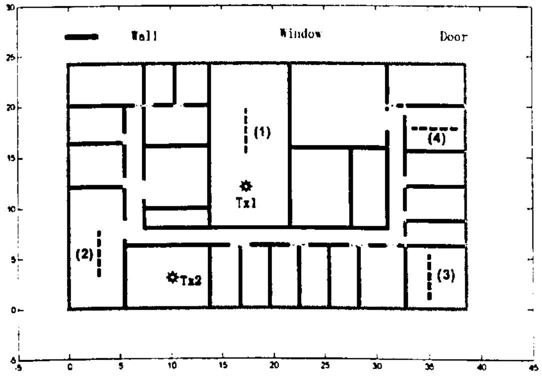

Figure 6.7: Layout of the fifth floor and the Tx and Rx locations.

6.3.2 Permittivity Effects

For a material of a finite thickness, the characteristics of its reflectivity and transmittivity are different when compared with those of a half-space material. Fig. 6.8 shows the reflection and transmission coefficients of a single-layered 12cm-thick lossless material at different incident angles against different ε_r values. A prominent effect of the finite thickness on the reflection and transmission coefficients is the "oscillation" phenomena observed in both coefficients. Compared to Fig. 6.1, it is observed that for a material of a finite thickness, its reflectivity is not monotonously increased as ε_r increases. Instead, the reflectivity of the material tends to be resonant at certain ε_r values. This resonance is a function of the dielectric parameters and thickness of the material, as well as the frequency of the incident wave. The transmittivity of a finite-thick material also has the same resonance characteristics. The variations of both the reflection and transmission coefficients are much more significant than those from a half-space material within the range of ε_r values considered.

In the simulation of the effects of different ε_r configurations on the predicted channel characteristics, different ε_r values were assigned to the internal walls, while σ of the internal walls and the dielectric parameters of other building walls were assumed as the reference values. This is because we consider that the most significant impacts on radio propagation caused by the building structures would be from the internal walls, since they are the major structures on each floor. Fig. 6.9 shows the reflection and transmission coefficients for a normal incidence on the internal walls for different ε_r values, where the circle points correspond to the permittivity values that we used in the simulations. ε_r of the internal walls were chosen as values of 4.0, 4.3, 5.0, 5.5, 6.3, 7.0, 7.4 and 8.0, and the reason of selecting these values is in an attempt to represent the "oscillation" phenomena of the reflectivity and transmittivity.

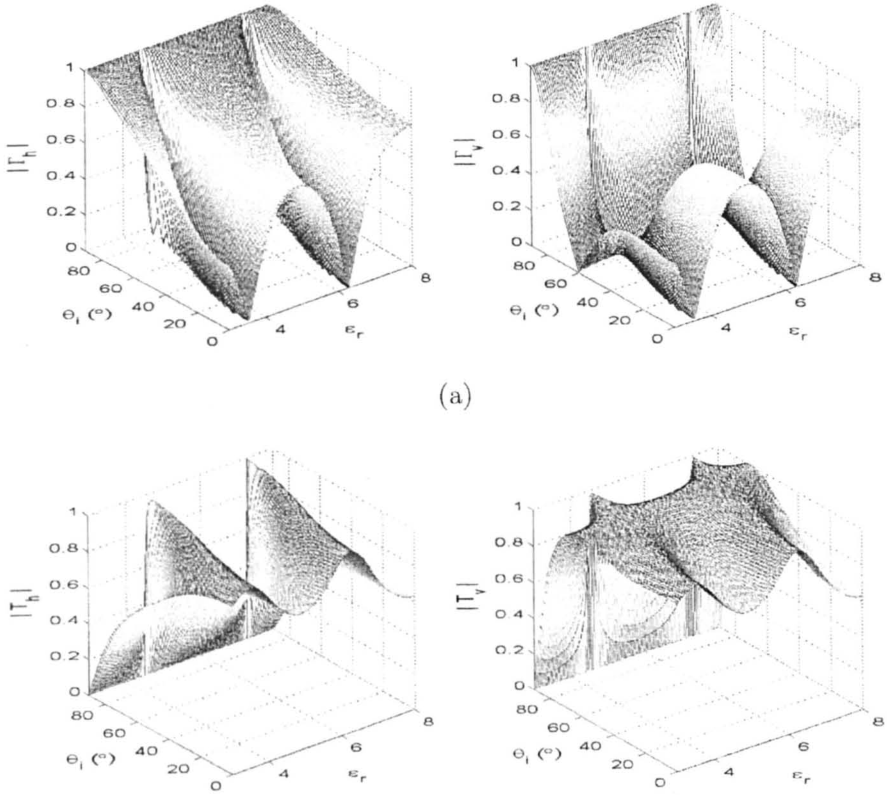

(a)

(b)

Figure 6.8: Magnitudes of the (a) reflection coefficient and (b) transmission coefficient of a 12cm-thick material with $\sigma = 0.0$ s/m versus different ε_r values.

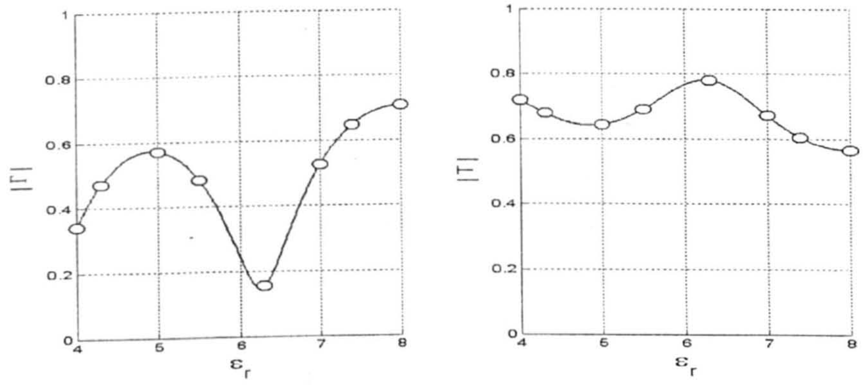

Figure 6.9: Magnitudes of the reflection and transmission coefficients of a 12cm-thick internal wall with $\sigma = 0.02$ s/m versus different ε_r values at a normal incidence.

(1) In the LOS/QLOS Region:

Fig. 6.10 shows the prediction results of the mean path loss $\overline{PL}$ and the mean RMS delay spread $\overline{\tau}_{rms}$ against different ε_r configurations in the two LOS routes on the second floor, and Fig. 6.11 shows the results in the LOS and QLOS regions on the fifth floor.

It is observed from Fig. 6.10 that in both LOS routes the predicted $\overline{PL}$ for different ε_r configurations is varied by as little as 1.5 dB. This phenomenon is similar to that observed in outdoor LOS prediction discussed previously, which indicates that the direct ray is the dominant mechanism governing indoor radio propagation in the LOS region. Even though the reflectivity of the internal walls appears to have large variations within the range of ε_r values considered, the variation of PL is insignificant due to small contributions of reflected waves from the surrounding structures to the received field strength. In contrast to the PL characteristics, the predicted $\overline{\tau}_{rms}$ in the LOS region for different ε_r configurations is changed significantly. Two folds of variation of $\overline{\tau}_{rms}$ is observed within the range of ε_r values considered. For example, the predicted minimum $\overline{\tau}_{rms}$ is under 8 ns for $\varepsilon_r = 6.3$, whereas the maximum $\overline{\tau}_{rms}$ is around 17 ns for $\varepsilon_r = 7.4$ in both routes. It is known by the definition of τ_{rms} that τ_{rms} of the radio channel is determined by the characteristics of all multiple reflected, transmitted and diffracted rays with respect to the direct ray. Both the strengths and time delays of all incoming multipath rays determine the channel τ_{rms} characteristics. Therefore, the channel τ_{rms} characteristics are more sensitive to the environment, and the reflectivity and transmittivity of the environmental structures can have significant effects on channel τ_{rms} characteristics. Interestingly, the variation of the predicted $\overline{\tau}_{rms}$ is not increased monotonously with the increase of ε_r. Instead, it follows the trend of the variation of the reflectivity of the internal wall with respect to its ε_r.

On the fifth floor, although the geometry is very different from the second floor, similar prediction results are observed as shown in Fig. 6.11: a small variation of predicted $\overline{PL}$ and a large variation of $\overline{\tau}_{rms}$. These indicate that in the LOS and QLOS regions, different ε_r configurations for the surrounding building structures have insignificant effects on PL, but can lead to significant variation of τ_{rms}.

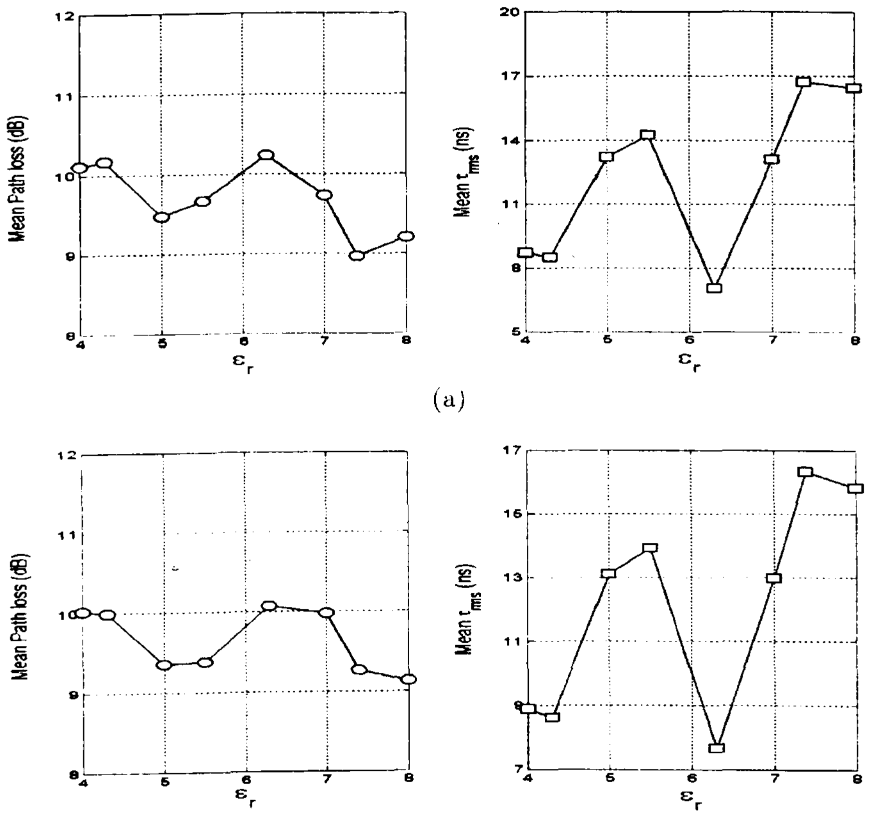

(a)

(b)

Figure 6.10: Variations of the predicted $\overline{PL}$ and $\overline{\tau}_{rms}$ versus different ε_r values in (a) Route (1) and (b) Route (2) on the second floor.

A detailed comparison of the power delay profile of the received signal for different ε_r configurations is helpful in understanding its effects on the predicted channel parameters. For this purpose, the power delay profile of the received signal at the mid-point in Route (1) on the second floor is derived and shown in Fig. 6.12. In the power delay profile, the strengths of all received multipath rays with different time delays are normalised to the strength of the strongest incoming ray (the direct ray in the LOS region).

Hence at $t = 0.0$ ns, the strength of the direct ray is 0 dB in power. Multiple reflected and diffracted rays from the surrounding structures can be clearly seen from the figure, with different degrees of attenuation and different time delays. In the power delay profile, the second and third arrived rays are the single reflected rays from the ceiling and floor, respectively. The strengths of these rays remain invariant for different ε_r values assigned to the internal walls. Other rays with longer time delays are those reflected from either walls or walls in combination with the ceiling and floor. As seen from the power delay profile of the received signal, the direct ray is always much stronger than the strengths of the other received multipath rays, confirming its dominant role in radio propagation in the LOS region.

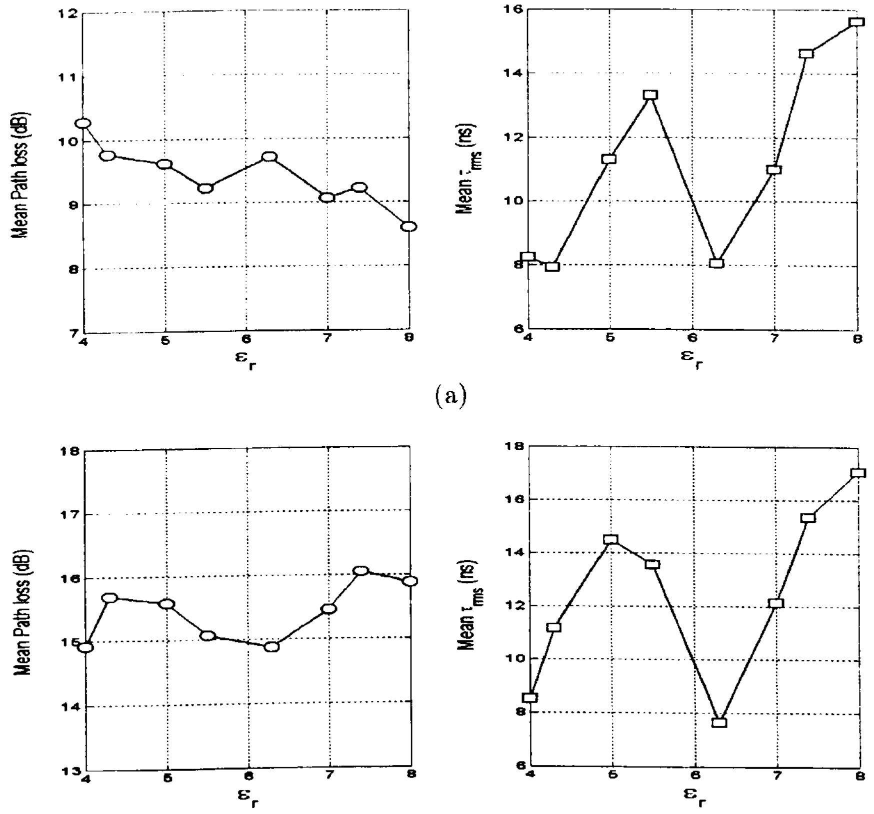

(a)

(b)

Figure 6.11: Variations of the predicted $\overline{PL}$ and $\overline{\tau}_{rms}$ versus different ε_r values in (a) Route (1) and (b) Route (2) on the fifth floor.

The effects of different ε_r configurations on the predicted τ_{rms} can be seen intuitively from the power delay profile. It is observed that for $\varepsilon_r = 4.3$ and $\varepsilon_r = 6.3$, the reflected rays after 40 ns are seriously attenuated to more than 30 dB with respect to the strength of the direct ray. In contrast, these reflected rays are still strong after 40 ns for $\varepsilon_r = 5.5$ and $\varepsilon_r = 7.4$. The incoming rays with time delays more than 40 ns (corresponding to 12 m in the difference of path length), are mostly those multiple transmitted-reflected rays from the walls which are invisible to the Rx. As seen in Figs. 6.8, the reflectivity and transmittivity of a dielectric material have reverse trends with respect to different ε_r values. The transmittivity of the internal walls for $\varepsilon_r = 6.3$ is higher than that for $\varepsilon_r = 7.4$. In contrast, the reflectivity of the internal walls for $\varepsilon_r = 7.4$ is higher than that for $\varepsilon_r = 6.3$. However, the degrees of variations of the reflectivity and transmittivity are different. For example, the transmission coefficient is 0.78 for $\varepsilon_r = 6.3$ and 0.61 for $\varepsilon_r = 7.4$ when the wave is normally incident on the wall, whereas the reflection coefficient is 0.66 for $\varepsilon_r = 7.4$ and 0.17 for $\varepsilon_r = 6.3$ for the same incident angle. This indicates that the reflectivity of the internal walls has a more significant impact on the signal attenuation for different ε_r values, compared to the impact of its transmittivity. Although multipath rays will experience various incident angles at different building structures, the reflectivity of the building structures still plays more significant effects on these rays. Consequently, the internal walls with $\varepsilon_r = 7.4$ produce stronger reflected fields at the Rx than those with $\varepsilon_r = 6.3$. These long-delayed strong transmitted-reflected signals cause higher τ_{rms}. The predicted path loss of the direct ray PL_{dir}, PL, and τ_{rms} at this point is shown in Table 6.2. The predicted PL values are very close to PL_{dir} for all ε_r configurations. In contrast, the predicted τ_{rms} is significantly changed within the range of 5.11 ~ 14.71 ns. It is noted that PL and τ_{rms} given in the table are different from $\overline{PL}$ and $\overline{\tau}_{rms}$ shown in Fig. 6.10 (a), because a single-point simulation is performed here. Nevertheless, the trends of variations of all predicted channel parameters given in the table are consistent with those shown in Fig. 6.10 (a).

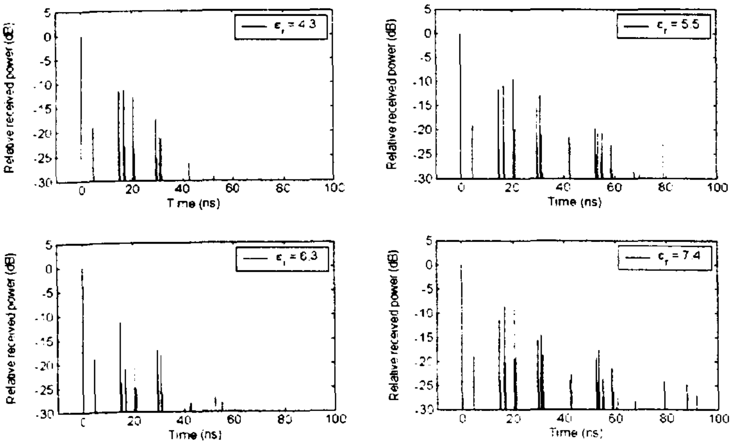

Figure 6.12: Predicted power delay profile at the mid-point in Route (1) on the second floor.

Table 6.2: Predicted PL_{dir}, PL and τ_{rms} for different ε_r configurations at the mid-point in Route (1) on the second floor.

	$\varepsilon_r = 4.3$	$\varepsilon_r = 5.5$	$\varepsilon_r = 6.3$	$\varepsilon_r = 7.4$
PL_{dir} (dB)	14.63	14.63	14.63	14.63
PL (dB)	13.98	13.48	14.28	13.16
τ_{rms} (ns)	7.98	12.74	5.11	14.71

(2) In the NLOS Region:

Figs. 6.13 and 6.14 show the predicted $\overline{PL}$ and $\overline{\tau}_{rms}$ in the two NLOS routes on the second floor and on the fifth floor, respectively. Again it is observed that $\overline{\tau}_{rms}$ can be changed dramatically within the range of ε_r values considered. On the other hand, unlike in the LOS region, the predicted PL characteristics in the NLOS region show a relatively large variation and the pattern of this variation is complex. About 6 dB of variation of $\overline{PL}$ in both routes on the second floor and 10 dB of variation in both routes on the fifth floor are seen. The predicted $\overline{PL}$ is reduced to the minima for $\varepsilon_r = 6.3$ in Route (3) on the second floor and for $\varepsilon_r = 7.0$ in Route (4) on the second floor, as well as in both routes on the fifth floor.

Visual inspection of the floor layouts in Fig. 6.6 shows that when the Rx is moved in Route (3) on the second floor, the direct ray crosses the internal walls at an incident angle of about 0°. When the Rx is moved in Route (4), the direct ray crosses the internal walls at an incident angle of about 50° ~ 60°. The reflectivity and transmittivity of the internal walls at these two different incident angles are shown in Fig. 6.15. Significant variations of both the reflectivity and transmittivity at these two incident angles are seen, where the ε_r value for determining the minimum reflectivity and the maximum transmittivity is changed from $\varepsilon_r = 6.3$ to about $\varepsilon_r = 7.0$ when the incident angle changes from 0° to 55°. This indicates that the strength of the received direct ray is strongly dependent on the angle at which it crosses the intercepting walls. The variations of the predicted $\overline{\tau}_{rms}$ generally conform to the variations of the predicted $\overline{PL}$.

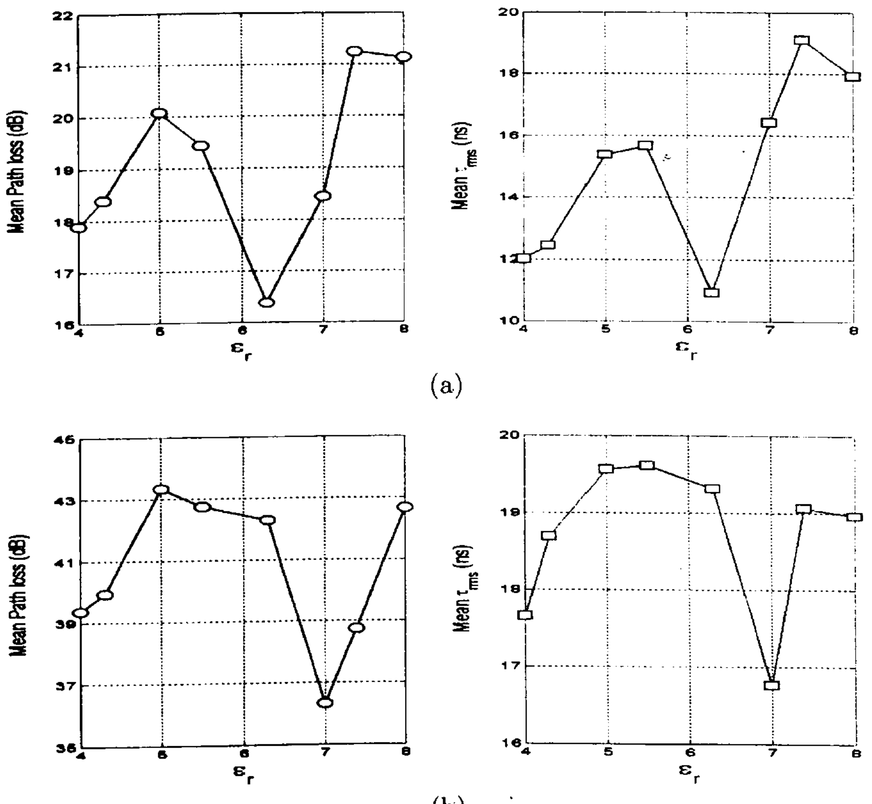

(a)

(b)

Figure 6.13: Variations of the predicted $\overline{PL}$ and $\overline{\tau}_{rms}$ versus different ε_r values in (a) Route (3) and (b) Route (4) on the second floor.

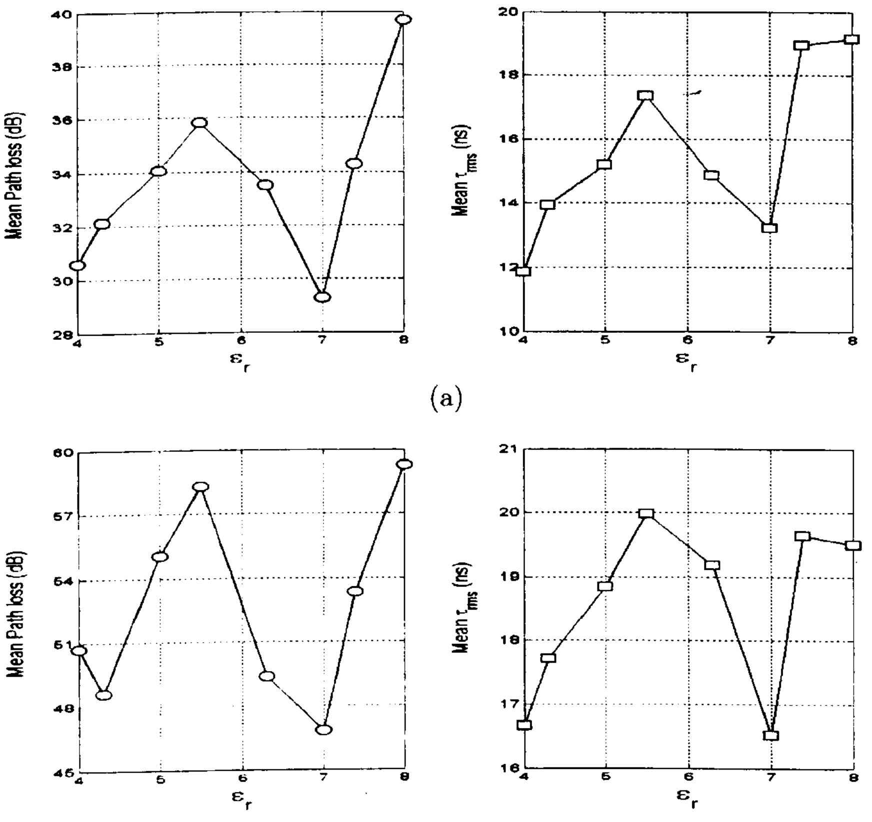

(a)

(b)

Figure 6.14: Variations of the predicted $\overline{PL}$ and $\overline{\tau}_{rms}$ versus different values of ε_r in (a) Route (3) and (b) Route (4) on the fifth floor.

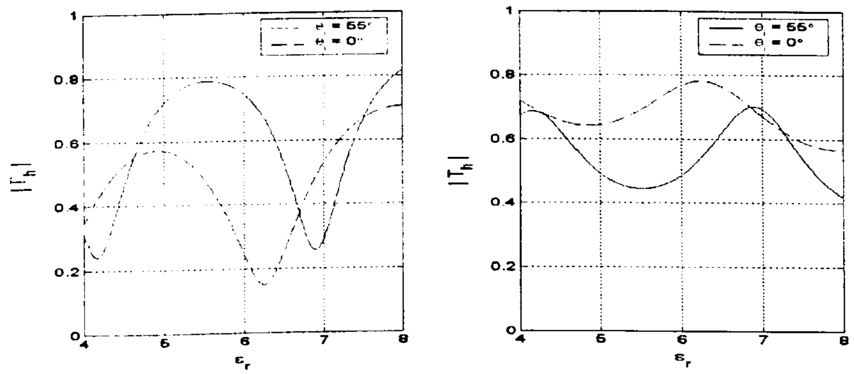

Figure 6.15: Horizontally polarised reflectivity and transmittivity of the internal wall versus different values of ε_r.

The power delay profile at the mid-point in Route (3) on the fifth floor for different ε_r configurations is shown in Fig. 6.16. It is seen that in the NLOS region, the direct ray is still the strongest signal arriving at the Rx among all the received multipath rays, however its dominant role in the received signal is less than in the LOS region. The predicted τ_{rms} are higher for $\varepsilon_r = 5.5$ and $\varepsilon_r = 7.4$ than those for $\varepsilon_r = 6.3$ and $\varepsilon_r = 7.0$. Also is observed is that for $\varepsilon_r = 7.0$, the multiple-reflected rays from surrounding structures are highly attenuated compared to those for $\varepsilon_r = 5.5$, resulting in less but more concentrated incoming rays within 30 dB relative to the strength of the direct ray, therefore yielding lower τ_{rms} than for other ε_r configurations.

The channel *PL* characteristics cannot be seen intuitively from the power delay profile of the received signal because the strengths of the received multipath rays are normalised to the strongest received ray. The predicted PL_{dir}, *PL* and τ_{rms} at this point is shown in Table 6.3. It can be seen that the contributing effect of the direct ray is less dominant in the NLOS region, however its strength still strongly determine the strength of received signal. This is particularly distinct for $\varepsilon_r = 7.0$ where the difference between PL_{dir} and *PL* is only about 2.5 dB.

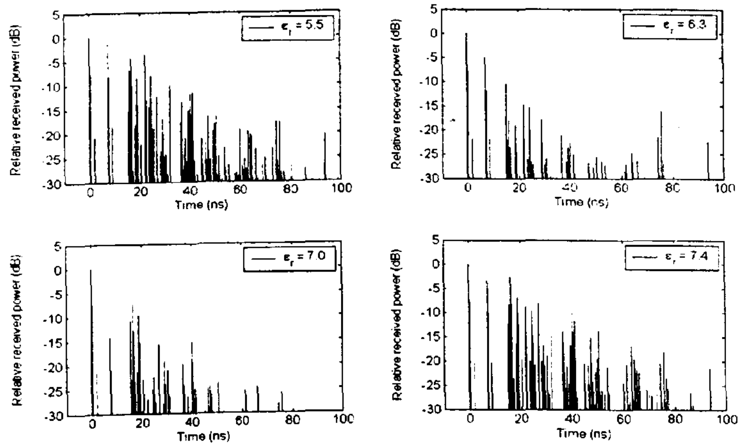

Figure 6.16: Predicted power delay profile at the mid-point in route 3 on the fifth floor.

Table 6.3: Predicted PL_{dir}, PL and τ_{rms} for different values of ε_r at the mid-point in Route 3 on the fifth floor.

	$\varepsilon_r = 5.5$	$\varepsilon_r = 6.3$	$\varepsilon_r = 7.0$	$\varepsilon_r = 7.4$
PL_{dir} (dB)	47.49	42.67	38.28	44.75
PL (dB)	40.81	39.70	35.88	38.22
τ_{rms} (ns)	17.31	16.08	12.88	17.89

6.3.3 Conductivity Effects

In this subsection, the effects of different σ configurations for the internal walls on the prediction results are studied. Figs. 6.7 shows the reflection and transmission coefficients of a 12cm-thick material at different incident angles against different σ values. The permittivity of the material is assumed as $\varepsilon_r = 5.0$. It is seen that as σ increases, the reflection coefficient of the material is not changed significantly, whereas the transmission coefficient is decreased monotonously until zero.

In the simulation of the effects of different σ configurations on the predicted channel characteristics, different σ values were assigned to the internal walls, while ε_r of the internal walls and the dielectric parameters of other building walls were assumed as the reference values. Fig. 6.18 shows the reflection and transmission coefficients for a normal incidence on the internal walls with different σ values, where the circle points correspond to σ values that we used in the simulations. The σ chosen were values of 0.00, 0.02, 0.04, 0.06, 0.08 and 0.10 s/m, and the reason of selecting these values is in an attempt to represent the trends of variations of the reflectivity and transmittivity.

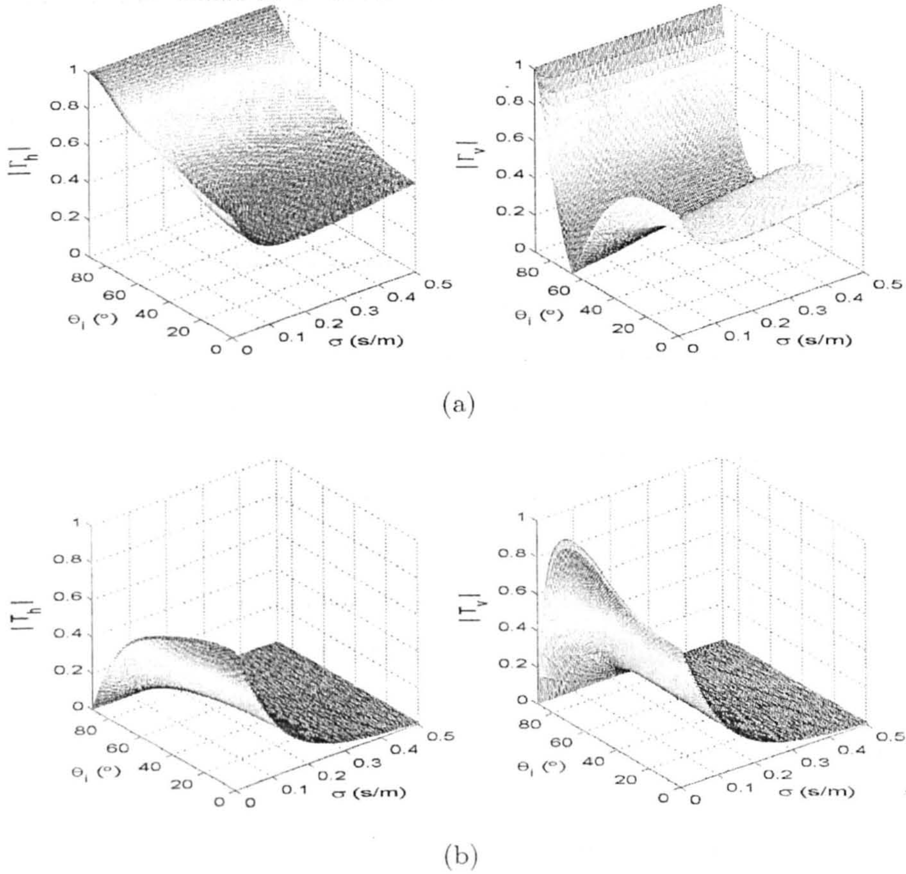

(a)

(b)

Figure 6.17: Magnitudes of the (a) reflection coefficient and (b) transmission coefficient of a 12cm-thick material with $\varepsilon_r = 5.0$ versus different σ values.

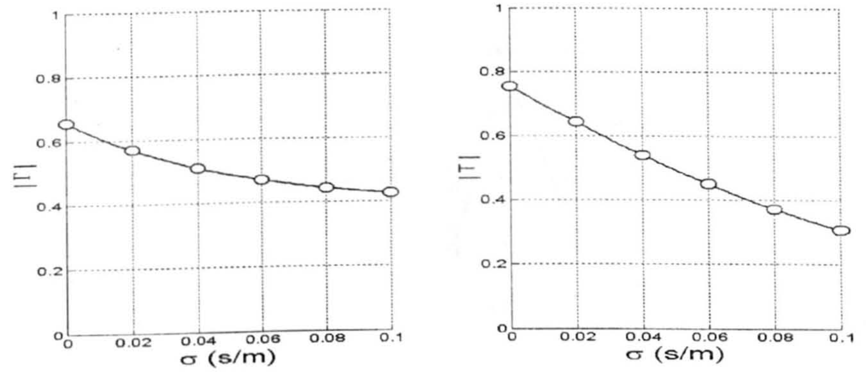

Figure 6.18: Magnitudes of the reflection and transmission coefficients of a 12cm-thick material with $\varepsilon_r = 5.0$ versus different σ values for a normal incidence.

(1) In the LOS/QLOS Region:

Fig. 6.19 shows the predicted $\overline{PL}$ and $\overline{\tau}_{rms}$ in the two LOS routes on the second floor; and Fig. 6.20 shows the prediction results in the LOS and QLOS regions on the fifth floor. It is observed from Fig. 6.19 that in both LOS routes the predicted $\overline{PL}$ for different σ configurations are changed by as little as 1 dB. This confirms the dominant role of the direct ray in radio propagation in the LOS region. In addition, because of small variation of the reflection coefficient of the internal walls with respect to σ , the strengths of the reflected fields are changed very little for different σ configurations. In contrast to $\overline{PL}$, the predicted $\overline{\tau}_{rms}$ in the LOS region is changed significantly with respect to σ , and two folds of variation is observed. As σ increases, the predicted $\overline{\tau}_{rms}$ is decreased rapidly for very low σ values and tends to be decreased slower for higher σ. For example, a decrease of about 5 ns of the predicted $\overline{\tau}_{rms}$ is observed from $\sigma = 0.0$ s/m to $\sigma = 0.02$ s/m. whereas a decrease of about 3 ns is observed from $\sigma = 0.02$ s/m to $\sigma = 0.10$ s/m. On the fifth floor, although the scenario is quite different from the second floor, similar prediction results are observed in Fig. 6.20, expect that in the QLOS region where the predicted $\overline{PL}$ is increased noticeably as σ increases. In the QLOS region, the direct ray is strongly attenuated by the intercepting walls with high σ .

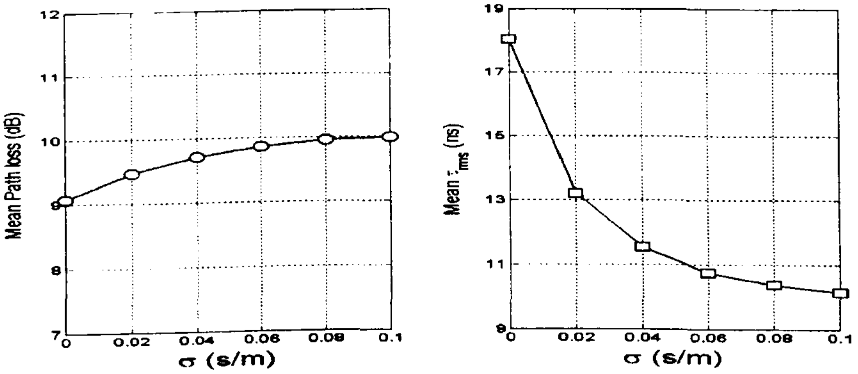

(a)

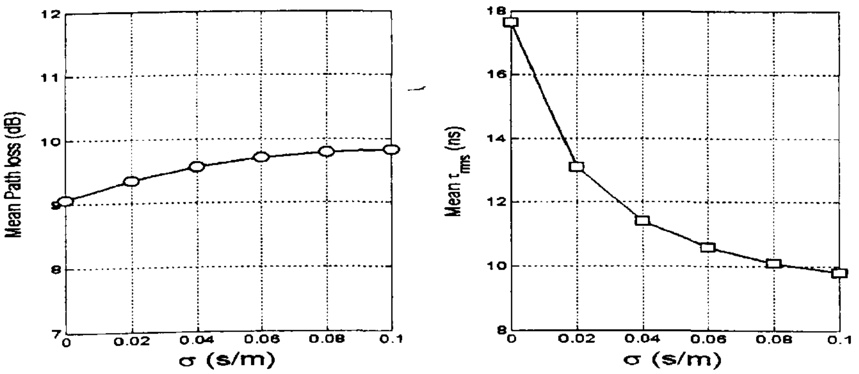

(b)

Figure 6.19: Variations of the predicted $\overline{PL}$ and $\overline{\tau}_{rms}$ versus different values of σ in (a) Route (1) and (b) Route (2) on the second floor.

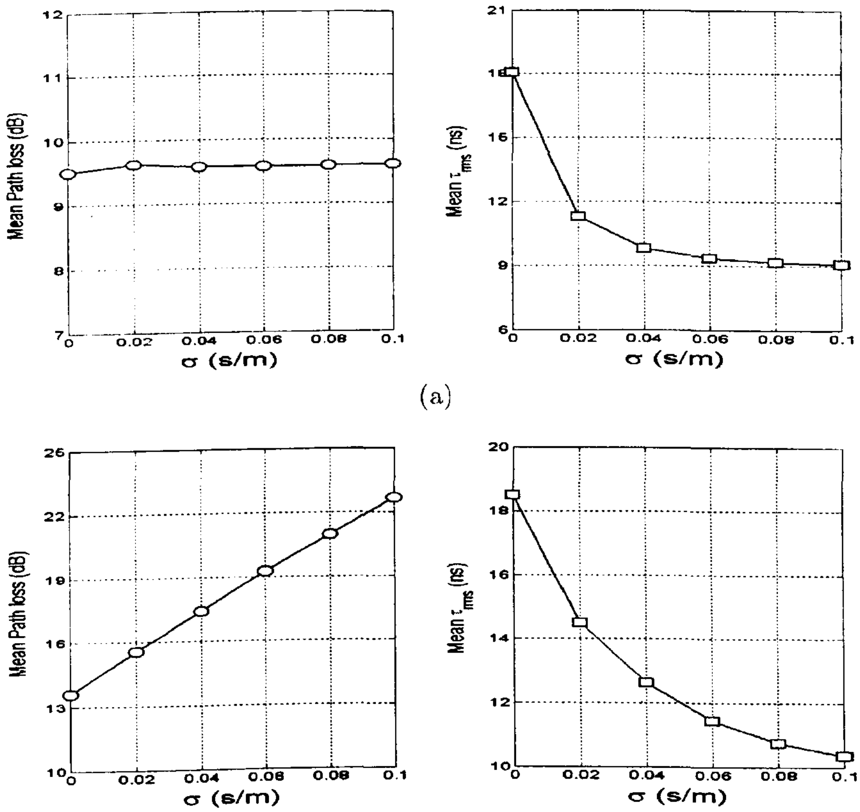

(a)

(b)

Figure 6.20: Variations of the predicted $\overline{PL}$ and $\overline{\tau}_{rms}$ versus different values of σ in (a) Route (1) and (b) Route (2) on the fifth floor.

The power delay profile of the received signal at the mid-point in Route (1) on the second floor is shown in Fig. 6.21, from which it is clearly seen that as σ increases, the received multipath rays reflected from surrounding structures are attenuated significantly. Unlike the characteristics of the reflectivity and transmittivity of the internal wall with respect to its ε_r, both the reflectivity and transmittivity of the internal wall are decreased with respect to its σ, but the degree of decrease of the transmittivity is much higher than that of the reflectivity. For multipath reflected rays incoming within short time delays (40 ns with respect to the direct ray), the strengths of the incoming directly reflected rays from the surrounding walls visible to the Rx are decreased insignificantly due to the response of the reflectivity of the internal wall to its σ. In contrast, for the received multipath rays with more than 40 ns time delays with respect to the direct ray, the signal strengths are decreased much more significantly due to the effects of σ on both the reflectivity and transmittivity. The longer time delay that the incoming ray experiences, the more likelihood that it crosses more internal walls, resulting in higher attenuation of the signal strength. Therefore σ configurations have a more significant impact on the received ray strength as its associated time delay is increased.

As σ increases, fewer strong reflected rays are received and hence the predicted $\bar{\tau}_{rms}$ is lower. The decrease of $\bar{\tau}_{rms}$ is monotonous, but not linearly, against the decrease of σ. This is due to the non-linear variation of the reflectivity and transmittivity of the internal wall with respect to its σ. As σ increases, multipath transmitted-reflected rays from the surrounding building structures with long distances to the Rx are attenuated more significantly. Consequently, for high σ, only those building structures visible to the Rx have strong impacts on the channel τ_{rms}. The predicted PL_{dir}, PL and τ_{rms} at this point is shown in Table 6.4. Dominant effect of the direct ray on the PL characteristic and the decreasing trend of the predicted τ_{rms} for different σ configurations are observed. Large decrease of τ_{rms} for low σ values and small decrease of τ_{rms} for high σ are clearly seen.

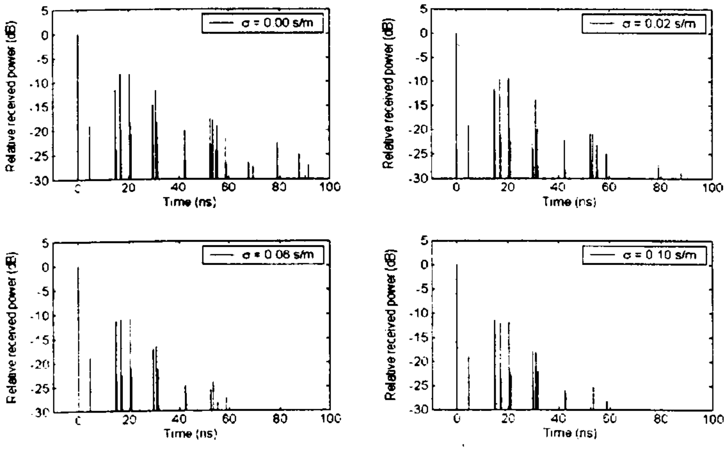

Figure 6.21: Predicted power delay profile at the mid-point in Route 1 on the second floor.

Table 6.4: Predicted PL_{dir}, PL and τ_{rms} for different values of σ at the mid-point in Route 1 on the second floor.

	$\sigma = 0.00$ s/m	$\sigma = 0.02$ s/m	$\sigma = 0.06$ s/m	$\sigma = 0.10$ s/m
PL_{dir} (dB)	14.63	14.63	14.63	14.63
PL (dB)	13.07	13.52	13.83	13.93
τ_{rms} (ns)	16.78	12.06	9.71	8.91

(2) In the NLOS Region:

Figs. 6.22 and 6.23 show the predicted $\overline{PL}$ and $\overline{\tau}_{rms}$ in the two NLOS routes on the second floor and on the fifth floor, respectively. Again it is observed that the predicted $\overline{\tau}_{rms}$ is decreased monotonously with large variation as σ increases, while the rate of this decrease tends to be smaller for higher σ. However, the variations of $\overline{\tau}_{rms}$ in different routes are not as uniform as those observed in the LOS routes as shown in Figs. 6.19 and 6.20. Compared to the LOS case, the environmental geometry has a much more significant impact on the channel $\overline{\tau}_{rms}$ in the NLOS region because it is a function of both strengths and time delays of individual received multipath rays and is highly site-dependent. Therefore, the variation of predicted channel $\overline{\tau}_{rms}$ in the NLOS region is expected to be less uniform than in the LOS region. As far as the *PL* characteristics are concerned, a large variation of *PL* (a few tens of dBs) is observed within the range of σ values considered. The predicted $\overline{PL}$ is monotonously increased with σ. This is because in the NLOS region, the direct ray and other received multipath rays generally cross many intercepting walls and will experience higher attenuations for higher σ.

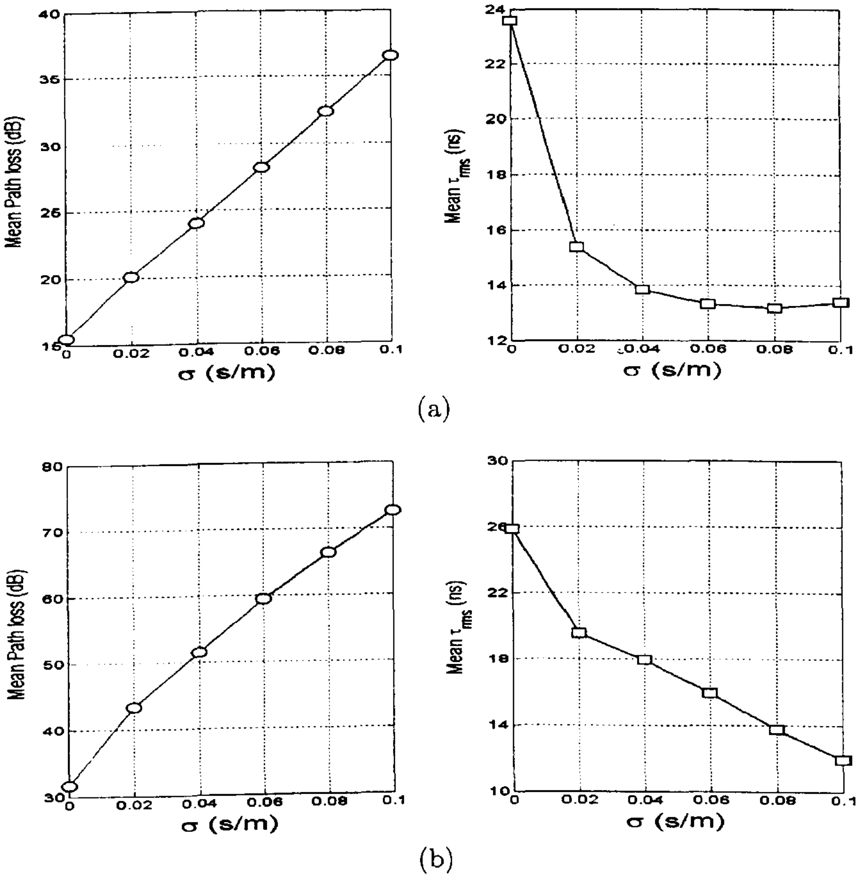

(a)

(b)

Figure 6.22: Variations of the predicted $\overline{PL}$ and $\overline{\tau}_{rms}$ versus different values of σ in (a) Route (3) and (b) Route (4) on the second floor.

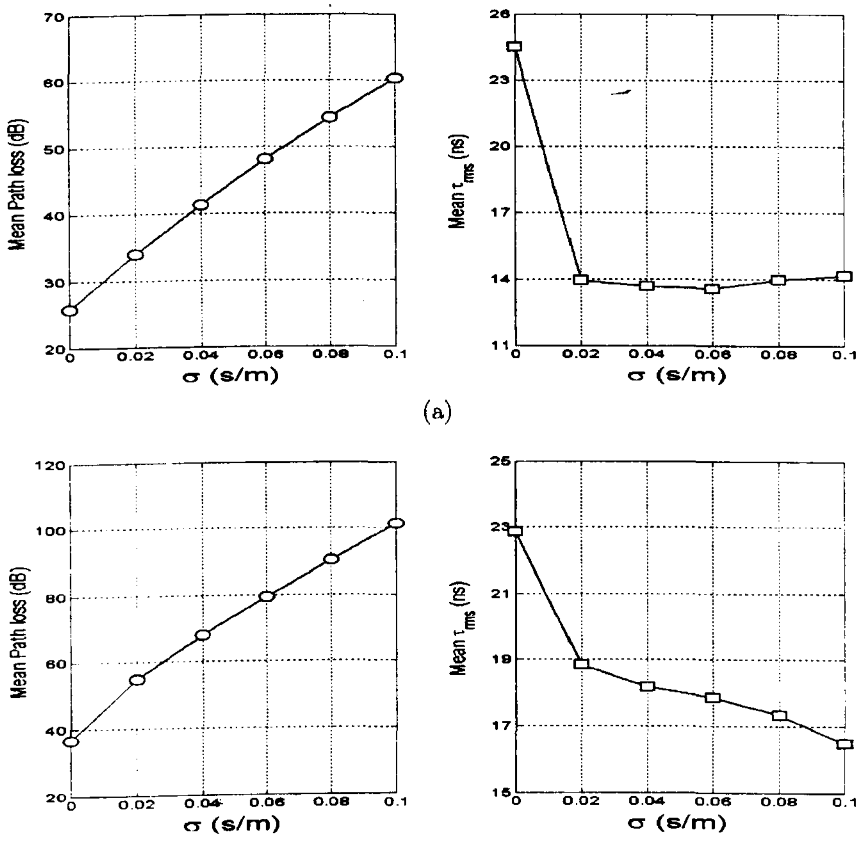

(a)

(b)

Figure 6.23: Variations of the predicted $\overline{PL}$ and $\overline{\tau}_{rms}$ versus different values of σ in (a) Route (3) and (b) Route (4) on the fifth floor.

Fig. 6.24 shows the received signal power delay profile at the mid-point in Route (3) on the fifth floor. It is seen as σ increases, fewer strong multipath rays are received and the power delay profile becomes more concentrated, resulting in a lower predicted τ_{rms}. On the other hand, the direct ray plays less dominant role in the received signal as σ increases. For example, there are a few received multipath rays with strengths comparable to that of the direct ray for $\sigma = 0.06$ s/m, while the direct ray is not the strongest received signal for $\sigma = 0.10$ s/m. The predicted PL_{dir}, PL and τ_{rms} at this point is shown in Table 6.5. Both PL_{dir} and PL are highly increased as σ increases, whereas the predicted τ_{rms} are decreased.

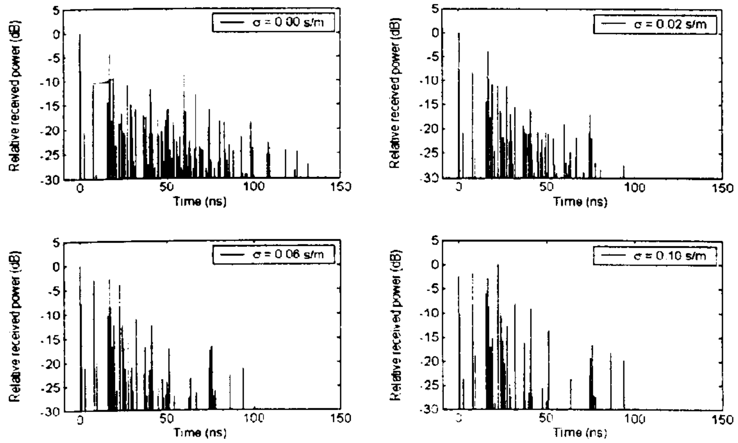

Figure 6.24: Predicted power delay profile at the mid-point in Route (3) on the fifth floor.

Table 6.5: Predicted PL_{dir}, PL and τ_{rms} for different values of σ at the mid-point in Route (3) on the fifth floor.

	$\sigma = 0.00$ s/m	$\sigma = 0.02$ s/m	$\sigma = 0.06$ s/m	$\sigma = 0.10$ s/m
PL_{dir} (dB)	35.93	44.68	61.01	77.22
PL (dB)	30.57	40.24	55.30	68.50
τ_{rms} (ns)	26.38	16.73	15.07	14.19

6.3.4 Thickness Effects

Unlike in the outdoor channel predictions where the building structures are characterised as half-space materials, in the indoor channel predictions, the thickness of a building structure must be taken into account for the calculation of its reflection and transmission coefficients. In practice, the thickness information of each building structure is given in the blueprint of the building layout. However, this information may not be very accurate in contrast to the real build-up of structures. Therefore, it is worth studying the sensitivity of the prediction results from the ray-tracing model to different thickness configurations. In this subsection, the effects of different thickness configuration are briefly discussed.

Figs. 6.25 shows the reflectivity and transmittivity of a single-layered building structure against different thickness. It is seen that the “oscillation“ phenomenon is existent, which is similar to the effects of ε_r of the material shown in Figs. 6.8. Therefore, the effects of different thickness configurations are expected to be similar to those of different ε_r configurations. To verify this assumption, the channel $\overline{PL}$ and $\overline{\tau}_{rms}$ are predicted in Routes (1) and (3) on the second floor. Looking at the constitutive parameters of each building structure, we find that there are two types of internal walls specified in the database, i.e., the thick internal walls of 18 cm and the thin internal walls of 12 cm. However, most of the internal walls on each floor are thin walls while few of them are thick walls. To simplify the simulation, only the thickness effects of the thin internal walls have been simulated. Fig. 6.26 shows the reflection and transmission coefficients for a normal incidence on the internal walls of different thickness d, where the circle points correspond to the thickness values that we used in the simulations. Nine values are assigned to the thickness of each internal wall, ranging from 10 cm to 14 cm in 0.5 cm increments.

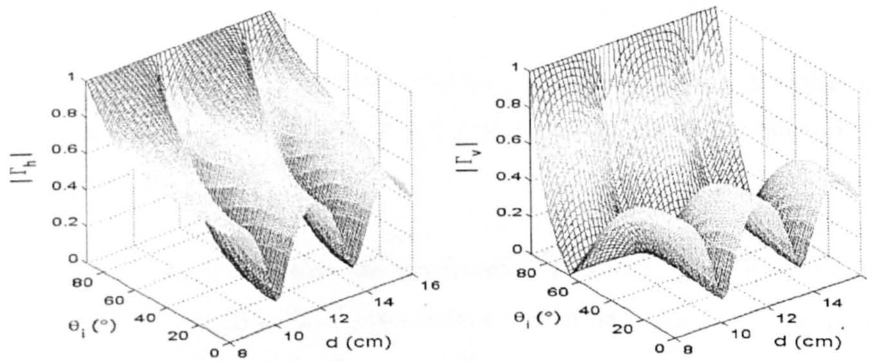

(a)

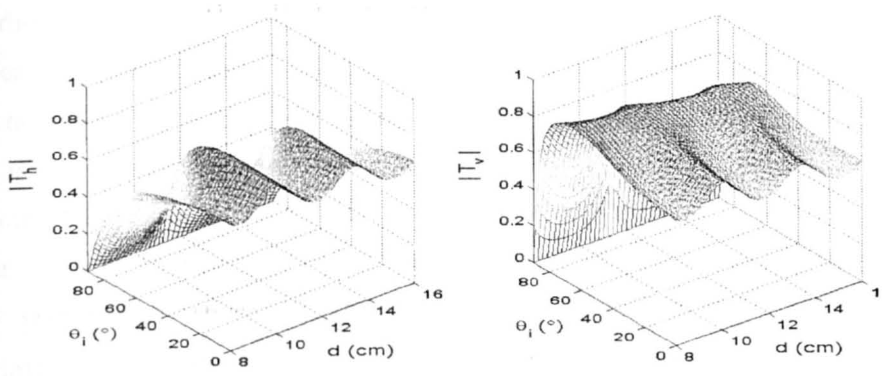

(b)

Figure 6.25: Magnitudes of the (a) reflection coefficient and (b) transmission coefficient of a material with $\varepsilon_r = 5.0$ and $\sigma = 0.0$ s/m versus different thicknesses.

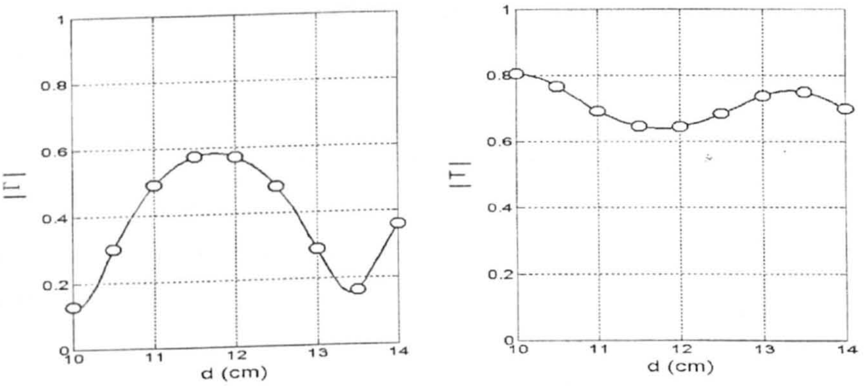

Figure 6.26: Magnitudes of the reflection and transmission coefficients of an internal wall with $\varepsilon_r = 5.0$ and $\sigma = 0.0$ s/m versus different thicknesses for a normal incidence.

Figs. 6.27 and 6.28 show the predicted $\overline{PL}$ and $\overline{\tau}_{rms}$ in Route (1) and in Route (3) on the second floor, respectively. Similar trends as shown in Figs. 6.10 (a) and 6.13 (a) are observed. The predicted $\overline{PL}$ in the LOS region shows small variation with different thicknesses, whereas a few dBs of variation following the trend of the variation of the reflectivity with respect to the thickness is observed in the NLOS region. On the other hand, the predicted $\overline{\tau}_{rms}$ in both the LOS and NLOS regions have variation of similar order. For example, the maximum variation of 23% (10 ns for d = 13.5 cm) of the predicted $\overline{\tau}_{rms}$ with respect to the reference simulation results (13 ns for d = 12 cm) are observed in Route (1); and the maximum variation of about 19% (12.7 ns for d = 13.5 cm) of the predicted $\overline{\tau}_{rms}$ with respect to that for d = 11.5 cm (15.6 ns) are observed in Route (3). The variation of the predicted $\overline{\tau}_{rms}$ in both regions generally follows the trend of the variation of the reflectivity of the internal wall with respect to its thickness.

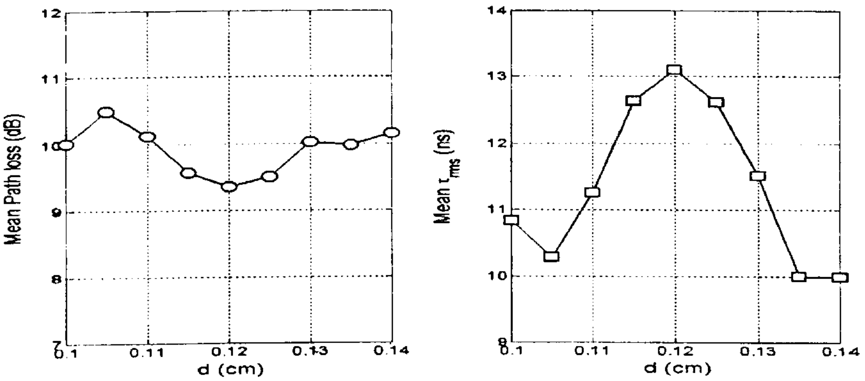

Figure 6.27: Variations of the predicted $\overline{PL}$ and $\overline{\tau}_{rms}$ versus different thicknesses in Route (1) on the second floor.

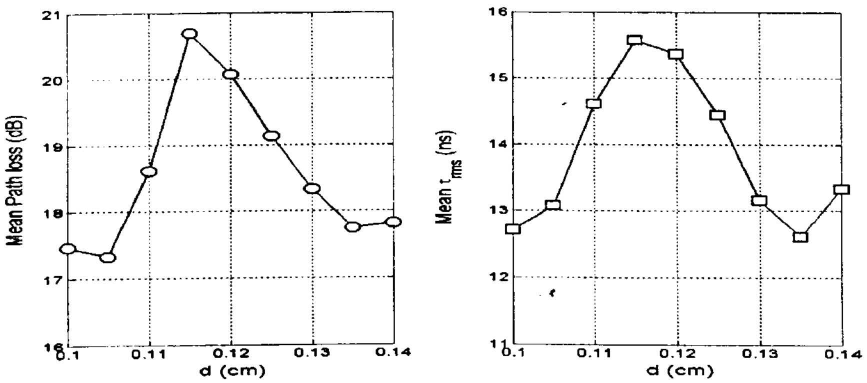

Figure 6.28: Variations of the predicted $\overline{PL}$ and $\overline{\tau}_{rms}$ versus different thicknesses in Route (3) on the second floor.

It also indicates from the simulation results that if the degree of inaccuracy of thickness information is small, the predicted channel *PL* and τ_{rms} characteristics do not have significant errors. For example, if the thicknesses of the internal walls are changed from 12.0 cm to 11.5 cm or 12.5 cm (around 5% inaccuracy), less than 2 dB of variations of *PL* from reference simulation results in both the LOS and NLOS regions are observed. The predicted τ_{rms} also show variations of less than 8% in both regions.

6.4 Summary

In this chapter, the influence of the accuracy of the building database is studied, in the sense that the sensitivity of prediction results from the ray-tracing model to different configurations of constitutive parameters for the building structures is examined.

Simulation results for outdoor environments show that *PL* is insensitive to the dielectric parameters of the building structures in the LOS region, however, it is sensitive in the NLOS region. The variation of the predicted *PL* follows the trend of the variation of the reflectivity with respect to ε_r and σ of the half-space building structures.

Simulation results in indoor environments show that the predicted channel *PL* and τ_{rms} characteristics are dependent on the dielectric parameters assigned to building structures. The predicted *PL* characteristics in the LOS region are shown insensitive to different dielectric parameters assigned to building structures, whereas it is dependent on the dielectric parameters used in the NLOS region. In the NLOS region, a few dBs of variation of *PL* is observed for different ε_r configurations, while a few tens of dBs variation of *PL* can be observed for different σ configurations.

These show that the channel *PL* characteristics are particularly sensitive to the σ configuration of building structures in the database.

The predicted channel τ_{rms} shows a great dependence on the dielectric parameter configurations. The variation of the predicted channel τ_{rms} follows the trend of variation of the reflectivity of building structure with respect to its ε_r. On the other hand, the predicted channel τ_{rms} is rapidly decreased from a high value for very low σ to a low value for higher σ, and the rate of this decrease is larger for lower σ and smaller for higher σ. The sensitivity of predicted channel τ_{rms} is observed similar in both LOS and NLOS regions.

The effects of different thickness configurations are similar to those for different ε_r configurations. From engineering point of view, the sensitivity of prediction results to the thickness information on the building structures is small in the UHF frequency band.

Simulation results for indoor scenarios show that the prediction results by the ray-tracing model are dependent on the configurations of constitutive parameters for the building structures in the database. The degree of such dependence is related to whether the Rx is in the LOS region or in the NLOS region. In view of this prediction sensitivity, we conclude that for an accurate prediction, a good knowledge of the dielectric properties of building structures is required.

Chapter 7

Summary and Future Work

7.1 Summary

The issues associated with radio wave propagation within indoor environments have been investigated. Two major objectives are achieved in this research: 1) *In-situ* characterisation of the dielectric properties of building materials; and 2) Development of a deterministic channel model for characterising radio propagation within indoor environments. Experimental and simulation results from this research are valuable for the design and planning of wireless radio systems within indoor environments.

For the characterisation of building materials, a free-space monostatic measurement system has been developed to measure the reflection coefficients of various building materials, from which the constitutive parameters (the permittivity, the conductivity and the thickness) of the material under test can simultaneously be determined. This measurement technique offers the following advantages:

- The technique provides non-destructive and non-contact measurements on materials in a wide frequency range;

- The technique has the advantage of easy configuration and the capability of measurements with access from only one side of the material under test;
- The system is portable and small in size.

These key features make the system particularly suitable for *in-situ* measurements on building materials. The technique has been validated by the measurements of the constitutive parameters of several material samples with known dielectric properties, in laboratory environments. In addition, the measurement system has been modified and employed for *in-situ* measurements of various building materials at the building of Department of Electrical Engineering in University of Liverpool. Good measurement results demonstrated the usefulness and reliability of the measurement technique. The knowledge of the dielectric properties of building materials is very useful for the investigation of radio wave propagation within indoor environments.

A three-dimensional image ray-tracing model based on the GO and UTD has been developed to simulate radio wave propagation within indoor environments. The model can provide comprehensive information on the radio channels. Given both geometrical and electromagnetic descriptions of the environment of interest, both the narrow- and wide-band channel parameters are obtained by computing the received power delay profile at the receiver.

A major deficiency of the ray-tracing model is the requirement of high computation time. This is due to the exhaustive search of ray-object intersections. A new ray tree algorithm has therefore been developed, using the illumination zone concept, to reduce any unnecessary ray-object intersection search in early stages. By projecting 3D structures into 2D space, the 3D ray-object intersection search can be implemented in 2D sense, and hence the ray tree can be generated by only considering the successive two objects in 2D space illuminated by an image. It has been demonstrated that the implementation of the ray tree algorithm can significantly reduce the computation time without any accuracy degradation.

The accuracy of the ray-tracing model has been evaluated by comparisons with other simulation results and measurement data. The number of reflections allowed in each ray path has been investigated in order to yield good prediction accuracy while keeping the computation time as low as possible. Afterwards, simulations of the channel path loss, RMS delay spread and the coherence bandwidth in the Electrical Engineering building has been performed to produce an insight of the statistical characteristics of the indoor channels in such environments. A simplified ray-tracing model has also been developed to overcome the high computation time of the ray-tracing model and the inaccuracy of the empirical approach. It is based on a consideration of the reflection effects of building structures but with first-order reflections only. An improvement on accuracy of the path loss prediction over the empirical approach has been demonstrated.

The effects of building dielectric parameters on the ray-tracing prediction have been investigated. The database incorporated with different dielectric parameters to represent the same building materials has been employed in the ray-tracing simulation to investigate the dependence of prediction results on the dielectric parameters employed. Simulation results for different indoor environments in both the LOS and NLOS regions have demonstrated that the predicted channel path loss and RMS delay are, in different degrees, dependent on the dielectric parameters employed in the database. This investigation gives a strong indication that incorporating appropriate dielectric parameters to represent the building materials is necessary for accurate characterisation of indoor radio channels. Therefore, the method used in this research for *in-situ* characterisation of building materials is recommended. Research results from this project are presented in [116][117][120][121].

7.2 Recommendation for Future Work

A free-space measurement technique using a monostatic system set up has been tested. Accuracy of the measurements could be further improved by: 1) Using a lens antenna with focused beam in order to minimise diffractions from the edges of the material under test. The material can therefore have a smaller size. 2) Refining the optimisation algorithm (The parameters of the deeper layers of a multi-layered material bear great error [26]). Moreover, for building materials with metallic bars inside such as reinforce concrete, extracting the effective dielectric parameters may be useful for the investigation of radio wave interactions with such materials.

The ray-tracing model has been successfully developed. A ray tree algorithm has been implemented to improve model efficiency. Projection of 3D structures into 2D planes simplifies the illumination zone test and subsequently the ray tracing procedure. However, redundant images are still possible in existence. This is because when a facet is projected as a line-segment, the lateral sides of the facet are not considered. Incorporating the information on the lateral sides of a facet will lead to more efficient ray tree with less redundancy.

Indoor channel simulations have demonstrated that the predicted path loss and RMS delay spreads are dependent on the values of the dielectric parameters of building materials. Using the free-space measurement system to obtain the dielectric parameters of the building materials and by incorporating this information into a database, the ray-tracing model can be used to extract channel parameters within any specific environment. The use of channel sounders to measure the channel parameters and compare with the simulation results is recommended. Such comparisons are believed to be very useful and can provide a quantitative insight into the accuracy of ray-tracing model.

In addition, recent studies have demonstrated the impressive theoretical capacity of wireless systems employing multiple antennas on both the Tx and Rx [111]. Designing these multiple-input multiple-output (MIMO) systems requires the channel information such as time of arrival (TOA), angle of arrival (AOA) and angle of departure (AOD) of each multipath component. The ray-tracing model developed in this research is useful to obtain the above channel information. A study on these channel characteristics using the model is also recommended.

Appendix A

Geometry of the Building and the Dielectric Parameters of Building Materials

In this appendix, Fig. A.1 ~ A.5 show the geometry of the building of Department of Electrical Engineer and Electronics, University of Liverpool. These geometry data are used as the input to the ray-tracing model. Table A.1 gives the corresponding constitutive parameters of the building structures.

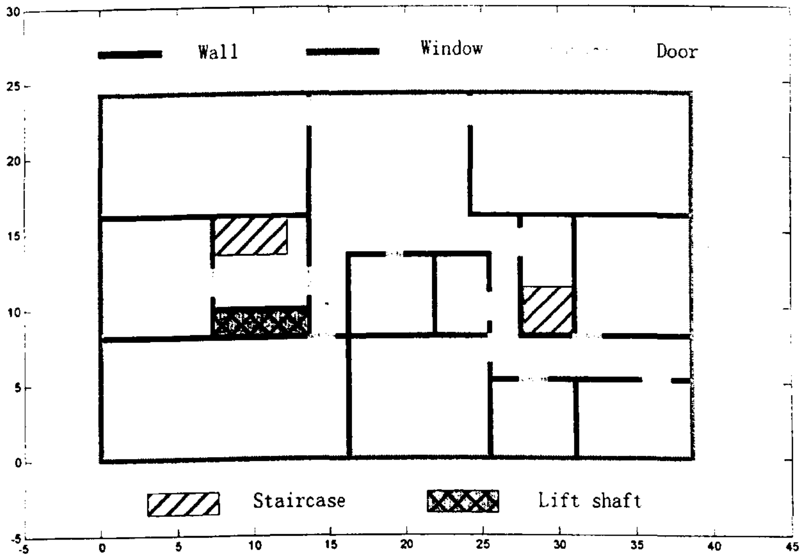

Fig A.1. Blueprint of the second floor of the Electrical Engineering Building.

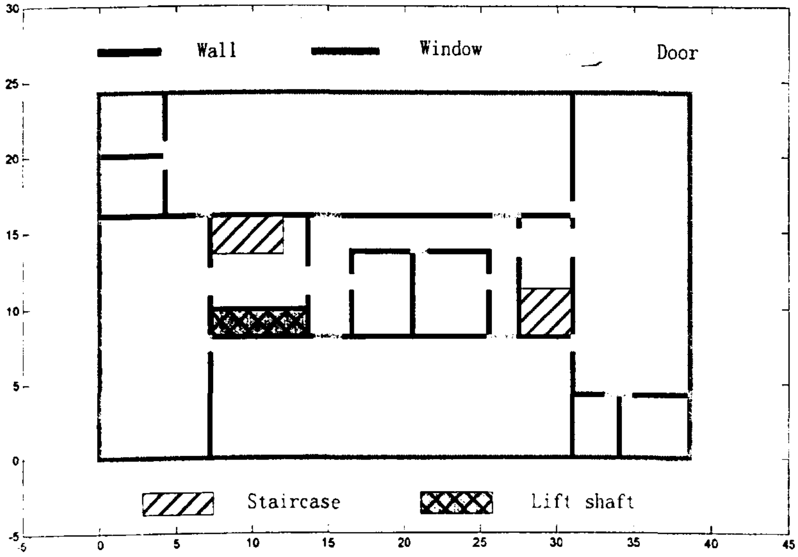

Fig A.2. Blueprint of the third floor of the Electrical Engineering Building.

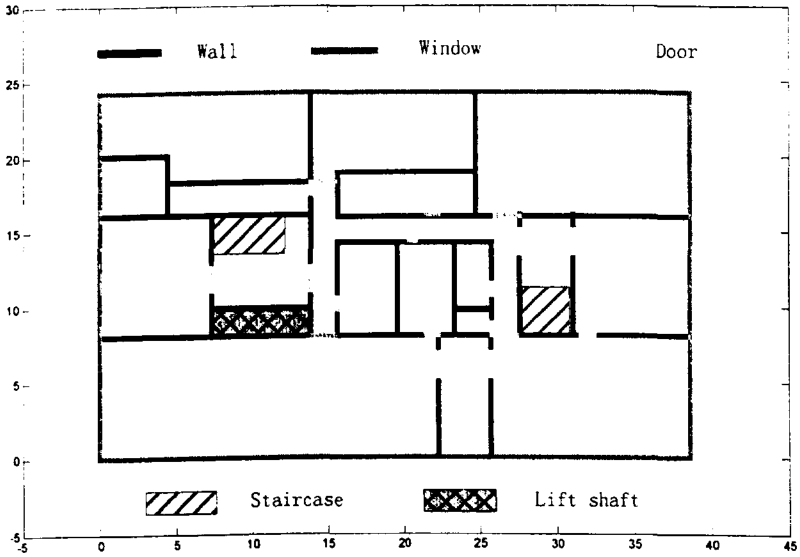

Fig A.3. Blueprint of the fourth floor of the Electrical Engineering Building.

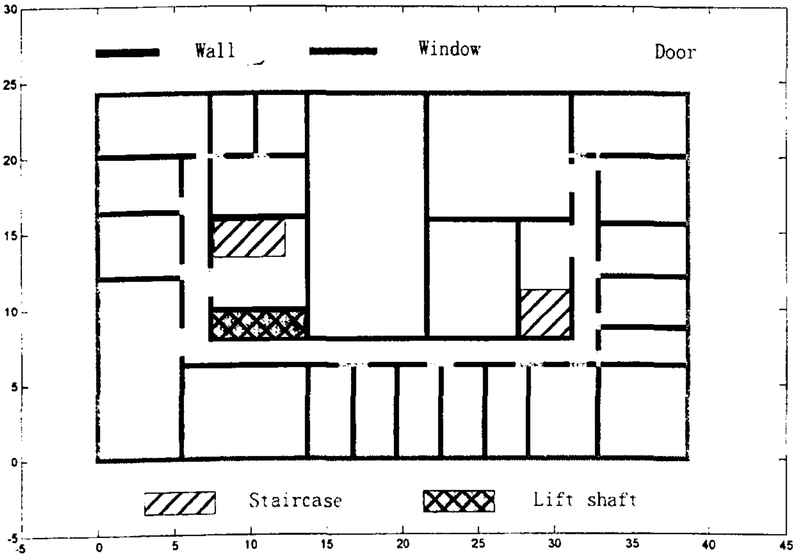

Fig A.4. Blueprint of the fifth floor of the Electrical Engineering Building.

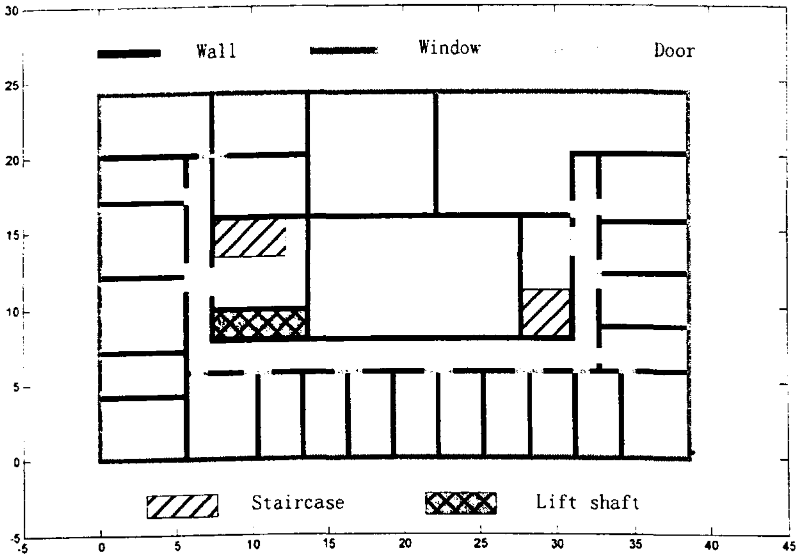

Fig A.5. Blueprint of the sixth floor of the Electrical Engineering Building.

Table A.1. Constitutive parameters of various building materials used in the database.

	Relative Permittivity ε_r	**Conductivity** σ **(s/m)**	**Thickness** d **(cm)**
External Wall	6.0	0.05	41.0
Internal Thick Wall	5.0	0.02	18.0
Internal Thin Wall	5.0	0.02	12.0
Ceiling and Floor	7.0	0.1	33.0
Wooden Door	3.0	0.001	4.5
Glass Window	3.5	0.001	2.5
Metallic Panel	1.0	1e+6	1.0

Appendix B

Derivation of the Reflection and Transmission Coefficients of a Multi-Layered Material

Consider a multi-layered medium with boundaries at $x = 0$, $-d_1$, $\ldots$ $-d_n$ as shown in Fig. B.1, and region t is semi-infinite medium. The permittivity and the permeability in each region l are denoted by $\hat{\varepsilon}_l$ and μ_l. For simplicity, we only consider the TE component. Solutions for the TM case can be obtained by duality with the replacements $\mathbf{E} \to \mathbf{H}$, $\mathbf{H} \to -\mathbf{E}$, and $\hat{\varepsilon} \leftrightarrow \mu$.

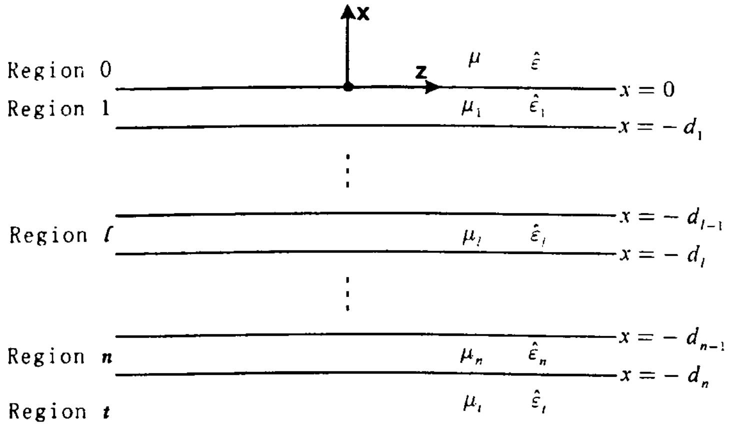

Figure B.1: Illustration of a multi-layered medium.

For TE wave whose electric field is perpendicular to x-z plane, the wave equations in region l are given by

$$E_{ly} = \left(A_l e^{jk_{lx}x} + B_l e^{-jk_{lx}x}\right) e^{jk_z z} \tag{B.1}$$

$$H_{lx} = -\frac{k_z}{\omega\mu_{lx}}\left(A_l e^{jk_{lx}x} + B_l e^{-jk_{lx}x}\right) e^{jk_z z} \tag{B.2}$$

$$H_{lz} = \frac{k_{lx}}{\omega\mu_{lz}}\left(A_l e^{jk_{lx}x} - B_l e^{-jk_{lx}x}\right) e^{jk_z z} \tag{B.3}$$

The wave amplitudes A_l and B_l are related to wave amplitudes in neighbouring regions by the boundary conditions. The boundary condition at $x = -d_l$ requires that E_y and H_z be continuous across the boundary, thus

$$A_l e^{-jk_{lx}d_l} + B_l e^{jk_{lx}d_l} = A_{l+1} e^{-jk_{(l+1)x}d_l} + B_{l+1} e^{jk_{(l+1)x}d_l} \tag{B.4}$$

$$\frac{k_{lx}}{\omega\mu_{lz}}\left(A_l e^{-jk_{lx}d_l} - B_l e^{jk_{lx}d_l}\right) = \frac{k_{(l+1)x}}{\omega\mu_{(l+1)z}}\left[A_{l+1} e^{-jk_{(l+1)x}d_l} - B_{l+1} e^{jk_{(l+1)x}d_l}\right] \tag{B.5}$$

A closed-form formula for the reflection coefficients (R) can be derived from Eqs. (B.4) and (B.5) as [67]:

$$A_l e^{-jk_{lx}d_l} = \frac{1}{2}\left[1 + \frac{\mu_{lz}k_{(l+1)x}}{\mu_{(l+1)z}k_{lx}}\right]\left[A_{l+1} e^{-jk_{(l+1)x}d_l} + R_{l(l+1)} B_{l+1} e^{jk_{(l+1)x}d_l}\right] \tag{B.6}$$

$$B_l e^{jk_{lx}d_l} = \frac{1}{2}\left[1 + \frac{\mu_{lz}k_{(l+1)x}}{\mu_{(l+1)z}k_{lx}}\right]\left[R_{l(l+1)} A_{l+1} e^{-jk_{(l+1)x}d_l} + B_{l+1} e^{jk_{(l+1)x}d_l}\right] \tag{B.7}$$

where

$$R_{l(l+1)} = \frac{1 - \mu_{lz}k_{(l+1)x} / \mu_{(l+1)z}k_{lx}}{1 + \mu_{lz}k_{(l+1)x} / \mu_{(l+1)z}k_{lx}} \tag{B.8}$$

is the reflection coefficient for TE waves in region l, caused by the boundary separating regions l and l+1. Forming the ratio of Eq. (B.6) to (B.7) leads to

$$\frac{A_l}{B_l}e^{-j2k_{lx}d_l} = \frac{1}{R_{l(l+1)}} + \frac{\left[1-\left(1/R_{l(l+1)}^2\right)\right]e^{-j2k_{(l+1)x}(d_{l+1}-d_l)}}{\left[1/R_{l(l+1)}\right]e^{-j2k_{(l+1)x}(d_{l+1}-d_l)} + \left(A_{l+1}/B_{l+1}\right)e^{-j2k_{(l+1)x}d_{l+1}}} \quad \text{(B.9)}$$

Eq. (B.9) express $\left(A_l/B_l\right)e^{-j2k_{lx}d_l}$ in terms of $\left(A_{l+1}/B_{l+1}\right)e^{-j2k_{(l+1)x}d_{l+1}}$ which can in turn be expressed by $\left(A_{l+2}/B_{l-2}\right)e^{-j2k_{(l+2)x}d_{l+2}}$, and so on until the transmitted region t, where $A_t/B_t = 0$, is reached. For medium illustrated in Fig. C.1, its reflection coefficient is derived using backward iteration process indicated in Eq. (B.9). Starting from the region n, the reflection coefficient attributable to the multi-layered medium, $R = A_0/B_0$, is obtained by n-iteration calculation of Eq. (B.9). This is a closed-form solution for the reflection coefficient expressed in continuous fractions.

For the calculation of transmission coefficient (T) for a multi-layered medium, Eqs. (B.6) and (B.7) are firstly expressed in a matrix form:

$$\begin{bmatrix} A_l e^{-jk_{lx}d_l} \\ B_l e^{jk_{lx}d_l} \end{bmatrix} = \bar{\boldsymbol{U}}_{l(l-1)} \begin{bmatrix} A_{l+1} e^{-jk_{(l+1)x}d_{l+1}} \\ B_{l+1} e^{jk_{(l+1)x}d_{l+1}} \end{bmatrix} \quad \text{(B.10)}$$

where $\bar{\boldsymbol{U}}_{l(l+1)}$ is a 2×2 matrix and called the backward propagation matrix, given by

$$\bar{\boldsymbol{U}}_{l(l+1)} = \frac{1}{2}\left(1+\frac{\mu_{lz}k_{(l+1)x}}{\mu_{(l+1)z}k_{lx}}\right)\begin{bmatrix} e^{jk_{(l+1)x}(d_{l+1}-d_l)} & R_{l(l+1)}e^{-jk_{(l+1)x}(d_{l+1}-d_l)} \\ R_{l(l+1)}e^{jk_{(l+1)x}(d_{l+1}-d_l)} & e^{-jk_{(l+1)x}(d_{l+1}-d_l)} \end{bmatrix} \quad \text{(B.11)}$$

It is noted that in the region t, d_t is not a physical parameter and we set $d_t = 0$. The backward propagation matrix for the multi-layered medium can be expressed in the form of the multiplication of each individual matrix between neighbouring regions as

$$\bar{\boldsymbol{U}} = \bar{\boldsymbol{U}}_{01}\cdot\bar{\boldsymbol{U}}_{12}\cdots\bar{\boldsymbol{U}}_{l(l+1)}\cdots\bar{\boldsymbol{U}}_{nt} \quad \text{(B.12)}$$

Incorporating (B.12), Eq. (B.10) can be modified to express the reflection and transmission coefficients for the multi-layered medium as

$$\begin{bmatrix} R \\ 1 \end{bmatrix} = \bar{U} \begin{bmatrix} 0 \\ T \end{bmatrix} = \begin{bmatrix} U_{11} & U_{12} \\ U_{21} & U_{22} \end{bmatrix} \begin{bmatrix} 0 \\ T \end{bmatrix} \tag{B.13}$$

from which the transmission coefficient attributable to the multi-layered medium is calculated by $T = 1/U_{22}$.

Indoor structures are, in some cases, assumed as single-layered material surrounded by free space medium. In this case, medium in region t illustrated in Fig. C.1 is the same as in region 0, and the reflection and transmission coefficients derived above for TE waves can be obtained as

$$R = \frac{R_{01}\left(1 - e^{j2k_{1z}d_1}\right)}{1 - R_{01}^2 e^{j2k_{1z}d_1}} \tag{B.14}$$

$$T = \frac{4e^{j(k_{1z} - k_{0z})d_1}}{\left(1 + k_{1x}/k_{0x}\right)\left(1 + k_{0x}/k_{1x}\right)\left(1 - R_{01}^2 e^{j2k_{1z}d_1}\right)} \tag{B.15}$$

where R_{01} is the reflection coefficient obtained from Eqs. (4.18) and (4.19). After manipulation, Eqs. (B.14) and (B.15) can be found identical to the asymptotic solution [86] which is commonly used for high frequency scattering by a single layered dielectric slab. However, for multi-layered medium, asymptotic solution becomes unmanageable and solution based on general electromagnetic wave scattering should be resorted to.

In view of duality, with the replacement $\mu \longrightarrow \hat{\varepsilon}$ in Eq. (B.8), the reflection coefficient derived from Eq. (B.9) and the transmission coefficient from Eq. (B.13) are equally applicable to TM waves.

Appendix C

Derivation of the Diffraction Coefficients of an Edge

The three-dimensional UTD diffraction coefficients are given by

$$D_{s,h} = D_1 + D_2 + R_{s,h}\left(D_3 + D_4\right) \tag{C.1}$$

where $D_{s,h}$ denotes the soft and hard diffraction coefficients, respectively. $R_{s,h}$ denotes the soft (perpendicular) and hard (parallel) reflection coefficients. We see that D_1 accounts for the diffracted field that compensates for the discontinuity in the GO field when o-face is shadowed; D_2, when the n-face is shadowed; D_3, when there is a reflection from the n-face; and D_4, when there is reflection from the o-face. These components of the diffraction coefficient are given by

$$D_1 = \frac{-e^{-j\pi/4}}{2n\sqrt{2\pi k}\sin\beta_0}\cot\left[\frac{\pi+(\phi-\phi')}{2n}\right]F\left[kLa^{+}(\phi-\phi')\right] \tag{C.2}$$

$$D_2 = \frac{-e^{-j\pi/4}}{2n\sqrt{2\pi k}\sin\beta_0}\cot\left[\frac{\pi-(\phi-\phi')}{2n}\right]F\left[kLa^{-}(\phi-\phi')\right] \tag{C.3}$$

$$D_3 = \frac{-e^{-j\pi/4}}{2n\sqrt{2\pi k}\sin\beta_0}\cot\left[\frac{\pi+(\phi+\phi')}{2n}\right]F\left[kLa^{+}(\phi+\phi')\right] \tag{C.4}$$

$$D_4 = \frac{-e^{-j\pi/4}}{2n\sqrt{2\pi k}\sin\beta_0}\cot\left[\frac{\pi-(\phi+\phi')}{2n}\right]F\left[kLa^{-}(\phi+\phi')\right] \tag{C.5}$$

where $F(x)$ is the transition function, used in UTD formulation to solve the problem in GTD, which is given by

$$F(x) = 2j\sqrt{x}e^{jx}\int_{\sqrt{x}}^{\infty} e^{-ju^2}du \tag{C.6}$$

The integral part of the transition function resembles a Fresnel integral and is calculated by numerical solutions as discussed in [74]; k is the wave number and

$$L = \frac{ss^{'}\sin^2\beta_0^{'}}{s+s^{'}} \tag{C.7}$$

The functions $a^{\pm}$ are defined as

$$a^{\pm}(\phi \pm \phi^{'}) = 2\cos^2\left[\frac{2n\pi N^{\pm} - (\phi \pm \phi^{'})}{2}\right] \tag{C.8}$$

and $N^{\pm}$ are integers that most nearly satisfy the following equations:

$$2n\pi N^{+} - (\phi \pm \phi^{'}) = \pi \tag{C.9}$$

$$2n\pi N^{-} - (\phi \pm \phi^{'}) = -\pi \tag{C.10}$$

Note that a^{+} and N^{+} are associated with the n-face and that a^{-} and N^{-} are associated with the o-face. In the original work by Keller, Kouyoumjian and Pathak, they all dealt with the diffraction problems at an edge in a perfectly conducting surface, therefore $R_{s,h}$ in Eq. (C.1) are ± 1. These UTD equations were later modified by Luebbers [87] to include reflection coefficients that modify the face reflection terms in the UTD equations as a heuristic approach to calculate fields around finite conductivity or dielectric wedges. When the surfaces of the wedge are non-perfectly conducting, $R_{s,h}$ refers to the reflection coefficients for soft or hard polarisation for the o-face with incident angle $\phi^{'}$, and for the n-face with incident angle $(n\pi - \phi)$, respectively.

Appendix D

The Software Package

During the research work, our 3D ray-tracing channel prediction model has been developed using Visual C++ (version 5.0) [119], a commercial window-based software capable of designing complex software systems. The algorithm is based on Geometric Optics (GO) and the Uniform Theory of Diffraction (UTD), in combination with the image method [53][54][118]. In this appendix, the hierarchy charts of the programme codes are given. Section D.1 describes the ray-tracing codes with traditional ray-searching method. Computation of the electromagnetic fields at each Tx-Rx configuration and the calculation of channel parameters are dealt with. Section D.2 describes the acceleration procedure implemented to enhance the computation efficiency of the traditional ray-searching method.

D.1 Ray-Tracing Programme

As described in Chapter 4, the ray-tracing programme takes input data of the geometrical and electromagnetic parameters of the scenario, as well as the locations and radiation patterns of the Tx and Rx. The input geometrical data of a facet are given in terms of its corner coordinate **W**, the normal vector $\hat{\mathbf{n}}$, and the **U** and **V** vectors, which are illustrated in Fig.

4.1. The input electromagnetic data of a facet are given in terms of the number of layers of the material (generally 1 or 2) and the constitutive parameters of each layer. Given the Tx and Rx locations, the ray-tracing programme starts to trace each ray originating from the Tx and reaching the Rx, and then computes the corresponding received field strength at the Rx. By combining the effects of all possible rays between the Tx and Rx, the channel parameters such as path loss and RMS delay spread can therefore be calculated.

The following diagram 'Ray-Tracing Structure' shows the hierarchical levels of the ray-tracing programme, in which four levels are under the top level 'Main'. The 'Main' diagram is essentially the main body of the ray-tracing codes, from which the channel parameters are calculated. The first-level subroutines are for the computation of the electromagnetic fields received by the Rx due to different propagation mechanisms. The second-level subroutines are for the computation of the electromagnetic fields of individual rays between the Tx and Rx. The ray-searching and the field computation procedures are included in this level. The third- and fourth-level subroutines are for the computation of intersections between the rays and the environmental structures and the subsequent field strengths. Table D.1 gives the functions of individual procedures shown in the diagram.

Ray-Tracing Structure

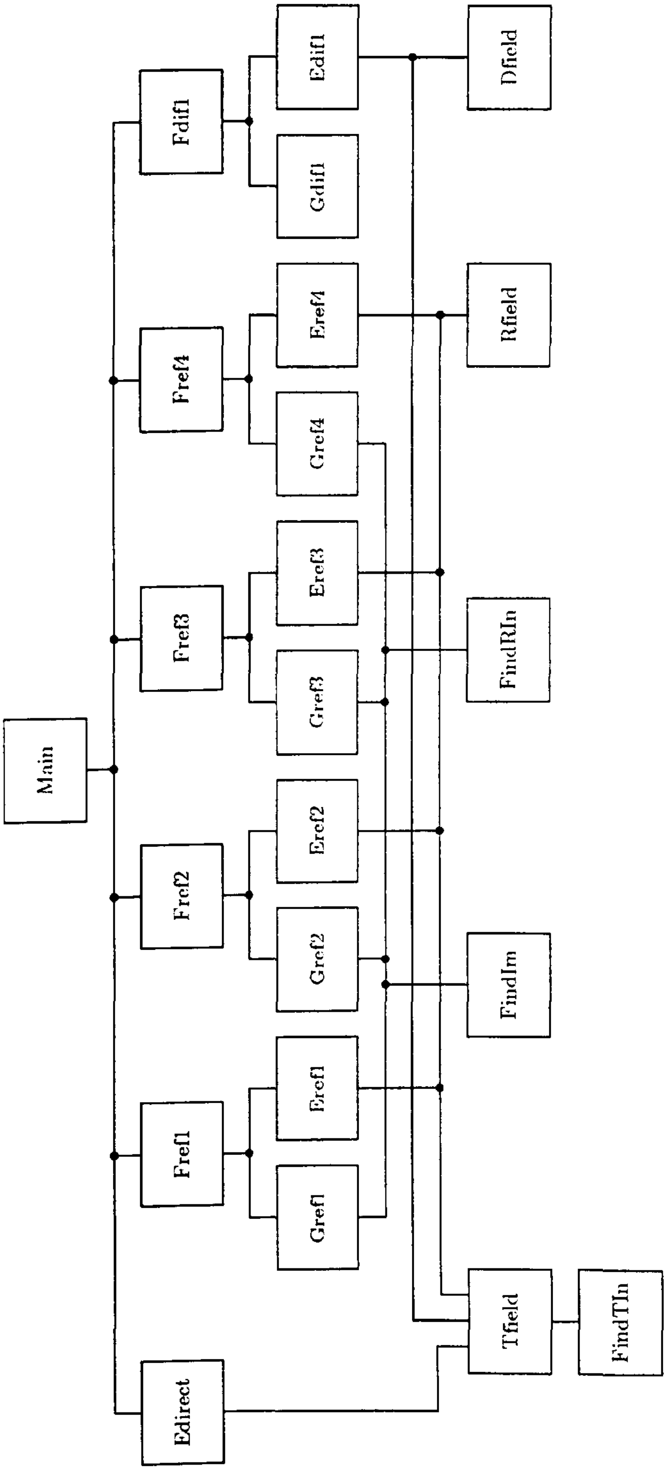

Table D.1: Functions of all subroutines in the diagram 'Ray-Tracing Structure'.

Name of subroutine	Function of subroutine
Main	Calculate the channel parameters of designated scenario
Edirect	Compute the direct field received by the Rx
Ffreq1	Compute fields of the 1st reflections
Ffreq2	Compute fields of the 2nd reflections
Ffreq3	Compute fields of the 3rd reflections
Ffreq4	Compute fields of the 4th reflections
Fdif1	Compute fields of the 1st diffractions
Gref1	Find the image and intersection for the 1st reflection
Gref2	Find the image and intersection for the 2nd reflection
Gref3	Find the image and intersection for the 3rd reflection
Gref4	Find the image and intersection for the 4th reflection
Gdif1	Find the image and intersection for the 1st diffraction
Eref1	Compute the 1st-order reflected fields
Eref2	Compute the 2nd-order reflected fields
Eref3	Compute the 3rd-order reflected fields
Eref4	Compute the 4th-order reflected fields
Edif1	Compute the 1st-order diffracted fields
FindIm	Find the image of a point with respect to a facet
FindRIn	Find the reflecting intersection on a facet
Tfield	Compute the transmitted field
Rfield	Compute the reflected field
Dfield	Compute the diffracted field on the 1st-order diffracting edge
FindTIn	Find the transmitting intersection on a facet

Main

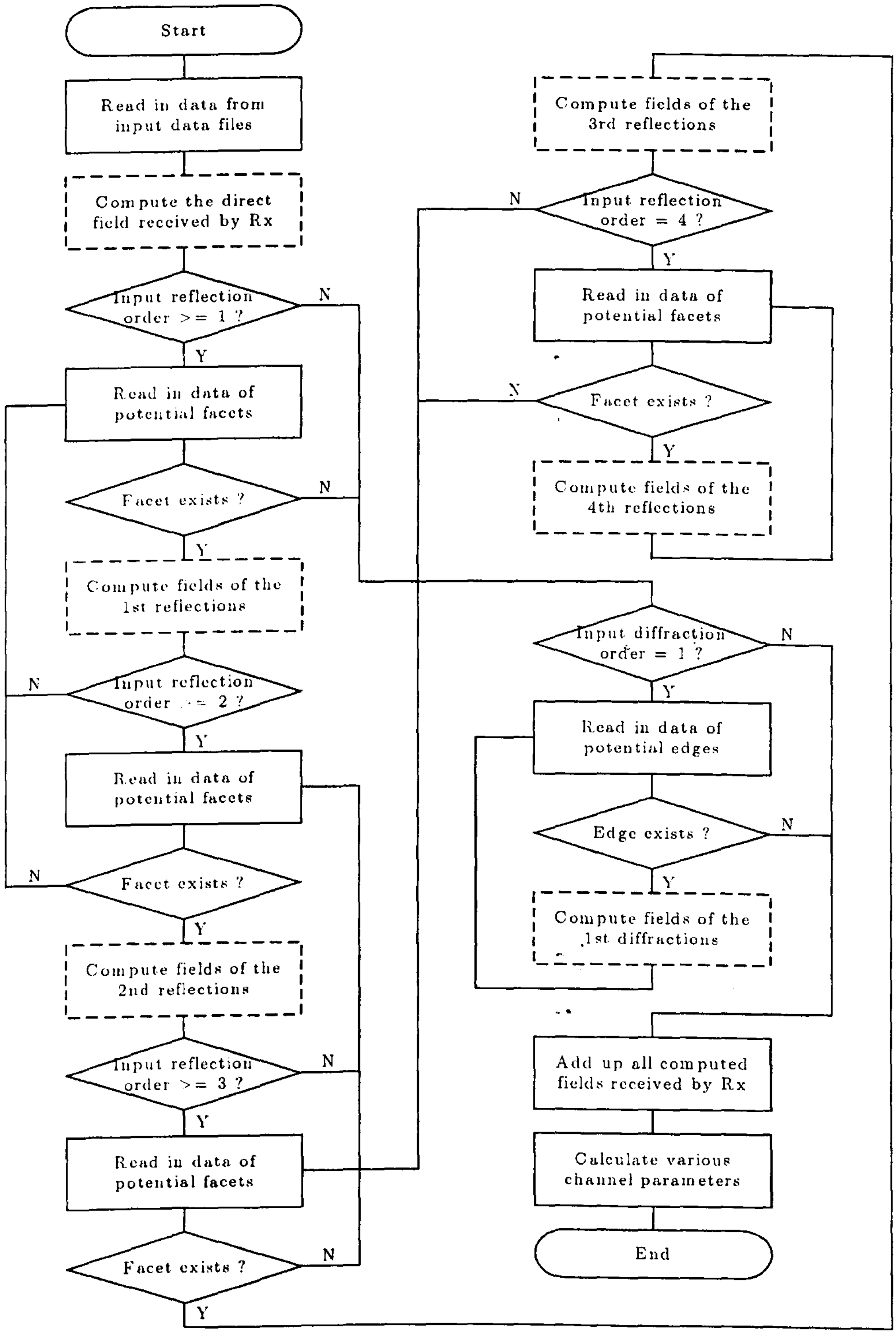
Start
Read in data from input data files
Compute the direct field received by Rx
Input reflection order >= 1 ?
Y
N
Read in data of potential facets
Facet exists ?
Y
N
Compute fields of the 1st reflections
Input reflection order >= 2 ?
Y
N
Read in data of potential facets
Facet exists ?
Y
N
Compute fields of the 2nd reflections
Input reflection order >= 3 ?
Y
N
Read in data of potential facets
Facet exists ?
Y
N
Compute fields of the 3rd reflections
Input reflection order = 4 ?
Y
N
Read in data of potential facets
Facet exists ?
Y
N
Compute fields of the 4th reflections
Input diffraction order = 1 ?
Y
N
Read in data of potential edges
Edge exists ?
Y
N
Compute fields of the 1st diffractions
Add up all computed fields received by Rx
Calculate various channel parameters
End

Edirect

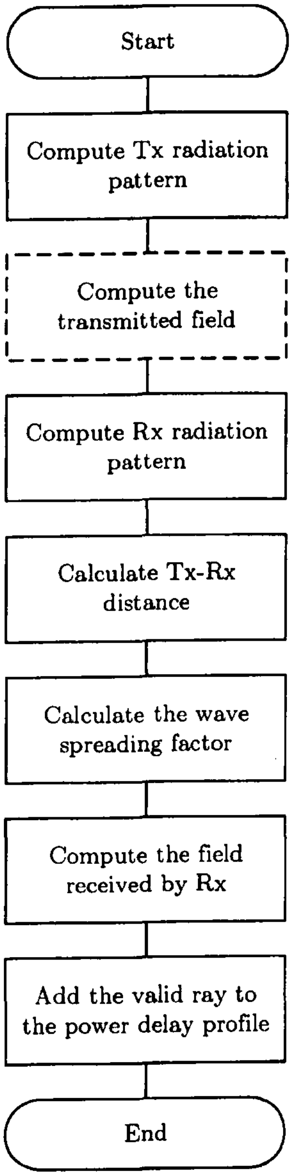

Frefl

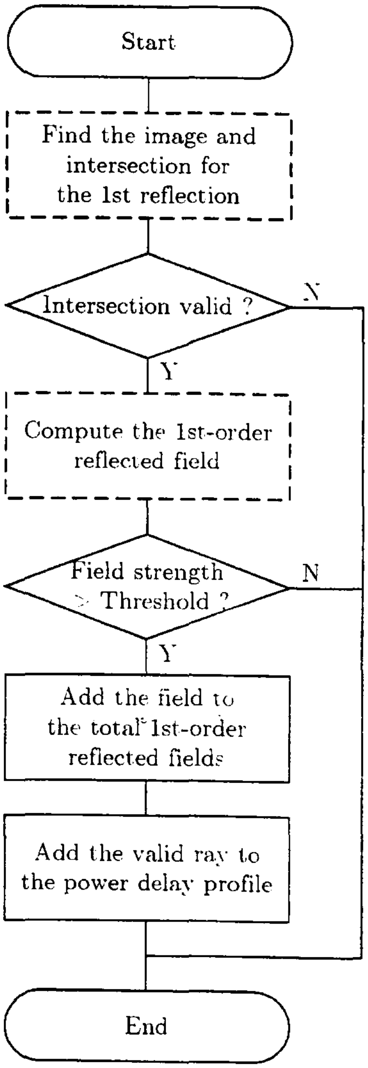

Fref2

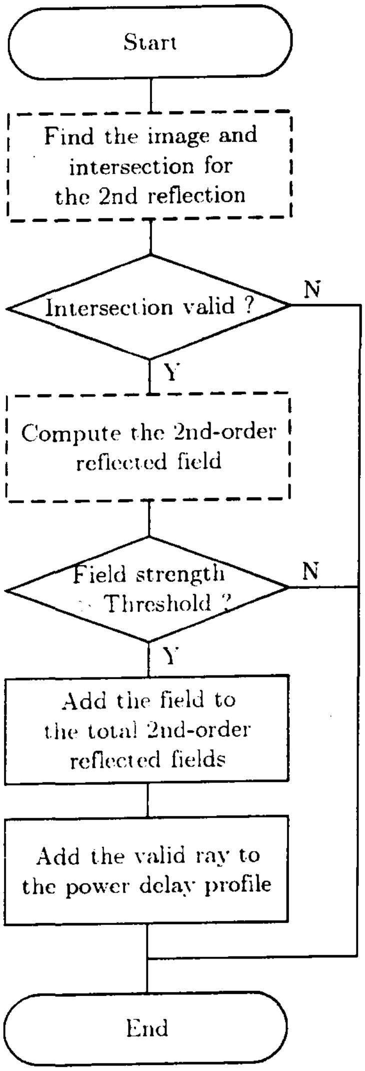
Start
Find the image and intersection for the 2nd reflection
Intersection valid ?
N
Y
Compute the 2nd-order reflected field
Field strength > Threshold ?
N
Y
Add the field to the total 2nd-order reflected fields
Add the valid ray to the power delay profile
End

Fref3

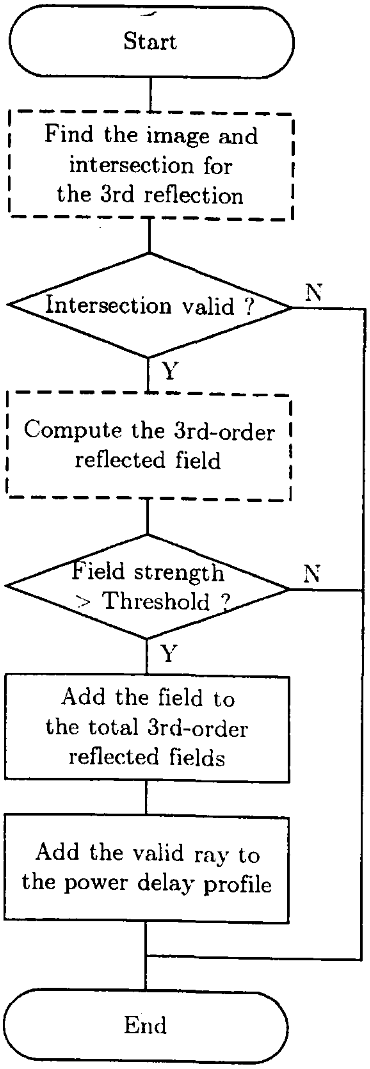
Start
Find the image and intersection for the 3rd reflection
Intersection valid ?
N
Y
Compute the 3rd-order reflected field
Field strength > Threshold ?
N
Y
Add the field to the total 3rd-order reflected fields
Add the valid ray to the power delay profile
End

Fref4

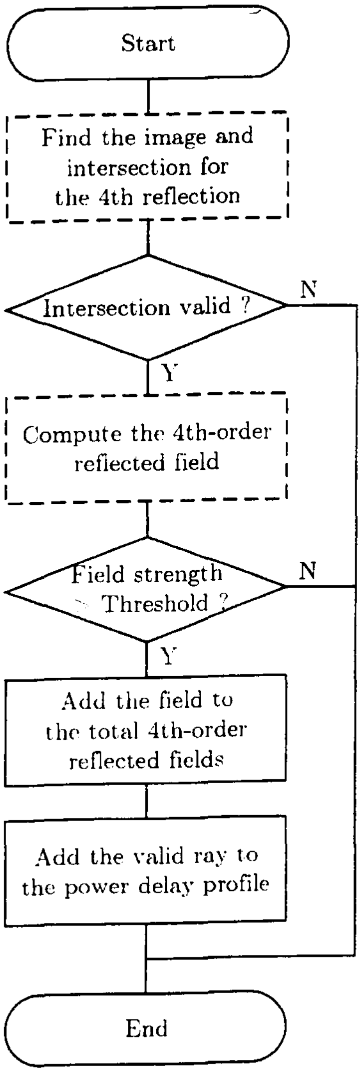
Start
Find the image and intersection for the 4th reflection
Intersection valid ?
N
Y
Compute the 4th-order reflected field
Field strength > Threshold ?
N
Y
Add the field to the total 4th-order reflected fields
Add the valid ray to the power delay profile
End

Fdif1

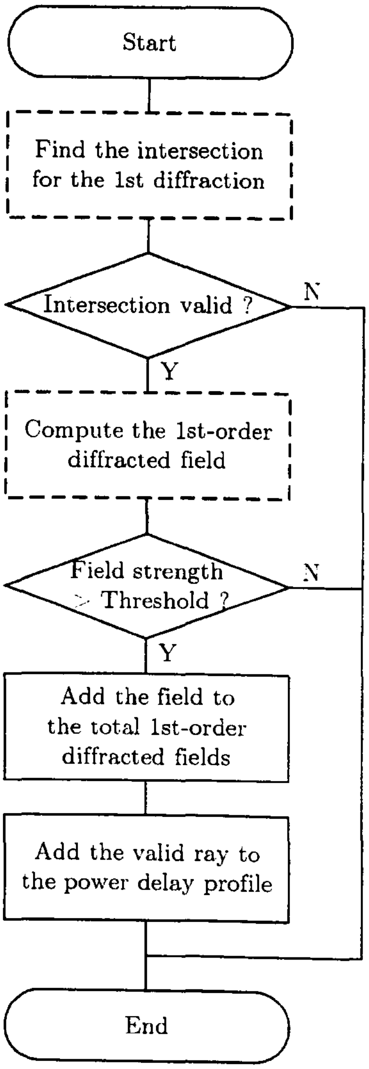
Start
Find the intersection for the 1st diffraction
Intersection valid ?
N
Y
Compute the 1st-order diffracted field
Field strength > Threshold ?
N
Y
Add the field to the total 1st-order diffracted fields
Add the valid ray to the power delay profile
End

Gref1

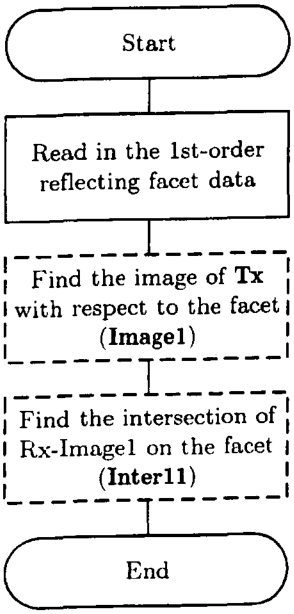
Start
Read in the 1st-order reflecting facet data
Find the image of **Tx** with respect to the facet (**Image1**)
Find the intersection of Rx-Image1 on the facet (**Inter11**)
End

Gref2

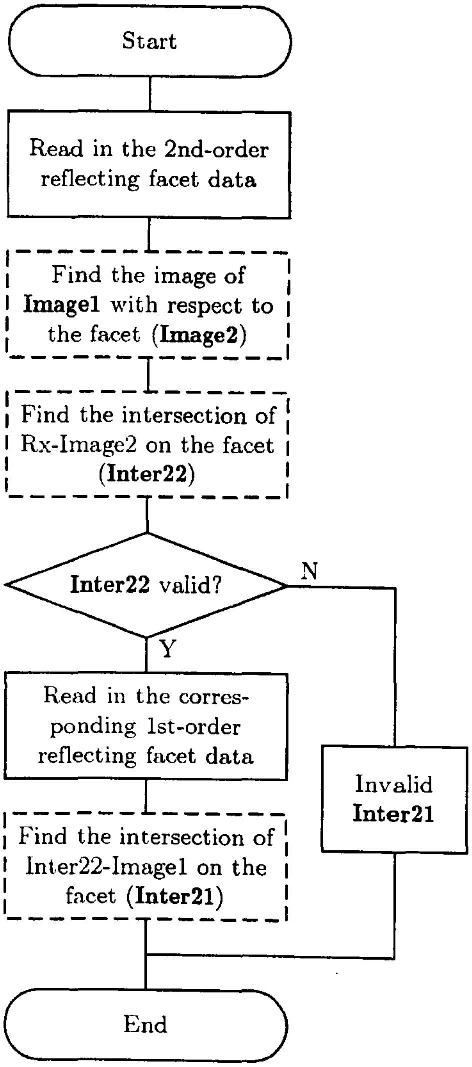
Start
Read in the 2nd-order reflecting facet data
Find the image of **Image1** with respect to the facet (**Image2**)
Find the intersection of Rx-Image2 on the facet (**Inter22**)
Inter22 valid?
N
Y
Read in the corresponding 1st-order reflecting facet data
Find the intersection of Inter22-Image1 on the facet (**Inter21**)
Invalid **Inter21**
End

Gref3

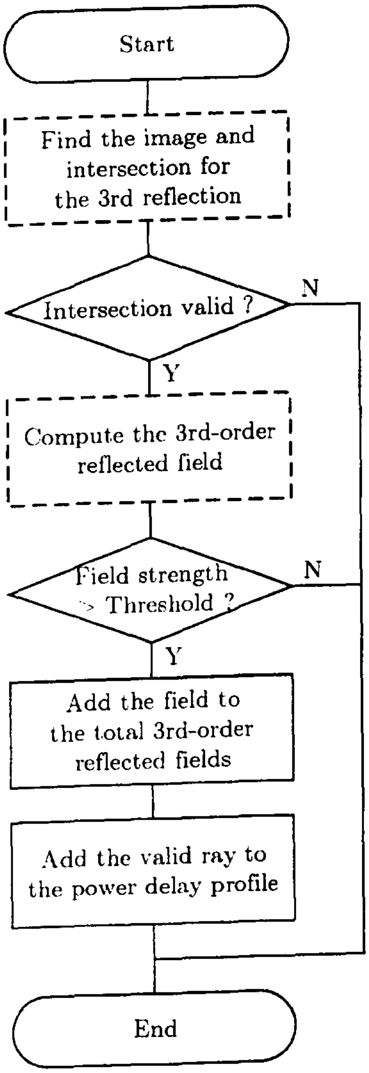
Start
Find the image and intersection for the 3rd reflection
Intersection valid ?
N
Y
Compute the 3rd-order reflected field
Field strength > Threshold ?
N
Y
Add the field to the total 3rd-order reflected fields
Add the valid ray to the power delay profile
End

Gref4

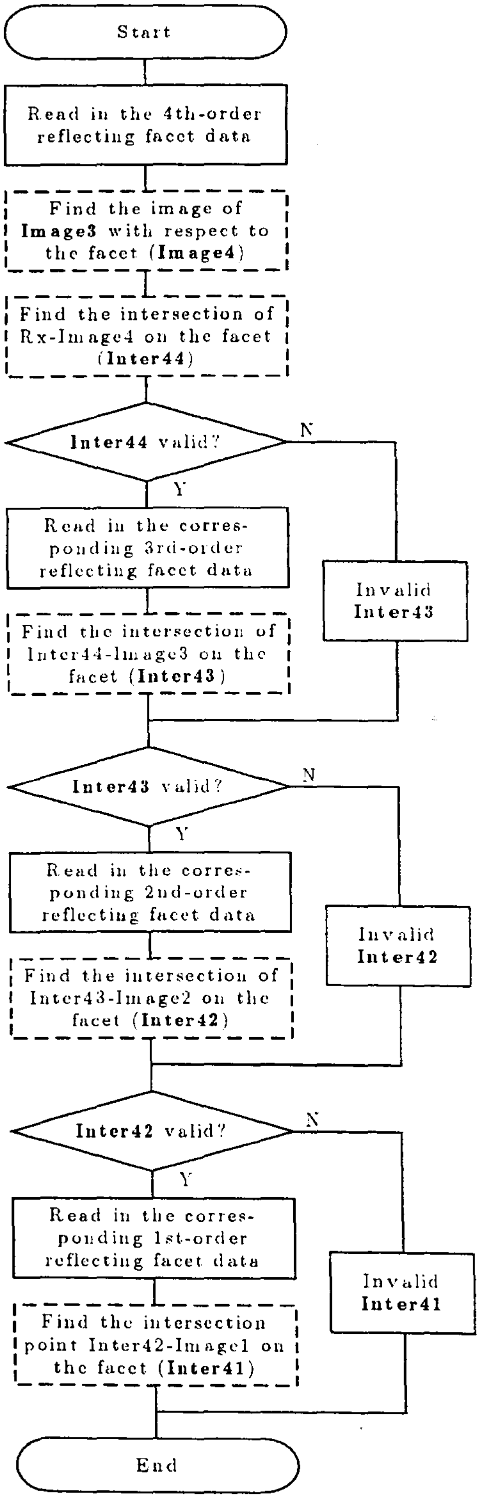
Start
Read in the 4th-order reflecting facet data
Find the image of Image3 with respect to the facet (Image4)
Find the intersection of Rx-Image4 on the facet (Inter44)
Inter44 valid?
N
Y
Read in the corresponding 3rd-order reflecting facet data
Find the intersection of Inter44-Image3 on the facet (Inter43)
Invalid Inter43
Inter43 valid?
N
Y
Read in the corresponding 2nd-order reflecting facet data
Find the intersection of Inter43-Image2 on the facet (Inter42)
Invalid Inter42
Inter42 valid?
N
Y
Read in the corresponding 1st-order reflecting facet data
Find the intersection point Inter42-Image1 on the facet (Inter41)
Invalid Inter41
End

Gdifl

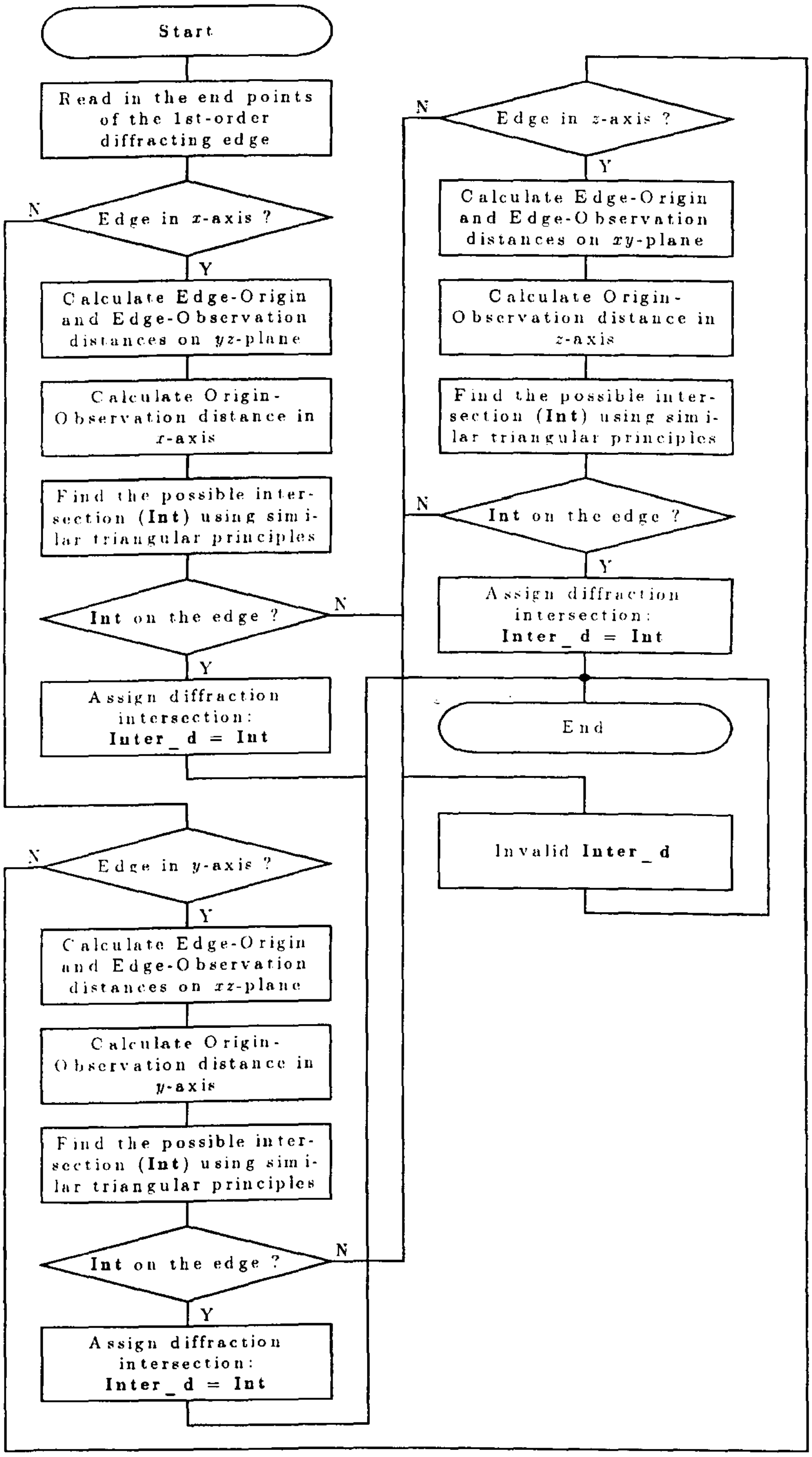
Start
Read in the end points of the 1st-order diffracting edge
Edge in x-axis ?
N
Y
Calculate Edge-Origin and Edge-Observation distances on yz-plane
Calculate Origin-Observation distance in x-axis
Find the possible intersection (**Int**) using similar triangular principles
Int on the edge ?
N
Y
Assign diffraction intersection: **Inter_d = Int**
Edge in y-axis ?
N
Y
Calculate Edge-Origin and Edge-Observation distances on xz-plane
Calculate Origin-Observation distance in y-axis
Find the possible intersection (**Int**) using similar triangular principles
Int on the edge ?
N
Y
Assign diffraction intersection: **Inter_d = Int**
Edge in z-axis ?
N
Y
Calculate Edge-Origin and Edge-Observation distances on xy-plane
Calculate Origin-Observation distance in z-axis
Find the possible intersection (**Int**) using similar triangular principles
Int on the edge ?
N
Y
Assign diffraction intersection: **Inter_d = Int**
End
Invalid **Inter_d**

Eref1

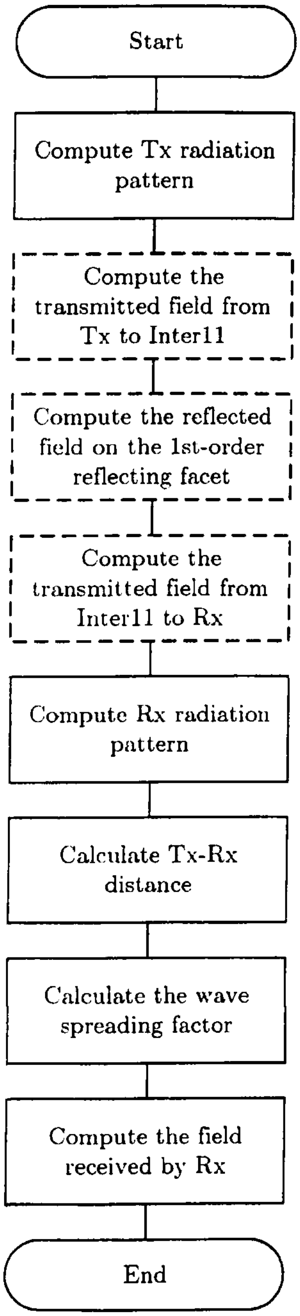
Start
Compute Tx radiation pattern
Compute the transmitted field from Tx to Inter11
Compute the reflected field on the 1st-order reflecting facet
Compute the transmitted field from Inter11 to Rx
Compute Rx radiation pattern
Calculate Tx-Rx distance
Calculate the wave spreading factor
Compute the field received by Rx
End

Eref2

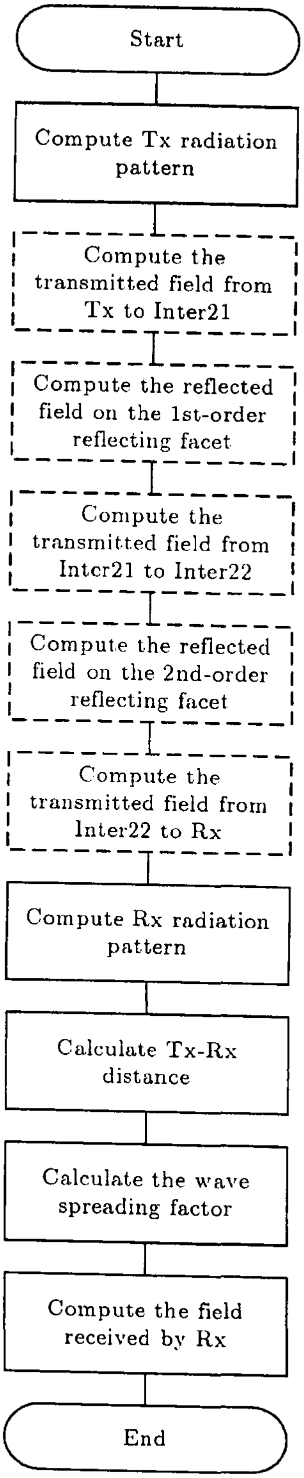
Start
Compute Tx radiation pattern
Compute the transmitted field from Tx to Inter21
Compute the reflected field on the 1st-order reflecting facet
Compute the transmitted field from Inter21 to Inter22
Compute the reflected field on the 2nd-order reflecting facet
Compute the transmitted field from Inter22 to Rx
Compute Rx radiation pattern
Calculate Tx-Rx distance
Calculate the wave spreading factor
Compute the field received by Rx
End

Eref3

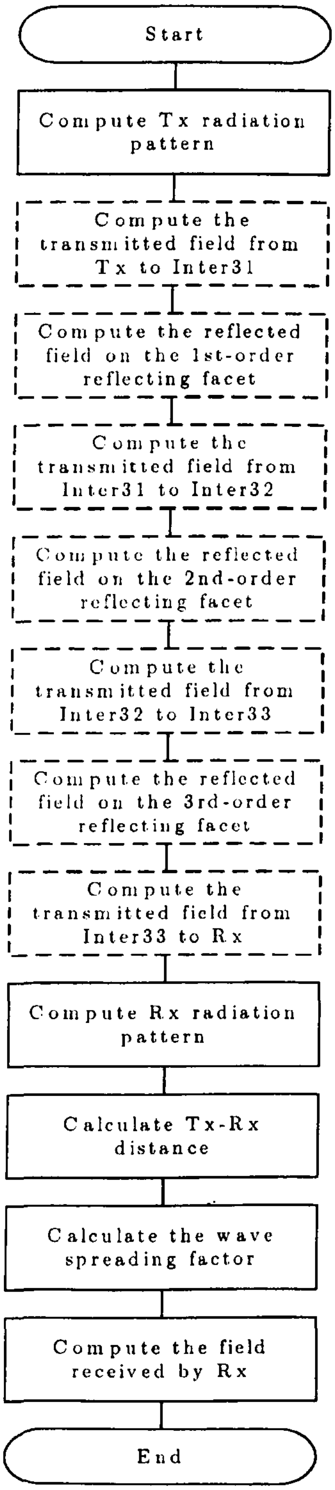
Start
Compute Tx radiation pattern
Compute the transmitted field from Tx to Inter31
Compute the reflected field on the 1st-order reflecting facet
Compute the transmitted field from Inter31 to Inter32
Compute the reflected field on the 2nd-order reflecting facet
Compute the transmitted field from Inter32 to Inter33
Compute the reflected field on the 3rd-order reflecting facet
Compute the transmitted field from Inter33 to Rx
Compute Rx radiation pattern
Calculate Tx-Rx distance
Calculate the wave spreading factor
Compute the field received by Rx
End

Edif1

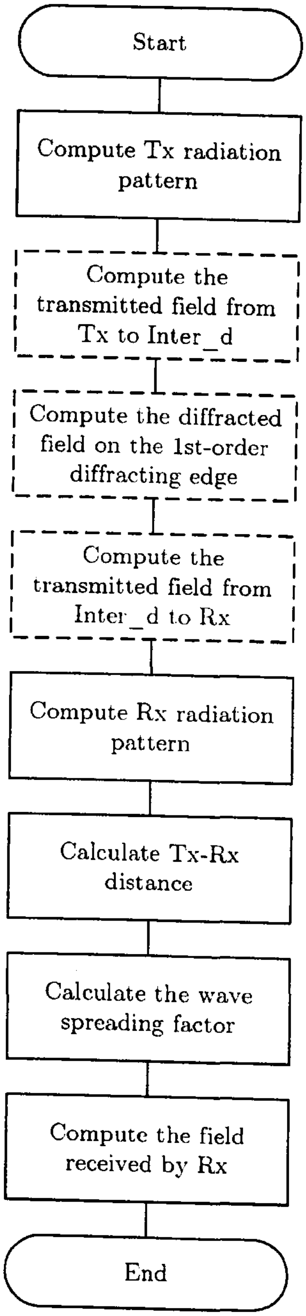
Start
Compute Tx radiation pattern
Compute the transmitted field from Tx to Inter_d
Compute the diffracted field on the 1st-order diffracting edge
Compute the transmitted field from Inter_d to Rx
Compute Rx radiation pattern
Calculate Tx-Rx distance
Calculate the wave spreading factor
Compute the field received by Rx
End

Eref4

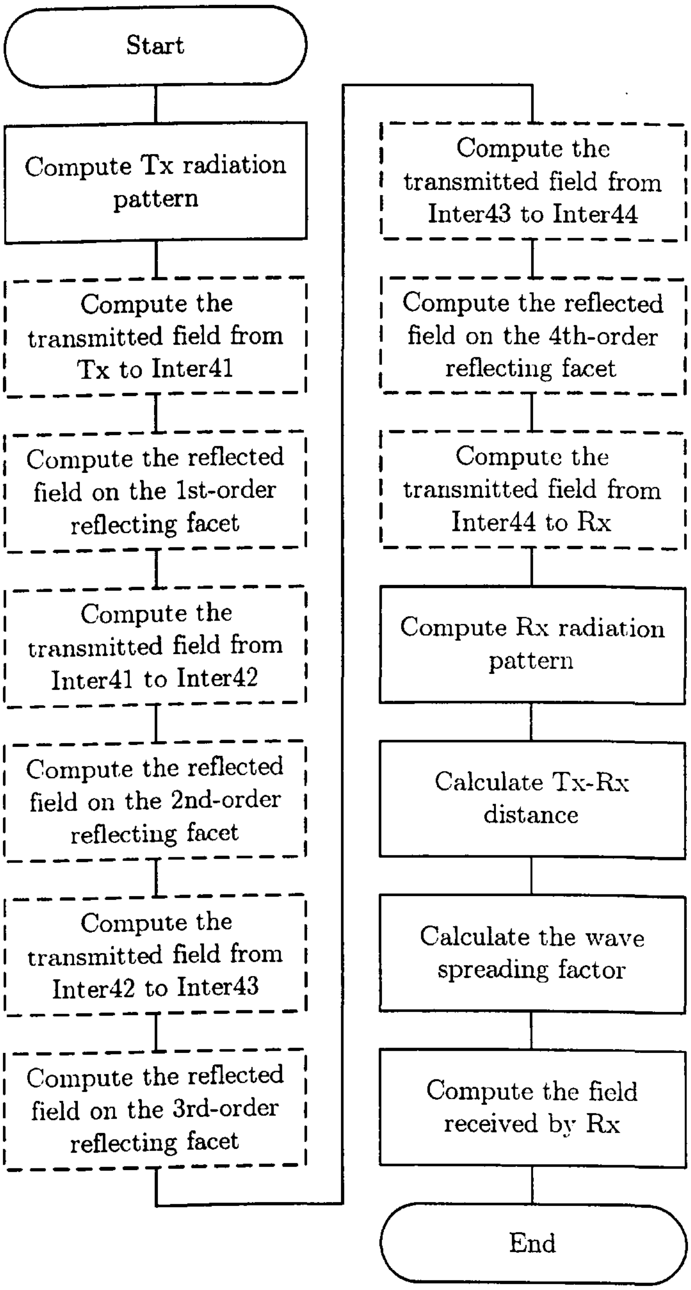
Start
Compute Tx radiation pattern
Compute the transmitted field from Tx to Inter41
Compute the reflected field on the 1st-order reflecting facet
Compute the transmitted field from Inter41 to Inter42
Compute the reflected field on the 2nd-order reflecting facet
Compute the transmitted field from Inter42 to Inter43
Compute the reflected field on the 3rd-order reflecting facet
Compute the transmitted field from Inter43 to Inter44
Compute the reflected field on the 4th-order reflecting facet
Compute the transmitted field from Inter44 to Rx
Compute Rx radiation pattern
Calculate Tx-Rx distance
Calculate the wave spreading factor
Compute the field received by Rx
End

FindIm

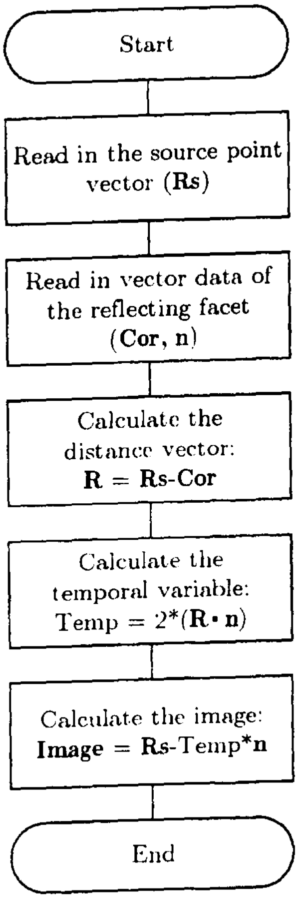

FindRIn

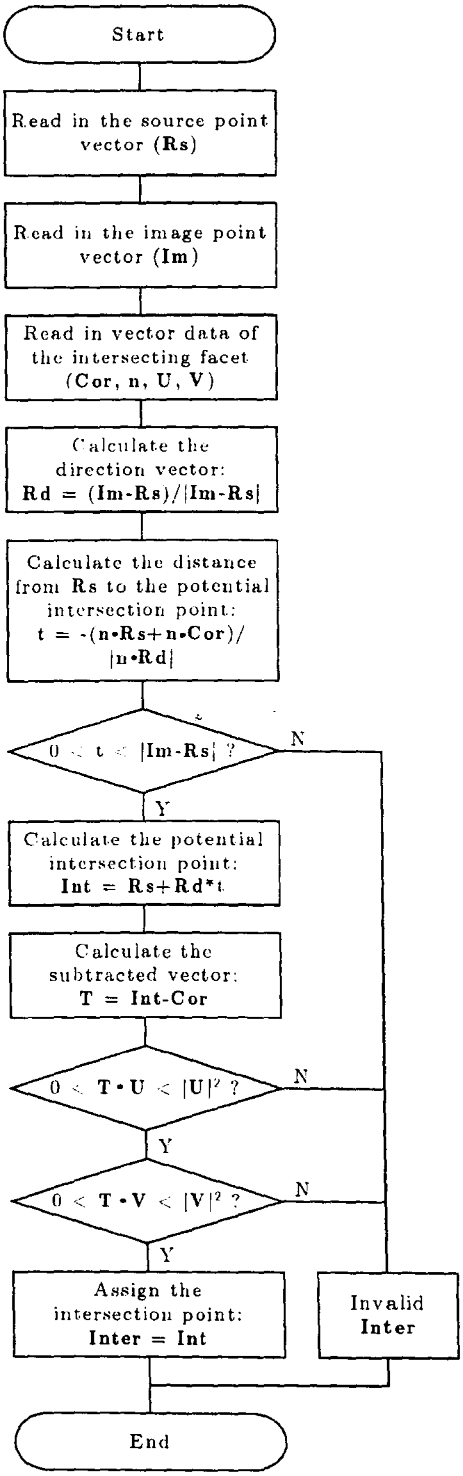

Tfield

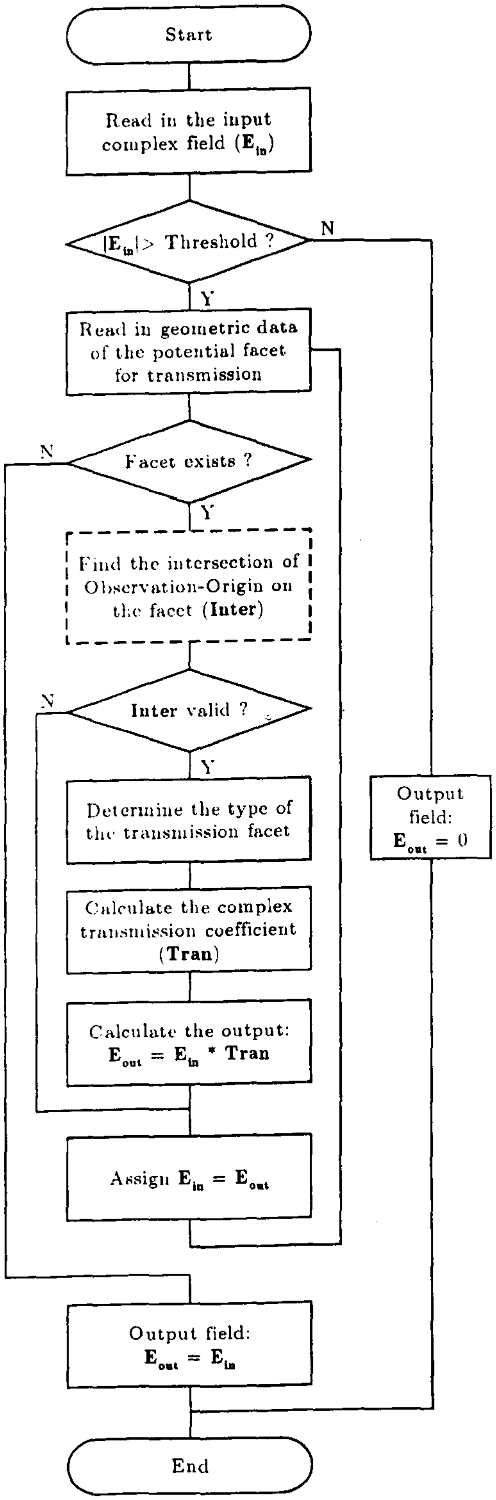

Rfield

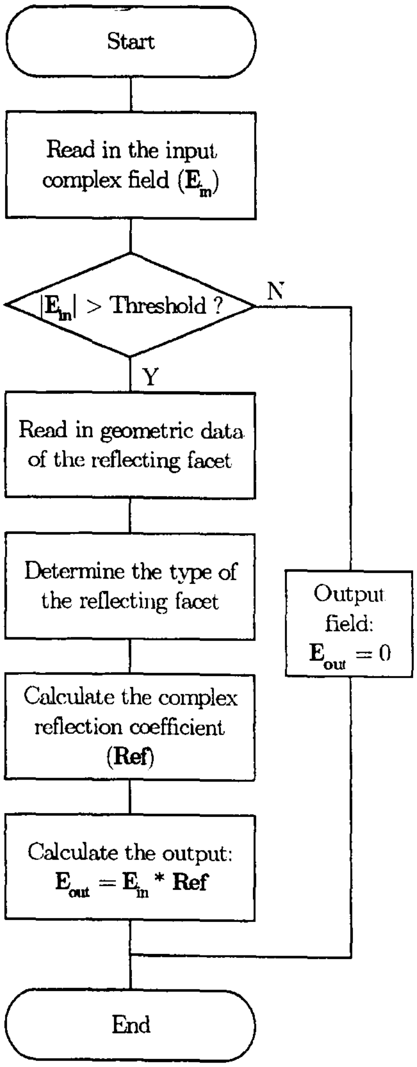

Dfield

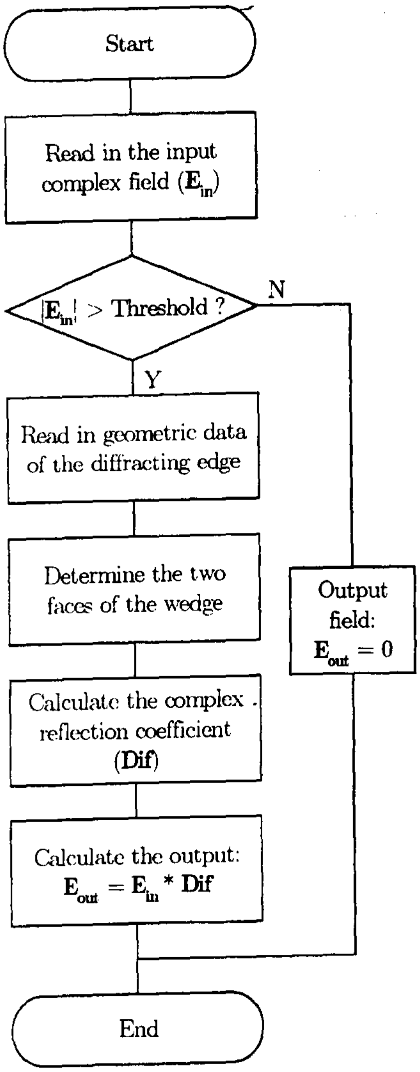

FindTIn

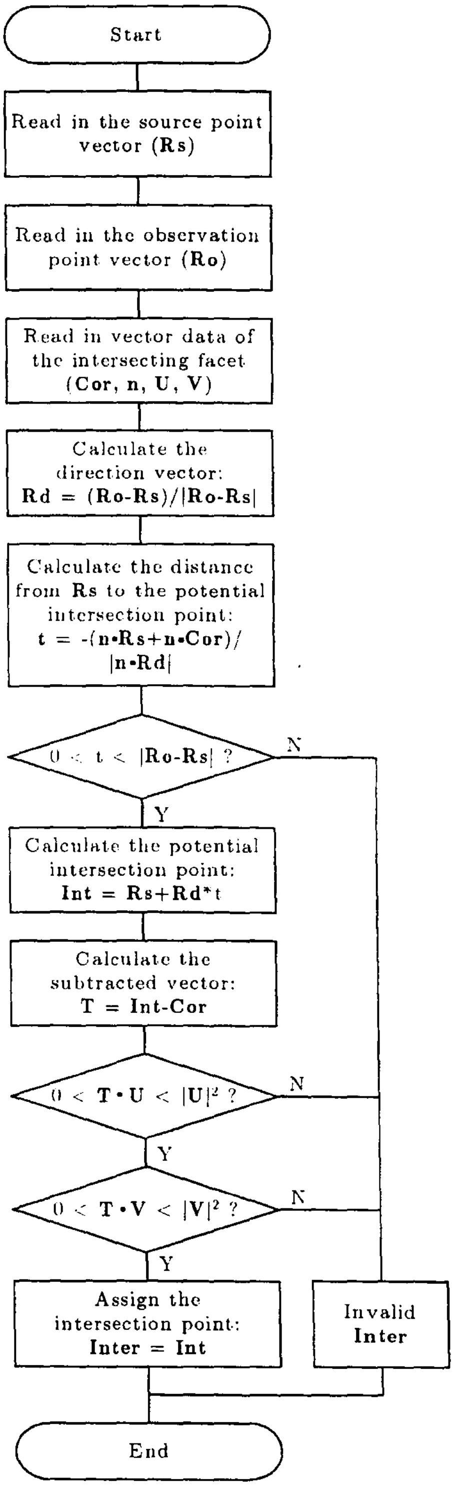

D.2 Ray-Tree Programme

As described in Section 4.4 of Chapter 4, a ray-tree algorithm based on the illumination zone concept and the projection of 3D scenario onto 2D plane has been developed to accelerate the ray-searching process in the ray-tracing method.

The following diagram 'Ray-Tree Structure' shows the hierarchical levels of the ray-tree programme. The 'Main' diagram is for the generation of the ray-tree with the order of reflections specified by user. Up to four reflections are considered in the ray-tree. The first level-subroutines are for the generation of ray-tree for each ordered reflection considered. 'FindIlluZone' is the essential part of the ray-tree codes, which is to find the illumination zone of the next-ordered reflecting facets. Projection of 3D facets onto 2D plane ('ProjectFacet') is incorporated to simplify the finding of illumination zones of a 3D facet. Table D.2 gives the functions of individual procedures shown in the 'Main' diagram. With the implementation of the ray-tree algorithm, the ray-searching process can be accelerated to a great extent, which helps to enhance the computation efficiency of the ray-tracing method.

Ray-Tree Structure

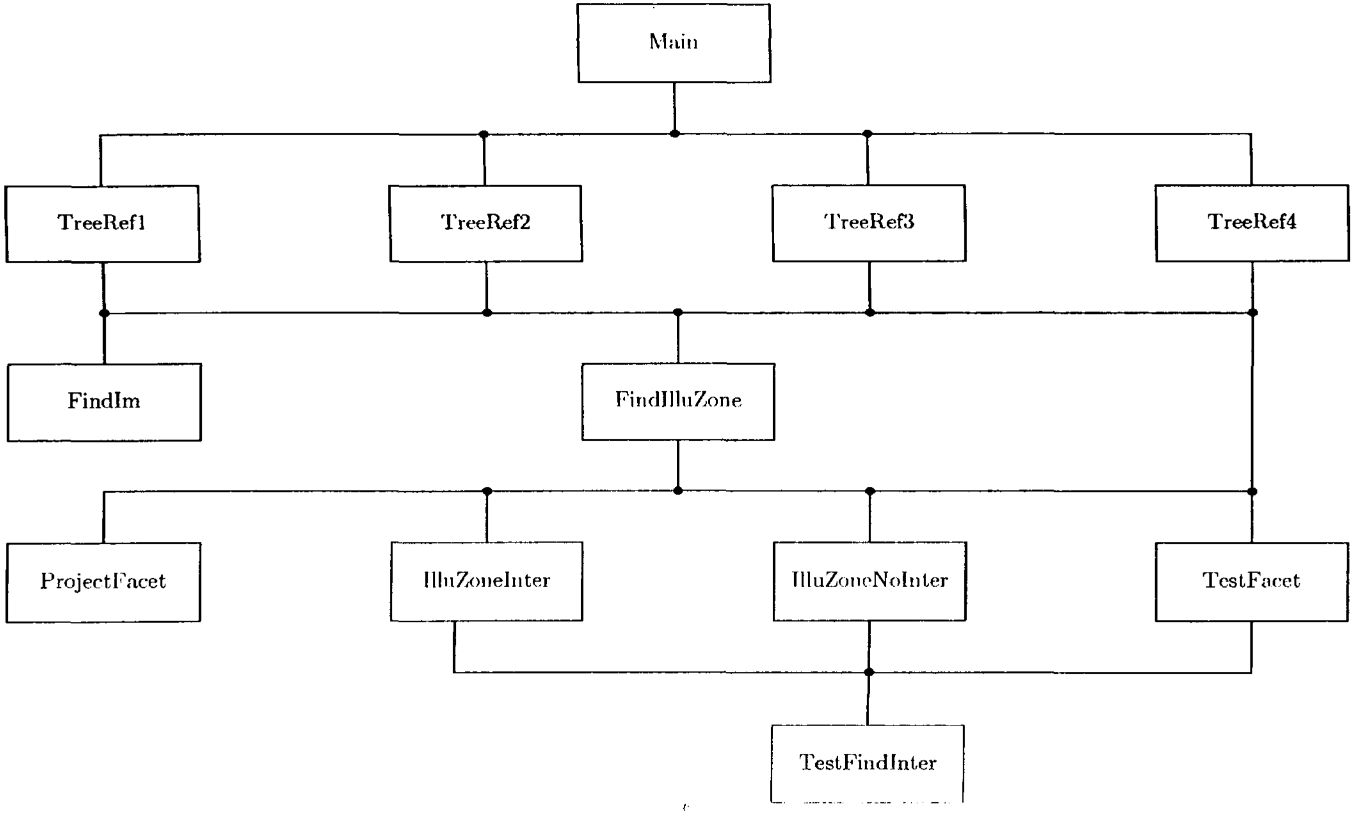

Table D.2: Functions of all subroutines in the diagram 'Ray-Tree Structure'.

Name of Subroutine	**Function of Subroutine**
Main	Generate the ray-tree with user-specified number of reflections
TreeRefl	Compute the ray tree of the 1st reflections.
TreeRef2	Compute the ray tree of the 2nd reflections.
TreeRef3	Compute the ray tree of the 3rd reflections.
TreeRef4	Compute the ray tree of the 4th reflections.
FindIm	Find the image of a point with respect to a facet.
FindIlluZone	Find the illumination zone of a facet with respect to another.
TestFacet	Test if a facet is within the illumination zone of another.
ProjectFacet	Project two related facets on a 2D plane.
IlluZoneInter	Define the illumination zone when two facets do not have an intersection.
IlluZoneNoInter	Define the illumination zone when two facets have an intersection.
TestFindInter	Test two related facets and find the intersection between them.

Main

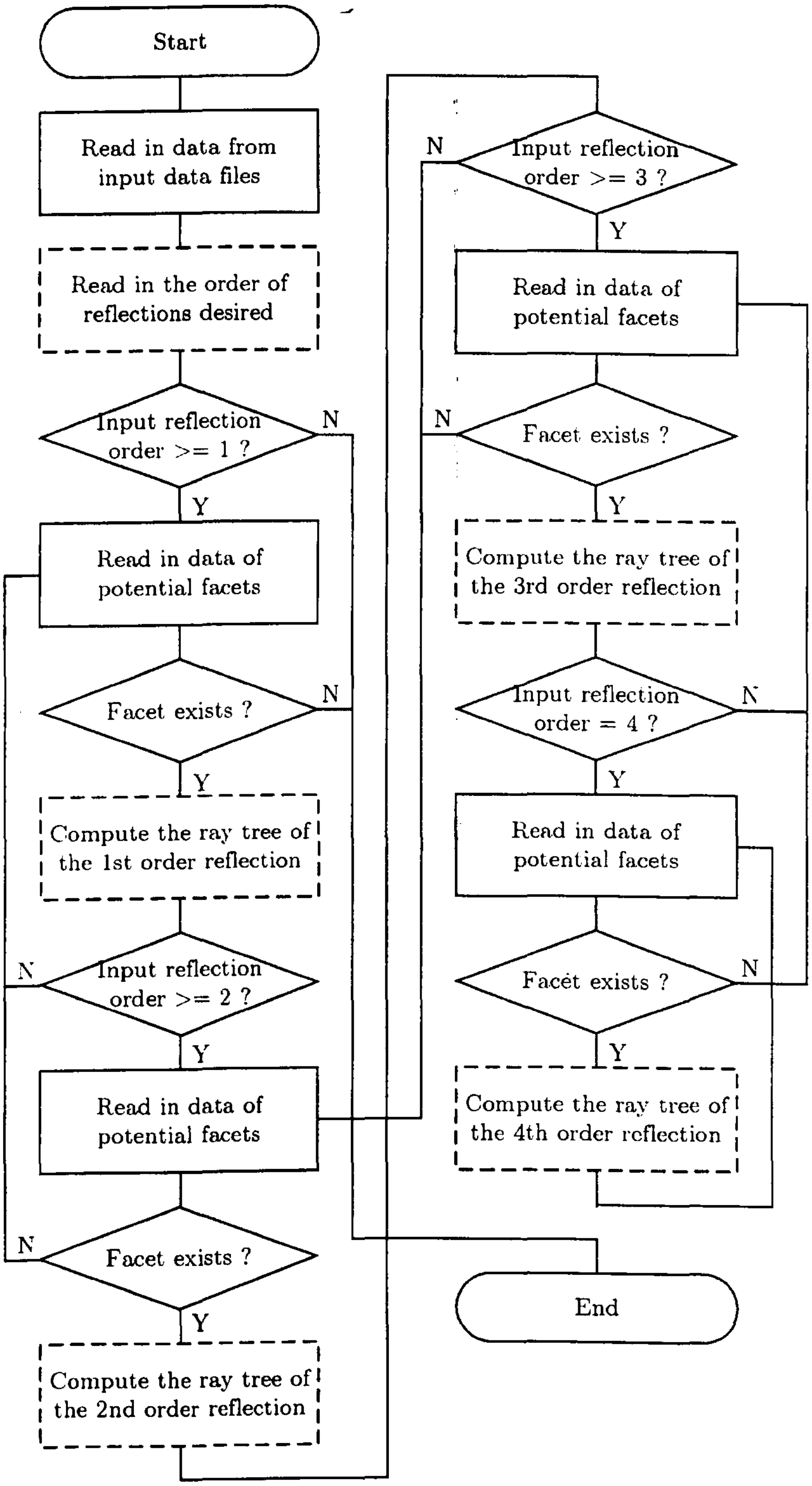
Start
Read in data from input data files
Read in the order of reflections desired
Input reflection order >= 1 ?
N
Y
Read in data of potential facets
Facet exists ?
N
Y
Compute the ray tree of the 1st order reflection
Input reflection order >= 2 ?
N
Y
Read in data of potential facets
Facet exists ?
N
Y
Compute the ray tree of the 2nd order reflection
Input reflection order >= 3 ?
N
Y
Read in data of potential facets
Facet exists ?
N
Y
Compute the ray tree of the 3rd order reflection
Input reflection order = 4 ?
N
Y
Read in data of potential facets
Facet exists ?
N
Y
Compute the ray tree of the 4th order reflection
End

TreeRef1

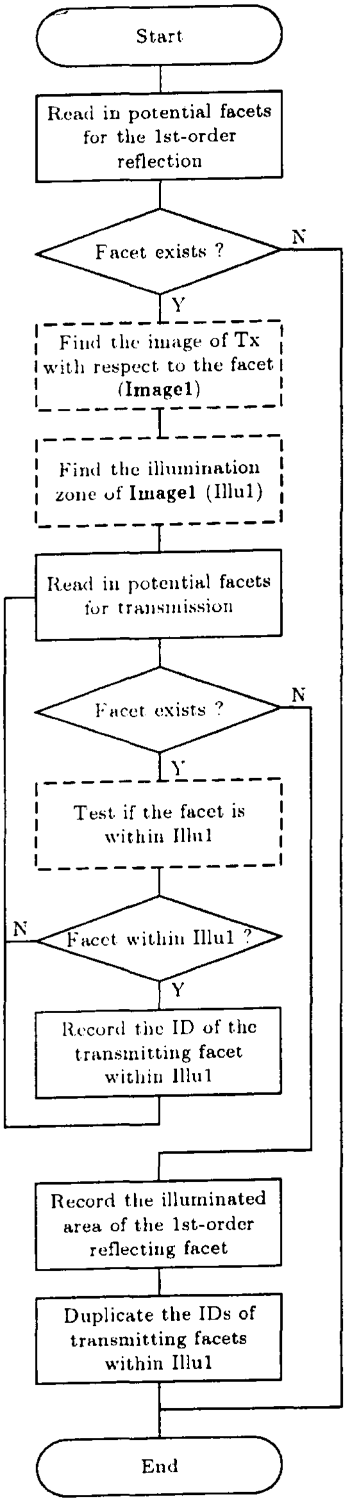

TreeRef2

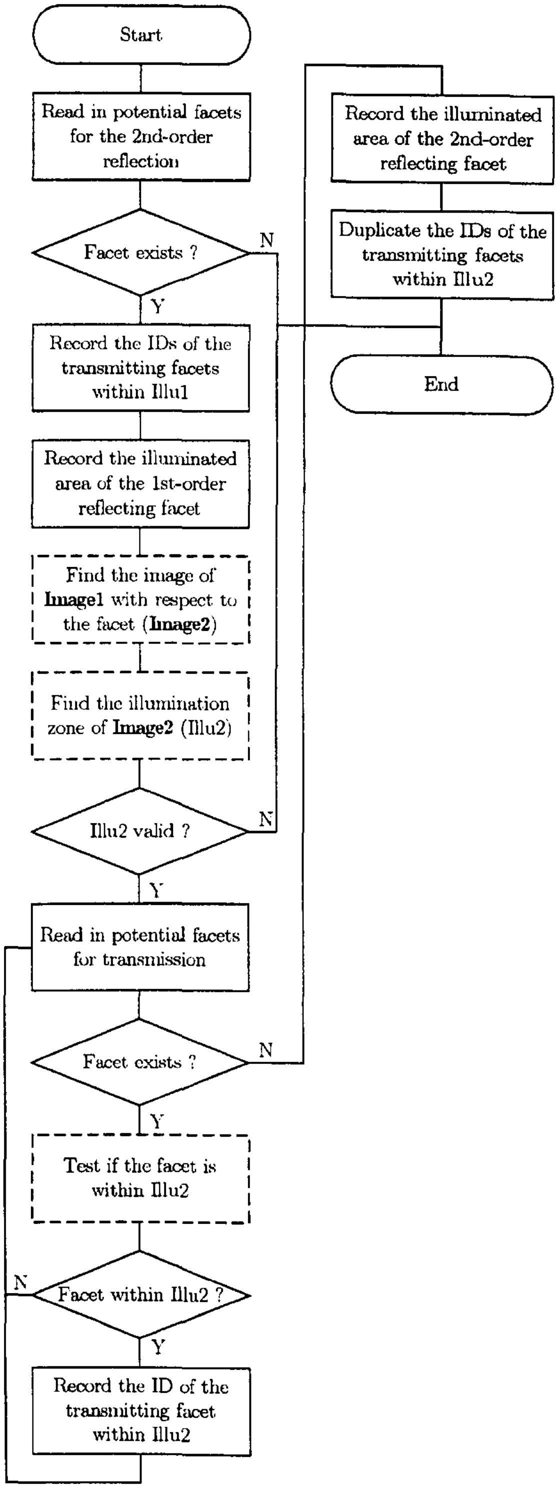

TreeRef3

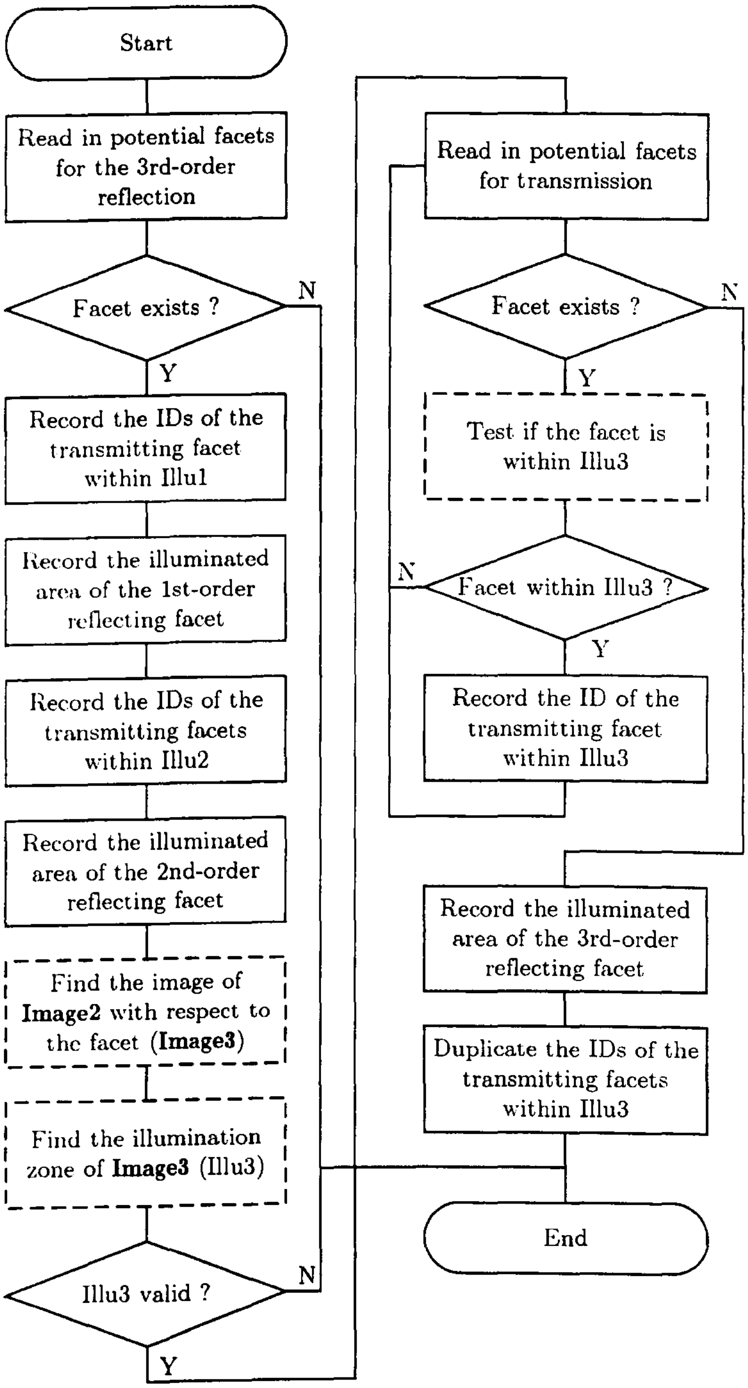
Start
Read in potential facets for the 3rd-order reflection
Facet exists ?
N
Y
Record the IDs of the transmitting facet within Illu1
Record the illuminated area of the 1st-order reflecting facet
Record the IDs of the transmitting facets within Illu2
Record the illuminated area of the 2nd-order reflecting facet
Find the image of **Image2** with respect to the facet (**Image3**)
Find the illumination zone of **Image3** (Illu3)
Illu3 valid ?
N
Y
Read in potential facets for transmission
Facet exists ?
N
Y
Test if the facet is within Illu3
N
Facet within Illu3 ?
Y
Record the ID of the transmitting facet within Illu3
Record the illuminated area of the 3rd-order reflecting facet
Duplicate the IDs of the transmitting facets within Illu3
End

TreeRef4

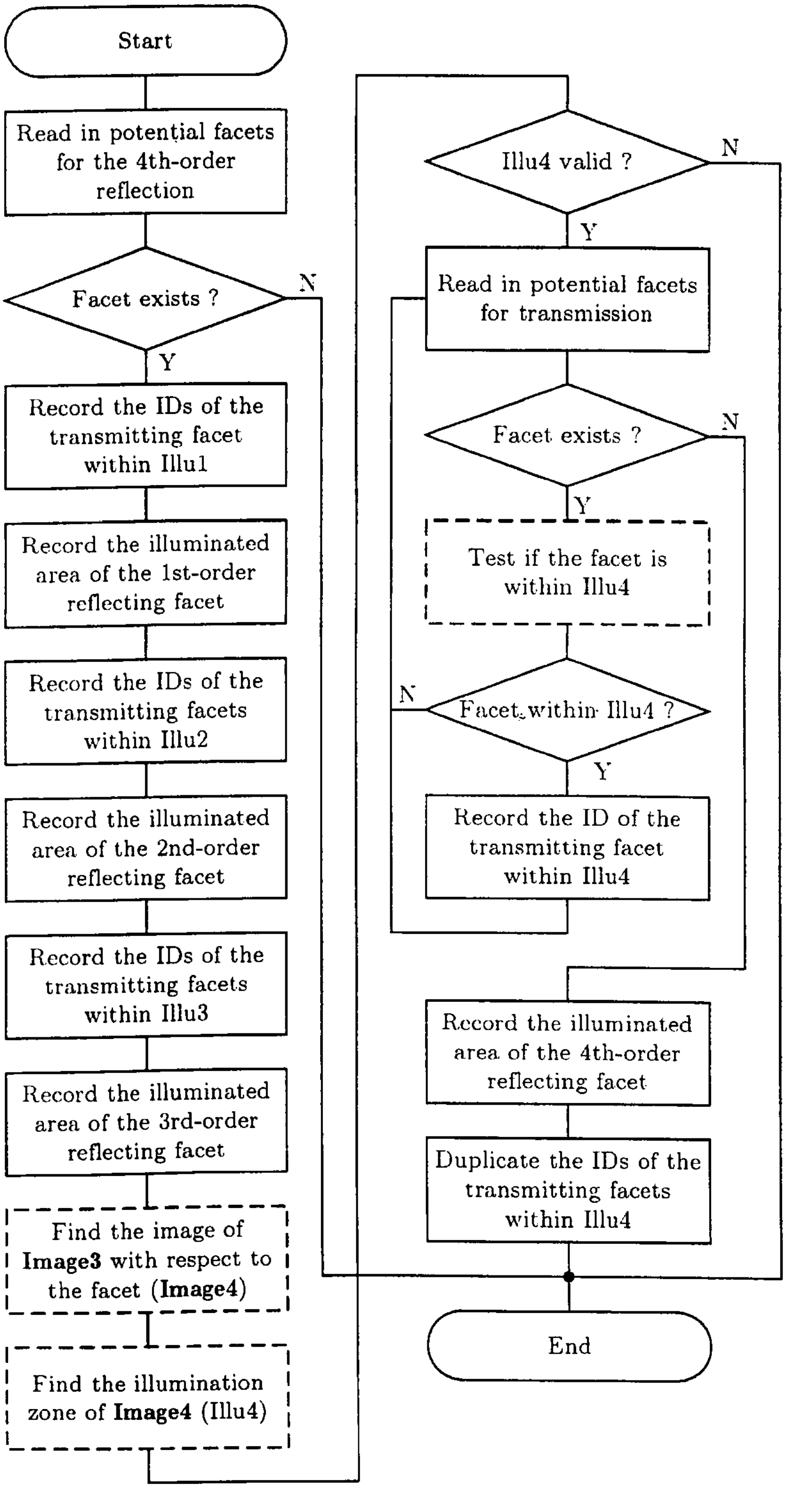
Start
Read in potential facets for the 4th-order reflection
Facet exists ?
N
Y
Record the IDs of the transmitting facet within Illu1
Record the illuminated area of the 1st-order reflecting facet
Record the IDs of the transmitting facets within Illu2
Record the illuminated area of the 2nd-order reflecting facet
Record the IDs of the transmitting facets within Illu3
Record the illuminated area of the 3rd-order reflecting facet
Find the image of **Image3** with respect to the facet (**Image4**)
Find the illumination zone of **Image4** (Illu4)
Illu4 valid ?
N
Y
Read in potential facets for transmission
Facet exists ?
N
Y
Test if the facet is within Illu4
N
Facet within Illu4 ?
Y
Record the ID of the transmitting facet within Illu4
Record the illuminated area of the 4th-order reflecting facet
Duplicate the IDs of the transmitting facets within Illu4
End

FindIlluZone

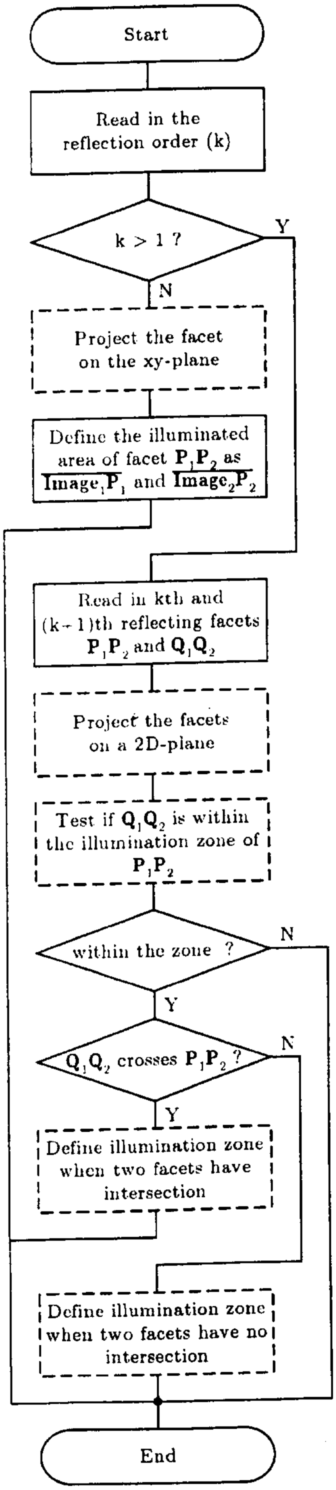

TestFacet

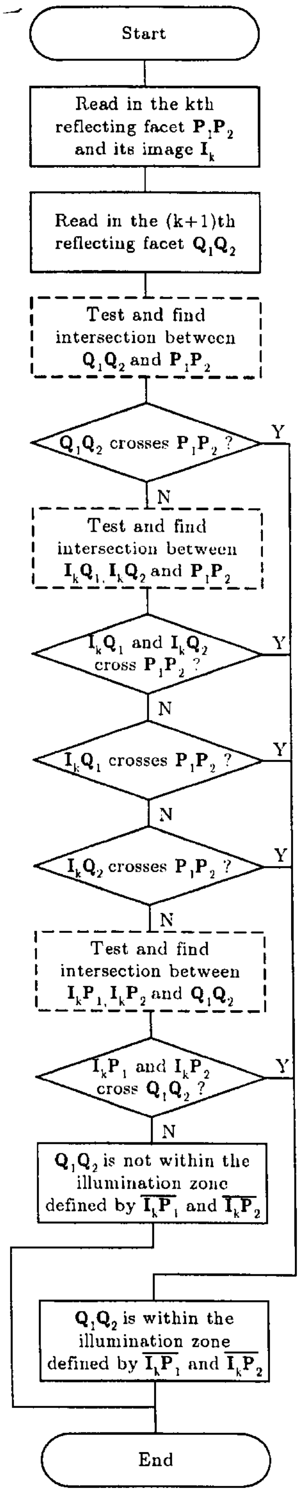

ProjectFacet

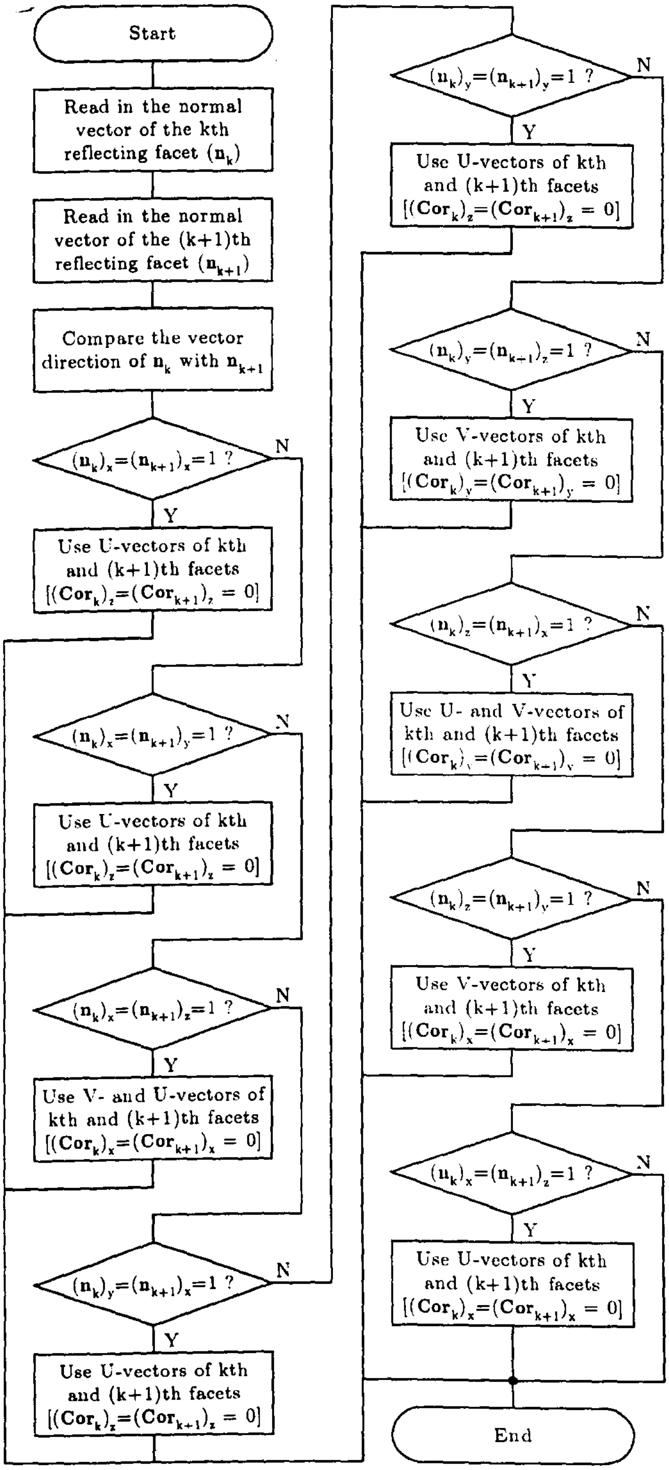

IlluZoneInter

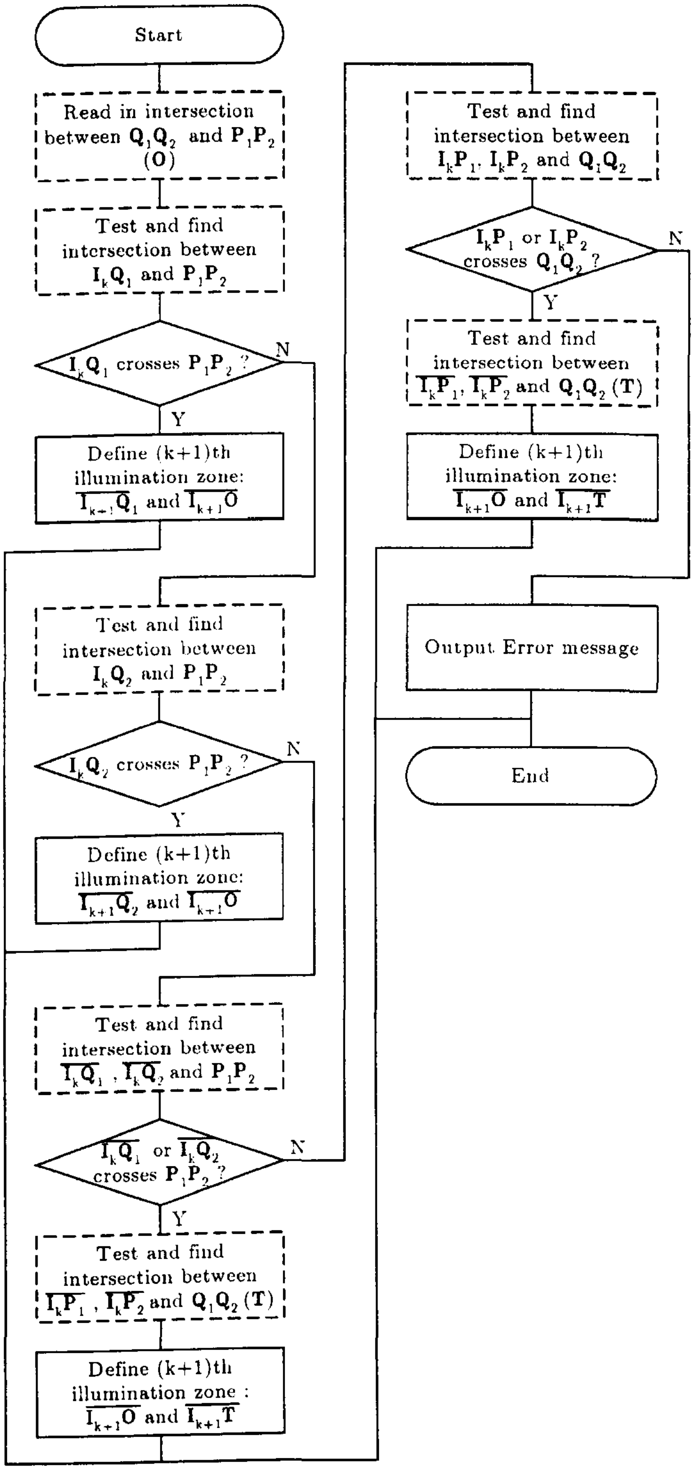

IlluZoneNoInter

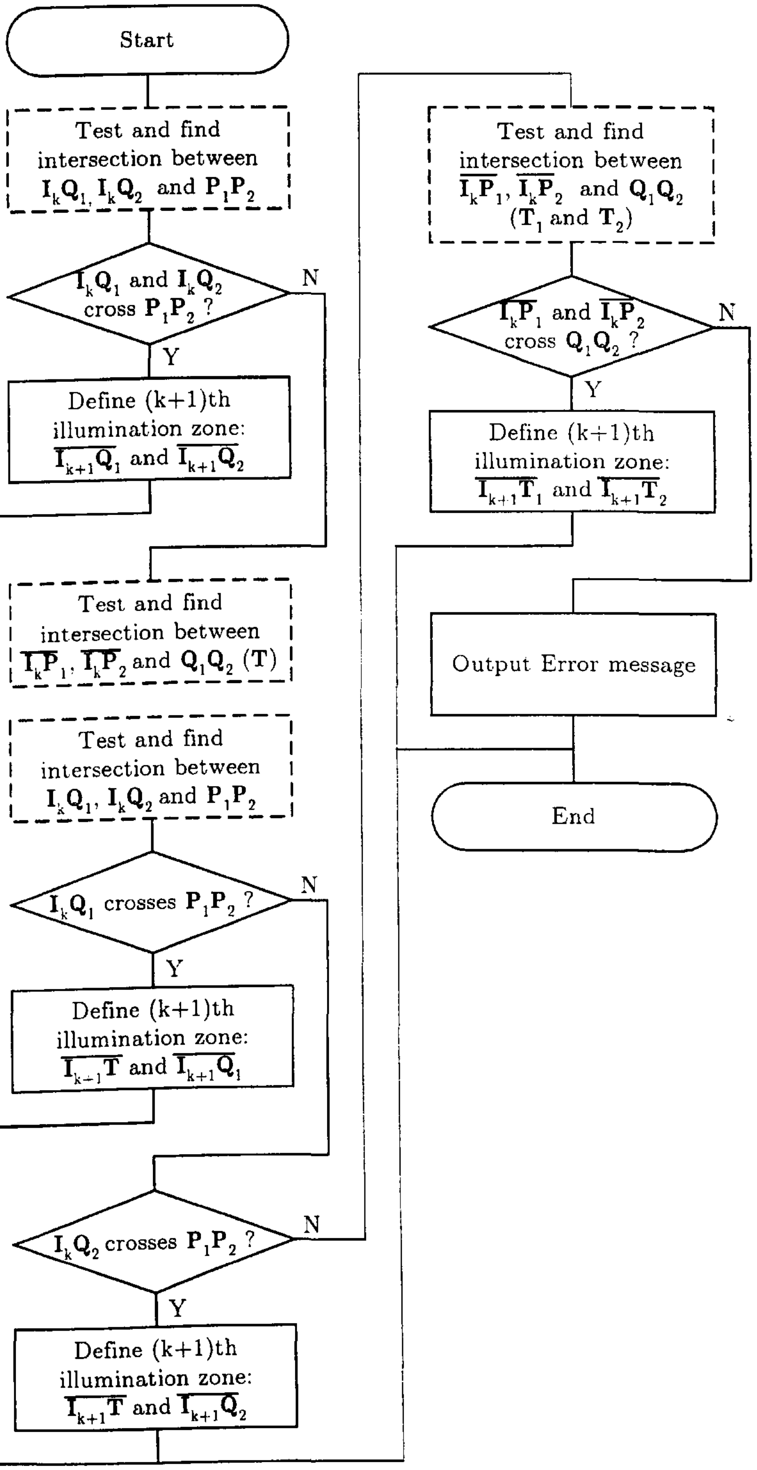

TestFindInter

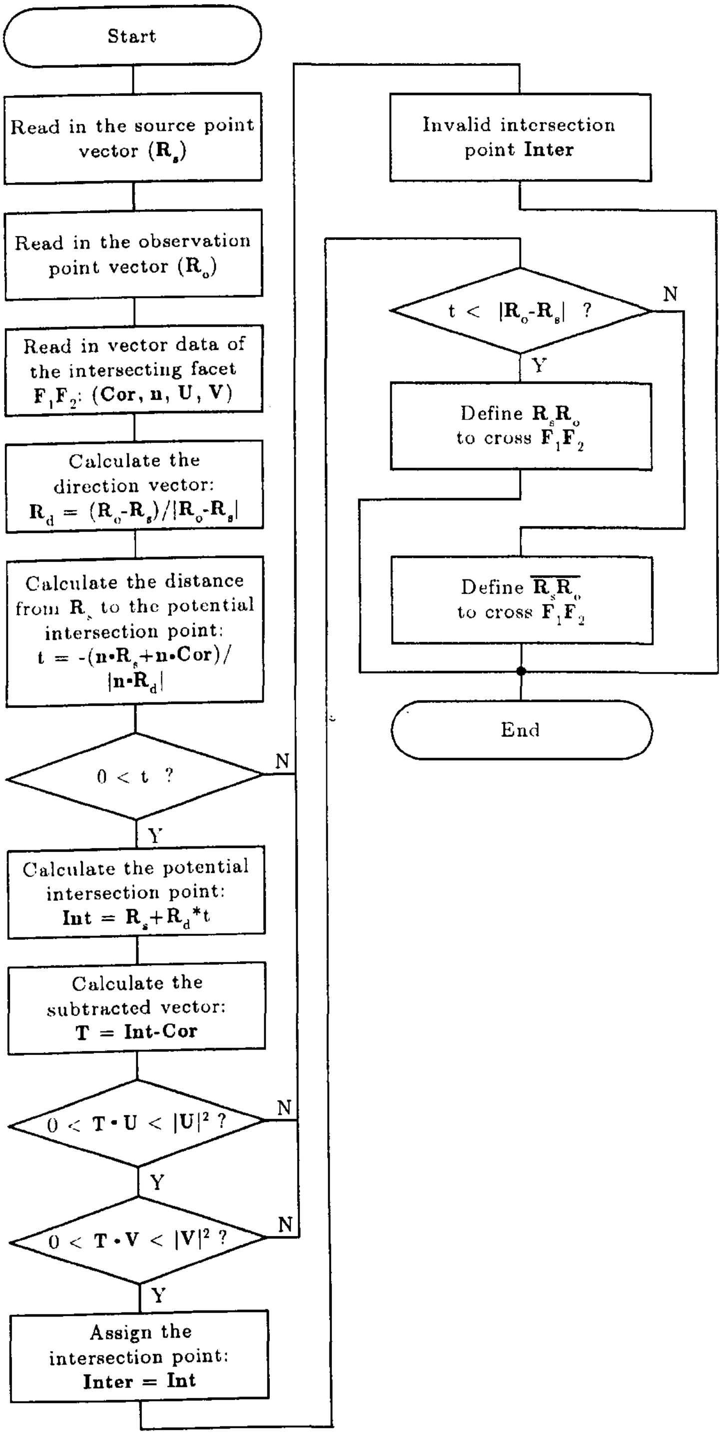

Bibliography

[1] R. Schneiderman, *Wireless personal Communications: The Future of Talk*, Piscataway, NJ: IEEE Press, 1994.

[2] R. Prasad, *Universal Personal Communications*, Norwood, MA: Artech House, 1998.

[3] R. Prasad, W. Mohr, and W. Konhauser, *Third Generation Mobile Communication Systems*, Norwood, MA: Artech House, 2000.

[4] S. Redl, M. Weber, and M. W. Oliphant, *GSM and Personal Communications Handbook*, Norwood, MA: Artech House, 1998.

[5] S. R. Saunders, *Antennas and Propagation for Wireless Communication Systems*, New York: John Wiley & Sons, Inc., 1999.

[6] IEEE 802.11 Web site, http://grouper.ieee.org/groups/802/16.

[7] K. J. Negus, A. P. Stephens, and J. Lansford, "HomeRF: Wireless Networking for the Connected Home", *IEEE Personal Communications*, Vol. 7, No. 1, pp. 20-27, February, 2000.

[8] J. C. Hartsen, "The Bluetooth Radio System," *IEEE Personal Communications*, Vol. 7, No. 1, pp. 28-36, February, 2000.

[9] T. S. Rappaport, *Wireless Communications: Principles & Practice*, Prentice-Hall, Inc., 1996.

[10] A. Kumar, "Measurement of Permittivity of Materials at Microwave Frequency: A Review", *EEIC/ICWA Exposition, Proceedings of the 19th*, pp. 73-77, 1989.

[11] J. J. Laurin, G. Tanneau, and C. Akyel, "Waveguide Permittivity Measurement Using Variable-Length Samples and An Uncalibrated

Reflectometer," *IEEE Transactions on Instrumentation and Measurement*, Vol. 45, No. 1, pp. 298-301, February, 1996.

[12] M. D. Janezic and J. A. Jargon, "Complex Permittivity Determination from Propagation Constant Measurements," *IEEE Microwave and Guided Wave Letters*, Vol. 9, No. 2, pp. 76-78, February, 1999.

[13] P. Delanghe and K. Blomme, et al, "Measurement of Low-Permittivity Materials Based on a Spectral-Domain Analysis for the Open-ended Coaxial Probe", *IEEE Transactions on Instrumentation and Measurement*, vol. 42, no. 5, pp. 879-886, 1993.

[14] J. Baker-Jarvis, M. D. Janezic, P. D. Domich, and R. G. Geyer, "Analysis of an Open-Ended Coaxial Probe with Lift-Off for Nondestructive Testing", *IEEE Transactions on Instrumentation and Measurement*, Vol. 43, No. 5, pp. 711-718, 1994.

[15] S. Bringhurst, M. F. Iskander, and M. J. White, "Thin Sample Measurements and Error Analysis of High Temperature Coaxial Dielectric Probes," *IEEE Transactions on Microwave Theory and Technology*, Vol. 45, pp. 2073-2083, December, 1997.

[16] G. Dhondt, D. De Zutter, and L. Martens, "An Improved Free-Space Modelling for Measuring Dielectric Properties of Materials," *IEEE Antenna and Propagation International Symposium Digest*, pp. 180-183, 1996.

[17] V. V. Varadan, K. A. Jose, and V. K. Varadan, "*In Situ* Microwave Characterisation of Nonplanar Dielectric Objects," *IEEE Transactions on Microwave Theory and Techniques*, Vol. 48, No. 3, pp. 388-394, March, 2000.

[18] J. Matlacz and K. D. Palmer, "Using Offset Parabolic Reflector Antennas for Free Space Material Measurement," *IEEE Transactions on Instrumentation and Measurement*, Vol. 49, No. 4, pp. 862-866, August, 2000

[19] R. T. Johnk, A. R. Ondrejka, and C. L. Holloway, "Time-Domain Free-Space Evaluations of Urethane Slabs with Finite-Difference

Time-Domain Computer Simulation," *IEEE Int. Symp. Digest on Electromagnetic Compatibility*, pp. 290-295, 1998.

[20] K. Otsuka, O. Hashimoto, and T. Ishida, "Measurement of Complex Permittivity of Low-Loss Dielectric Material at 94 GHz Frequency Band Using Free-Space Method," *Microwave and Optical Technology Letters*, Vol. 22, No. 5, pp. 291-292, September, 1999.

[21] O. Landron, M. J. Feuerstein, and T. S. Rappaport, "A Comparison of Theoretical and Empirical Reflection Coefficients for Typical Exterior Wall Surfaces in a Mobile Radio Environment," *IEEE Transactions on Antennas and Propagation*, Vol. 44, No. 3, pp. 341-351, March, 1996.

[22] Z. Ma and S. Okamura, "Permittivity Determination Using Amplitudes of Transmission and Reflection Coefficients at Microwave Frequency," *IEEE Transactions on Microwave Theory and Techniques*, Vol. 47, No. 5, pp. 546-550, May, 1999.

[23] http://www.adtest.co.za/Anritsu.htm

[24] D. Huston, K. Maser, J. Hu, B. Weedon, and C. Adam, "Bridge Deck Evaluation with Ground Penetrating Radar," *Proceedings GPR '98 7th International Conference on Ground-Penetrating Radar*, pp. 595-599, September, 1998.

[25] J. R. Wait, *Wave Propagation Theory*, Pergramon Press, USA, 1981.

[26] M. Nakhkash, Y. Huang and M.T.C Fang, "Application of the Multilevel Single-Linkage Method to One-Dimensional Electromagnetic Inverse Scattering Problem", *IEEE Transactions on Antènna and Propagation*, vol. 47, no. 11, pp. 1658-1676, 1999.

[27] N. S. Nahman and M. E. Guillaume, "Deconvolution of Time Domain Waveforms in the Presence of Noise," Nat. Bur. Stands. (US) Tech. Note 1047, Oct, 1981.

[28] E. C. Jordan and K. G. Balmain, *Electromagnetic Waves and Radiating systems*, Englewood-Clifs: Prentice-Hall, 1968.

[29] D. K. Ghodgaonkar, V. V. Varadan, and V. K. Varadan, "Free-Space Measurement of Complex Permittivity and Complex

Permeability at Microwave Frequencies," *IEEE Transactions on Instrumentation and Measurement*, Vol. 39, No. 2, pp. 387-394, April, 1990.

[30] W. A. van Cappellen, R. V. de Jongh, and L. P. Ligthart, "Potentials of Ultra-Short-Pulse Time-Domain Scattering Measurements," *IEEE Antennas and Propagation Magazine*, Vol. 42, No. 4, pp. 35-45, August, 2000.

[31] J. D. Parsons, *The Mobile Radio Propagation Channel, 2^{nd} ed.*, New York: John Wiley & Sons, Inc., 2000

[32] S. Y. Seidel and T. S. Rappaport, "Site-Specific Propagation Prediction for Wireless In-Building Personal Communication System Design," *IEEE Transactions on Vehicular Technology*, Vol. 43, No. 4, pp. 879-891, November, 1994.

[33] J. Shapira, "Channel Characteristics for Land Cellular Radio, and Their Systems Implications," *IEEE Antennas and Propagation Magazine*, Vol. 34, No. 4, pp. 7-16, August, 1992.

[34] H. T. Friis, "A Note on a Simple Transmission Formula," *Proc. IRE*, Vol. 34, pp. 254-256, 1946.

[35] T. A. Sexton and K. Pahlavan, "Channel Modelling and Adaptive Equalisation of Indoor Radio Channels," *IEEE Journal on Selected Areas in Communications*, Vol. JSAC-5, pp. 128-137, February, 1987.

[36] B. Glance and L. J. Greenstein, "Frequency Selective Fading Effects in Digital Mobile Radio with Diversity Combining," *IEEE Transactions on Communications*, Vol. COM-31, No. 9, pp. 1085-1094, September, 1983.

[37] W. C. Y. Lee, *Mobile Communications Engineering*, New York: McGraw-Hill, 1982

[38] A. Taflove, *Computational Electrodynamics: The Finite-Difference Time-Domain Method*, Norwood MA: Artech House, 1995.

[39] A. S. Glassner, *An Introduction to Ray Tracing*, San Diego, CA: Academic Press, 1989.

[40] J. D. Foley, S. K. van Dam, and J. F. Hughes, *Computer Graphics: Principles and Practice*, New York: Addison-Wesley, 1995.

[41] U. Dersch and E. Zollinger, "Propagation Mechanisms in Microcell and Indoor Environments," *IEEE Transactions on Vehicular Technology*, Vol. 43, No. 4, pp. 1058-1066, November, 1994.

[42] T. S. Rappaport, S. Y. Seidel, and K. R. Schaubach, "*Site-Specific Propagation for PCS System Design*," in *Wireless Personal Communications*, M. J. Feuerstein and T. S. Rappaport, eds., Boston: Kluwer Academic Publishers, pp. 281-315, 1993.

[43] K. R. Schaubach and N. J. Davis, "Microcellular Radio-Channel Propagation Prediction," *IEEE Antennas and Propagation Magazine*, Vol. 36, No. 4, pp. 25-34, August, 1994.

[44] S. Y. Tan and H. S. Tan, "Improved Three-Dimensional Ray Tracing Techniques for Microcellular Propagation Models," *Electronics Letters*, Vol. 31, No. 17, pp. 1503-1505, August, 1995.

[45] G. Liang and H. L. Bertoni, "A New Approach to 3-D Ray Tracing for Propagation Prediction in Cities," *IEEE Transactions on Antennas and Propagation*, Vol. 46, No. 6, pp. 853-863, June, 1998.

[46] S. C. Kim, B. J. Guarino, *et al*, "Radio Propagation Measurements and Prediction Using Three-Dimensional Ray Tracing in Urban Environments at 908 MHz and 1.9 GHz," *IEEE Transactions on Vehicular Technology*, Vol. 48, No. 3, pp. 931-946, May, 1999.

[47] K. R. Chang and H. T. Kim, "Prediction of Beam Tilting Effects Using an Enhanced Ray Launching Model in the Urban Area," *IEEE Transactions on Vehicular Technology*, Vol. 49, No. 3, pp. 734-743, May, 2000.

[48] S. Y. Tan and H. S. Tan, "Modelling and Measurements of Channel Impulse Response for an Indoor wireless Communication System," *IEE Proceedings – Microwaves Antennas and Propagation*, Vol. 142, No. 5, pp. 405-410, October, 1995.

[49] H. Suzuki and A. S. Mohan, "Ray Tube Tracing Method for Predicting Indoor Channel Characteristics Map," *Electronics Letters*, Vol. 33, No. 17 pp. 1495-1496, August, 1997.

[50] J. H. Tarng and D. W. Perng, "Modelling and Measurement of UHF Radio Propagating through Floors in A Multifloored Building," *IEE Proceedings - Microwaves Antennas and Propagation*, Vol. 144, No. 5, pp. 359-363, October, 1997.

[51] Z. Yun, M. F. Iskander and Z. Zhang, "Fast Ray Tracing Procedure Using Space Division With Uniform Rectangular Grid," *Electronics Letters*, Vol. 36, No. 10, pp. 895-897, May, 2000.

[52] S. Y. Tan, T. W. Ang, and H. S. Tan, "A Ray-Tracing Model for Multipath Propagation Prediction in Picocellular Environments," *Microwave and Optical Technology Letters*, Vol. 25, No. 6, pp. 371-375, June, 2000.

[53] M. F. Catedra, *Cell Planning for Wireless Communications*, Boston: Artech House Publishers, 1999.

[54] D. A. McNamara, C. W. I. Pistorius, and J. A. G. Malherbe, *Introduction to The Uniform Geometrical Theory of Diffraction*, London: Artech House, 1990.

[55] S. J. Fortune, D. M. Gay, *et al*, "WISE Design of Indoor Wireless Systems: Practical Computation and Optimization," *IEEE Computational Science & Engineering*, Vol. 2, No. 1, pp. 58-68, SPR,1995.

[56] J. H. Tarng, W. R. Chang, and B. J. Hsu, "Three-Dimensional Modelling of 900-MHz and 2.44-GHz Radio Propagation in Corridors," *IEEE Transactions on Vehicular Technology*, Vol. 46, No. 2, pp. 519-527, May, 1997.

[57] W. Honcharenko, H. L. Bertoni, and J. L. Dailing *et al*, "Mechanism Governing UHF Propagation on Single Floors in Modern Office Builidngs," *IEEE Transactions on Vehicular Technology*, Vol. 41, pp. 496-504, November, 1992.

[58] J. H. Tarng and T. R. Liu, "Effective Models in Evaluating Radio Coverage on Single Floors of Multifloor Buildings," *IEEE Transactions on Vehicular Technology*, Vol. 48, No. 3, pp. 782-789, May, 1999.

[59] J. Zhong, B. H. Li, H. X. Wang, H. Y. Chen, and T. K. Sarkar, "Efficient Ray-Tracing Methods for Propagation Prediction for Indoor Wireless Communications," *IEEE Antennas and Propagation Magazine*, Vol. 43, No. 2, pp. 41-49, April, 2001.

[60] W. Stutzman and G. Thiele, *Antenna Theory and Design*, New York: Wiley, 1981.

[61] S. Kim, b. Bougerolles and H. L. Bertoni, "Transmission and Reflection Properties of Interior Walls," *Proceedings of IEEE Third Annual International Conference on Universal Personal Communications*, pp. 124-128, 1994.

[62] M. Barbiroli, C. Carciofi, G. Falciasecca, M. Frullone, and P. Grazioso, "A Measurement-Based Methodology for the Determination of Validity Domains of Prediction Models in Urban Environment," *IEEE Transactions on Vehicular Technology*, Vol. 49, No. 5, pp. 1508-1515, September, 2000.

[63] G. E. Athanasiadou, A. R. Nix, and J. P. McGeehan, "A Microcellular Ray-Tracing Propagation Model and Evaluation of its Narrow-Band and Wide-Band Predictions," *IEEE Journal on Selected Areas in Communications*, Vol. 18, No. 3, pp. 322-335, March, 2000.

[64] H. R. Anderson, "Building Corner Diffraction Measurements and Predictions Using UTD," *IEEE Transactions on Antennas and Propagation*, Vol. 46, No. 2, pp. 292-295, February, 1998.

[65] C. A. Balanis, *Advanced Engineering Electromagnetics*, New York: John Wiley, 1989.

[66] H. Bremmer and S. W. Lee, "Geometrical Optics Solution of Reflection from an Arbitrarily Curved Surface," *Radio Science*, vol. 17, pp. 1117-1131, 1982.

[67] J. A. Kong, *Theory of Electromagnetic Waves*, New York: Wiley, 1975.

[68] M. Schneider and R. J. Luebbers, "A General, Uniform Double Wedge Diffraction Coefficient," *IEEE Transactions on Antennas and Propagation*, Vol. 39, No. 1, pp. 8-14, January, 1991.

[69] T. S. Rappaport, "Characterization of UHF Multipath Radio Channels in Factory Buildings," *IEEE Transactions on Antennas and Propagation*, Vol. 37, pp. 1058-1069, August, 1989.

[70] R. A. Valenzuela, O. Landron, and D. L. Jacobs, "Estimating Local Mean Signal Strength of Indoor Multipath Propagation," *IEEE Transactions on Vehicular Technology*, Vol. 46, No. 1, pp. 203-212, February, 1997.

[71] H. W. Son and N. H. Myung, "3-D Ray Tracing Technique for Wave Propagation in Urban Environments," *Electronics Letters*, Vol. 35, No. 11, pp. 932-933, May, 1999.

[72] Y. L. C. de Jong and M. H. A. J. Herben, "Prediction of Local Mean Power Using 2-D Ray-Tracing-Based Propagation Models," *IEEE Transactions on Vehicular Technology*, Vol. 50, No. 1, pp. 325-331, January, 2001.

[73] J. B. Keller, "Geometrical Theory of Diffraction," *J. Opt. Soc. of America*, Vol. 52, No. 2, pp. 116-130, February, 1962.

[74] R. G. Kouyoumjian and P. H. Pathak, "A Uniform Geometrical Theory of Diffraction for an Edge in a Perfectly Conducting Surface," *Proc. IEEE*, Vol. 62, pp. 1448-1461, November, 1974.

[75] S. H. Chen and S. K. Jeng, "An SBR/Image Approach for Indoor Radio Propagation in a Corridor," *IEICE Transactions on Electronics*, Vol. E78-C, No. 8, pp. 1058-1062, August, 1995.

[76] S. H. Chen and S. K. Jeng, "A SBR/Image Approach for Radio Wave Propagation in Indoor Environments with Metallic Furniture," *IEEE Transactions on Antennas and Propagation*, Vol. 45, No. 1, pp. 98-106, January, 1997.

[77] R. P. Torres, L. Valle, M. Domingo, S. Loredo, and M. C. Diez, "CINDOOR: An Engineering Tool for Planning and Design of Wireless Systems in Enclosed Spaces," *IEEE Antennas and Propagation Magazine*, Vol. 41, No. 4, pp. 11-21, August, 1999.

[78] J. Horikoshi, K. Tanaka, and T. Morinaga, "1.2 GHz Band Wave Propagation Measurements in Concrete Building for Indoor Radio Communications," *IEEE Transactions on Vehicular Technology*, Vol. VT-35, No. 4, pp. 146-152, November, 1986.

[79] Y. Wang, S. Safavi-Naeini, and S. K. Chaudhuri, "A Hybrid Technique Based on Combining Ray Tracing and FDTD Methods for Site-Specific Modelling of Indoor Radio Wave Propagation," *IEEE Transactions on Antennas and Propagation*, Vol. 48, No. 5, pp. 743-754, May, 2000.

[80] C. F. Yang, B. C. Wu, and C. J. Ko, "A Ray-Tracing Method for Modeling Indoor Wave Propagation and Penetration," *IEEE Transactions on Antennas and Propagation*, Vol. 46, No. 6, pp. 907-919, June, 1998.

[81] L. Zheng, "Indoor Mobile Radio Channel Characterisation," *M.Sc. thesis*, University of Liverpool, 1999.

[82] L. Talbi, "Effect of Frequency Carrier on Indoor Propagation Channel," *Electronics Letters*, Vol. 36, No. 15, pp. 1309-1310, July, 2000.

[83] H. W. Arnold, R. R. Murray and D. C. Cox, "815 MHz Radio Attenuation Measured Within Two Commercial Buildings," *IEEE Transactions on Antennas and Propagation*, Vol. 37, No. 10, pp. 1335-1339, October, 1989.

[84] J. Kivinen, X. Zhao, and P. Vainikainen, "Empirical Characterization of Wideband Indoor Radio Channel at 5.3 GHz," *IEEE Transactions on Antennas and Propagation*, Vol. 49, No. 8, pp. 1192-1203, August, 2001.

[85] S. Chatterjee and B. Price, *Statistical Models in Applied Science*, USA: Jonn Wiley & Sons, 1975.

[86] W. D. Burnside and K. W. Burgener, "High Frequency Scattering by a Thin Lossless Dielectric Slab," *IEEE Transactions on Antennas and Propagation,* Vol. AP-31, No. 1, pp. 104-110, January, 1983.

[87] R. J. Luebbers, "Finite conductivity Uniform GTD Versus Knife Edge Diffraction in Prediction of Propagation Path Loss," *IEEE Transactions on Antennas and Propagation*, Vol. AP-32, pp. 70-76, January, 1984.

[88] S. C. Kim, H. L. Bertoni, and M. Stern, "Pulse Propagation Characteristics at 2.4 GHz Inside Buildings," *IEEE Transactions on Vehicular Technology*, Vol. 45, No. 3, pp. 579-592, August, 1996.

[89] Z. Ji, T. K. Sarkar, and B. Li, "Analysis of The Effects of Walls on Indoor Wave Propagation Using The FDTD Method," *Microwave and Optical Technology Letters*, Vol. 29, No. 1, pp. 19-21, April, 2001.

[90] H. L. Bertoni, *Radio Propagation for Modern Wireless Systems*, New Jersey: Prentice Hall, 2000.

[91] G. E. Athanasiadou and A. R. Nix, "A Novel 3-D Indoor Ray-Tracing Propagation Model: The Path Generator and Evaluation of Narrow-Band and Wide-Band Predictions," *IEEE Transactions on Vehicular Technology*, Vol. 49, No. 4, pp. 1152-1168, July, 2000.

[92] I. Cuinas and M. G. Sanchez, "Measuring, Modelling, and Characterizing of Indoor Radio Channel at 5.8 GHz," *IEEE Transactions on Vehicular Technology*, Vol. 50, No. 2, pp. 526-535, March, 2001.

[93] J. H. Tarng, R. S. Chang, J. M. Huang, and Y. M. Tu, "A New and Efficient Hybrid Model for Estimating Space Diversity in Indoor Environment," *IEEE Transactions on Vehicular Technology*, Vol. 49, No. 2, pp. 457-466, March, 2000.

[94] G. E. Corazza, V. Degli-Esposti, M. Frullone, and G. Riva, "A Characterization of Indoor Space and Frequency Diversity by Ray-Tracing Modeling," *IEEE Journal on Selected Areas in Communications*, Vol. 14, No. 3, pp. 411-419, April, 1996.

[95] S. Loredo, L. Valle, and R. P. Torres, "Accuracy Analysis of GO/UTD Radio-Channel Modeling in Indoor Scenarios at 1.8 and 2.5 GHz," *IEEE Antennas and Propagation Magazine*, Vol. 43, No. 5, pp. 37-51, October, 2001.

[96] F. A. Agelet, A. Formella, J. M. H. Rabanos, F. Isadi de Vicente, and F. P. Fontan, "Efficient Ray-Tracing Acceleration Techniques for Radio Propagation Modelling," *IEEE Transactions on Vehicular Technology*, Vol. 49, No. 6, pp. 2089-2104, November, 2000.

[97] V. Degli-Esposti, G. Lombardi and C. Passerini, "Measurement and Ray-Tracing Prediction of Indoor Channel Parameters," *Electronics Letters*, Vol. 34, No. 22, pp. 2167-2168, October, 1998.

[98] K. Rizk, J. F. Wagen, and F. Gardiol, "Two-Dimensional Ray-Tracing Modelling for Propagation Prediction in Microcellular Environments," *IEEE Transactions on Vehicular Technology*, Vol. 46, No. 2, pp. 508-518, May, 1997.

[99] V. Degli-Esposti, G. Lombardi, C. Passerini, and G. Riva, "Wide-Band Measurement and Ray-Tracing Simulation of the 1900-MHz Indoor Propagation Channel: Comparison Criteria and Results," *IEEE Transactions on Antennas and Propagation*, Vol. 49, No. 7, pp. 1101-1110, July, 2001.

[100] H. Hashemi, and D. Tholl, "Statistical Modelling and Simulation of RMS Delay Spread of Indoor Radio Propagation Channels," *IEEE Transactions on Vehicular Technology*, Vol. 43, No. 1, pp. 110-120, February, 1994.

[101] W. C. Jakes, *Microwave Mobile Communications*, New York: Wiley, 1974.

[102] G. J. M. Janssen, P. A. Stigter, and R. Prasad, "Wideband Indoor Channel Measurements and BER Analysis of Frequency Selective Multipath Channels at 2.4, 4.75, and 11.5 GHz," *IEEE Transactions on Communications*, Vol. 44, No. 10, pp. 1272-1288, October, 1996.

[103] M. S. Varela and M. G. Sanchez, "RMS Delay and Coherence Bandwith Measurements in Indoor Radio Channels in the UHF

Band," *IEEE Transactions on Vehicular Technology*, Vol. 50, No. 2, pp. 515-525, March, 2001.

[104] J. M. Keenan and A. J. Motley, "Radio Coverage in Buildings," *BT Telecom Journal*, Vol. 8, No. 1, pp. 19-24, Jan, 1990.

[105] S. Y. Seidel and T. S. Rappaport, "914 MHz Path Loss Prediction Models for Indoor Wireless Communications in Multifloored Buildings," *IEEE Transactions on Antennas and Propagation*, Vol. 40, No. 2, pp. 207-217, 1992.

[106] G. M. Whitman, K. S. Kim, and E. Niver, "A Theoretical Model for Radio Signal Attenuation Inside Buildings," *IEEE Transactions on Vehicular Technology*, Vol. 44, No. 3, pp. 621-629, August, 1995.

[107] S. Y. Tan and H. S. Tan, "A Theory for Propagation Path-Loss Characteristics in a City-Street Grid," *IEEE Transactions on Electromagnetic Compatibility*, Vol. 37, No. 3, pp. 333-342, August, 1995.

[108] A. G. Kanatas, I. D. Kountouris, G. B. Kostaras, and P. Constantinou, "A UTD Propagation Model in Urban Microcellular Environments," *IEEE Transactions on Vehicular Technology*, Vol. 46, No. 1, pp. 185-193, February, 1997.

[109] K. Rizk, J. F. Wagen, and F. Gardiol, "Influence of Database Accuracy on Two-Dimensional Ray-Tracing-Based Predictions in Urban Microcells," *IEEE Transactions on Vehicular Technology*, Vol. 49, No. 2, pp. 631-642, March, 2000.

[110] K. W. Cheung, J. H. M. Sau, and R. D. Murch, "A New Empirical Model for Indoor Propagation Prediction," *IEEE Transactions on Vehicular Technology*, Vol. 47, No. 3, pp. 996-1001, August, 1998.

[111] J. Wallace, and M. A. Jensen, "Modelling the Indoor MIMO Wireless Channel", *IEEE Transactions on Antennas and Propagation*, Vol. 50, No. 5, pp. 591-599, May, 2002.

[112] A. H. G. Rinnooy Kan and G. T. Timmer, "Stochastic global optimization methods. Part II: multi level methods," *Mathematical Programming*, Vol. 39, pp. 57-78, 1987.

[113] M. Nakhkash, "The Application of Ground Penetrating Radar to the Characterisation of Multi-Layered Media," *Ph.D. thesis*, University of Liverpool, 1999.

[114] P. E. Gill, W. Murray, and M. H. Wright, *Practical Optimisation*, Academic Press, London, 1981.

[115] J. D. Kraus and D. A. Fleisch, *Electromagnetics: with applications*, McGraw-Hill, Boston, 1999.

[116] J. T. Zhang, M. Nakhkash, and Y. Huang, "In-situ Characterisation of Building Materials", *11th IEE International Conference on Antenna and Propagations*, pp. 269-274, March, 2001.

[117] J. T. Zhang, M. Nakhkash, and Y. Huang, "Electromagnetic Imaging of Layered Building Materials," *Measurement Science and Technology*, Vol. 12, pp. 1147-1152, August, 2001.

[118] S. Naruniranat, "A Three-dimensional Image Ray Tracing Methodfor Indoor Wireless Channel Characterisation," *Ph.D. thesis*, University of Liverpool, 2000.

[119] http://msdn.microsoft.com/visualc/#

[120] http://www.impactenvironmental.com/links/gssi.htm

[121] J. T. Zhang and Y. Huang, "Indoor Channel Characteristics Comparisons for The Same Building With Different Dielectric Parameters," *50th IEEE International Conference on Communications*, USA, April, 2001.

[122] J. T. Zhang and Y. Huang, "Investigation of Building Dielectric Properties and the Effects on Indoor Radio Channel," *12th IEE International Conference on Antenna and Propagations*, UK, April, 2003.